Aus der Radiologischen Universitätsklinik der Universität Heidelberg
Abteilung für Radioonkologie und Strahlentherapie
Ärztlicher Direktor: Prof. Dr. med. Dr. rer. nat. Jürgen Debus

A Comprehensive Framework for Dose Calculation in Intensity-Modulated Lung Cancer Particle Therapy

**Inauguraldissertation zur Erlangung des
Doctor scientiarum humanarum an der Medizinischen Fakultät Heidelberg
der Ruprecht-Karls-Universität**

vorgelegt von

Noa Nikola Homolka

geboren in

Sindelfingen

2024

Dekan: Herr Prof. Dr. Michael Boutros
Doktorvater: Herr Prof. Dr. Oliver Jäkel

For my family.

Contents

Acronyms

List of Figures

List of Tables

Introduction

Lung cancer is one of the most prevalent types of cancer worldwide, accounting for a significant portion of cancer diagnoses and mortality. In 2022, lung cancer was the most frequently diagnosed cancer globally, with approximately 2.5 million new cases, representing 12.4 % of all cancer cases. It remains the leading cause of cancer-related deaths, with a mortality rate of 16.8[1] (Ferlay et al. 2024). As a result, addressing lung cancer remains one of the greatest challenges in modern healthcare.

The most common type of lung cancer is Non-Small Cell Lung Cancer (NSCLC). Current treatment options include a combination of chemotherapy, surgery, and radiotherapy. It is estimated, that 50 % to 60 % of all patients require radiotherapy (Atun et al. 2015). Radiotherapy can be administered using X-rays, electrons, or heavier ions such as protons or carbon ions, a method known as particle therapy. Particle therapy is gaining increasing interest worldwide due to its unique advantages in treating cancers, particularly in terms of dose distribution and minimizing damage to surrounding healthy tissue. Interest in particle radiotherapy has grown significantly since the first treatments were conducted at the Lawrence Berkeley Laboratory in 1954. Since then, the number of patients treated each year is increasing rapidly. In the past 5 to 6 years[2], this number has doubled with 36 700 proton and 6600 carbon ion patients in 2023 (PTCOG 2024b). Today, there are 120 clinical proton therapy facilities and 15 carbon ion therapy facilities in operation worldwide, with more than 30 additional centers currently under construction (PTCOG 2024a).

Ion therapy offers several physical advantages over traditional X-ray radiotherapy due to the characteristic dose distribution of the beam. The finite range and low entrance dose of ion beams allow for the creation of a Spread Out Bragg Peak (SOBP), which can be modulated to conform to the shape of the tumor (Schulz-Ertner and Tsujii 2007). This results in higher doses delivered to the tumor while minimizing exposure to surrounding normal tissues, thereby improving tumor control with reduced toxicity in adjacent organs. Intensity Modulated

[1] per 100 000, Age-Standardized Rate (World)
[2] Data from December 2023

Particle Therapy (IMPT) using protons and carbon ions is emerging as a promising treatment approach due to these benefits (Grutters et al. 2010).
However, treating lung tumors with ion therapy presents several challenges. Significant intrafractional respiratory motion or interplay effects with the relative movement between the beam complicate accurate dose delivery (Knopf et al. 2011; Langen and Jones 2001; Lomax 2008). Additionally, the heterogeneity of lung tissue limits the accuracy of treatment planning algorithms (Grassberger et al. 2014).
The heterogeneity effects are caused by Multiple Coulomb Scattering (MCS) as ion beams traverse complex density distributions within the lung. This can lead to a degradation of the Integrated Depth Dose (IDD), potentially resulting in under-dosage of the tumor and unwanted dose distal to the target. Analytic algorithms were found to dramatically and consistently overestimate the delivered dose by up to 46 % in the target (Taylor et al. 2017). While Monte Carlo (MC) simulations offer improved modeling compared to analytical Pencil Beam (PB) algorithms, treatment planning systems are not able to predict these effects due to insufficient information about sub-Computed Tomography (CT)-resolution structures. Despite these advancements, analytical algorithms remain essential for their speed and utility, for instance in providing an overview of dose distribution.
It is therefore necessary to describe and model the degradation mathematically. Previous investigations have already proposed models based on the assumption of a Gaussian range degradation (Titt et al. 2015). This has been further expanded by using a density modulation of lung tissue voxels for MC codes (Baumann et al. 2017). Additionally, an analytical convolution method for the proton absorbed dose was implemented in the open source treatment planning toolkit matRad (Winter et al. 2020).
The objective of this work is to develop a dose calculation module for the evaluation of treatment plans for lung tumors. This involves the implementation of degradation models for both absorbed and biologically effective dose calculations for analytical PB and MC methods. For analytical PBs, this is achieved by building on the previous implementation of analytical convolution and refining it for Relative Biological Effectiveness (RBE)-weighted dose and carbon ions. For MC, the density sampling technique is applied using a developed simple binomial distribution. Given these considerations, the development and integration of a comprehensive MC interface and framework for proton and carbon ion therapy within the matRad toolkit. The goal is to gain a better understanding of treatment planning under the influence of lung degradation and to investigate the impact on the absorbed and biologically effective dose distributions for protons and carbon ions. This project was funded by the German Cancer Aid Foundation (Deutsche Krebshilfe).

II Background

The aim of this chapter is to provide a comprehensive summary of the scientific and technical background relevant to the research presented in this thesis. It covers the fundamental concepts of radiotherapy, including photon and particle radiotherapy, and important physical quantities, such as absorbed dose and Linear Energy Transfer (LET). It discusses the topic of radiobiology, including the Linear Quadratic Model (LQM) and Relative Biological Effectiveness (RBE) models for protons and heavier ions. Finally, the treatment planning workflow is described including patient imaging, dose calculation and plan evaluation.

II.1 Radiotherapy

II.1.1 Ionizing Radiation and Dose

This section introduces basic physical concepts of radiotherapy, such as the interactions and subsequent energy loss of photons and heavier particles while traveling through a medium.

II.1.1.1 Photon Interactions

When traveling through media, the intensity of a photon beam is attenuated by various processes, predominating in different energy ranges. For photons, these processes include:

1. **Rayleigh scattering**: An elastic interaction between the photon and the atom and subsequent scattering of the photon.

2. The **photoelectric effect**: The absorption of a photon and subsequent ejection of orbital electron (photoelectron)

3. **Compton scattering**: An inelastic interaction between photon and atomic electron which leads to an ejected electron and a scattered photon.

4. **Pair production**: The generation of an electron-positron pair from a photon with energy above 1.02 MeV in the presence of the nucleus as collision partner.

The attenuation of a photon beam traversing a material can be described using *Lambert-Beer*'s law (Johns and Cunningham 1983) with the linear attenuation coefficient μ ($[\mu] = \mathrm{cm}^{-1}$):

$$N(z) = N_0 e^{-\mu z} \quad . \tag{II.1}$$

The mass attenuation coefficient μ/ρ per mass density ρ of the absorber is shown for water in Fig. II.1. In the lower ($E_\gamma < 0.1\,\mathrm{MeV}$) and higher ($E_\gamma > 1\,\mathrm{MeV}$) energy region, the photoelectric effect and pair production are dominating, respectively. For energies used in radiotherapy (1 MeV to 15 MeV), Compton scattering is the predominant type of interaction.

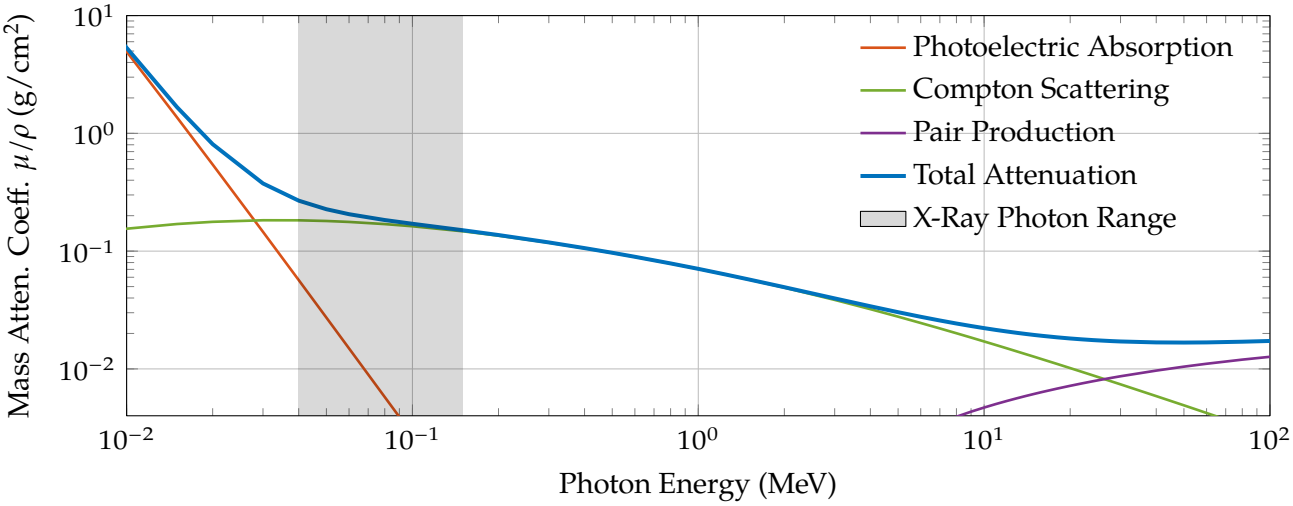

Figure II.1: Total photon mass attenuation coefficient μ/ρ for water as a function of photon energy. It is the sum of three fundamental processes: Photoelectric absorption (—), Compton scattering (—) and pair production (—) which dominate at different energy ranges. Data taken from Berger et al. (2005).

II.1.1.2 Particle Interactions

In comparison to photons, particles loose their energy continuously until they come to a complete stop and have deposited all of their kinetic energy. These consist of several fundamental interaction processes (Newhauser and Zhang 2015):

1. **Coulomb interactions with atomic electrons**: Mostly inelastic collisions with the shell electrons of the absorber material resulting in ionization of the target atom and is the main source of energy loss for clinical beams (electronic stopping S_{el}).

2. **Coulomb interactions with atomic nuclei**: Mostly elastic interaction with an atomic nucleus (S_{nuc}) which does not lead to significant energy loss, but heavy scattering (Schlegel et al. 2018). For ions, inelastic interactions are rare and generate Bremsstrahlung (S_{rad}). For heavy charged particles, both processes are regarded as negligible for energy loss.

3. **Inelastic nuclear reaction**: For high energy ions, the primary particle may break through the Coulomb barrier of the target nucleus and directly collide. This results in the emission of secondary particles, nuclear fragments or prompt gamma rays.

Stopping Power / Energy Loss. The quantity that governs the shape of the depth dose is the stopping power. The mass stopping power ($\left[\frac{S}{\rho}\right] = \mathrm{MeV\,cm^2/g}$) can be written as a sum of the individual processes, electronic, nuclear and radiative stopping power (ICRU 2011):

$$\frac{S}{\rho} = \frac{S_{el}}{\rho} + \frac{S_{rad}}{\rho} + \frac{S_{nuc}}{\rho} \quad . \tag{II.2}$$

For protons and heavy ions, the energy loss $\mathrm{d}E/\mathrm{d}x$ is mainly dependent only on the (mass) electronic stopping power S_{el}, which can be described using the *Bethe-Bloch* formula (Bethe 1930; Bloch 1933; Johns and Cunningham 1983; Schlegel et al. 2018)

$$\frac{1}{\rho}\frac{\mathrm{d}E}{\mathrm{d}x} = \frac{S_{el}}{\rho} = k \cdot \frac{Z_T}{A} \cdot \frac{Z_P^2}{\beta^2} \cdot \ln\left(\frac{2m_e c^2 \cdot \beta^2}{I^2 \cdot (1-\beta^2)}\right) - \beta^2 - \frac{\delta}{2} + C \quad , \tag{II.3}$$

with the particle and target charge Z_P and Z_T, relativistic velocity $\beta = v/c$ and the excitation potential of the target atom I. Several correction terms have been added over the years, including the density correction $\frac{\delta}{2}$ and the shell correction C. Fig. II.2 shows the stopping power in dependence of the residual range in water. Just before the particles are fully stopped, the stoppoing power increases and shows a peak (the Bragg peak). This increase in stopping power causes an increase and peak in the absorbed dose as well.

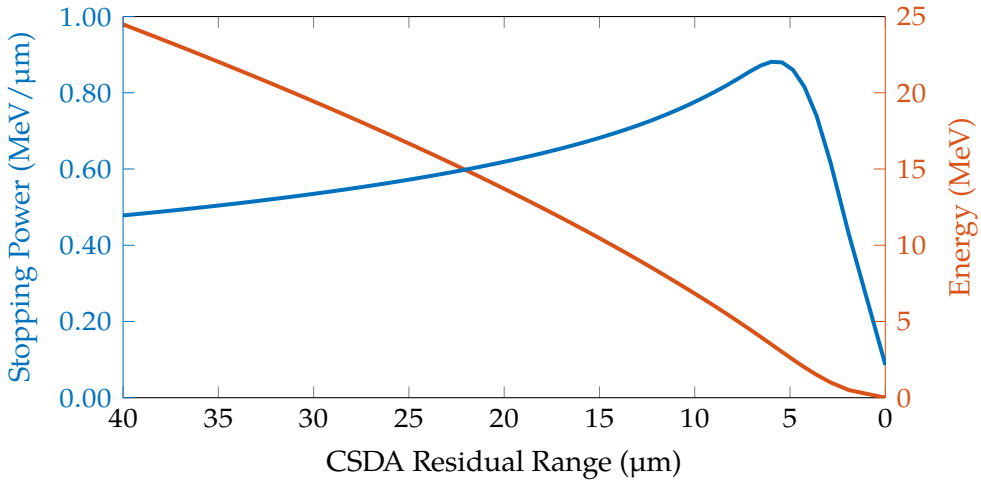

Figure II.2: Stopping power (—) and energy (—) of carbon ions in dependence of the residual range in water. The stopping power increases with decreasing particle energy (and therefore range) and shows a peak (the Bragg peak) just before the particles are fully stopped. Data from Berger et al. (2005).

Multiple Coulomb Scattering. Single elastic coulomb interactions lead to scattering of the incident ion (Rutherford scattering) with a scattering angle dependent on $\sin^{-4}\theta$. However, most materials in clinical radiotherapy are of substantial thickness, enough to cause many small-angle scattering events. These Multiple Coulomb Scattering (MCS) processes not only contribute to the energy loss but also scattering of the beam particles. In the most common approximation of their cumulative effect (Molière's theory), a normal distribution of the individual scattering angles θ_r is assumed, where the change per unit path length can be described by the *scattering power* $\mathrm{d}\langle\theta_r^2\rangle/\mathrm{d}x$. MCS is one of the main reasons of the different lateral bream profiles of different ions (Fig. II.3).

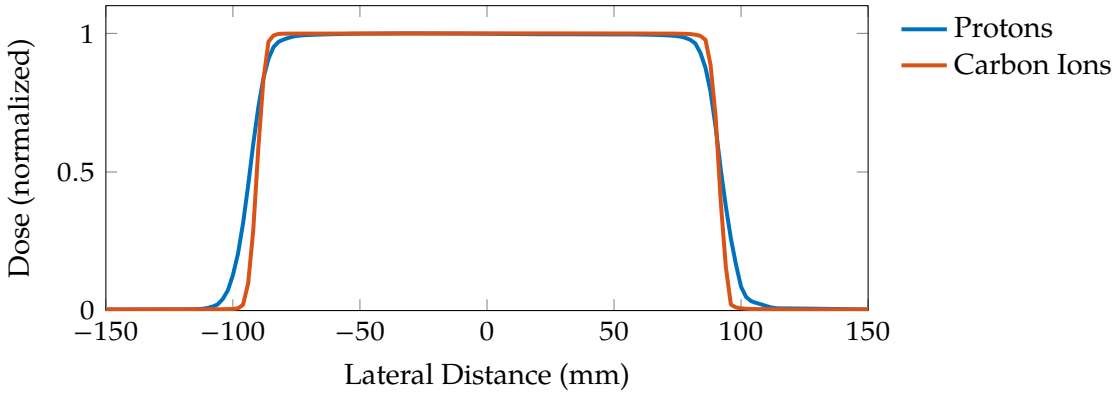

Figure II.3: Lateral penumbra of 95 MeV protons (—) and 200 MeV/u carbon ions (—) in water, compared for equal beam widths. Adapted from Byun et al. (2021).

Straggling. The energy loss and deflections of individual particles are stochastic processes. The difference of the experienced energy loss of individual particles results, with depth, in an increasingly wide energy spectrum, which follows an approximately Gaussian profile σ_E. The energy straggling translates to a range straggling with Gaussian profile $\sigma_R = \sigma_E/(\frac{dE}{dx})$ (Schlegel et al. 2018). This process is called energy straggling which, among other things, determines the width of the Bragg peak and peak to plateau ratio. The range straggling can be incorporated into the depth dose using a convolution with the aforementioned Gaussian profile (Bortfeld 1997),

$$D(z) = \frac{1}{\sqrt{2\pi}\sigma}\int_0^{R_0} \hat{D}(\tilde{z})e^{-(z-\tilde{z})^2/2\sigma^2}\mathrm{d}\tilde{z} \quad . \tag{II.4}$$

Range. The particle range in a certain medium is defined by their energy loss and scattering. The relationship of the particle range with its energy approximately follows a power law, with individual parameters α and p for different materials (Bortfeld 1997; Schlegel et al. 2018):

$$R(E_0) = \alpha E_0^p \quad . \tag{II.5}$$

Based on a fit to available data, this can be used as a simple way to calculate the energies for given ranges and vice versa (Section III.1.4.1).
While the projected range gives the distance without deviations, the mean range of a particle or particle beam can be calculated using the Continuous Slowing Down Approach (CSDA), where a continuous energy loss along the particle track is assumed. It is a good approximation for the mean range of a particle or beam and can be calculated by integrating the inverse of the stopping power over the particle deceleration to $E = 0$:

$$R_{\mathrm{CSDA}}(E) = \int_E^0 \frac{1}{S(E')} \mathrm{d}E' \quad . \tag{II.6}$$

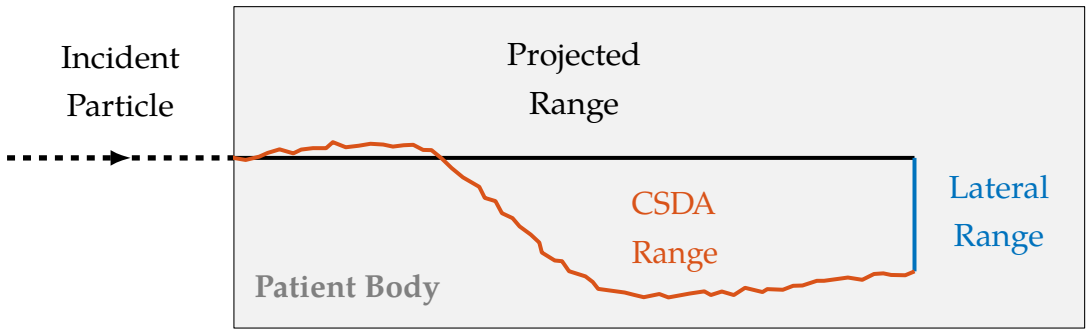

Figure II.4: Illustration of projected vs CSDA range. Adapted from Schlegel et al. (2018).

II.1.1.3 Absorbed Dose

The absorbed dose D ($[D] = 1\,\mathrm{Gy} = 1\,\mathrm{J/kg}$) is defined as

$$D = \frac{\mathrm{d}\bar{E}_{ab}}{\mathrm{d}m} \quad , \tag{II.7}$$

where $\mathrm{d}\bar{E}$ describes the mean energy absorbed in the unit mass $\mathrm{d}m$ of a certain medium (Schlegel et al. 2018). Since the absorbed energy differs between materials, it has to be specified as reference. However, the absorbed dose only considers the purely physical effects of the radiation and disregards potential biological effects *in vivo*.
Depth dose profiles for photons, protons and carbon ions are shown in Fig. II.5. For photons, the dose builds up upon entering the medium due to secondary electrons induced by the primary radiation, which are the dominating source of energy deposition and have a finite range depending on the photon energy (Schlegel et al. 2018). For protons and carbon ions, the dose profile shows the characteristic Bragg peak, caused by an increase in stopping power as the particles slow down (see Fig. II.2, velocity dependence β^{-2} in Eq. II.3). Additionally, the Bragg peak becomes increasingly sharp with increasing particle mass due to higher stopping power (Z_P^2-dependency in Eq. II.3) and less scattering. During the collision process, heavy ions break up into fragments which causes a fragmentation tail after the peak.

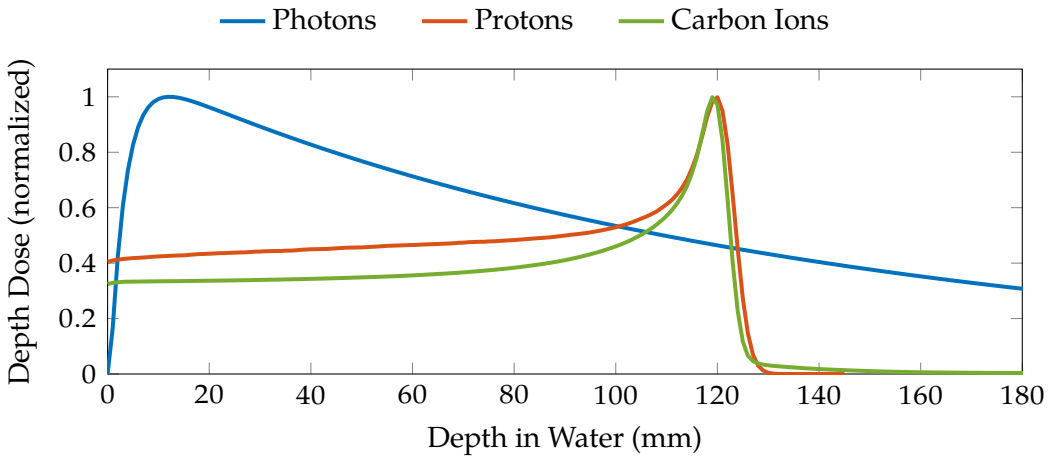

Figure II.5: Normalized depth dose profiles of 6 MeV photons (—), 129.46 MeV protons (—) and 244.92 MeV/u carbon ions (—) in water, calculated using matRad. For photons, the dose builds up at the entrance because of secondary electrons. For protons and carbon ions, the dose profile shows the characteristic Bragg peak, which is sharper for carbon ions. Proton and carbon ion energies were chosen to achieve similar peak depth.

II.1.1.4 Linear Energy Transfer (LET)

The Linear Energy Transfer (LET) ($[\mathrm{LET}] = \mathrm{keV}/\mu\mathrm{m}$) is a measure for the energy transferred to a medium through energy loss to electronic interactions of an ionizing particle per unit length. It is given as the stopping power until a cut-off energy, i.e., the maximum energy of secondary electrons Δ (ICRU 2011), within a radius of the track defined by the cut-off energy:

$$\mathrm{LET}_\Delta = \frac{\mathrm{d}E_\Delta}{\mathrm{d}x} \underset{\Delta\to\infty}{=} S_{el} \quad . \tag{II.8}$$

If $\Delta = \infty$, the unrestricted LET equals the stopping power S_{el}.
The LET in dependence of depth for protons is shown in Fig. II.6. Since the LET is related to the stopping power, it increases with lower particle energy (as seen towards the Bragg peak).

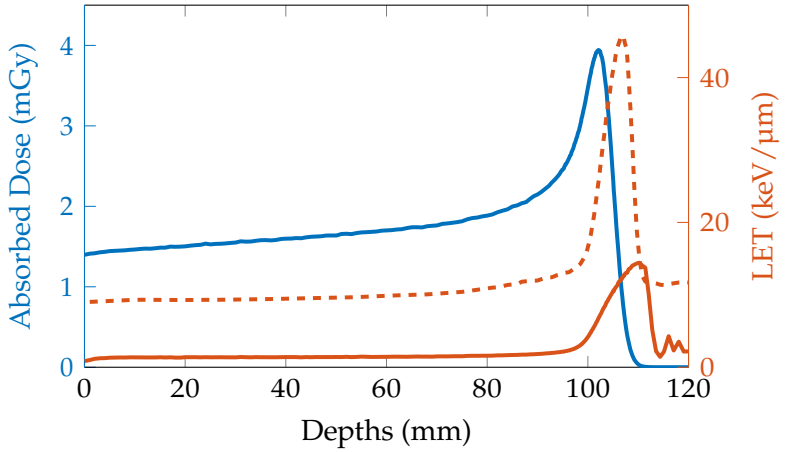

Figure II.6: Proton absorbed depth dose (—) and corresponding dose averaged LET (—) in dependence of depth for a mean energy of $E_\mathrm{p} = 118.21\,\mathrm{MeV/u}$. The LET rises as the particle slows down. The LET for a helium beam with similar range and energy ($E_\mathrm{He} = 117.18\,\mathrm{MeV/u}$) is much larger (- -).

The LET is used to differentiate densely ionizing radiation (high-LET radiation), such as heavy ions, carbon or slow protons, and thinly ionizing radiation (low-LET radiation), such as high energy particles and photons (Schlegel et al. 2018). For photons, the mean LET of secondary particle spectrum is referenced. In radiotherapy, high-LET radiation may be desired, as the dose is deposited closely to the track and their damage is less likely to be repaired (Joiner and Kogel 2009, see. Section II.2.2). Furthermore, the LET can be used for biological optimization and the calculation of RBE. There, a dose averaged LET (LET_D) is mostly used which is calculated by weighting with the deposited local dose.

II.1.2 Irradiation Techniques

The main goal of radiotherapy is the delivery of a homogeneous dose to the target (the tumor), while minimizing dose to healthy tissue and Organs At Risk (OARs). This can be achieved using several techniques that are briefly discussed in this section. In addition to the beam delivery problem, there are multiple external factors that make this process difficult, such as range uncertainties, inhomogeneous tissue geometries or organ motion.

II.1.2.1 Photon Radiotherapy

Beam generation. Traditionally, simple Röntgen tubes (X-ray tubes) with energies in the high kV range were used for radiotherapy. A hot cathode produces an electron beam, that can either be directly used for therapy or used to generate Bremsstrahlung with a continuous energy spectrum and limited energy range. A commonly used method still today, due to its simplicity and cost-effectiveness, is irradiation with a synthetic Cobalt-60 (^{60}Co) source. Decaying ^{60}Co emits the 2 characteristic photon energies 1.17 MeV and 1.33 MeV, which produce a favorable depth dose compared to simple Röntgen tubes. However, the treatment field has to be intricately collimated (Schlegel et al. 2018).
Today, a clinical photon beam is typically generated using an electron LINear ACcelerator (LINAC), which produces a highly focused electron beam. In a similar way as traditional Röntgen tubes, the generated electrons can either be directly used for therapy (after the generation of an expanded electron field) or steered onto a tungsten target which generates ultra hard Bremsstrahlung. The produced electron energies typically range between 6 MeV to 18 MeV (Schlegel et al. 2018).

Technique. One of the current state of the art techniques for photon radiotherapy treatment is Intensity Modulated RadioTherapy (IMRT). A Multi Leaf Collimator (MLC) is used in combination with multiple modulated beams from different directions. The MLC consists of individually movable tungsten leaves oriented to match the shape of the tumor. The beams themselves are modulated to increase the target dose and decrease the dose to OARs

(Fig. II.7), which results in very homogeneous dose distributions. The irradiation fields can either be static or rotated continuously around the patient while modulating the rotational speed, dose rate and the position of the MLC leaves. This technique is called Volumetric-Modulated Arc Therapy (VMAT) and produces the best target dose conformity compared to other IMRT techniques (Schlegel et al. 2018).

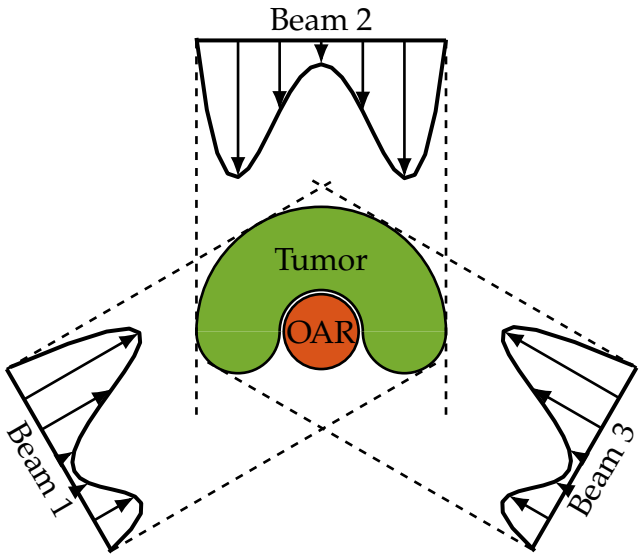

Figure II.7: IMRT setup for an example kidney shaped tumor with an OAR. It consists of 3 treatment beams whose intensities are modulated individually. They are modulated such that the parts of the beam striking the OAR have lower intensities compared to those targeting the tumor. Adapted from Schlegel et al. (2018).

II.1.2.2 Particle Radiotherapy

Beam generation. The generation of particle beams is much more challenging compared to photon beams. It requires expensive – and in case of synchrotrons, building-sized – accelerators. As a result, only a few facilities exist worldwide. In order to reach sufficient treatment depths, particles have to be accelerated to significantly higher energies compared to the photon or electron energies. Energies of ~30 MeV to 200 MeV are needed for protons or even ~100 MeV/u to 400 MeV/u for carbon ions (Schlegel et al. 2018).
These energies are realized using ring accelerators such as *cyclotrons* and *synchrotrons* that produce almost mono-energetic beams (Schlegel et al. 2018). For protons, mostly cyclotrons are used, where the proton is continuously accelerated and kept on a circular path by a magnetic field (Fig. II.8a). The path radius increases with particle energy until they are ejected into a continuous beam. In a synchrotron, particles are pre-accelerated and injected into a circular path and accelerated at each revolution, producing a pulsed beam current when spilled (Fig. II.8b). The advantages of a cyclotron are their relatively compact size and their continuous beam. However, synchrotrons allow for precise and on-demand energy selection and enable the acceleration of various different ion types, such as protons, helium, carbon or oxygen ions (also in the same machine).

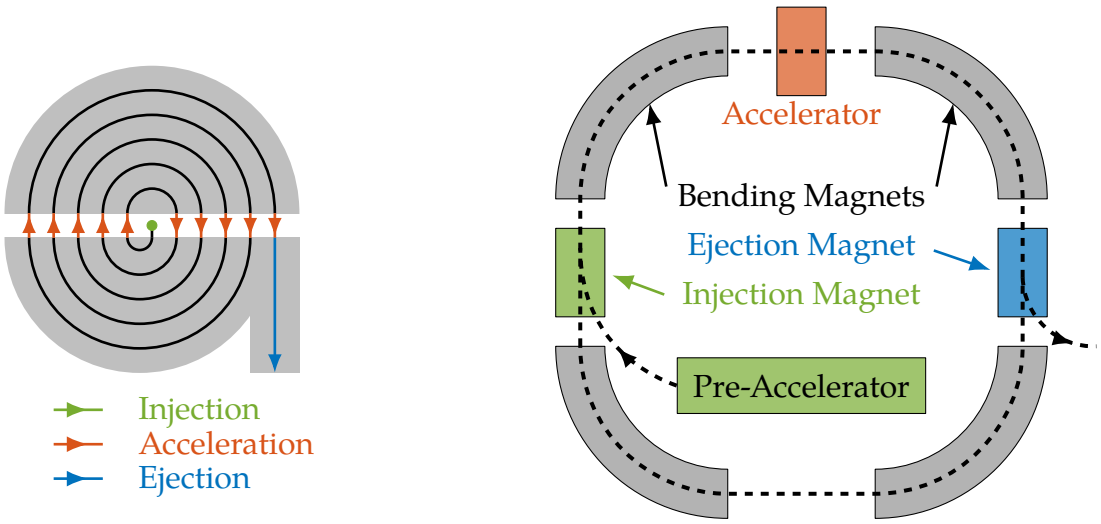

(a) Schematic drawing of a cyclotron.

(b) Schematic drawing of a synchrotron.

Figure II.8: Schematic drawings of a cyclotron (a) and synchrotron (b). A cyclotron uses an oscillating electromagnetic field to accelerate charged particles. In a synchrotron, particles are injected in an accelerator ring, where they are accelerated at each revolution. Adapted from Schlegel et al. (2018).

Technique. The *pencil beam scanning* technique exploits the characteristics of particle dose deposition using individual dose points (Fig. II.9). In combination with Intensity Modulated Particle Therapy (IMPT), scanning magnets control the beam position. The penetration depth is controlled by selecting different beam energies in the accelerator or by insertion of range shifter plates. The beam intensity is controlled by the control and monitoring system. This way, nearly every tumor shape can be individually modeled to deliver a highly homogeneous dose (Hall 2004; Lomax et al. 2001). 3D IMPT is the current state of the art treatment technique for most tumors that are treated using ions.

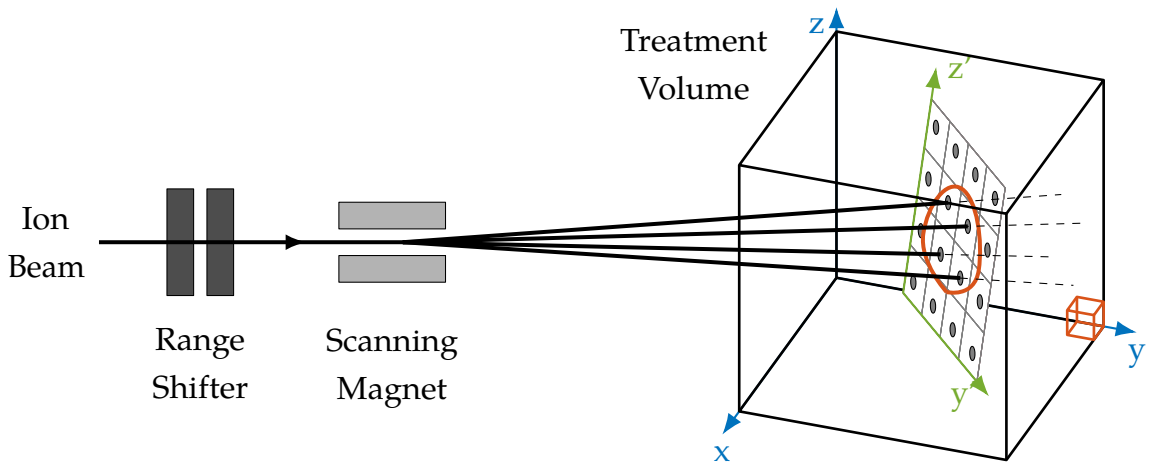

Figure II.9: IMPT active scanning setup where the individually modulated beam spots (●) are spatially targeted using scanning magnets and different energy layers from the accelerator or by using a range shifter. This way, the target volume (—) within the discretized patient geometry is covered.

II.2 Radiobiology

A living organism or a a cell will react differently to ionizing radiation compared to a water phantom. While the interactions can be spread out over the whole volume of a cell, the localized damage to the nucleus and the DNA is the major cause of potentially irreparable damage to the cell. The energy deposition and therefore (desired) biological effect happens in 3 phases (Joiner and Kogel 2009; Schlegel et al. 2018):

1. **Physical** processes in the range of 10^{-18} s to 10^{-14} s are the direct interaction between the radiation and the cells causing ionization cascades through secondary electrons and atomic excitations.

2. Within 10^{-3} s to several minutes, in subsequent **chemical** reactions, atomic bonds break and free radicals are produced.

3. Early **biological** reactions (after hours to months) can include skin or organ damage through the killing of stem cells, while late reactions (after months to years) can include fibrosis, nerve damage or even secondary radiation-induced tumors.

Cells have a number of repair mechanisms to counteract the induced damage, which may differ between healthy and tumor cells and depend on the complexity of the damage:

1. Single Strand Breaks (SSBs) are breakages in only one DNA strand and can therefore be easily restored from the complementary strand.

2. Double Strand Breaks (DSBs) are complete breakages of both strands, that need more sophisticated repair mechanisms.

3. Accumulation of SSBs and DSBs (cluster damages) are more prevalent in high-LET radiation due to their localized energy deposition and are hard to repair.

Often, supplying blood vessels do not grow as fast as the tumor, causing an hypoxic and acidic micro environment, which further influences the balance between damage and repair (Joiner and Kogel 2009). In order to quantify the radiation response in cells after irradiation with a certain dose, *in vitro* cell cultures were irradiated with varying doses and their ability to divide after the irradiation measured, so-called clonogenic assays. On this basis, the LQM was developed (Section II.2.1). The LQM allows to derive dose prescriptions for different irradiation schedules, like the total dose and the number of irradiation sessions or fractions (fx) it is applied in (Schlegel et al. 2018).

II.2.1 Linear Quadratic Model (LQM)

Based on these clonogenic assays, the resulting cell SF after n irradiations with the single dose d and the total dose $D = nd$ can be calculated using

$$\mathrm{SF}(D) = exp\left(-n(\alpha d + \beta d^2)\right) \quad . \tag{II.9}$$

α (1/Gy) and β (1/Gy^2) are model fitting parameters describing the radiosensitivity of the cell towards the radiation type (Schlegel et al. 2018). Usually, the ratio of these parameters is given and ranges from 8 Gy to 15 Gy for early reacting tissues and 1 Gy to 4 Gy for late reacting tissues. For tumors, α/β ratios are often higher in a range of 5 Gy to 15 Gy. The LQM is well supported by data for a dose range of roughly 1 Gy/fx to 5 Gy/fx and extrapolation may compromise the validity (Joiner and Kogel 2009). Furthermore, it is assumed that enough time has passed for the repair of non-lethal damages without going through mitosis. Example cell survival curves for α/β ratios of 2 Gy and 10 Gy as well as fraction doses of 2 Gy/fx and 5 Gy/fx are shown in Fig. II.10. Cells with small α/β ratios (early responding) show a large fractionation effect compared to large α/β (late responding). A lower fraction dose increases the fractionation effect compared to a higher dose per fraction, so the number of fractions has to be increased for the same effect. The concept of Equivalent Dose (EQD) can be used to convert between these isoeffective fractionation schemes (Withers et al. 1983):

$$\mathrm{EQD}_2 = D_1 \cdot \frac{d_1 + \alpha/\beta}{d_2 + \alpha/\beta} \quad . \tag{II.10}$$

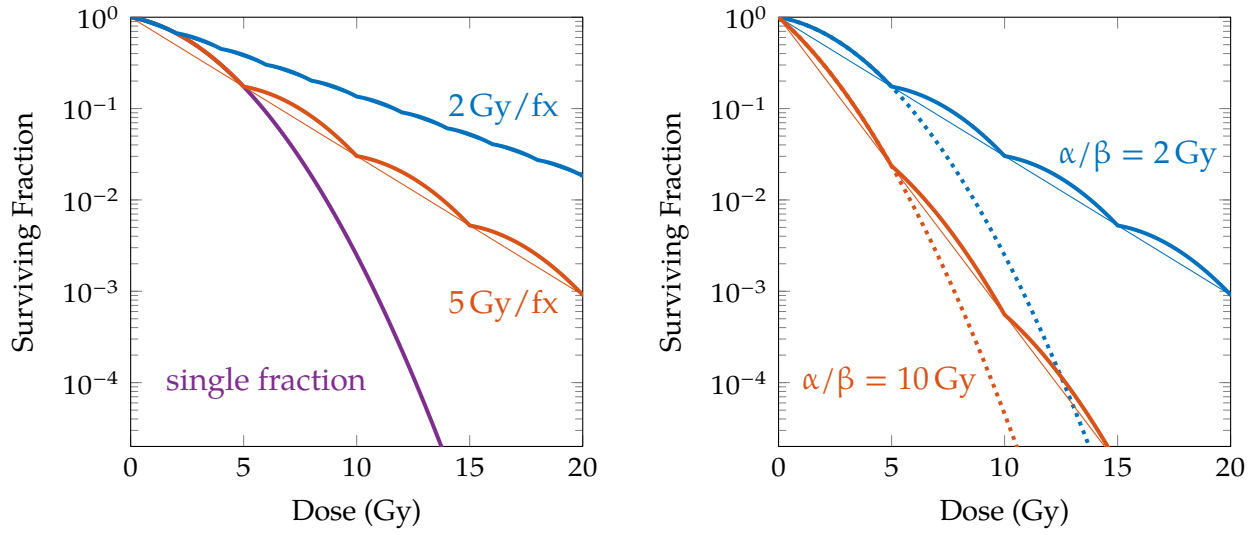

(a) Surviving Fractions (SFs) for $\alpha/\beta = 2$ Gy for a single fraction (—) and 2 Gy/fx and 5 Gy/fx (—, —).

(b) SFs for single fractions (···, ···) and 5 Gy/fx for $\alpha/\beta = 2$ Gy and 10 Gy (—, —).

Figure II.10: Cell survival curves calculated using the LQM for different fractionation schemes (a) and different α/β ratios (b). Lower doses per fraction and small α/β ratios increase the fractionation effect compared to higher doses per fraction and large α/β ratios.

Application. The *biological effect* ϵ (Jones et al. 2001) is defined as:

$$\epsilon = -\ln(\mathrm{SF}) = n(\alpha d + \beta d^2) \quad . \tag{II.11}$$

For very low dose rates (for $d \to 0$ and $n \to \infty$), the maximum isoeffective dose is called extrapolated total dose (Joiner and Kogel 2009) or *Biologically Effective Dose (BED)* and is defined as:

$$\mathrm{BED} = \frac{\epsilon}{\alpha} = D\left(1 + \frac{d}{\alpha/\beta}\right) \quad . \tag{II.12}$$

For the purpose in dose calculation algorithms (see Section II.3.2.2), an important property of the biological effect ϵ (and therefore the BED) is its additivity, especially when combining multiple fractions of a treatment (Jones et al. 2001).
Even though the LQM was developed on the basis of in vitro cell cultures, it can still be applied to patients, if the boundary conditions are met and α/β is known with acceptable accuracy. Then, it serves as a simple and effective model to describe the effect of fractionated irradiation. Additionally, the parameters can be adjusted to better reflect the *in vivo* behavior through empirical, retrospective analysis of large patient cohorts (Kirkpatrick et al. 2008).

Extensions. While the initial LQM is only valid for 1 Gy to 5 Gy, it can be extended to larger doses, which is important for e.g. the Local Effect Model (LEM), where very high local doses are assumed (Section II.2.2.1). For this, an empirical parameter is added with the transition dose d_t:

$$\mathrm{SF}(d) = \begin{cases} \exp(-\alpha d - \beta d^2) & d < d_t \\ \exp(-\alpha d - \beta d^2 - s_{max}(d - d_t)) & d \geq d_t \end{cases} \quad . \tag{II.13}$$

There are several additional factors that may counteract the cell damage induced by radiation (Schlegel et al. 2018). In addition to cell repair, cells can undergo mitosis and repopulate between treatments, therefore potentially increasing the surviving fraction. Furthermore, cells are more susceptible to radiation in certain cell cycle phases, which can lead to a decreased effectiveness during the treatment or consecutive treatment. Furthermore, the oxygen content in the cells has an impact on the radiation resistance, where hypoxic cells (mostly tumors due to their fast-growing nature) are more resistant. However, during the treatment, reoxygenation of these regions can occur and enhance the effect of the radiation.

II.2.2 Relative Biological Effectiveness (RBE)

Irradiating tumors with high-LET radiation (densely ionizing radiation such as low-energy protons, helium or carbon ions) leads to a higher biological effect for the same dose compared to low-LET radiation (loosely ionizing radiation such as photons or electrons). High-LET particles deposit their dose and therefore their damage much more confined compared to photons which leads to more unrepairable damages to the cells (Schlegel et al. 2018). In order to quantify the higher effect, the Relative Biological Effectiveness (RBE) is defined as

$$\mathrm{RBE} = \left.\frac{D_{reference}}{D_{ion}}\right|_{isoeffective} , \tag{II.14}$$

where $D_{reference}$ and D_{ion} are the isoeffective doses that lead to the same cell survival and in turn the same biological effect. The RBE strongly depends on the type of radiation used for irradiation and as the reference. Most commonly used as reference dose are 250 kVp X-rays or ^{60}Co γ-rays (Joiner and Kogel 2009). Additionally, the RBE depends on the biological properties of the cell (α/β), the beam quality, the dose and whether or not a fractionation scheme is being used (Joiner and Kogel 2009; Karger and Peschke 2017; Schlegel et al. 2018). RBE values reported in literature vary greatly for the aforementioned parameters but range from 0.7 to 1.6 for protons (*in vivo*) (Karger and Peschke 2017; Paganetti et al. 2002) and 1.26 to 5.04 for carbon ions (Karger and Peschke 2017). In clinical practice, a constant RBE of 1.1 is most commonly used (Paganetti et al. 2019; Schlegel et al. 2018, see Section II.2.2.1).
Multiplying the particle dose D_{ion} with the respective RBE leads to an isoeffective, RBE-weighted photon dose

$$D_{\gamma} = \mathrm{RBE} \cdot D_{ion}, \tag{II.15}$$

with units given in Gy. RBE-weighted dose is one of the most important quantities in this thesis and in clinical use, since it allows to compare particle dose distributions to photon dose distributions and among each other. Additionally, photon doses vary a lot less and are commonly better described and known (Schlegel et al. 2018).
The RBE-weighted particle dose can be analytically calculated from photon radiosensitivity parameters α/β and the *effect* ϵ (Wilkens and Oelfke 2004):

$$\mathrm{RBE} \times D_{\mathrm{ion}} = \frac{\sqrt{\alpha_{\gamma}^2 + 4\beta_{\gamma} \cdot \epsilon_{ion}} - \alpha_{\gamma}}{2\beta_{\gamma}} \quad . \tag{II.16}$$

Dependence on LET. Even though radiation with higher LET is more effective in damaging the cell compared to photons and their specific RBE depends on more parameters; generally speaking, higher LET radiation leads to higher RBE. The energy is deposited very locally, thus causing more DSBs and hence more damage to the cell. The RBE dependence of LET is

shown in Fig. II.11 for three different SFs. As depicted, the RBE also increases with higher SF and therefore towards lower doses. For small doses, the RBE reaches its maximum, which can be calculated from $\alpha_{ion}/\alpha_{\gamma}$ (Schlegel et al. 2018). This behavior was observed in experimental data (Paganetti 2014). For very high LETs larger than 100 keV/µm, the RBE decreases again. Even though more energy is deposited in the cell, it does not led to more damage. This effect is therefore called "Overkill"-effect (Joiner and Kogel 2009).

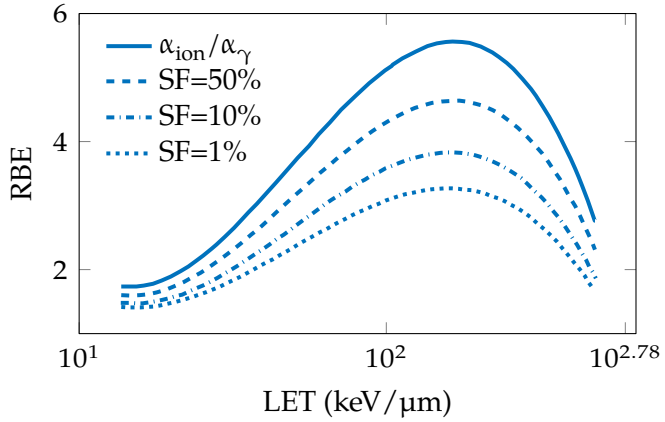

Figure II.11: RBE for CHO-K1 cells as a function of LET for different SFs as well as the case for small doses. With increasing LET, the RBE first increases and decreases again for high LETs ("Overkill"-effect). For a given LET, the RBE increases with larger SF or towards smaller doses. Qualitative representation. Figure adapted from Schlegel et al. (2018).

II.2.2.1 RBE Models

As previously discussed, the RBE depends on multiple factors such as LET, dose, ion type or biological factors. Since the biological effects are currently still poorly understood (McMahon 2021), the RBE can be estimated using simplified RBE models. Past research showed that LET correlated with RBE. As a result, variable RBE models are mostly based on LET (Mairani et al. 2016; McNamara et al. 2015; Wedenberg et al. 2013). More sophisticated biological models debate LET as a suitable predictor for RBE and search for different correlations of the RBE, such as the Repair-Misrepair-Fixation (RMF) model (Carlson et al. 2008) which links DSBs to cell death and therefore biological effect. Generally, an inconsistent $\mathrm{LET_d}$ calculation can potentially impact the corresponding RBE and using a different surrogate such as the beam quality Q was found to significantly improve RBE prediction (Kalholm et al. 2023).
The following section gives a short overview over the limited list of (mostly LET based) RBE models used in this thesis for protons and carbon ions.

Protons. Usually, when considering the higher biological effectiveness of protons in a clinical setting, a constant RBE of 1.1 is recommended and used (ICRU 2007). This means, that over all energies, protons are assumed to be 10% more efficient compared to photons. This can be considered a sensible approximation, since the LET only increases for very

low energies and therefore only at the distal edge of the Bragg peak (Schlegel et al. 2018). However, since the dose falls of around the distal edge of the target, the increasing LET causes an increase in RBE and could mitigate the advantageous sharp dose falloff to some degree (McNamara et al. 2015; Paganetti 2014; Paganetti et al. 2019). As a result, it can be worthwhile to include a variable RBE for protons in those regions, since the RBE depends on many more factors (see above), and there have been several publications addressing and developing variable RBE models. A more detailed comparison of various proton RBE models can be found in McNamara et al. (2020a).
Multiple phenomenological models were developed based on a parameterization of the LQM (Eq. II.17) fitted to experimental data. The equation provides a relationship of RBE on dose, dose averaged LET_d and α/β, without the need of particle specific biological parameters (Carabe-Fernandez et al. 2007; Karger and Peschke 2017):

$$\text{RBE} = \frac{1}{2D_{ion}}\left(\sqrt{\left(\frac{\alpha}{\beta}\right)_{ph}^{2} + 4D_{ion}\left(\frac{\alpha}{\beta}\right)_{ph}\text{RBE}_{max} + 4D_{ion}^{2}\text{RBE}_{min}} - \left(\frac{\alpha}{\beta}\right)_{ph}\right) \quad . \tag{II.17}$$

RBE_{max} corresponds to the maximum RBE at dose $\to 0$, depending on $(\alpha/\beta)^{-1}$ and LET_d, while RBE_{min} describes the asymptotic RBE towards high doses. Specific parameterizations of the implemented models can be found in Section III.1.1.2. Reported typical RBE values for both models range from less than 1 to more than 2 (McMahon 2021), which would not be a negligible effect.

Heavy Ions. RBE estimation for heavy ions, such as helium or carbon ions, is more complex and particularly difficult due to their high LET. Compared to protons, ions deposit their energy highly localized around their traveled path, therefore create more localized damage and are usually more effective in destroying cells. There are several models available across the world like the LEM. The LEM is a generalized model for all clinically relevant ions developed at the Gesellschaft für SchwerIonenforschung mbH (GSI) (Scholz and Kraft 1996; Scholz et al. 1997). For protons, similar to the already described proton models, it leads to an RBE higher than 1.1 at the distal edge of the Bragg peak (Schlegel et al. 2018).
The model is used for scanning beams to calculate the local RBE at each point in the radiation field and links cell survival SF_{cell} to the deposited energy (Schlegel et al. 2018). It assumes that, on a microscopic scale within the cell nucleus, the biological effect is independent of the radiation type and is only determined by the microscopic doses deposited by the incident particles. It considers the density of double strand breaks caused by the localized energy depositions which is averaged over the volume of the nucleus. In other words, the probability that a hit with a certain LET causes a cell kill event (Karger and Peschke 2017).

The survival fraction of a hit cell can be defined as the integral over the relevant volume

$$\ln(\mathrm{SF}_{cell}) = \int_V \ln(\mathrm{SF}_\gamma(d))\frac{dV}{V} \quad , \tag{II.18}$$

where d is the sum of the local dose contributions and SF_γ is the photon-survival curve. It is assumed that the relevant volume is the size of the nucleus (approximated with a cylinder with $r = 5\,\mu\mathrm{m}$), since the damage is done to the DNA (Schlegel et al. 2018). From this, the average survival fraction between multiple cells can be calculating by modeling the ion track distribution for a certain dose including potential fragments with MC simulations (Schlegel et al. 2018). Comparing this dose with the photon dose with the same cell survival, the RBE can be calculated (Eq. II.14). Furthermore, an $1/r^2$ dependency for the microscopic ion energy deposition is assumed with a constant energy loss below $r_{min} = 10\,\mathrm{nm}$ and is cut off after maximum range r_{max} of the secondary electrons. Since the local dose deposition can include very large doses above 100 Gy, the high dose extension of the LQM (Section II.2.1) has to be used (Schlegel et al. 2018).

Further Development of the LEM II-IV. Inaccuracies between calculated and measured *in vitro* RBE data led to further development as LEM II until LEM IV. LEM II improves how the density of the DSBs are estimated and also considers indirect effects from free radicals (Elsässer and Scholz 2007) and LEM III made improvements on the track structure (Elsässer et al. 2008). LEM IV, the latest iteration, uses Monte Carlo (MC) simulations to estimate the distribution of DNA damage, which is assumed to be directly linked to the biological effect. It is based on the idea that similar patterns of DSBs will lead to similar biological effects, which is a deviation from the earlier LEM versions. However, only LEM I has been primarily used clinically (Schlegel et al. 2018).

II.3 Treatment Planning

Treatment planning is a crucial step in radiation therapy and describes the workflow from tumor imaging to a final dose distribution ready to be delivered. This workflow is summarized in Fig. II.12. Based on the imaged tumor and target volume definition, specific plan parameters are set and the dose is calculated in terms of a Dose influence matrix (Dij). The plan parameters are subsequently optimized to best cover the target volume and minimize the dose to OARs. To ensure that the generated dose distribution satisfies the pre-set conditions, a plan analysis is performed that can make reoptimizations necessary. Reoptimizations continue until the treatment plan is validated and ready for patient delivery. In this section, the individual steps of the treatment planning workflow are described in more detail.

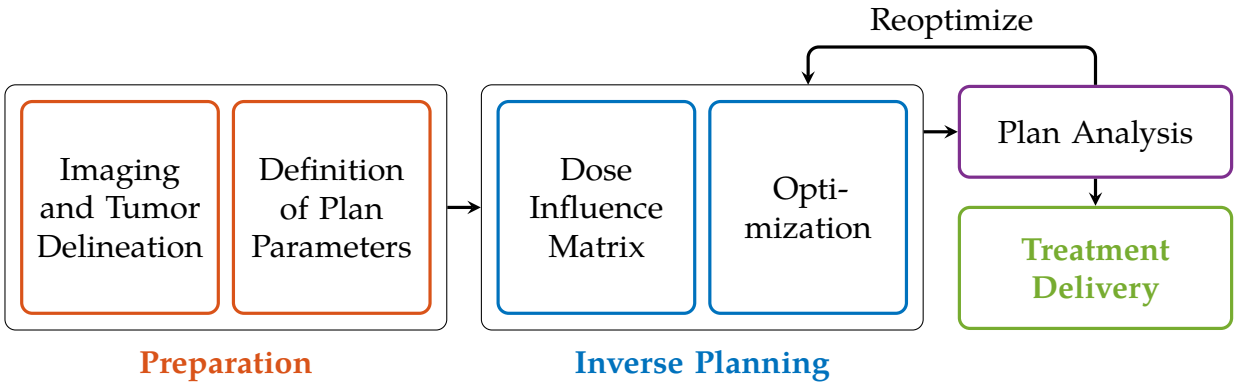

Figure II.12: General clinical treatment planning workflow. The target is identified and delineated using one or multiple imaging techniques. Based on a set of defined plan parameters the dose is calculated and optimized to best cover the target volume and minimize the dose to OARs. A plan analysis can make reoptimizations necessary until the treatment plan is validated and can be delivered to the patient.

II.3.1 Imaging and Volume Definition

II.3.1.1 Computed Tomography (CT)

In a modern Computed Tomography (CT) machine, photons are generated in one or two rotating X-ray tubes. Electrons are released in a heating element (cathode) and accelerated with an applied voltage towards the anode, where photons are generated. The energy spectrum of the X-ray photons is dependent on the tube voltage with which the electrons are accelerated. Typical peak tube voltages range of 80 kVp to 140 kVp. The generated X-ray photons travel through the patient and are measured in the detectors on the opposite side. The measured transmission intensities are then mathematically reconstructed using an algorithm such as filtered back projection. The resulting Hounsfield Units (HUs) represent the attenuation of the X-ray radiation in a specific voxel (Table II.1) on a scale of −1000 HU to ~2000 HU, while the grayscale 12-bit image stores these values in the range of −1024 HU

to 3071 HU (Greenway et al. 2015; Schlegel et al. 2018). The HU is linked through linear transformation to the linear attenuation coefficient of the material relative to that of water:

$$\mathrm{HU} = \left(\frac{\mu_{material} - \mu_{water}}{\mu_{water}} \right) \times 1000 \quad . \tag{II.19}$$

It mainly determines the energy loss experienced by the treatment radiation and is therefore an essential quantity for treatment planning and dose calculation. Since CT is a quantitative imaging modality, the measured HUs in a CT image provide information about the relative Stopping Power (rSP), which is needed to calculate the range of particles for a certain energy. The HUs can be converted to rSP by using experiment-based Hounsfield LookUp Tables (HLUTs) which store the respective rSP for each HU. The HU to rSP conversion will be described in detail in Section III.1.1.1.

Table II.1: CT numbers for common tissues and compounds at 120 kVp, measured in HU. (Schlegel et al. 2018)

Organ/tissue	Hounsfield Units
Air	−1000 HU / −1024 HU
Lung	−900 HU to −500 HU
Fat	−100 HU to −70 HU
Water	0 HU
Soft tissue	20 HU to 70 HU
Cortical bone	350 HU to 2000 HU
Titanium	higher HU

4D Computed Tomography (4D-CT). 4D-CT is a method of creating time resolved 3D CT images of the patient. Multiple CT images acquired for different times result in a 3D image for several point in time within e.g. a breathing cycle. It serves as an imaging technique that allows for visualization of tumor or organ movement within a breathing cycle, that stabilization and immobilization of the patient cannot account for (Kwong et al. 2015).

II.3.1.2 Volume Definition

Current clinical treatment planning is always based on a CT image of the patient. Alone or in combination with other imaging modalities like Magnetic Resonance Imaging (MRI) and Positron Emission Tomography (PET), the tumor and important nearby organs are delineated into the following segmentations (Burnet et al. 2004). These segmentations are also graphically schematized in Fig. II.13.

1. The **Gross Tumour Volume (GTV)** is the delineated volume of the tumor that is visible in the used imaging modality.

2. The **Clinical Target Volume (CTV)** encompasses the GTV and a margin for tumor infiltration that cannot be accurately defined and therefore has to be based on clinical experience.

3. The **Interal Target Volume (ITV)** considers internal patient movement and uncertainties in the tumor position, which may move due to e.g. breathing or organ filling.

4. The **Planning Target Volume (PTV)** is the largest target volume and further encompasses an additional safety margin for patient positioning and the setup. Usually, an underdosing or squared deviation dose constraint is applied to ideally apply the prescribed dose to the whole PTV.

5. **Organs At Risk (OARs)** such as lung and heart are delineated and usually applied with an overdosing dose constraint to minimize the dose delivered to these organs.

Volumes of OARs and the PTV can overlap and negatively affect dose calculations. For instance, a highly penalized OAR objective can result in an underdosage of the PTV, while a good dose coverage in the PTV might cause an OAR overdosage.

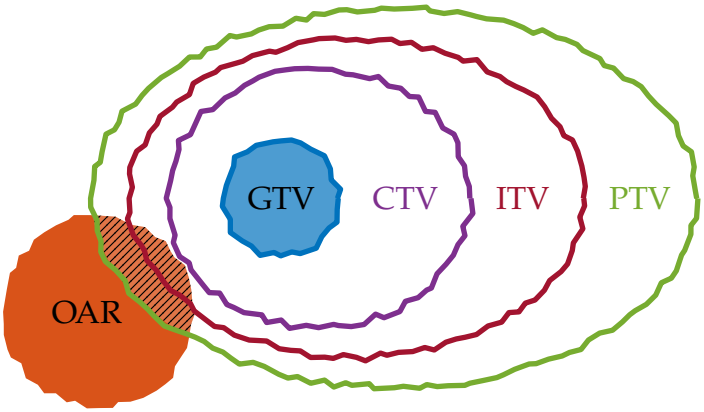

Figure II.13: Volume concepts used in radiotherapy planning. The GTV, CTV, ITV, and PTV, as well as the OARs are denoted. Overlapping volumes (▨) can have an impact on the dose calculation, and might lead to insufficient PTV coverage or undesired dose levels for the OAR.

II.3.2 Dose Calculation

In order to plan the radiation treatment of a patient, the dose distributions delivered by an incident beam to the patient need to be accurately calculated. The first step in any dose calculation workflow is the definition of beam parameters, such as position, angle, or energy, according to the degrees of freedom of the available irradiation modality and machine. A grid of treatment spots is defined within the voxelized patient geometry (CT image) based on the available tumor segmentations (Fig. II.9). In a subsequent step, dose calculation algorithms are employed which are based on deterministic methods or MC simulations (Section II.3.2.2). This process is performed for each unique beam orientation when irradiating from various angles.

II.3.2.1 Water Equivalent Path Length (WEPL)

The range of a beam is dependent on the experienced attenuation on the path through the patient. It is dependent on the specific density of each traversed voxel and the length of the path within that voxel (Fig. II.14a). This length is often represented in terms of the equivalent length of a voxel purely filled with water. The resulting water-equivalent depth or *radiological depth*, often also called Water Equivalent Path Length (WEPL) or Water Equivalent Thickness (WET), is a fundamental quantity used in dose calculation. It can be calculated using

$$z_{rad} = \sum_{i=1}^{N} l_i \rho_i \quad , \tag{II.20}$$

as the sum over the individual density contributions (Fig. II.14b) with voxel density ρ_i and the path through the voxel l_i (Schlegel et al. 2018).

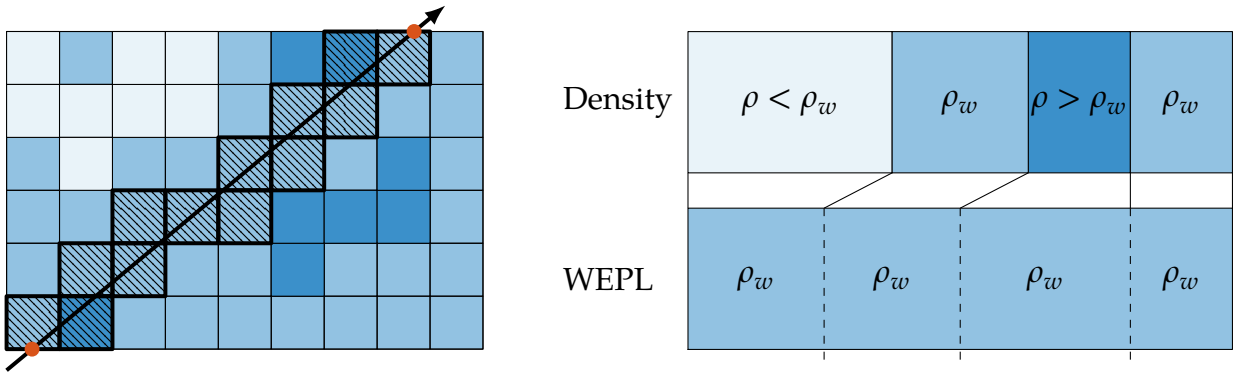

(a) Visualization of the beam path through a voxelized geometry using ray tracing.

(b) Visualization of the WEPL depending on low density and higher density voxels.

Figure II.14: Visualization of ray tracing (a) and WEPL (b), which are crucial components of dose calculation. Ray tracing follows the direct path of the beam through the patient geometry, where each traversed voxel contributes to the overall experienced attenuation. The sum of these individual densities is called the WEPL. It represents the thickness of an idealized water column that would cause the same amount of energy loss as the traversed medium.

II.3.2.2 Dose Calculation Algorithms

Deterministic dose calculation work by analytically calculating the delivered dose based on approximated beam and material properties. Although they are fast and convenient, they may be less accurate in regions with steep dose gradients or heterogeneous materials.
Since only the density of the center is included in the dose calculation and the depth dose is properly scaled, the lateral component does not take density differences into account. While accurate in homogeneous media, a limitations of the pencil beam model includes heterogeneous media, especially compared to MC simulations (Taylor et al. 2017).

Deterministic Pencil Beam Calculation. Pencil beam based dose calculation is a fast method and models the dose deposition of a thin pencil beam originating from a point source based on precalculated dose models.
The dose is calculated based on a convolution of the primary energy fluence Ψ and a pencil beam or point spread kernel K that models the energy transfer from secondary particles. K represents the lateral profile, that is independent of the position of the pencil beam. The dose at a point $(x_p, y_p, z_{\mathrm{rad}})$ is defined as

$$D(x_p, y_p, z_{rad}) = \iint_{-\infty}^{\infty} \Psi(x,y) F(x,y) * K(x - x_p, y - y_p, z_{rad}) \mathrm{d}x\mathrm{d}y \quad . \tag{II.21}$$

The transmission factor $F \in (0,1)$ describes the influence on the intensity of the primary fluence field that may be caused by a collimator or the intensity modulation in case of intensity modulated particles. Usually, the pencil beam kernel K is radially symmetric, so that only the radial distance from the center of the pencil beam $r = \sqrt{x_p^2 + y_p^2}$ is considered. K is also polyenergetic and depends on the radiological depth. To avoid calculating the integral for each energy step, the convolution kernel can be separated into a depth-dependent and depth-independent component using singular value decomposition (Bortfeld et al. 1993).
For **particles**, K can be analytically calculated from a laterally Gaussian shaped dose component L and the Integrated Depth Dose (IDD) in beam direction Z:

$$K(x, y, z_{rad}) = L(x, y, z_{rad}) \cdot Z(z_{rad}) = \frac{1}{\sqrt{2\pi\sigma_x^2}} \mathrm{e}^{-\frac{(x-\mu_x)^2}{2\sigma^2}} \cdot \frac{1}{\sqrt{2\pi\sigma_y^2}} \mathrm{e}^{-\frac{(y-\mu_y)^2}{2\sigma^2}} \cdot Z(z_{rad}) \quad . \tag{II.22}$$

Usually, depth-dependent measurements of the beam width $\sigma_{\mathrm{M}}(z_{\mathrm{rad}})$ and the depth dose $Z(z_{\mathrm{rad}})$ are used (Schlegel et al. 2018). The depth dose is scaled to the correct depth based on the measured radiological depth. The beam width is calculated from the initial beam width before the patient and the depth-dependent component: $\sigma^2(z_{\mathrm{rad}}) = \sigma_{\mathrm{init}}^2 + \sigma_{\mathrm{M}}^2(z_{\mathrm{rad}})$.

Similar to the calculation of the absorbed dose, the calculation of the RBE-weighted dose resorts to depth-dependent α and β curves stored for different α/β ratios. Fig. II.15 shows the absorbed dose as well as corresponding α and β for $E = 210.79\,\mathrm{MeV/u}$ of the *carbon_generic* machine data set.

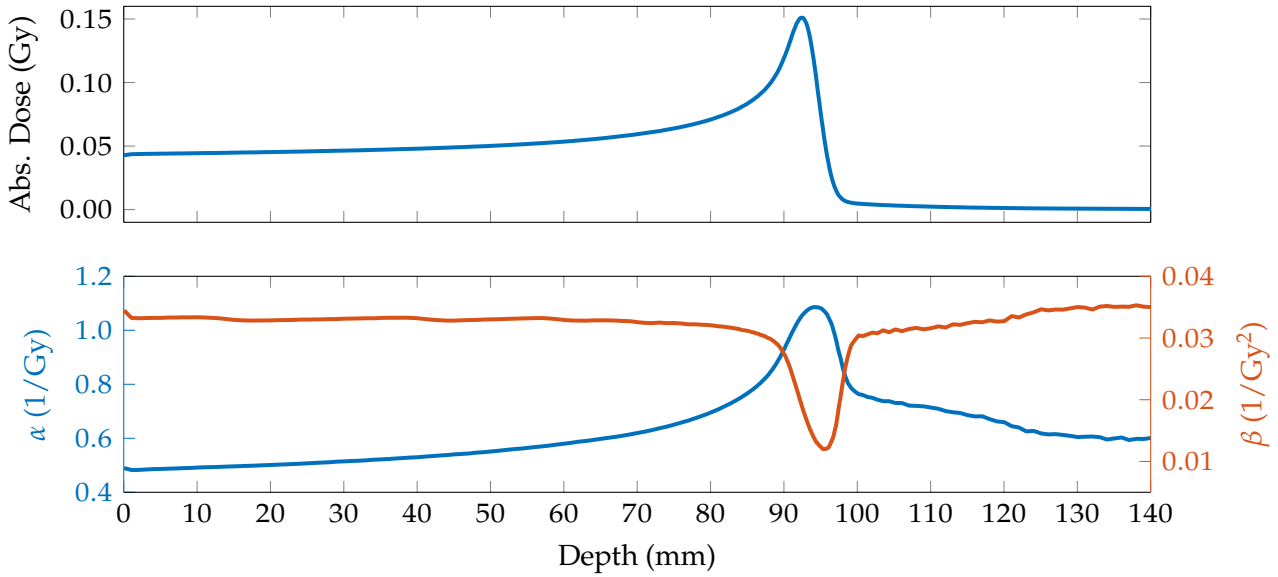

Figure II.15: Carbon α and β with depths for $E = 210.79\,\mathrm{MeV/u}$ of the *carbon_generic* machine data set. Shown are α and β curves for a α/β ratio of 2 Gy.

Monte Carlo dose calculation. MC methods simulate the path of individual particles through the medium that is determined by the physics of particle transport as a series of interactions The interactions of the individual primary particles and subsequently generated particles such as secondary electrons or fragments are calculated based on stochastic distributions (Schlegel et al. 2018). The computational accuracy depends on both the considered physical processes and the individual cross sections. MC codes are considered the most accurate method for physical dose calculation and is thus considered the "gold standard" compared to other dose calculation approaches. However, MC methods require a large number of samples and repetitions due to their stochastic nature, resulting in longer computation times compared to other approximate and deterministic algorithms. In order to exploit their respective strengths, they are often used in synergy. For instance, an initial dose calculation and optimization could be performed quickly with deterministic methods while a recalculation with MC methods could accurately verify the dose distribution.

II.3.3 Plan Evaluation

Treatment plans are evaluated by numerous means, including visual inspection of dose distribution and Dose Volume Histograms (DVHs) as well as several forms of volume statistics or outcome models based on Normal Tissue Complication Probability (NTCP).

Fig. II.16a shows an axial slice of an example proton prostate treatment plan at the isocenter plane. The associated DVH is shown in Fig. II.16b which directly visualizes the volumetric dose distribution over the whole volume to objectively analyze and rate an optimized treatment plan. Shown are the quality indicators D_{95} and D_{50} and the deviation from an optimal dose coverage with a steep (ideally vertical) dose gradient. In general, D_x describes the dose that x% of the target volume receives (Schlegel et al. 2018). D_2 for instance serves as a good representation of the maximum dose delivered to the target volume, eliminating localized spikes in the dose. Analogously, V_x is the volume, that receives a higher dose than x (Gy) or a percentage of the prescribed dose. Additional useful metrics include the Homogeneity Index (HI) (ICRU 2010)

$$\mathrm{HI} = (D_2 - D_{98})/D_{50} \quad . \tag{II.23}$$

Although there are multiple common definitions for the HI, this is the most common one in literature (Kataria et al. 2012). A treatment plan is considered increasingly homogeneous with values of HI $\to 0$. The Conformity Index (CI) describes how well the dose conforms to the target volume with minimal irradiation to the OAR:

$$\mathrm{CI} = \frac{V_{\mathrm{target},95\%}}{V_{\mathrm{target}} V_{95\%}} \quad . \tag{II.24}$$

$V_{\mathrm{target},95\%}$ is the target volume receiving 95 % of the prescribed dose, $V_{95\%}$ is the total volume receiving that dose and V_{target} is the volume of the target. Optimal values are CI $\to 1$.

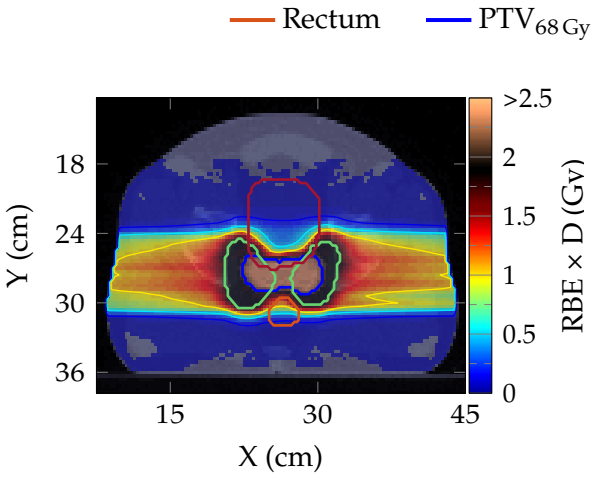

(a) Axial slice at the isocenter of a proton prostate treatment plan, calculated using matRad.

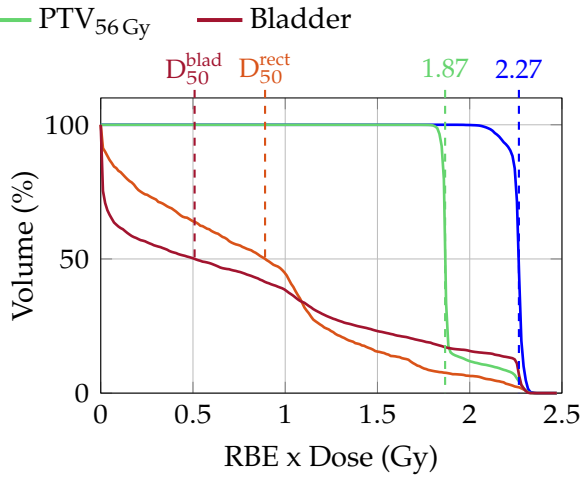

(b) Associated DVH with annotated prescribed doses and example quality indicators D_{50} for both OARs.

Figure II.16: Prostate treatment plan using protons (a), calculated using matRad and optimized for constant RBE. Overlaid are isodose lines at 0.1, 0.5 and 1 Gy, the segmented target volumes $PTV_{68\,Gy}$ and $PTV_{56\,Gy}$, and OARs bladder and rectum. (b) shows the associated DVH for the mentioned segmented volumes. Prescribed doses for both PTVs and example quality indicator D_{50} for both OARs have been annotated.

II.3.3.1 (N)TCP Models

Normal Tissue Complication Probability (NTCP) and Tumor Control Probability (TCP) models like the Lyman-Kutcher-Burman-Model (LKBM) (Burman et al. 1991; Kutcher et al. 1991; Kutcher and Burman 1989; Lyman 2021) or Niemierko-model (Niemierko 1999) describe the complication or control probability depending on the dose in the irradiated volume. The NTCP is defined for a specific clinical endpoint, e.g. type of symptom, complication or tumor control and takes the difference of serial organs and parallel organs into account. Serial organs are very susceptible to damage done to a single functional subunit of a serial organ that can cause irreversible damage to the entire organ. On the other hand, a damaged subunit of a parallel organ can be compensated for by the remaining subunits (Schlegel et al. 2018). Therefore, the protection of serial organs like the spinal cord is generally viewed as more crucial than protecting parallel organs like the liver. The different NTCPs can then be viewed in DVHs and taken into account by treatment planning software through optimization.

II.3.4 Inverse Planning and Dose Optimization

While forward dose calculation describes the (re-) calculation of a dose distribution according to an available treatment plan, *inverse treatment planning* requires the calculation of the beam properties based on the desired dose in the target.
This problem is tackled by defining a *Dij*, where each matrix entry contains the individual raw dose contributions of beam j to a certain voxel i. Each entry has a distinct contribution towards the overall dose and is weighted accordingly with a factor w_j. The dose d in a voxel i can therefore be calculated as the sum of the individual contributions:

$$d_i = \sum_j D_{ij} w_j \quad . \tag{II.25}$$

For a constant Dij, the individual spot weights are determined by an optimization algorithm. The calculation and optimization for constant RBE uses the same formalism for absorbed dose. RBE-weighted dose calculation and optimization for variable RBE is done on the basis of the biological effect (Eq. II.11) and depend on the radiosensitivity parameters α_i and β_i in the individual voxels (Wilkens and Oelfke 2005). The biological effect is given as

$$\epsilon_i = \alpha_i \sum_j D_{ij} w_j + \beta_i \left(\sum_j D_{ij} w_j \right)^2 = \sum_j A_{ij} w_j + \left(\sum_j B_{ij} w_j \right)^2 \quad , \tag{II.26}$$

where $A_{ij} = \alpha_{ij} D_{ij}$ and $B_{ij} = D_{ij} \sqrt{\beta_{ij}}$ are the αD and $\sqrt{\beta} D$ matrices. Similarly to Eq. II.25, A_{ij} and B_{ij} are calculated once per beam setup and the individual spot weights can be determined using an optimization algorithm.

II.3.4.1 Plan Optimization

The plan optimization is performed to maximize the therapeutic outcome while simultaneously minimizing dose to OARs and potential adverse effects. With treatment planning for IMRT, the optimization or *inverse planning* step in the workflow is a highly complex problem. The prescribed dose has to be homogeneously distributed over the target volume. The aim of the optimization is to find the optimal dose distribution by minimizing an objective function $\mathcal{F}$. The objective function is the sum of the individual objectives $f_m(d)$ which are weighted using a penalty factor p_m.

$$\mathcal{F}(d) = \sum_m p_m f_m(d) \tag{II.27}$$

The objective function can contain multiple dose objectives or constraints set for different organs (Table II.2a). The objectives f typically include *squared overdosing* constraints for OARs that limit the maximum allowed dose to those organs. Parallel organs like the liver can have more flexible and less stringent dose constraints, while the constraints for serial organs such as the spinal cord must be handled more strictly. A *squared deviation* constraint set for target volumes penalizes both under- and overdosage.
The optimization for the biological effect is defined in the same way as Eq. II.27

$$\mathcal{F}(\epsilon) = \sum_m p_m f_m(\epsilon) \quad . \tag{II.28}$$

Additionally, effect objectives can be set for the individual organs (Table II.2b).

Table II.2: Common dose objectives used in radiotherapy. The dose objectives are expressed as a function of the number of voxels N and the Heaviside function Θ, which restricts constraints on under- and overdosing (Bennan 2021; Wieser et al. 2017b).

(a) Dose objectives for the optimization of the absorbed dose as a function of the dose within each voxel d_i relative to a reference dose d_{ref} of the referenced segmented volume.

Squared overdosing	$f_{sq.overdoseage} =$	$\frac{1}{N}\sum_i^N \Theta(d_i - d_{ref})(d_{ref} - d_i)^2$
Squared underdosing	$f_{squnderdoseage} =$	$\frac{1}{N}\sum_i^N \Theta(d_{ref} - d_i)(d_{ref} - d_i)^2$
Squared deviation	$f_{sqdeviation} =$	$\frac{1}{N}\sum_i^N (d_{ref} - d_i)^2$
Mean dose	$f_{mean} =$	$\frac{1}{N}\sum_i^N d_i$

(b) Dose objectives for the optimization of the biological effect as a function of the effect within each voxel ϵ_i relative to a reference effect ϵ_{ref} of the referenced segmented volume.

Squared overdosing	$f_{sqoverdoseage} =$	$\frac{1}{N}\sum_i^N \Theta(\epsilon_i - \epsilon_{ref})(\epsilon_{ref} - \epsilon_i)^2$
Squared underdosing	$f_{squnderdoseage} =$	$\frac{1}{N}\sum_i^N \Theta(\epsilon_{ref} - \epsilon_i)(\epsilon_{ref} - \epsilon_i)^2$
Squared deviation	$f_{sqdeviation} =$	$\frac{1}{N}\sum_i^N (\epsilon_{ref} - \epsilon_i)^2$
Mean dose	$f_{mean} =$	$\frac{1}{N}\sum_i^N \epsilon_i$

Minimizing $\mathcal{F}$ in Eq. II.27 or Eq. II.28 leads to an optimal set of weights $w*$ in combination with the Dij (Eq. II.25) so that the resulting dose or effect satisfies the preset conditions:

$$w* = \underset{w \geq 0}{\operatorname{argmin}} \ \mathcal{F}(w) \quad . \tag{II.29}$$

Optimization Example. As an example of dose optimization, a *Spread Out Bragg Peak (SOBP)* is constructed using 10 overlapping and weighted individual Bragg peaks. The weights were optimized using the *fmincon* optimizer for a squared deviation dose objective comparing the resulting enveloping dose profile and an ideally rectangle shaped profile. An illustration is shown in Fig. II.17.

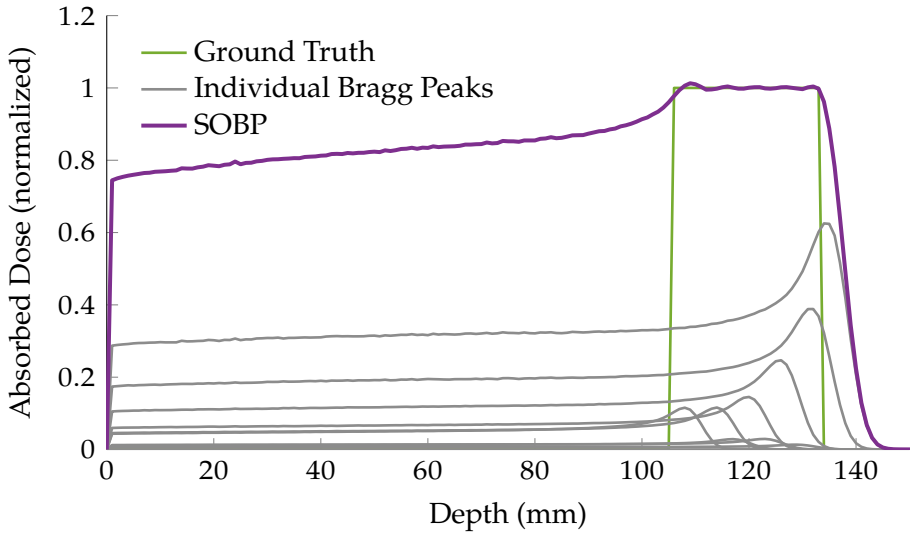

Peak	Weight
1	0.0390
2	0.0158
3	0.0387
4	0.0345
5	0.0463
6	0.0598
7	0.0595
8	0.1308
9	0.0122
10	0.5634

Figure II.17: Example illustration of a typical analytical SOBP for protons (—) consisting of 10 weighted individual peaks with initial energies between 118.21 MeV to 134.81 MeV (—). Weights were optimized manually for a simple squared deviation from an ideal sharp SOBP (—) using the *fmincon* optimizer (Table III.5). Normalized weights are shown on the right.

II.3.5 Uncertainties in Treatment Planning of Lung Tumors

The treatment planning workflow introduces various sources of uncertainty that restrict the accuracy of dose delivery and subsequently impact treatment outcome (van Herk 2004). These include setup and range uncertainties, internal organ motion, dose calculation or the beam degradation caused by inhomogeneous tissues. It is the combination of these uncertainties that make the treatment planning for lung tumors especially challenging. Therefore, it is essential to explore and potentially address these uncertainties.

1. **Setup and range uncertainties**: Setup uncertainties refer to discrepancies between the internal anatomy and the external patient position, resulting in day-to-day variations in tumor position. These variations can lead to an additional underdosing of the tumor

and overdosing of organs at risk (Cho et al. 2002). Additional error sources include inaccurate conversions from HUs from CT images to rSP or element composition, as well as uncertainties in tumor delineation. As a consequence, an adequate safety margin like an increased PTV is required to increase the probability of a homogeneous dose to the CTV (van Herk 2004).

2. **Internal motion**: Shifts or motion of internal organs and therefore the tumor, cause the treatment beam to miss the target and deteriorate the dose distribution (Langen and Jones 2001). This includes both intra-fractional motion (within a treatment) due to heartbeat or breathing motion as well as inter-fractional motion (between treatments) due to tumor shrinkage or organ filling (Lomax 2008). Organ motion in combination with active pencil beam scanning can lead to *interplay effects* since the beam delivery and the target position are not synchronized. This can lead to a severe deterioration of the dose homogeneity in the target. Available techniques developed to compensate for organ motion to some extent include image guidance, gating or 4D-CT planning implemented in dose calculation tools (Cole et al. 2014).

3. **Dose calculation**: As a result, the choice of the dose calculation tool and algorithm can severely impact the treatment planning workflow and consequently the delivered dose distribution. Different dose calculation methods have been employed over the years, becoming more and more sophisticated with increasing available processing power. For instance, fast analytical dose calculation can rapidly calculate and optimize a dose distribution, while slower MC simulations can accurately simulate the physical processes, leading to a more realistic dose distribution.

4. **Degradation of the depth dose**: Lastly, porous or inhomogeneous materials cause straggling within the beam and therefore underdosage of the target and additional dose outside of the target. This effect has been described in more detail in Section III.2.1 and has been investigated in recent years (Baumann et al. 2019; Ringbæk et al. 2020; Titt et al. 2015; Winter et al. 2020), but has so far not been acknowledged or compensated for in clinical treatment planning and has not been investigated for multiple ion species. Phantom studies on the impact of dose degradation in comparison to the intra- and interfractional motion showed that for some cases, this could be negligible (Baumann et al. 2019; Flatten et al. 2019). However, larger dose differences were reported as well, that should not be neglected. Also, since other uncertainties are investigated and mitigated using techniques such as robust treatment planning or beam delivery methods like tracking, the dose degradation might rise in significance.

III

Materials and Methods

In order to model and analyze the depth-dose degradation effects, arising from microscopic lung tissue inhomogeneities, across multiple dose-calculation algorithms, a consistent dose calculation and Treatment Planning System (TPS) is needed. This system must be capable of handling deterministic pencil-beam dose calculation as well as Monte Carlo algorithms. This chapter starts with a description of the dose calculation framework within matRad that has been built in this work, followed by a theoretical description of the developed and applied lung degradation model, leading to the patient cases and treatment modalities studied in this work.

III.1 Implementation of a Monte Carlo Interface

Interfacing MC simulations through matRad serves multiple purposes, including the calculation of dose influence matrices and subsequent optimization, allowing for the flexible recalculation of dose distributions in any order and with any modality. This integration also streamlines processes such as automatic export of the parameter files controlling the simulations and import of calculated dose cubes. The parameter files are built on the fly from existing building blocks and parameters specified within matRad. This section highlights the technical development and implementation of two different MC engines.

III.1.1 Introduction to matRad

The open source software matRad (Ackermann et al. 2020; Wieser et al. 2017b) is used in this thesis for calculating deterministic pencil beams. It serves as a generalized planning platform for intensity-modulated photon, proton and heavy ion therapy and in this thesis, for implementing a dose degradation correction as well as an interface for Monte Carlo algorithms. matRad is written in MATLAB (The MathWorks Inc. 2022) and developed for research and education purposes.

III.1.1.1 Geometry and Coordinate System

Coordinate Systems. matRad uses the Left-Posterior-Superior (LPS) coordinate system, a right-handed coordinate system (Fig. III.1). The voxel coordinates are defined through the x, y and z axes that point towards the left, posterior and superior direction of the patient, respectively. However, due to MATLAB's display conventions, the x and y coordinates are permuted in the representations of CT and dose cubes (stored with $[Y, X, Z]$ and are permuted to $[X, Y, Z]$). This has to be accounted for when reading or writing data in the MC simulations. The rotation of the gantry around the patient are defined using the *gantry angle* ϕ as a clockwise rotation around the z-axis and the *couch angle* θ as a counterclockwise rotation around the y-axis (Fig. III.1). In addition to the above described world coordinate system, during dose calculation, the Beam's Eye View (BEV) coordinate system is used. It is defined only in respect to the direction of the current ray.

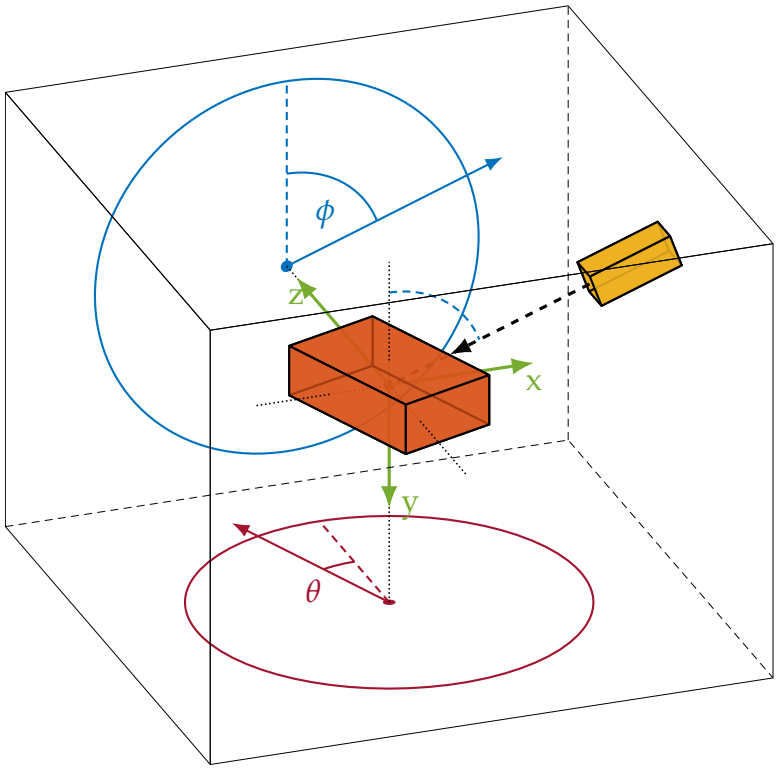

Figure III.1: Schematic drawing of the patient box (—), positioned in the world with axis (—), couch- and beam angles (—, —). Also shown is the irradiation direction and nozzle (—).

Voxel, Rays and Bixel. For active scanning beam delivery, each target plane (energy layer) is divided into a grid of spots or *bixel* (Fig. II.9). Each spot is generated by a *ray* within the treatment beam. Each of these rays is responsible for one spot on multiple energy layers and therefore contains positional information for the ray tracing algorithm as well as energy and focus information.

Density Correction and Material Conversion. The HU values by the CT image have to be converted to rSP values usable for dose calculation. To realize this, Hounsfield LookUp Tables (HLUTs) are used. In matRad, a default HLUT is used for most cases, if no other HLUT is requested. This default HLUT is shown in Fig. III.2. Besides its application in stopping power calculations, the HLUT can also be used for the derivation of density values. For this, rSP values can be treated as density values by scaling them with the density of water. Therefore, all materials are regarded as water-equivalent, when using the HLUT.

HU	rSP to Water
-1024	0.001 *
-999	0.001
-90	0.950
-45	0.990
0	1
100	1.095
350	1.199
3000	2.505

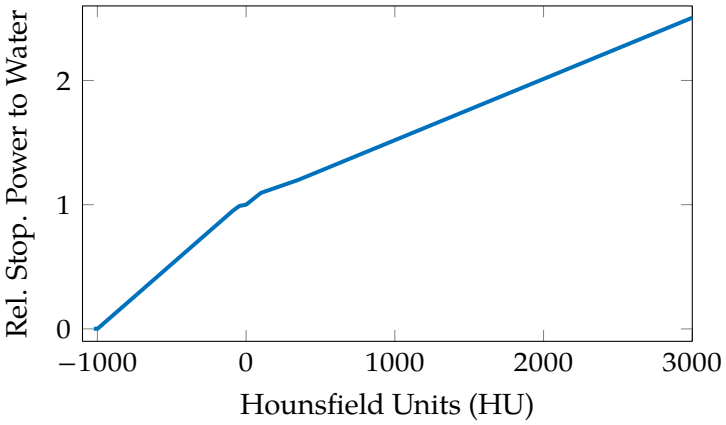

Figure III.2: Default matRad HLUT used in analytical and MC dose calculations. The values are both shown tabulated (left) as well as graphically (right). *For backwards conversion to HUs, the minimum rSP would need to be slightly adjusted to $9.999 \cdot 10^{-4}$ g/cm^3 so that the HLUT becomes bijective.

Beam Sources. The suitable source definition depends on the used dose calculation algorithm. For analytical algorithms, beam information is directly stored in the machine data depending on depth. In the data, focus information for multiple energies, geometrical information and, for each energy, kernel information (see Section II.3.2.2) is stored.

III.1.1.2 Variable RBE Models

The RBE-weighted dose can be calculated from basic parameters of the LQM and the effect (Eq. II.16), where the effect can be calculated from the αD and $\sqrt{\beta} D$ Eq. II.26. There are multiple variable proton RBE models available, two of which are currently fully implemented in matRad. The McNamara variable RBE model (MCN) andWedenberg variable RBE model (WED) (McNamara et al. 2015; Wedenberg et al. 2013) are both phenomenological, mathematical models based on a parameterization of the LQM (Section II.2.2.1). This parameterization relates the RBE to $\mathrm{RBE}_{max}/\mathrm{RBE}_{min}$ Eq. II.17, that are directly dependent on LET:

$$RBE_{max} = p_0 + p_1 \cdot LET_d \cdot \frac{1}{\alpha/\beta} \tag{III.1}$$

$$RBE_{min} = p_2 + p_3 \cdot LET_d \cdot \sqrt{\alpha/\beta} \quad . \tag{III.2}$$

These parameters differ between the models (McNamara et al. 2015; Wedenberg et al. 2013) and are defined as

$$p_0^{MCN} = 0.999064 \qquad p_0^{WED} = 1$$
$$p_1^{MCN} = 0.35605 \qquad p_1^{WED} = 0.434$$
$$p_2^{MCN} = 1.1012 \qquad p_2^{WED} = 1$$
$$p_3^{MCN} = -0.0038703 \qquad p_3^{WED} = 0 \quad .$$

Ion α_{ion} and β_{ion} can then be calculated using

$$\alpha_{ion} = RBE_{max} \cdot \alpha_\gamma \tag{III.3}$$
$$\beta_{ion} = RBE_{min}^2 \cdot \beta_\gamma \quad . \tag{III.4}$$

The photon radiosensitivity parameters α_γ and β_γ depend on the tissue type (see Section II.2.1). However, since a dynamic α/β is not implemented in the used version of matRad, they were set to a constant $\alpha_\gamma = 1/\mathrm{Gy}$ and $\beta_\gamma = 0.05/\mathrm{Gy}^2$ ($\alpha/\beta = 2\,\mathrm{Gy}$).

Figure Fig. III.3 shows a comparison of the absorbed depth dose, dose for a constant RBE of 1.1 and the RBE-weighted depth doses calculated using both the MCN and WED RBE models. For the variable RBE models, a slightly higher than 1.1 RBE in the plateau region becomes apparent as well as a significantly higher RBE in the Bragg peak region.

For carbon ions, the RBE calculation is based on the LEM model, where precalculated and depth-dependent kernels for α and β are stored in the machine data set.

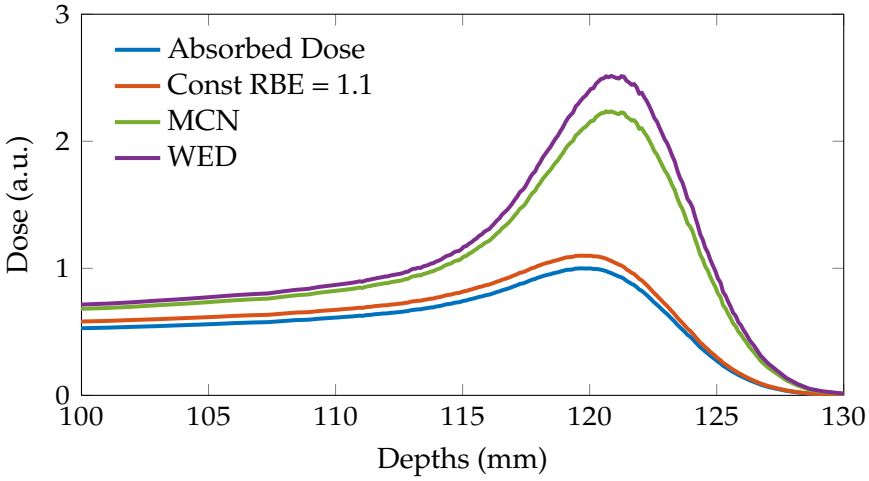

Figure III.3: Comparison of RBE-weighted depth doses analytically calculated from data stored in the *protons_generic* machine data set for a mean energy of 134.68 MeV. Profiles were normalized to the maximum of the absorbed depth dose. Shown are the absorbed dose and doses for a constant RBE of 1.1 and the two variable RBE models MCN and WED.

III.1.2 Integrated Monte Carlo Codes

There are several MC simulation frameworks available. They classify as either slow but broad and universal implementations for photons, protons and heavy ions such as TOPAS, or faster specialized programs for a single purpose/particle such as MCsquare for protons. The interface controls these MC engines through overarching functions, which directs the workflow into the MC engine specified in the plan structure. The engines are then managed through separate dose calculation functions and engine-specific classes. Most importantly, a consistent function and variable structure is maintained, which allows calculated parameters and dose cubes to be seamlessly used by other native matRad functions. This comprehensive and modular approach not only facilitates investigations into degradation in the scope of this thesis, but also provides a robust interface for researchers to test their code using MC as well as develop new features easily and efficiently.
Both described engines can be run locally through the interface automatically within a defined workflow. Since calculation can take a long time, local execution can be skipped, which allows an external calculation on a server or cluster. The simulated dose cubes can subsequently be seamlessly read-in using a built-in import functionality. In case of a cluster, this boosts the computation time immensely and makes even larger patient treatment plans or Dij calculations viable, that usually take from multiple hours to even days to finish.

III.1.2.1 Many-Core Monte Carlo (MCsquare)

The open source MC dose calculation tool-kit Many-Core Monte Carlo (MCsquare) is a MC engine that has been massively parallelized and optimized for computational efficiency (Souris et al. 2016; Souris et al. 2019). It was originally developed for the Intel Xeon Phi coprocessor, that allowed a high level of parallelization while still possessing the advantages of a Central Processing Unit (CPU). However, it is not dependent on a dedicated multi-core CPU but offers significant performance improvements on regular CPUs. It uses a *class-II condensed history algorithm*, that is designed to improve the efficiency of MC simulations by combining several particle interactions below a specified threshold into a single event. As a result, MCsquare offers fast physical dose calculation for proton beams.

Coordinate Systems. MCsquare uses a left-handed coordinate system, which means cube coordinates need to be flipped along the x dimension. Within the MCsquare parameter files, an offset to the isocenter is applied to center the coordinates on the individual voxels.
Due to how the angle is counted, only the gantry angle ϕ has to be recalculated using

$$\phi_{MCsquare} = (180° - \phi_{matRad}) \,(\mathrm{mod}\ 360°) \quad , \tag{III.5}$$

while the couch angle θ remains invariant.

Voxel, Rays and Bixel. In case the dose grid differs from the grid of the CT image - which is often the case - the CT image is resampled to the dose grid using matRad. Since the resampling is done before the MCsquare functionality is executed, no separate scoring grid or voxel transformations have to be implemented.

The major beam-specific quantities like particle type and irradiation angle are defined once for each beam. In MCsquare, energy layers are defined for each beam with individual bixels for each layer. There, a lookup table for energy-specific information like energy spread and focus information is used. This proves highly efficient, especially if only one focus information is provided for each unique energy.

Density Correction and Material Conversion. The definition of a specific material consists of the assignment of a material to a HU range and the conversion of that HU to usable densities. In MCsquare, the HLUT can directly be loaded using the `HU_Density_Conversion` config file (Souris et al. 2021).

The material conversion is controlled by a separate predefined `HU_Material_Conversion` config file, that is loaded through the interface (see Lst. A.1). It defined a respective material for a specified range of HUs through the usage of a material identifier (e.g. material 17 for water), that serves as a link to separately stored stopping powers and material properties such as atomic components (Table III.1).

Beam Sources. Each particle source is defined by the mean energy of the beam (as a description of the particles' mean range) together with the energy spread as a percentage of the mean energy. The energy spread by default is defined as a percentage of the nominal energy defined in the treatment plan, that might differ from the mean energy (Perl et al. 2012; Souris et al. 2021).

Defined by the distribution of particle velocities, the particles in a beam occupy a certain elliptic region in the phase space called the beam *emittance* ϵ. The emittance at the nozzle is used as a parametric description of the phase space and is defined by the optical parameters spot size (in mm), divergence (unitless, but equal to rad), and the correlation between the two (unitless, -0.99 to 0.99). A more detailed description as well as a translation of the needed parameters from matRad machine data is described in detail in Section III.1.4.

Scoring. As an optimized engine for absorbed dose, the choice of scorer is limited to absorbed dose, LET and respective Dij. Through the interface, the scored LET can be used to calculate α, β and RBE using variable LET-based RBE models (Section II.2.2.1) outside of the actual MCsquare simulation (Section III.1.6).

III.1.2.2 TOol for PArticle Simulation (TOPAS)

TOol for PArticle Simulation (TOPAS) is a powerful multipurpose MC interface code written in C++, which builds on the physics simulation toolkit Geant4 (Agostinelli et al. 2003; Allison et al. 2006; Allison et al. 2016). It models the transport and interactions of particles in matter for applications such as high energy, accelerator physics or medical applications. As a result, TOPAS is a powerful tool that provides a robust framework and offers a high level of complexity for the dose calculation of a variety of particles such as photon, protons and heavy ions (Faddegon et al. 2020; Perl et al. 2012). The implemented parameter control system allows mix and matching of implemented simulation modules such as particles sources, geometries or dose scorers. The latter expands to variable RBE scorers for protons and carbon ions with an available extension (Polster et al. 2015).
Implemented in this thesis is TOPAS version 3.8.1 with the physics list containing the Geant4 modules 'g4em-standard_opt4', 'g4h-phy_QGSP_BIC_HP', 'g4decay','g4h-elastic_HP', 'g4stopping', 'g4ion-QMD', and 'g4radioactivedecay'.

Coordinate Systems. Similar to matRad, TOPAS uses a right-handed coordinate system. However, the beam direction is defined in positive z instead of y. As a result, a series of rotations and translations has to be performed. TOPAS uses a default clockwise rotation, so the imported angles from matRad have to be multiplied by -1. After applying the (inverse) gantry and couch angles, the isocenter is defined and rotated by 90° around the x and y direction, respectively. Based on the previous rotations, the nozzle is defined shifted to its position. Finally, the image cube is placed into the geometry and shifted to the isocenter:

$$\begin{aligned} T_{x,y,z} &= \text{DicomOrigin}_{x,y,z} - \text{IsoCenter}_{x,y,z} \\ &= 0.5 \cdot \text{resolution}_{x,y,z} \cdot (\text{cubeDim}_{x,y,z} + 1) - \text{isoCenter}_{x,y,z} \quad . \end{aligned} \tag{III.6}$$

Applying the rotations to the overall coordinate system ensures that important quantities such as the gantry, couch and nozzle angles remain invariant. This allows for a simple visual comparison between the plans and generated files, and the phantom or patient cubes can be placed and the dose can be read back in without the need of further rotation.

Voxel, Rays and Bixel. Similar to MCsquare, in case of differing dose and CT grid, the CT image is resampled to the dose grid using matRad so that no separate scoring grid or voxel transformations had to be implemented. The major beam-specific quantities are defined once for each beam. For the ray-specific quantities, the developed interface uses ”Time Features”, where the spots are split in time by 10 ms increments (Perl, Joseph et al. 2023). Each time feature represents a single bixel with a unique combination of energy, locational information and fluence defined by the optimized Dij weights.

Density Correction and Material Conversion. Analogously to MCsquare, materials are assigned to different HU ranges and converted to usable densities (see Lst. A.2).
In TOPAS, the density correction for different HU sections was defined using a Schneider converter (Schneider et al. 1996; Schneider et al. 2000). The density correction follows the equation (Perl, Joseph et al. 2023)

$$\text{Density} = (\text{Offset} + (\text{Factor} \cdot [\text{FactorOffset} + \text{HU}])) \cdot \text{DensityCorrection} \quad . \tag{III.7}$$

For the simplest form of density correction – offset = 1 and factor = 0 – the density read by TOPAS equals the density set as the `DensityCorrection` vector. It can then directly be set by interpolating the HLUT over integer HUs. Importantly, the default minimum imaging value of –1000 HU was adjusted to –1024 HU.
Similar to MCsquare, the material conversion is defined for different ranges of HUs that are specified as the vector variable `SchneiderHUToMaterialSections`. For each set section of HUs, a material is created that is described using the molecular composition (weighted molecular components) of each material and the mean excitation energy. Table III.1 shows the implemented data for the three material sections used in this thesis. To minimize material overhead, the data was constrained to the main elements hydrogen, carbon, nitrogen, and oxygen and was subsequently normalized.

Table III.1: Mean excitation energies $I_{0,\text{mean}}$ (in eV) and element compositions used for MC material converters. Data was taken from the NIST material database (Berger et al. 2005). To minimize material overhead, the data is constrained to hydrogen, carbon, nitrogen, and oxygen and subsequently normalized.

Material	Density (g/cm^3)	$I_{0,\text{mean}}$ (eV)	Hydrogen (%)	Carbon (%)	Nitrogen (%)	Oxygen (%)
Air	$1.20 \cdot 10^3$	85.7	0.00	0.01	76.51	23.48
Water	1.00	78.0	11.19	88.81	0.00	0.00
Lung	1.05	75.3	10.24	10.34	2.90	76.53

Beam Sources. For the simplest beam model implemented in TOPAS (called `Type = "Beam"` in TOPAS), the beam shape can be described by a set of parameters that control the position distribution of the particles at the nozzle.
A *phase space* particle source (called `Type = "PhaseSpace"` in TOPAS) is the representation of the particle beam by its parameters in the phase space. These parameters are the distribution of the positions and the directional velocities of the particles that cross a given surface (Wiedemann 2015). It serves as a snapshot of the particle movement at this surface and can be loaded directly in TOPAS as a particle source. Such recorded phase space data is available for multiple scanner models, but can also be directly recorded in TOPAS.

In order to use the same parameters for both MC engines, the emittance beam model (called `Type = "emittance"`) was used in TOPAS and implemented in the interface. It uses the same values for optical parameters as MCsquare that are therefore generated using a joint fitting pipeline (Section III.1.4). There are other beam source types available such as volumetric or environment sources. However, they are not highlighted here as they are not used for the implemented interfaces.

Scoring. Since TOPAS is a more comprehensive MC engine, the choice of scorer is more complicated compared to MCsquare. The interface was built to facilitate the choice of appropriate scorer and includes a modular system that automatically includes the needed scorers for absorbed dose as well as RBE calculations or adds manually requested scorers. Additionally, despite requiring a considerable investment of time, a Dij can be scored. Within the proton RBE extension, scored LET is directly used to calculate α, β and RBE using variable LET-based RBE models (Section II.2.2.1).
For **heavy ions**, no extension is available for phenomenological models. Instead, the LEM model is used, that has been introduced theoretically in Section II.2.2.1. In TOPAS, the LEM model was implemented based on precalculated and tabulated values of α and β for multiple different fragments of the original particle depending on the kinetic energy per nucleon. A table for LEM I was generated using the open source simulation toolkit 'Survival' (Manganaro et al. 2018). The table is generated based on set photon radiosensitivities and by specifying the parameters for the nuclear radius r_{nuc} and the dose limit for the LQM D_t, after which it is assumed to be linear. The table was generated using the parameters $r_{nuc} = 5\,\mu m$, $D_t = 29\,Gy$, $\alpha_\gamma = 0.1\,Gy$, and $\beta_\gamma = 0.05\,Gy$. Fig. III.4 shows an overview of the α and β data generated using the survival code for different particles in relation to their energy.

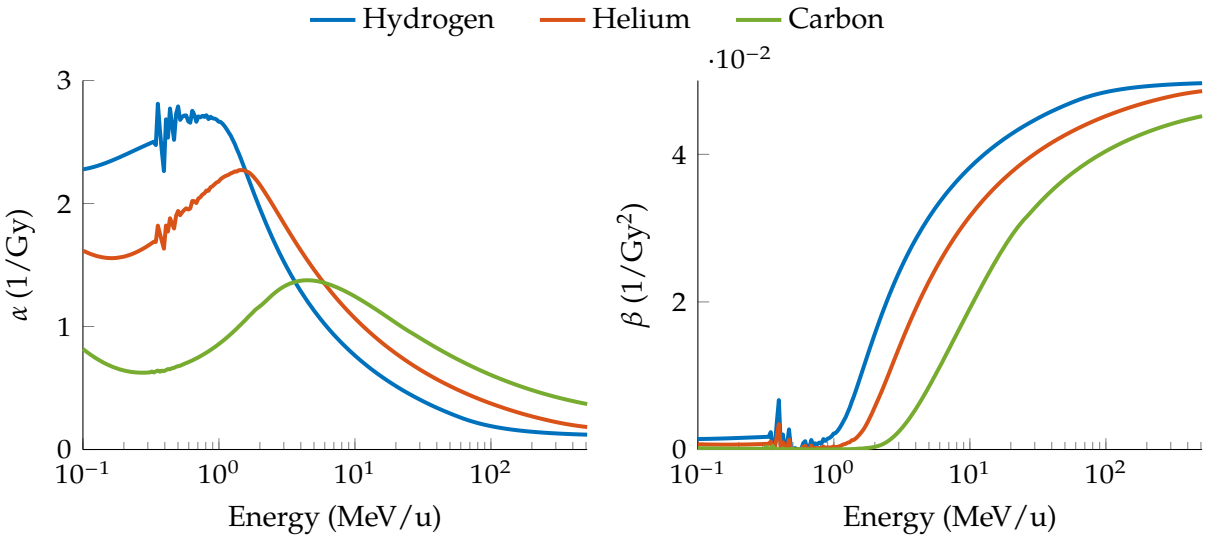

Figure III.4: Comparison of energy-dependent α (left) and β (right) data generated using the 'Survival' code (Manganaro et al. 2018). The table was generated using the parameters $r_{nuc} = 5\,\mu m$, $D_t = 29\,Gy$, $\alpha_\gamma = 0.1\,Gy$, and $\beta_\gamma = 0.05\,Gy$.

III.1.3 Development of Suitable Machine Data Sets

To assess the compatibility and validity of the MC interface and evaluate the impact of inhomogeneities and subsequent degradation correction on dose distributions, a foundational machine data set is required. This machine data set should yield consistent results across all modalities, particularly within a simple water phantom.
To maximize the accuracy and compatibility between analytical pencil beams and MC simulations in the scope of this thesis, emittance and energy spectrum were fixed to the values used in the simulations and are used for subsequent treatment plan calculations. However, both the emittance and energy spectrum can generally be derived from an existing machine data set on the fly from basic parameters (Section III.1.4).

III.1.3.1 Protons

The *protons_generic* machine data set contains data for 81 energy entries from 46.23 MeV to 199.18 MeV which corresponds to mean ranges of 20 mm to 260 mm with an equidistant spacing of 3.0 mm. Based on the ranges, the energies were calculated using Eq. III.10 with the fitted values from Table III.3a.
MC simulations were conducted on a cylindrical water phantom in vacuum using TOPAS. A new phantom was constructed for each energy step, which consisted of a 0.1 mm depth grid from 0 to 1.2 times the expected peak position. Additionally, to estimate the lateral dose component, it was devided into 25 cylindrical sections with a radial spacing of 1 mm. The simulations were based on a fixed Gaussian energy spectrum with $\sigma_E = 1\,\%$ and $E_{mean} = E_{nom.}$. A double Gaussian emittance was chosen, using the initial focus 3.44 mm as spot sizes $\sigma_{x,y}$. Furthermore, fixed values were set for the nozzle to isocenter distance (500 mm) and the Source to Axis Distance (SAD) (10^4 mm).

Absorbed Dose and LET. The resulting absorbed dose was subsequently evaluated with respect to depth and averaged radially, with weighting based on the area of the radial segments. The IDD was converted to units of MeV $\cdot$ cm^2/(g $\cdot$ primary). Similarly, the LET distributions were evaluated with depth and weighted with dose, since low-dose areas have a higher uncertainty in its value.

Lateral Dose. The lateral dose profiles were weighted using the area of the radial segments and subsequently fitted using a radial double Gaussian lateral beam model:

$$D_{lat}(x, \sigma_1, \sigma_2, w) = \frac{1-w}{2\pi(\sigma_1^2 + \sigma_{ini}^2)} e^{-\frac{x^2}{2(\sigma_1^2+\sigma_{ini}^2)}} + \frac{w}{2\pi(\sigma_2^2 + \sigma_{ini}^2)} e^{-\frac{x^2}{2(\sigma_2^2+\sigma_{ini}^2)}} \quad . \tag{III.8}$$

The fit was performed using a non-linear least squares regression with the parameters maxFunEval = 10^6, maxIter = 10^4, tolFun = 10^{-10} and tolX = 10^{-8}. The constraints and starting values set for the invidiual parameters are summarized in Table III.2. Fig. III.5 shows an example lateral fit for 99.61 MeV of the *protons_generic* machine data set.

Table III.2: Fit parameters for fitting of the lateral absorbed dose profiles. For each subsequent depth n, the starting values and constraints were set based on the previously fitted entry. For carbon ions, the weight constraints at subsequent depths were also set to be dependent on the previous entry.

parameter	constraints	starting value
weight	0.01 to 1	0.1
$\sigma_1(1)$	0 to $(\sigma_{ini} + 500)$	σ_{ini}
$\sigma_2(1)$	0 to $(\sigma_{ini} + 500)$	$\sigma_{ini} + 10$
$\sigma_{1,2}(n)$	0 to $0.9 \cdot \sigma_{1,2}(n-1)$	$\sigma_{1,2}(n-1) + 1$

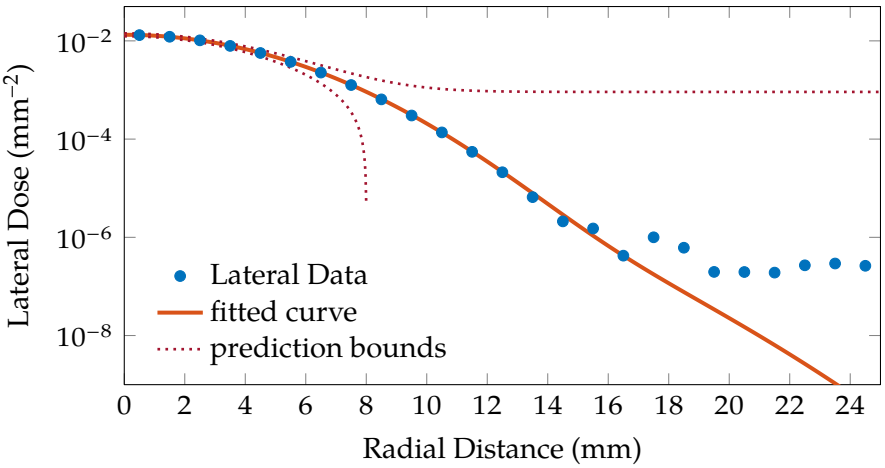

Figure III.5: Lateral profile for 99.61 MeV of the *protons_generic* machine data set at phantom entry, including the fitted double Gaussian profile (—) with 95 % prediction bounds.

Air Correction. Since the original simulations were performed in vacuum, an air widening correction for emittance was applied for analytical calculations to account for widening in air in front of the patient. The focus information for an originally parallel beam was adjusted using an air-widening lookup table that was simulated using TOPAS.

III.1.3.2 Carbon Ions

The *carbon_generic* machine data was generated analogously to the *protons_generic* machine data set. It also contains data for 81 energy entries from 82.78 MeV/u to 385.61 MeV/u, which corresponds to the same mean ranges of 20 mm to 260 mm with an equidistant spacing of 3.0 mm. Based on the proton ranges, the carbon energies were calculated using Eq. III.10 with the fitted values from Table III.3a.
MC simulations were conducted for these energies on a cylindrical water phantom in vacuum using TOPAS. A new phantom was constructed for each energy step, which consisted of a 0.1 mm depth grid from 0 to 1.8 times the expected peak position. A longer phantom compared to protons is needed to capture the tail after the peak. To estimate the lateral dose component, it was devided into seven cylindrical sections with a radial spacing of 2 mm. The simulations were based on a fixed Gaussian energy spectrum with $\sigma_E = 1\,\%$ and $E_{mean} = E_{nom.}$, as well as a double Gaussian emittance. Instead of using a fixed value for all energies, the values for the spot width were interpolated from the *carbon_HIT* data set and rounded to 2 places. The data set was provided to the department by the Heidelberg Ion-Beam Therapy Center (HIT) facility and was used to validate matRad against the SyngoRT[1] TPS used at HIT (Wieser et al. 2017b). Furthermore, fixed values were set for the nozzle to isocenter distance (1000 mm) and the SAD (6500 mm).
Data was extracted and fitted using the same workflow and parameters as described in Section III.1.3.1. Similarly to the LET for protons, the simulated α and β distributions were evaluated with depth and weighted with dose for statistical reasons. For carbon ions, no data for the air correction was available.

III.1.3.3 Characterization of the Simulated Machine Data Sets

Example calculations were performed for nine equidistant energy indices from 10 to 50 (70.70) to 154.80) on the long 350 mm box phantom (Section III.1.7.1). Single pencil beams with uniform weights were calculated using matRad, MCsquare and TOPAS for both absorbed and RBE-weighted dose. For protons, RBE-weighted dose distributions were calculated using the variable RBE model MCN, RBE-weighted dose distributions for carbon ions were calculated using the LEM model. MC dose distributions were calculated using 10^7 histories. Resulting dose distributions were evaluated laterally and with depth by averaging over the 5×5 most central voxels through the Bragg peak. Additionally, the global γ index was calculated using the [1 mm/1 %] criterion with 1 interpolation point.

[1] Siemens Healthineers, Erlangen, Germany

III.1.4 Analytical Beam Parameters for MC Simulations

In order to enable downwards compatibility with existing kernel data sets and to facilitate the usage of the MC interface for new users based on measured depth dose and lateral scattering curves, necessary beam parameters can derived solely based on the analytical machine data available in matRad. These include the mean energy of the particles with energy spread and emittance parameters.

The *mean energy* can directly be calculated from the respective mean range using a range-energy relationship, that is unique for different particles. The *energy spread* is defined as the standard deviation of the beam energy at the nozzle and can be approximated using an analytical beam representation (Bortfeld 1997). The analytical description of the depth dose of the used particles is essential and depends on the knowledge about their range-energy and energy-range relationship (Bortfeld 1997).

The methods and implementations described in Sections III.1.4.2 and III.1.4.3 were developed in cooperation with Meder (2020).

III.1.4.1 Range-Energy Relationship

Fig. III.6 shows particle range in relationship to their energy per nucleon (Data was taken from Berger et al. (2005)). The relationship follows a power law (Eq. II.5), which can be inverted for the energy-range relationship:

$$R(E) = \alpha \cdot E^p \tag{III.9}$$

$$E(R) = a \cdot R^b = \frac{1}{\alpha^{1/p}} \cdot R^{1/p} \quad . \tag{III.10}$$

A fit to Eq. III.9 was performed separately for protons, helium and carbon ions. The *NonlinearLeastSquares* method in MATLAB was used with default settings. In order to avoid uncertainties from energies below or above the energies given in machine data sets and to get an optimal fit for the most used energies, the fitted range was constricted to 10 mm to 350 mm.

Based on the resulting fit parameters for Eq. III.9, the parameters of Eq. III.10 were calculated. Both sets of parameters are documented in Table III.3. Generally, the fits for protons and helium ions were very good, represented by an R^2 of 1.0000. Carbon fits were slightly inferior with $R^2 = 0.9998$. It is worth noting that the relationship between range and energy per nucleon is the same for protons and helium, which is due to the quadratic scaling of the Bethe-Bloch equation Eq. II.3 with the particle's charge. Specifically for these two particles, the charge squared is equivalent to the number of nucleons.

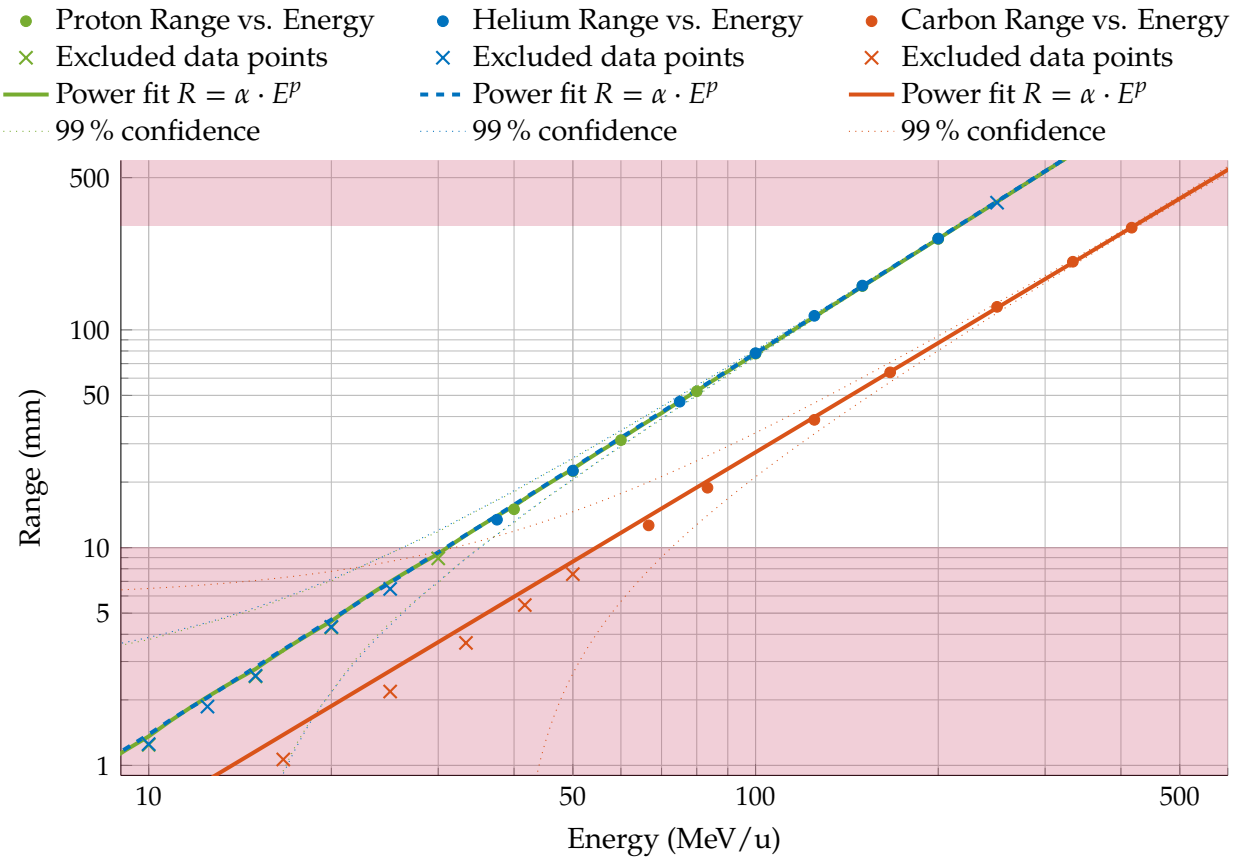

Figure III.6: Fitted range-energy relationship for protons, helium and carbon ions. The range was constrained to 10 mm to 300 mm, which correlates to the approximate range of the machine data sets available in matRad. The remaining data points were fitted according to the power law (Eq. III.9). The fit was performed using the *NonlinearLeastSquares* method in MATLAB with default settings. Data taken from Berger et al. (2005).

Table III.3: (a) Parameters of the range-energy relationship fitted to available data. Fits are shown in Fig. III.6 and were performed based on data from Berger et al. (2005). (b) Subsequently, the parameters for the inverse energy-range relationship (Eq. III.10) were calculated.

(a) Fitted parameters of the range-energy relationship described in Eq. III.9.

parameter	unit	Proton	Helium	Carbon
α	$(\mathrm{MeV/u})/\mathrm{mm}^{1/p}$	0.02383	0.02461	0.01270
p	unitless exponent	1.756	1.751	1.667
R^2	unitless	1.000	1.000	0.9998

(b) Calculated parameters for the energy-range relationship described in Eq. III.10.

parameter	unit	Proton	Helium	Carbon
a	$\mathrm{mm}/(\mathrm{MeV/u})^{1/b}$	8.397	8.295	13.72
b	unitless exponent	0.5694	0.5711	0.5999

III.1.4.2 Approximation of the Energy Spectrum

Mean Energy. The particle energy specified in the machine data is not used due to the uncertainty regarding the type of stored beam energy, for instance accelerator or source energy without beam modifiers. As already mentioned, the mean energy can directly be calculated from the respective mean range using the range-energy relationships specified in Table III.3a. However, the stored range usually describes the position of the Bragg peak, the maximum of the IDD.

A good and practical approximation for the mean range of the particles or CSDA range R_{CSDA} (see Eq. II.6), the r_{80} can be used (Berger 1993). The r_{80} describes the range where the dose has fallen to 80 % after the Bragg peak. To increase the accuracy and agreement of the MC simulations, the r_{80} value can be adjusted to account for potential range offsets as defined in the machine data. Additionally, an air offset correction is applied, taking into account the air distance from the nozzle to the phantom surface. For the machine data sets used in this thesis, the air offset correction is 0.

Energy Spread. For protons, based on the analytical dose model done by Bortfeld (1997), the energy spread can be obtained using the initial range of the particles R_0 and the Full Width Half Maximum (FWHM) of the Bragg peak in the depth dose, that is stored in the machine data. It is assumed that the total energy spread of a beam, denoted as σ_{tot}, arises from the squared sum of two components (Bortfeld (1997), Eq. (19)):

$$\sigma_{tot}^2 = \sigma_{mono}^2 + \sigma_{E,0}^2 \left(\frac{dR_0}{dE_0} \right)^2 \quad . \tag{III.11}$$

The first term originates solely from the depth-dependent range straggling of an initially mono-energetic beam $\sigma_{mono}(R_0)$, assuming no initial energy spread. The second term corresponds to the standard deviation of an initial Gaussian energy spectrum $\sigma_{E,0}$, that has been transformed into a Gaussian range spectrum (see Section II.1.1.2). To calculate the energy spread, Eq. III.11 can be rearranged, so that

$$\sigma_{E,0} = \sqrt{\frac{\sigma_{tot}^2 - \sigma_{mono}^2}{\alpha^2 p^2 E_0^{2p-2}}} \quad , \tag{III.12}$$

where the parameters α and p originate from the energy-range relationship (Eq. III.10 and Table III.3b). For this, $\sigma_{mono}(R_0)$ can be calculated using

$$\sigma_{mono}^2(R_0) \approx \alpha' \frac{p^3 \alpha^{2/p}}{3p-2} R_0^{3-2/p} \quad , \tag{III.13}$$

where α' is a quantity dependent on the stopping material (Bortfeld 1997, Eq. (17)). σ_{tot} can be calculated from the depth dose, that is stored in the machine data. The FWHM can be directly measured and can then be translated into the straggling width using

$$\sigma_{tot} = \left(\frac{\text{FWHM}}{w_{\tilde{\xi}}} \right)^2 \quad . \tag{III.14}$$

The term $w_{\tilde{\xi}}$ can be determined through an approximation of the original depth dose function (Bortfeld 1997, Eq. (15)) by neglecting constant factors and focussing on z-dependent factors only:

$$\tilde{D}(\tilde{\xi}) = e^{-\tilde{\xi}^2/4} \mathcal{D}_{-1/p}(-\tilde{\xi}) \quad , \tag{III.15}$$

where $\tilde{\xi} = \frac{R_0 - z}{\sigma}$, $\mathcal{D}$ is the parabolic cylinder function and p is the exponent of the range-energy relationship (Eq. III.10 and Table III.3b). The FWHM of Eq. III.15 directly equals to $w_{\tilde{\xi}}$ in Eq. III.14 and can be used to convert general FWHM measurements of the depth dose into the straggling width σ and vice versa. Eq. III.15 was numerically evaluated for the FWHM using Wolfram | Alpha[2] for the different particles. This resulted in values of

$$\begin{aligned} w_{\tilde{\xi},\text{p}} &= 6.289 \\ w_{\tilde{\xi},\text{He}} &= 6.337 \\ w_{\tilde{\xi},\text{C}} &= 7.335 \quad . \end{aligned}$$

While the calculation of $w_{\tilde{\xi},\text{He}}$ and $w_{\tilde{\xi},\text{C}}$ originates from the individually fitted range-energy relationship, the subsequent calculation of the energy spread in Eq. III.13 requires the material parameter α', which was approximated to $\alpha' = 0.0087\,\text{MeV}^2/\text{mm}$ by Bortfeld (1997).

III.1.4.3 Approximation of Beam Optic Parameters

In addition to the particles' energy and energy spread, that have been calculated above, a full description of an emittance particle source requires the optical parameters at the beam source, i.e., the nozzle exit (see Section III.1.2.1). Dependent on the particle energy, the *Courant-Snyder* formula links the optical parameters spot size $\sigma_{x,y}(z)$ at position z along the beam axis to the optical parameters at the isocenter ($z = 0$):

$$\begin{aligned} \sigma_x^2(z) &= \sigma_x^2(0) - 2 \cdot \rho_{x\theta}(0) \cdot \sigma_x(0) \cdot \sigma_\theta(0) \cdot z + \sigma_\theta^2(0) \cdot z^2 \\ \sigma_y^2(z) &= \sigma_y^2(0) - 2 \cdot \rho_{y\phi}(0) \cdot \sigma_y(0) \cdot \sigma_\phi(0) \cdot z + \sigma_\phi^2(0) \cdot z^2 \quad , \end{aligned} \tag{III.16}$$

[2] https://www.wolframalpha.com/input?i=roots+of+exp%28-xi%5E2%2F4%29*ParabolicCylinderD%5B-1%2F1.756%2C-xi%5D+-+0.5*1.53486

where $\rho_{x\theta}$ and $\rho_{y\phi}$ are the correlation coefficients and σ_θ and σ_ϕ are the beam divergences in x and y direction (Huang et al. 2018; Souris et al. 2021). For a divergent beam, as most clinical beams are, both divergence and correlation are positive. x and y components are weighted against each other to form the elliptic phase space.
The matRad machine data file provides the focussing information including a table that contains the spot size of the beam dependent on the distance from the nozzle traveled in air ($\sigma_x(z)$). The emittance parameters can then be extracted by fitting this data to the Courant-Snyder formula (Eq. III.16). Note that the formula is defined so that the patient is positioned at the isocenter $z = 0$ in negative z direction from the nozzle, so the table has to be adjusted accordingly (Souris et al. 2021). Firstly, a correction for the different sigmas is performed that accounts for additional scattering in air, which is not considered by the Courant-Snyder equation. Subsequently, a least-squares polynomial fit is performed, fitting the correlation coefficient $\rho_{x\theta}$ and the divergence σ_θ to the Courant-Snyder equation (Eq. III.16) using the following fit parameters:

parameter	constraints	starting value
correlation	–0.99 to 0.99	0.9
divergence	−Inf to Inf	0.1

After the fit, the spot size at the nozzle can be directly calculated using Eq. III.16 and the nozzle location (nozzle-to-isocenter distance). The correlation coefficient and the divergence can be calculated using the following equations deducted from Eq. III.16 (Huang et al. 2018):

$$\sigma_\theta(z) = \sigma_\theta(0) \tag{III.17}$$

$$\rho_{x\theta}(z) = \frac{\rho_{x\theta}(0)\sigma_x(0) - \sigma_\theta(0)z}{\sigma_x(z)} \quad . \tag{III.18}$$

Even though the particle source could be asymmetrical in x and y direction, our implementation assumes a uniform spot geometry. Theoretically, using a 2D fit with second set of parameters for σ_x, ρ_θ and σ_θ in both x and y direction, defining a double Gaussian, could result in a more accurate description. However, in this implementation, only a single Gaussian model is used, so all secondary parameters are set to 0. In case emittance data is already available in the machine data, the approximation pipeline is skipped.

III.1.5 Postprocessing of the Particle Spot List

For Monte Carlo dose calculation, the number of bixel or spots, computation time and particle statistics are related in the following way:

1. Forward calculation: The selected number of histories is divided across the individual spots. For very large treatment plans with a high number of spots, the histories have to be increased in order to gain enough current for each spot for beam delivery, which in turn increases the computation time.

2. Reverse optimization: Each bixel is calculated with an equal number of particles in order to obtain a Dij for later optimization. Here, the number of spots directly influences the computation time.

In both cases, it is expected to be advantageous to reduce the number of spots in a treatment plan while simultaneously keeping a similar accuracy or increasing the accuracy with similar computation time. Therefore, it was worthwhile to investigate possible code optimization and potential time savings by reducing the individual spots.

III.1.5.1 Spot Removal Technique

A spot removal technique was investigated which, after analytical plan optimization, removed spots below a certain weight threshold. There are are multiple options of defining the weight threshold based on the total number of weights, the mean weight, or the maximum weight. Fig. III.7 shows the percentage of total removed spots depending on the weight threshold for the 3 different spot removal definitions. For this thesis a weight threshold τ relative to the mean weight was chosen such that the weight w_i is given by

$$w_i = \begin{cases} 0, & \text{if } w_i \leq \tau \cdot \text{mean}(w) \\ w_i, & \text{if } w_i > \tau \cdot \text{mean}(w) \end{cases} . \tag{III.19}$$

It was expected that these spots, that were optimized to have very small weights, would contribute less to the overall dose distribution and could potentially be removed. After removing the small weights, the plan was reoptimized in order to adapt the plan to the reduced number of weights and attribute the removed fluence to the remaining weights. In order to avoid creating additional spots below the selected threshold, the new minimum weight was set as the minimum weight threshold for the optimization.

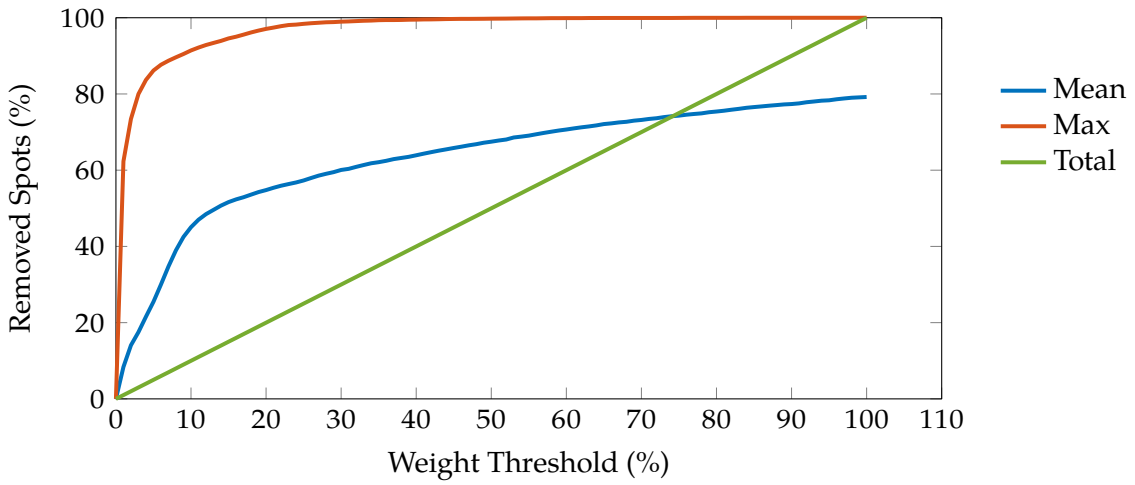

Figure III.7: Removed spots in relation to the set weight threshold as a percentage of the mean, maximum and total weight. The mean threshold was chosen for the remainder of the thesis for its ability to filter out extremely low weights without removing a high percentage of spots.

III.1.5.2 Evaluation of Treatment Plans with Removed Spots

The accuracy of the treatment plans with reduced weights was investigated using an example *liver* treatment plan (Section III.1.7.1). A base-line full treatment plan for *protons_generic* using the *constRBE* model was first calculated analytically within matRad using a bixel width of 3 mm for a total of 8050 initial bixels. Spot removal was performed for increasing weight thresholds of 1 % to 100 % and each plan subsequently reoptimized. For 3, 10 and 50 %, additional MC simulations were performed in TOPAS using 10^7 histories.
To quantify the accuracy of the plans with removed spots, the plans were evaluated regarding dose differences, quality indicators, as well as the γ pass rates compared to the full plan.

III.1.6 LET Distribution-Based RBE-Weighted Dose Calculation

In matRad and other Pencil Beam (PB) algorithms, depth-dependent LET is stored as an average particle property in water and is accumulated as a dose-weighted average over all beamlet contributions. The LET in turn is used to calculate the effect and the RBE-weighted dose distribution Eqs. II.16, II.26 and III.3. Using a dose-weighted LET and dose-weighted α and β accumulation, there is no mathematical difference computing the biological components on the fly per beamlet or from resulting α, β, and LET distributions.
For MC algorithms, the LET needs to be estimated from the individual events, which means that a particle property needs to be averaged. TOPAS scores the deposited energy in the respective medium weighted by the material density. Consequently, TOPAS reports a form of density-normalized LET ($\left[\mathrm{LET}_{D,TOPAS}\right] = \mathrm{MeV/mm/(g/cm^3)}$), which is conceptually similar to a dose-weighted average since both dose-weighting and density-normalization treat LET as a particle property independent of density (Granville and Sawakuchi 2015). On the other hand, MCsquare reports the LET as a material property that is weighted with the rSP to output in $\left[\mathrm{LET}_{D,MCsquare}\right] = \mathrm{keV/\mu m}$ (Deng et al. 2020). While these units are often used interchangeably (Smith et al. 2021), the result more relates to LET as a material-property depending on the materials density.
Since there was no native implementation of RBE calculation in the used MCsquare version, RBE considerations rely only on recalculation of the RBE based on the scored LET distributions.

RBE-weighted dose distributions. A PB proton treatment plan was calculated for a simple water phantom with a voxel size of 3 mm, bixel width of 3 mm and equal dose grid. Three separate beams with $\phi = 0$, 120 and 240° were chosen. The plan was optimized on a constant RBE of 1.1 and subsequently recalculated using the MCN model with PBs and TOPAS. Separately, the RBE-weighted dose distributions were calculated only based on the calculated sLET distributions.
In addition to the homogeneous water phantom, RBE-weighted dose distributions were calculated on the homogeneous lung phantom using PBs, MCsquare and TOPAS using the same parameters as above, but for single vertical beam. RBE-weighted dose distributions were calculated based on: 1. The LET calculated for PBs and MCsquare, 2. The unmodified TOPAS LET distribution, normalized with density, 3. The TOPAS LET converted to rSP-weighted LET by multiplying the LET with the local voxel rSP.

III.1.7 Patient Study

III.1.7.1 Patient and Phantom Overview

Long Box Phantom. For the evaluation of single Bragg peaks with a fixed energy, a cuboid water phantom ($HU = 0$) was used in the simulation studies. The phantom dimensions were 350 × 30 × 30 mm with a CT resolution of 1 mm^3. A target volume was positioned at the distal end of the phantom to avoid error messages in matRad. This setup allows for a precise analysis of the dose distributions and penetration depth of single Bragg peaks in a homogeneous medium.

Simple Box Phantom. Similarly, the simplePhantom_3mm was constructed as a pure cuboid water phantom. Phantom dimensions were set to 165 × 90 × 90 mm with a more clinically realistic CT resolution of 3 mm^3. A 15 mm air section ($HU = -1024$) was placed at the entrance. Note that the matRad convention on dimension ordering is $[y, x, z]$. The dose objectives were set to 60 Gy in the target with a squared deviation dose constraint with a penalty of 200. A squared overdosing constraint was set for the contour with 40 Gy and a penalty of 200. Treatment plans were calculated with 30 fractions and on a 3 mm^3 dose grid.

Prostate Phantom. The prostate phantom is a phantom shipped with the matRad release. It contains data for a male pelvis with dimensions of 549 × 549 × 270 mm and a resolution of 3 mm^3. Fig. III.8 shows CT slices in 3 orientations through the isocenter. The isocenter is located at $[x, y, z] = [263.3, 265.9, 124.0]$ mm, which corresponds to a slice position of $[88, 89, 41]$. The dose constraints used for the calculation and optimization of treatment plans are summarized in Table III.4. Treatment plans were calculated on a 3 mm^3 dose grid for 30 fractions.

Table III.4: Used dose constraints for the prostate and liver phantom.

	Segmentation	Dose	Constraint	Penalty
Prostate	Rectum / Bladder	50	Squared Overdosing	300
	$PTV_{56\,Gy}$	56	Squared Deviation	1000
	$PTV_{68\,Gy}$	68	Squared Deviation	1000
	Body	30	Squared Overdosing	100
Liver	PTV	45	Squared Deviation	1000
	skin	25	Squared Deviation	300

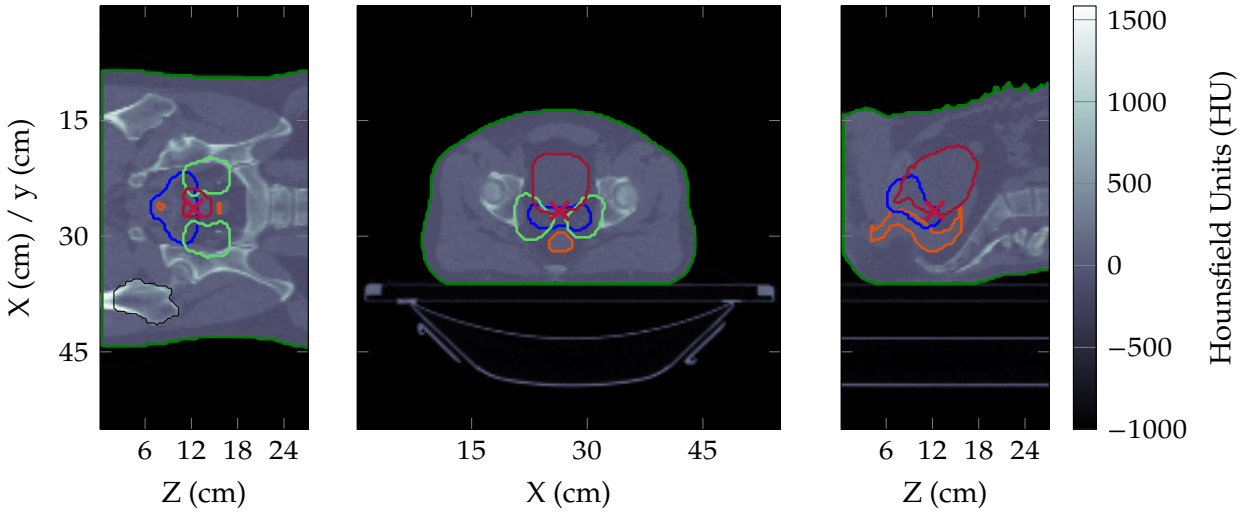

Figure III.8: Coronal (left), axial (center) and sagittal slice (right) in the isocenter of the prostate phantom. Drawn are segmentations of $PTV_{68\,Gy}$ (—), $PTV_{56\,Gy}$ (—), bladder (—), rectum (—), and body (—). The isocenter was marked with a red cross.

Liver phantom. The liver phantom is a phantom shipped with the matRad release. It contains data for the torso with dimensions of $651 \times 651 \times 420$ mm and a voxel size of $3 \times 3 \times 2.5$ mm. Fig. III.9 shows CT slices in 3 orientations through the isocenter. The isocenter is located at $[x, y, z] = [265.8, 296.7, 316.4]$ mm, which corresponds to a slice position of $[89, 99, 127]$. The dose constraints used for the calculation and optimization of treatment plans are summarized in Table III.4. Treatment plans were calculated on a $3 \times 3 \times 2.5$ mm dose grid for 30 fractions.

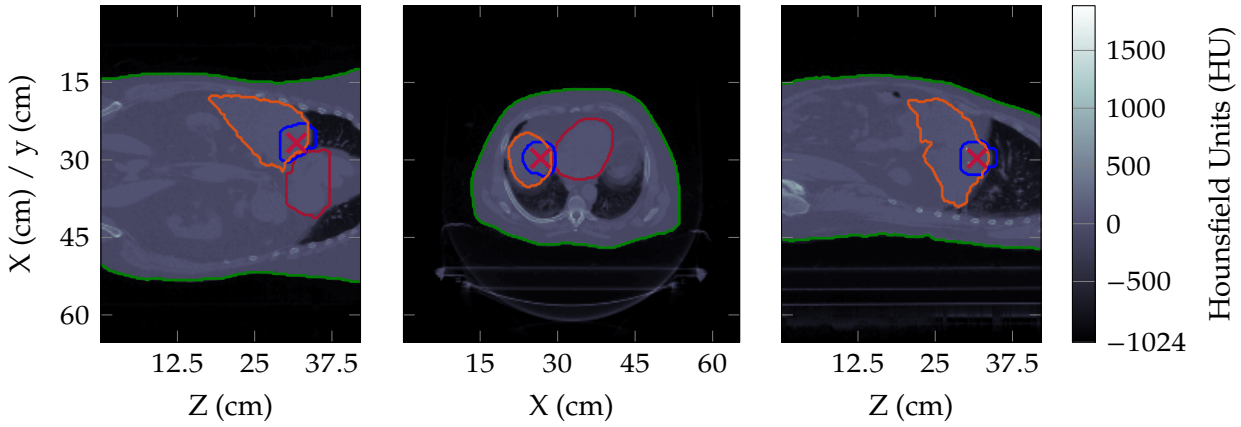

Figure III.9: Coronal (left), axial (center) and sagittal slice (right) in the isocenter of the liver phantom. Drawn are segmentations of PTV (—), heart (—), liver (—), and body (—). The isocenter was marked with a red cross.

III.1.7.2 Spread-Out Bragg Peaks for Protons and Carbon Ions

A simple SOBP was calculated using matRad and the *protons_generic* machine data set on the simplePhantom_3mm phantom (Section III.1.7.1). A vertical beam entry with a gantry angle $\phi = 0°$, couch angle $\theta = 0°$, and a 3 mm bixel width were chosen. The plan was optimized with respect to constant RBE with a prescribed dose of 2 Gy in the target. The plan was subsequently recalculated using the variable RBE model MCN. In addition to the analytical pencil beams, the plan was also recalculated using MCsquare and TOPAS with 10^8 histories, respectively. Since MCsquare does not intrinsically score RBE, the RBE-weighted dose was calculated numerically based on the scored LET (Section III.1.6). The resulting treatment plans were then evaluated in terms of visual dose distributions and absolute difference between the MC engines and matRad. Longitudinal central profiles were calculated for the 7×7 most central voxel columns and averaged. A gamma analysis, comparing the MC engines to matRad, was performed with a [3 mm/3 %] criterion and 0 interpolation points. For carbon ions using the *carbon_generic* machine data set, the same workflow was used. The plan was optimized with respect to RBE-weighted dose using the LEM model. The optimized plan was subsequently recalculated using TOPAS with 10^8 histories.

III.1.7.3 Prostate Phantom Constant RBE

A treatment plan for the prostate phantom (Section III.1.7.1) was calculated on a 3 mm^3 dose grid using matRad using the *protons_generic* machine data set. Two opposing beams with gantry angles $\phi = 90°$ and 270°, couch angles $\theta = 0°$ and 0°, and a 3 mm bixel width were chosen. The plan was optimized with respect to constant RBE-weighted dose. The particle spots were processed and 3 % of spots below the mean weight were removed. This resulted in 24.7 % of spots removed. The treatment plan was then recalculated using MCsquare and TOPAS using 10^8 histories.
The calculated treatment plan was evaluated visually in terms of axial dose slices through the isocenter, DVH and the γ index, which was calculated with the [3 mm/3 %] criterion and 1 interpolation point. Emphasis was placed on both target volumes $PTV_{68\,Gy}$ and $PTV_{56\,Gy}$, as well as the 2 most affected OARs rectum and bladder.

III.1.7.4 Liver Phantom Variable RBE and Carbon Ions

A treatment plan for the liver phantom (Section III.1.7.1) was calculated on a $3 \times 3 \times 2.5$ mm dose grid using matRad using the *protons_generic* machine data set. One single beam with gantry angle $\phi = 315°$, couch angle $\theta = 0°$, and a 3 mm bixel width were chosen. The plan was optimized with respect to constant RBE-weighted dose. The particle spots were then processed and 3 % of spots below the mean weight were removed. This resulted in 24.4 % of spots removed. The treatment plan was then recalculated for variable RBE using the MCN

and WED model using matRad as well as MCsquare and TOPAS with 10^8 histories. For matRad and MCsquare, the WED model was recalculated based on LET.
The calculated treatment plans were evaluated visually in terms of axial dose slices through the isocenter, DVH and the γ index, which was calculated with the [3 mm/3 %] criterion and 1 interpolation point. Emphasis was placed on the target volume, liver and heart.

Similarly, the treatment plan was calculated for carbon ions. Here, the plan was calculated for the *carbon_generic* machine data set in matRad and directly optimized on RBE-weighted dose using the LEM model. The spot list was optimized for a 3 % weight threshold with 6.6 % of spots removed. The plan was then recalculated with TOPAS using 10^7 histories.

III.2 Dose Degradation Correction

Lung tissue, or any porous or inhomogeneous material (foam, spongy materials, lung tissue, lung substitute materials), present an additional challenge for the dose calculation for lung tumors due to its erratic material density and fine structure. This causes the originally sharp Bragg peak to become broadened or "smeared out" (Sawakuchi et al. 2008; Urie et al. 1986), which has also been observed in phantom measurements for 3D-printed and other porous lung substitutes (Dal Bello 2017; Flatten et al. 2019; Ringbæk et al. 2017; Sell et al. 2012).
The total effect of the degradation of individual beams has the potential to negatively impact the desired dose distribution, causing low dose regions in the target and a large portion of healthy tissue receiving unwanted dose (España and Paganetti 2011; Goitein 1977; Urie et al. 1986). However, clinical TPS normally assume a non-broadened Bragg peak, since no information about microscopic tissue characteristics can be obtained with a conventional CT scanner, that only provides an averaged representation of the lung (for reasons of reducing cost and the radiation exposure to the patient). Consequently, an unrealistically sharp distal dose falloff for each beam and an incorrect dose distribution are predicted.
This, in turn, poses an additional challenge for accurate treatment planning (España and Paganetti 2011). It becomes essential to better understand and address this effect by employing mathematical models that account for the degradation.

III.2.1 Lung Microstructure and Effect on Dose

Lung tissue, or any porous or inhomogeneous material (foam, spongy materials, lung tissue, lung substitute materials), present an additional challenge for the dose calculation for lung tumors due to its erratic material density and fine structure.
This is particularly pronounced in tissues like lung parenchyma, that contain inhomogeneities on a sub-millimeter scale with high local density variations (Section III.2.1.1). In addition to the regular range straggling effect, this adds statistical fluctuations to the proton range which are known as *degradation* (Section III.2.1.2). It causes a lowered peak-to-entrance dose ratios and significantly degraded distal falloffs.

III.2.1.1 Lung Structure

The human lung is made up of several different structures, varying greatly in size (See Fig. III.10). The large bronchi and blood vessels range in size up to a few cm and the smaller bronchioles with sizes in range of ~0.5 mm to 2 mm. The small alveoli with sizes around ~250-300 µm are located surrounding those larger air ducts and take up the largest fraction of the total lung volume (Nahar et al. 2013; Weibel and Gomez 1962). All those structures consist of water or soft tissue with similar densities in the range of 1 g/cm^3 to 1.05 g/cm^3

and are filled with air with a density of approximately $10^{-3}\,\mathrm{g/cm^3}$. This provides a very fine and inhomogeneous structure, that only becomes apparent when imaged using a Micro-CT (μCT) (Robinson et al. 2005). However, in treatment planning, the small structure sizes in the lung cannot be sufficiently resolved with clinical CT scans that only have voxel sizes typically ranging from 1 mm to 3 mm and are therefore only represented in their mean densities.

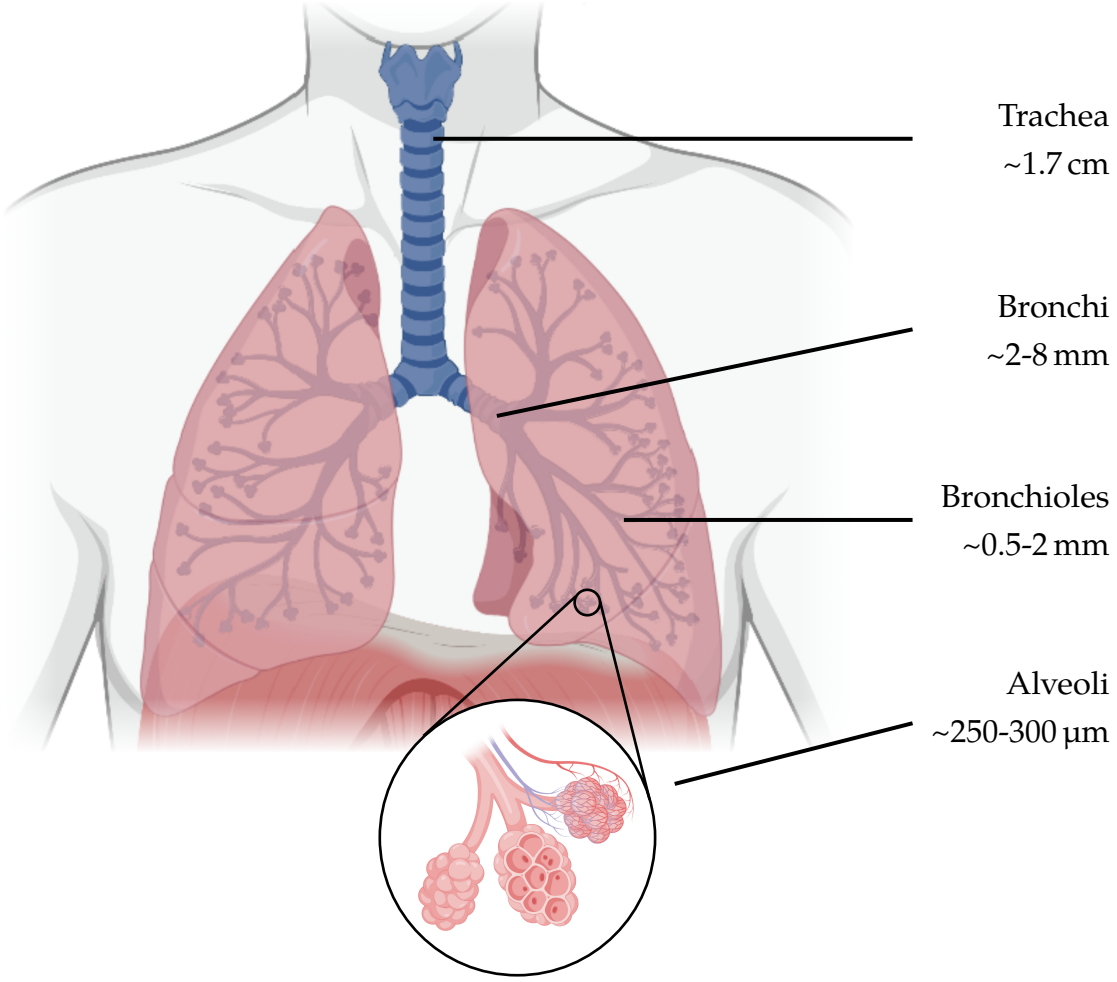

Figure III.10: Structures of the human lung. Out of scale diagram of the human lung with relevant structures, the larger air ducts (bronchi and bronchioles) as well as the surrounding small alveoli. Figure adapted from (Vikan 2024). Corresponding typical structure sizes (diameter) have been annotated (Nahar et al. 2013).

III.2.1.2 Resulting Degradation

In lung tissue, large density differences on a microscopic scale result in locally different WEPL. Side by side beams could therefore experience a significantly different attenuation on their paths. This is found to be mainly attributed to the occurrence of MCS within the density inhomogeneities (Goitein and Sisterson 1978; Sawakuchi et al. 2008). Particles might pass through more lung tissue with a high density and others through more air cavities with a low density, essentially being slowed down unevenly, resulting in different ranges. This leads to additional range straggling (Section II.1.1.2) of the particles, much stronger than what would

be anticipated for homogeneous tissue with the same WEPL and molecular composition (Sawakuchi et al. 2008). A slight shift in depth of the Bragg peak is observed, and for multiple particles, a widening effect that can be mathematically described as a Gaussian convolution with the pristine peak (Titt et al. 2015).

The Modulation Power. In order to describe the Gaussian degradation kernel based on intrinsic parameters, the modulation power P_{mod} is introduced. As a material quantity, it describes the amount of degradation that is introduced by a specific material. It links the Gaussian convolution σ with the WET of the traversed lung tissue (Baumann et al. 2017; Witt 2014):

$$P_{\text{mod}} \equiv \frac{\sigma^2}{\text{WET}} \approx d \cdot (1 - p_l) \cdot \frac{\rho_{mat}}{\rho_{\text{H}_2\text{O}}} \quad . \tag{III.20}$$

For a single voxel, this can be expressed through the density p_l, the size of the substructures d and the density of the solid lung tissue ρ_{mat} (Ringbæk et al. 2017). A higher modulation power causes a more severe the introduced degradation is. Typical values of the modulation power are in the range of 100 µm to 800 µm (Baumann et al. 2017; Burg et al. 2021; Witt 2014).

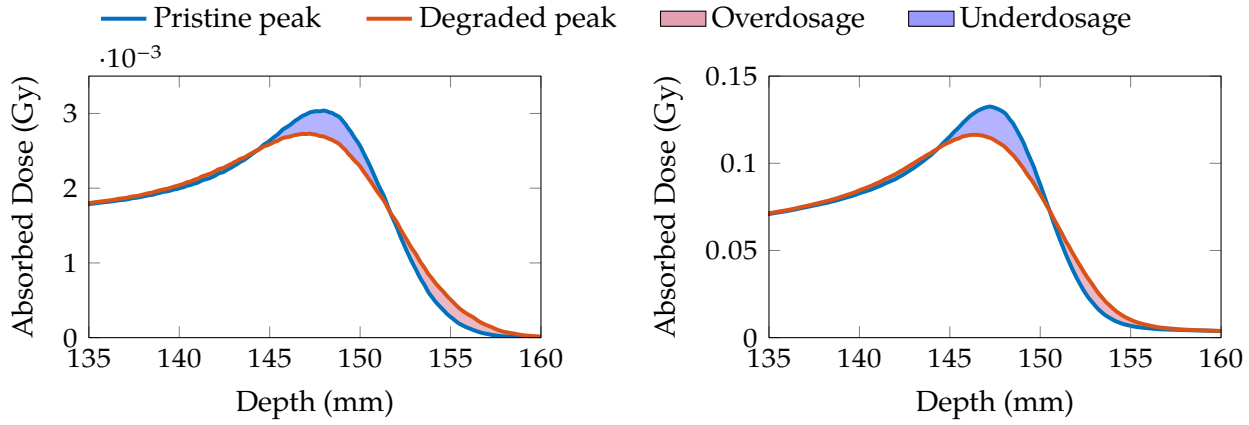

(a) Pristine and degraded proton pencil beams with energy $E = 133.05\,\text{MeV/u}$.

(b) Pristine and degraded carbon pencil beams with energy $E = 252.07\,\text{MeV/u}$.

Figure III.11: Single proton (a) and carbon ion (b) homogeneous and degraded dose curves, analytically calculated in matRad using the available *protons_generic* and *carbon_generic* machine data sets (see Section III.1.3). Degraded depth doses were analytically calculated using a Gaussian convolution of 10 (protons) and 13 (carbon ions) with a degradation sigma $\sigma^2_{\text{deg}} = 4.58\,\text{mm}^2$ calculated from $P_{\text{mod}} = 800\,\mu\text{m}$ and a lung depth of 28 mm. The difference between the pristine and degraded curves has been shaded as overdosage and underdosage.

Degraded Depth Dose. A comparison between example pristine and degraded proton and carbon ion depth dose distributions is shown in Fig. III.11. The depth doses have been directly analytically calculated from the available machine data without regarding any phantom or patient geometry. Using a worst-case modulation power $P_{\text{mod}} = 800\,\mu\text{m}$ as well as a representative maximum of WEPL measured in patient data sets (see Section III.2.4.1), a

severe degradation can be observed that is particularly pronounced for carbon ions The degradation effect leads to a similar overdosage in front of the peak as well as to a wider distal fall-off. While this serves as a simplified illustration of the dose over- and underestimation due to the degradation in a homogeneous phantom, a similar scenario is expected for multiple pencil beams in more complex phantoms or patients treatment plans.

III.2.2 Macroscopic Modeling of Microscopic Lung Tissue

Calculating the dose distribution on a μCT would incorporate the described degradation and lead to a degraded depth-dose (España and Paganetti 2011). However, this process is neither clinically feasible nor desired due to the increased X-ray exposure to the patient to generate a μCT. In order to take the degradation originating from microscopic inhomogeneities in the lung tissue into account, it is therefore essential to develop correction algorithms based on mathematical models of the degradation.

III.2.2.1 The Binary Voxel Model

Based on measurements, a simple statistical model for describing the degradation has been proposed (Titt et al. 2015). They postulated, that the degradation introduced by microscopic lung inhomogeneities can be described using a simple model of range degradation. While undergoing regular range straggling (Section II.1.1.2), the individual particles on their different paths through the microscopic sub-voxels interact with different sub-structures of drastically different material densities. For lung tissue, particles interacting with these sub-structures would encounter a different series of air and lung voxels. With this *binary voxel model*, the content of a single voxel would then be statistically independent and could be described with a Bernoulli process. Consequently, the radiological depth then becomes binomially distributed.

Approximation using a Normal Distribution. As an approximation, the broadening of the depth dose for a large number of traversed voxels can be incorporated using a convolution of the reference depth dose with a Gaussian or normal distribution (Titt et al. 2015; Witt et al. 2015; Witt 2014). The distribution depends on the size of sub-structures d, the density ρ_{mean} and the thickness of the porous material D (Ringbæk et al. 2017). These parameters can be effectively summarized by the modulation power P_{mod}, a material quantity describing the intrinsic uncertainty (Eq. III.20). Not only is it a direct measure of the strength of the degradation, it also provides a link between the WEPL and the width of the Gaussian employed in the convolution process.
Additional measurements and simulations were performed for porous materials with uniformly distributed sub-structures. The binary voxel model and its approximation through a

convolution with a normal distribution was able to replicate these measurements (Dal Bello 2017; Ringbæk et al. 2017). However, for more complex beam paths through macroscopic structures in the lung, this approximation does not hold true. In those homogeneous regions, the energy loss straggling from homogeneous materials or sections also causes a similar degradation effect, even though not as strong.

Approximation Using a Poisson Distribution. A successful implementation of the binary voxel model into an MC engine was carried out by Baumann et al. (2017). They introduced and tested a mathematical degradation model capable of replicating the depth dose degradation on low resolution structures, such as CT voxels with dimensions in the millimeter range. In their approach, a series of dose calculations was performed. For each simulation, instead of the range, the individual CT voxel densities within the lung were sampled from a precalculated normal distribution with width σ. Averaging these dose calculations resulted in a degraded depth dose distribution. Since the normal distribution could contain non-physical negative values when looking at individual voxels, it was further approximated using a shifted Poisson distribution. It is obtained by fitting the Poisson distribution in such a way that, after undergoing 20 successive convolutions (representing the traversal of multiple voxels), would result in the normal distribution for the entire target. The Poisson distribution was then generalized for non-integer WEPLs by replacing the factorial function by the Gamma function. In order to maintain the mean density, a single high weight at WEPL $= 0\,\mathrm{mm}$ was added, making this distribution somewhat artificial. Additionally, it has to be individually and numerically determined for each P_{mod}, lung voxel density and voxel size, which requires extensive precalculation.

III.2.2.2 Binomial Voxel-Sampling Degradation Model

The density sampling approach is based on the repeated calculation of different samples with varying lung densities in each sample. The resulting dose distributions are then accumulated and averaged. Based on the original proposition that the radiological depth is binomially distributed (Titt et al. 2015), Baumann et al. (2017) used a normal distribution to approximate and sample the lung voxel densities (Section III.2.2). However, the densities of each individual voxel could be directly sampled based on a simple binomial distribution. This simple and easily obtainable distribution would allow each individual voxel to be sampled from a different distribution with individual parameters according to its individual density and potentially different modulation power.

Development of the Binomial Distribution. The base assumption is that a particle on its path through the lung encounters a set number of microscopic substructures n in each voxel, which are attributed to either lung tissue or air. The probability of a substructure being lung

tissue directly corresponds to the density of the voxel p_l. Consequently, the probability of a substructure being air is $(1 - p_l)$. To obtain probability values from the CT image, the measured density values have to be scaled based on the density of the solid lung ρ_{mat}:

$$p_l = \frac{\rho_{CT}}{\rho_{mat}} \quad . \tag{III.21}$$

The probability can therefore be described using a binomial distribution, where a sample drawn from that distribution has the density x:

$$F(x) = \binom{n}{x} \cdot p_l^x \cdot (1 - p_l)^{n-x}, \quad n \in \mathbb{N},\ p \in [0, 1] \quad . \tag{III.22}$$

The number of substructures n depend on the edge length D of the voxel in beam direction and the size of the substructures d,

$$n = \frac{D}{d} \quad , \tag{III.23}$$

where d can be derived directly from a given modulation power P_{mod} (Eq. III.20). By sampling from a binomial distribution (Eq. III.22) and dividing by n, a set of $n + 1$ equidistant values (normalized densities) between 0 and 1 is obtained with mean p_l, which represents the probability of the voxel being lung tissue. Consequently, the mean μ and variance ν of the samples need to be divided by n and n^2 respectively, yielding the expressions

$$\frac{\mu_{\text{bino}}[x]}{n} = \frac{np}{n} = p \tag{III.24}$$

$$\frac{\nu_{\text{bino}}[x]}{n^2} = \frac{np(1-p)}{n^2} = \frac{p(1-p)}{n} \quad . \tag{III.25}$$

To obtain lung density samples, the sampled probability values are multiplied by the density of the solid lung tissue ρ_{mat} (Eq. III.21). In this work, ρ_{mat} was set to $1.05\,\mathrm{g/cm^3}$ (Table III.1, Material database from Berger et al. (2005)).

The binomial distribution is only defined for integer n (Eq. III.22). However, the number of substructures calculated in Eq. III.23 can be any positive real number and would therefore have to be rounded. Since most lung voxels have similar densities, rounding to the nearest integer would result in very few distinct values for n. Consequently, it is worthwhile to find a suitable continuous approximation of the binomial distribution.

Approximation with a Beta Distribution. In Bayesian inference, the *beta distribution* is a conjugate prior to the binomial distribution, therefore preserves the mathematical structure of the binomial distribution. As a result, a beta distribution was implemented as a continuous approximation of the binomial distribution. Using mean and variance of the binomial distribution (Eqs. III.24 and III.25) and the method of moments, the parameters of the beta

distribution $B(\alpha, \beta)$ can be estimated:

$$\alpha = \mu \cdot \left(\frac{\mu(1-\mu)}{\nu} - 1 \right) = p(1-p) \tag{III.26}$$

$$\beta = (1-\mu) \cdot \left(\frac{\mu(1-\mu)}{\nu} - 1 \right) = (1-p)(n-1) \quad . \tag{III.27}$$

Since the parameters α and β must be non-negative, it follows from Eq. III.26, that $n > 1$ and $p < 1$. Physically, this is not an issue, since a number of substructures smaller than 1 and a density larger than 1 (solid lung tissue) have no importance in this case. A normalized histogram of 10^6 samples of the beta approximation is shown in Fig. III.12. Furthermore, the benefit of the beta approximation is that the mean μ and variance ν are conserved:

$$\mu_{\text{beta}}[x] = \frac{\alpha}{\alpha + \beta} = p \tag{III.28}$$

$$\nu_{\text{beta}}[x] = \frac{\alpha\beta}{(\alpha+\beta)^2(\alpha+\beta+\alpha)} = \frac{p(1-p)}{n} \quad . \tag{III.29}$$

Example Distributions. A histogram of the beta approximation for different input parameters is shown in Fig. III.12 together with a comparison of samples drawn from the discrete binomial distribution as well as the derived continuous beta distribution.

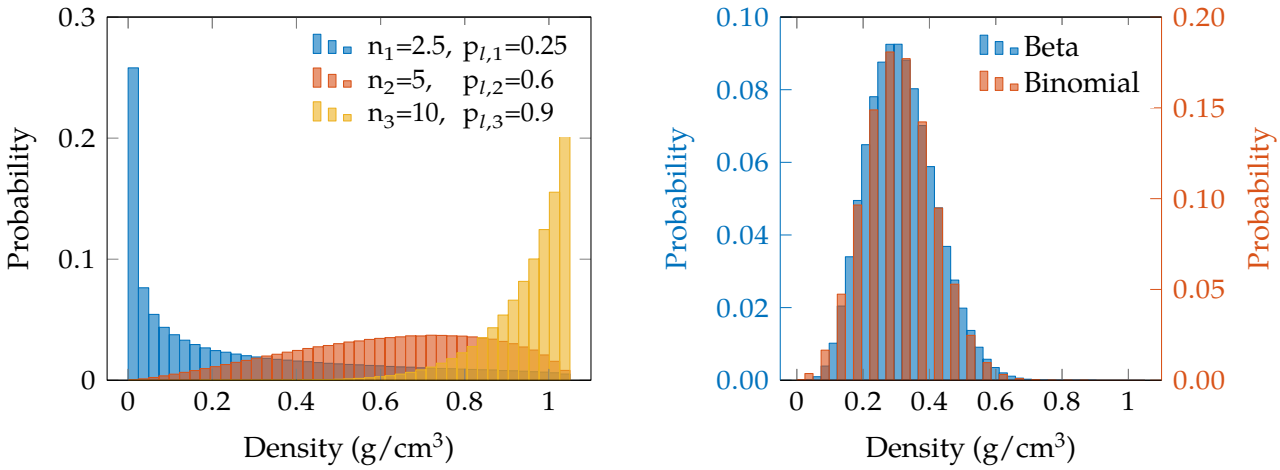

(a) Beta distribution with different parameters.

(b) Comparison of a beta and binomial distribution.

Figure III.12: (a) Histogram of 10^8 samples drawn from 3 different beta distributions with different number of substructures n_i and lung densities $p_{l,i}$. (b) Histogram of 10^8 density samples drawn from a continuous beta distribution (left axis) and a discrete binomial distribution (right axis) using $n = 22$ and $p_l = 0.3$.

III.2.2.3 Sampling Technique Evaluation

This section covers the testing and evaluation of the density sampling technique. Notably, this includes the equivalence with the convolution method and the inclusion of non-rectangular angles in the sampling.

Equivalence with Convolution. The analytical dose degradation calculation is performed only on the depth dose without consideration of the lateral part. In contrast, the sampling is performed over a number of individual complete dose calculations, that consist of both lateral and depth part that cannot be separated. To estimate eventual differences between the two methods, a study was done directly on the machine data (Fig. IV.25). Sampling was performed separately on both the depth dose (Z) and the already calculated absorbed dose ($L*Z$). The lateral dose component was calculated analogously to the regular dose calculation algorithm. It uses a squared Gaussian probability density function with $(x-\mu)=0$:

$$\text{Lat} = C \cdot \frac{1}{2\pi}\left(\frac{1-w}{\sigma_1^2+\sigma_{ini}^2}+\frac{w}{\sigma_2^2+\sigma_{ini}^2}\right) \quad , \tag{III.30}$$

which disregards the radial distance that is usually applied during regular dose calculation. For a single Gaussian model, only σ_1 is available with $w=0$. It includes a correction factor C, that converts the units of the IDD to Gy.
For the degradation correction, 28 mm of lung tissue with a density of $0.211\,\mathrm{g/cm^3}$ was assumed together with a modulation power of 800 µm. For this, lung tissue was attributed to a section of the depth vector that impacts both the position of the Bragg peak and could subsequently be replaced with the calculated lung densities of the beta distribution in case of density sampling. The sampling was performed for a virtual 1 mm CT resolution with 10^5 samples.

Oblique Angles. Due to the sampling distribution being dependent on the voxel size, performing sampling for oblique angles may induce a difference in dose. Instead of the voxel size, the mean path length through that voxel could be used, which depends on the incident angle and only equals the voxel size for orthogonal hits. Assuming a planar couch angle $\theta=0$, the voxel size d is adjusted by a multiplication factor that only depends on the gantry angle ϕ:

$$d_\phi = d \cdot \left((1-\sqrt{2}/2)\cdot|\cos(2\phi)|+\sqrt{2}/2\right) \quad . \tag{III.31}$$

This results in a smaller effective voxel size and therefore smaller number of substructures n (Eq. III.23). For the "worst case" of 45°, this means a reduction by $\sqrt{2}/2$.
In order to evaluate this, treatment plans were calculated for *Patient 3*, a patient case with planar treatment angles. A patient treatment plan was calculated using protons and constant RBE. The plan was calculated without any degradation correction and was then recalculated using the Analytical Probabilistic Modelling (APM) algorithm as well as using analytical density sampling with and without the angle correction. The plans were subsequently evaluated in terms of quality indicators in the PTV.

III.2.3 Dose Calculation in Lung

This section highlights the different implementations of dose degradation correction in different dose calculation modalities. It describes the machine data sets for use in analytical degradation correction and the implementation of the binomial voxel sampling model. Furthermore, the calculation of RBE-weighted dose distributions is introduced.

III.2.3.1 Analytical Dose Calculation

Since the degradation effects are treated as a simple Gaussian convolution (Titt et al. 2015), they can be implemented by convolving the depth dose with a Gaussian, whose width σ_{deg} represents the strength of the degradation and is directly calculated from the modulation power and the depth of the peak (Eq. III.20):

$$D_{deg}(z) = G(\sigma_{deg}) * D(z, \mu_c, \sigma_c, w_c) \quad . \tag{III.32}$$

This convolution can be carried out either numerically on the basis of the depth dose, or analytically by using an analytical representation of the depth dose.
The *APM framework* provides such an analytic representation of the beam profile by weighted superposition of a series of sub-Gaussian components (Bangert et al. 2013). The IDD can be calculated as the weighted sum of individual fitted sub-Gaussian components c, characterized by mean μ_c, width σ_c and weight w_c (Fig. III.13):

$$D(z, \mu_c, \sigma_c, w_c) = \sum_c w_c \cdot \frac{1}{\sqrt{2\pi\sigma_c^2}} \cdot \exp\left(-\frac{(z-\mu_c)^2}{2\sigma_c^2}\right) \quad . \tag{III.33}$$

The degradation effects were included in the depth dose by an analytical convolution using a Gaussian degradation kernel. The analytical convolution is simplified by adding the degradation width to the original homogeneous width ($\sigma_c + \sigma_{deg}$).

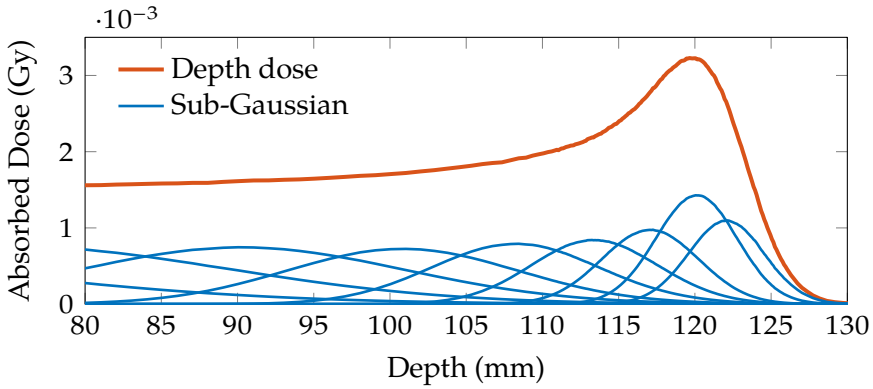

Figure III.13: Illustration of the substitution of a single Bragg peak with 10 individual Gaussian sub-profiles using the APM framework for a proton energy of $E = 129.46\,\mathrm{MeV/u}$.

Generation of APM Compatible Machine Data Sets. In order to use the analytical convolution degradation correction, a Gaussian sub-division of the depth dose needs to be implemented into the machine data set for each energy.

For the *protons_generic* machine data, the depth dose was divided into 10 sub-Gaussian components and subsequently optimized utilizing the APM fit routine (Bangert et al. 2013; Wieser et al. 2017a) using the *fmincon* optimizer[3] with the parameters listed in Table III.5. Using the same fit parameters, the depth dose of the *carbon_generic* machine data set was divided in 13 sub-Gaussians. Initial values for the mean, σ, and weights were derived from the nearest energy index in the data fitted by Wieser et al. (2017a). Because of resulting large differences for the first three energies, these were reoptimized using lower bounds of 0 with a constraint toleerance of 10^{-12}.

Table III.5: Fit parameters for the *fmincon* optimizer used to optimize the sub-Gaussians of the APM routine. The lower bounds at 0.5 are crucial to avoid artifacts when convolving the Gaussians. However, for the first 3 energies, all lower bounds were set to 0, since larger differences were observed between fitted and original depth dose.

bounds weight	0.5 to 10^4
bounds σ	0.5 to 10^4
bounds mean	0 to 10^4
maxFunctionEvaluations	1e6
MaxIterations	1e5
StepTolerance	1e-12
ConstraintTolerance	1e-8
algorithm	interior-point

The fits lead to differences between the original depth dose and the new depth dose calculated from the fitted sub-Gaussians, increasing with particle energy. The mean and maximum relative differences in dependence of the energy identifier are shown in Fig. III.14. For the Z component, the maximum values observed for the mean and maximum relative difference were 0.07 % and 0.48 % for protons, respectively. For carbon ions, the measured mean relative differences were similar compared to protons with oveerall larger maximum differences. Maximum values observed for the mean and maximum relative difference were 0.10 % and 1.11 %, respectively. The fitted αD and $\sqrt{\beta} D$ fits (only for carbon ions) lead to respective maximum mean relative differences of 0.16 % and 0.10 %.

[3] `https://de.mathworks.com/help/optim/ug/fmincon.html`

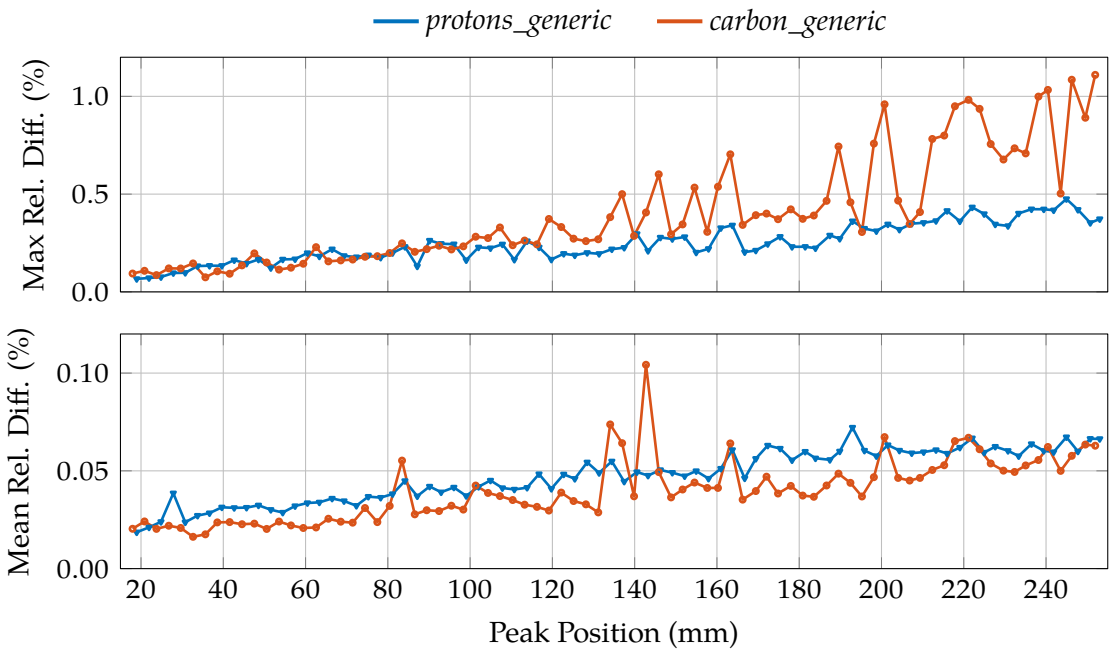

(a) Mean and maximum relative differences of the depth dose.

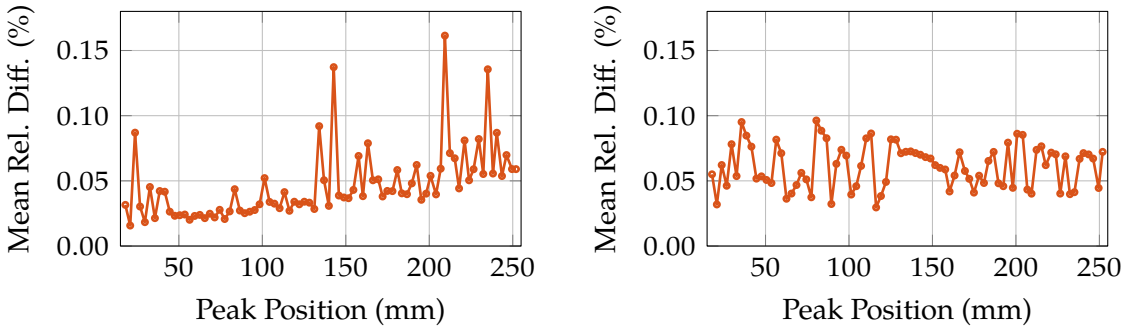

(b) Mean relative differences of the αD (left) and $\sqrt{\beta}D$ (right) for the carbon machine data set.

Figure III.14: Relative differences observed between the original depth dose and the new depth dose calculated from the fitted sub-Gaussians for each individual energy identifier in terms of peak position, for the *protons_generic* and *carbon_generic* machine data sets. The original depth dose is still stored in the data set and is used for all calculations not associated with heterogeneity correction.

Implementation in matRad. For the absorbed dose of protons, Winter et al. (2020) included the analytical convolution of the depth dose with a Gaussian degradation kernel into matRad using the *APM framework*. Multiple methods for were implemented for the convolution. However, the "voxelwise" convolution was found to be the most consistent concerning heterogeneity boundaries and the ray tracing employed in the pencil-beam algorithm (Winter 2018). The dose contributions of each voxel within the dose calculation cube are calculated with an individual convolution determined from the lung WEPLs at the corresponding voxels (using Eq. III.33). This method is used for all analytical degradation calculations in this thesis. Provided a fitted machine data set, this implementation of the analytical convolution for protons can be straightforwardly used for any ion type.

Density Sampling in matRad. To compare the developed density sampling method (Section III.2.2.2) between modalities, it was not only implemented in MC but also in matRad. For each lung voxel, the density was sampled from the individually derived beta distribution and subsequently converted to HU using the default HLUT (Fig. III.2). This process is described in more detail in Section III.2.3.2. The analytical dose is then calculated normally for a set number of samples N_s based on an individually adjusted CT for each sample.

III.2.3.2 Monte Carlo Dose Calculation

The convolution approach described above is fast and yields promising results. However, it can not be straightforwardly transferred to MC.
The calculation of the degraded dose has been implemented into MC using density sampling (Section III.2.2.2). For each lung voxel, the density was sampled from the individually derived beta distribution and subsequently converted to HU using the default HLUT (Fig. III.2). To avoid interpolation errors resulting in an altered sampling distribution, the density sampling is performed on the (resampled) dose grid. Note that the lung voxels inside of the PTV (including the irradiation margins) are not considered for the calculation of the WEPL.
Since the MC simulation relies on a density and material conversion, it is necessary to modify the existing density conversion to accurately transcribe the sampled densities into the MC code. In oder to not accidentally override existing density conversions, the HUs chosen for the sampling was appended after the highest HU found in the HLUT. This then essentially serves as a very detailed lookup table for the density conversion. The respective material converters were adjusted in turn and a new material section was appended which assigns a material to the sampled densities (see Lsts. A.5 and A.6). The sampled densities can either be regarded as a water-equivalent material with a lower density, or as lung tissue. In the scope of this thesis, the MC material conversion for the sampled densities was set to be lung tissue. In the same way, to represent all lung voxels with lung material even for homogeneous calculations, an additional lung section was inserted for all homogeneous calculations involving lung tissue (see Lsts. A.3 and A.4).
The dose is then scored for a set number of samples N_s based on an individually adjusted CT and material conversion for each sample.

III.2.3.3 Biological Dose Calculation

Analytical Convolution. The analytical convolution was originally implemented only for absorbed dose. However, for a comprehensive degradation correction pipeline, it is essential to take the RBE of the used ions into account. The *analytical* RBE-weighted dose is calculated through the biological effect and therefore αD and $\sqrt{\beta} D$ (Eq. II.26). For the calculation of RBE-weighted dose, the convolution is performed directly on precalculated αD and $\sqrt{\beta} D$

profiles. These can be either fitted APM profiles or can be calculated on the fly from the LET using a variable RBE model. In this thesis, for the *carbon_generic* machine data set, αD and $\sqrt{\beta}D$ were fitted using APM. For the *protons_generic* machine data set, αD and $\sqrt{\beta}D$ were calculated numerically. The RBE-weighted dose is calculated from the already convolved αD and $\sqrt{\beta}D$ with subsequently applied lateral contribution.

Monte Carlo. The degraded absorbed dose is implemented by using density sampling (Section III.2.3.2). The RBE-weighted dose for MC is then simulated by simply using an additional α and β scorer for the same density cube.

III.2.3.4 Comparison of Analytical and Numerical Convolution

To demonstrate the feasibility of calculating RBE-weighted depth dose profiles including degradation correction and the equivalence of numerical and analytical convolution in this scope, a proof of concept analysis was conducted using the *carbon_generic* machine data set for $E = 231.34\,\mathrm{MeV/u}$. Similar to the lung phantom (Section III.2.4.2), the degradation was modeled for 28 mm of traversed lung with a density of $0.2108\,\mathrm{g/cm^3}$ ($\widehat{=}\mathrm{WET} = 5.90\,\mathrm{mm}$). A chosen modulation power of $P_{\mathrm{mod}} = 250\,\mu\mathrm{m}$ and 800 µm results in heterogeneity sigmas of $\sigma^2_{hetero} = 1.48\,\mathrm{mm^2}$ and $4.72\,\mathrm{mm^2}$, respectively (Eq. III.20). Two different methods were compared. First, each Gaussian sub-component of the fitted αD and $\sqrt{\beta}D$ profiles was *convolved analytically* with the Gaussian degradation kernel using APM (Eq. III.33). Secondly, the unperturbed (not fitted) αD and $\sqrt{\beta}D$ profiles were also *convolved numerically* with the same degradation kernel.

III.2.4 Lung Patient and Phantom Overview

This section provides a summary of the patient cases and phantoms utilized in this thesis for the evaluation of the degradation effects and the subsequent degradation correction methods. This encompasses four pre-selected patient data sets for full treatment plans, which covered a wide range of tumor sizes and depths. Additionally, three lung phantoms were designed for testing and proof of concept purposes.

III.2.4.1 Lung Patient Data Sets

The patient data sets were evaluated and compared based on tumor size, couch and gantry angles as well as the statistics of the WEPL of the lung tissue that a treatment beam experiences. For this reason, virtual treatment plans were calculated for each data set using the *protons_generic* machine data set. For all beams, a manual ray tracing was performed, calculating the rays' respective total WEPL_{tot} from patient surface to the respective first voxel of the PTV. As a result, the lung voxels inside of the PTV (including the irradiation margins) are not considered for the calculation of the WEPL. Note that they are also not considered in the implemented density sampling method (Section III.2.3.2). To isolate the influence of the lung tissue on the total WEPL, the specific lung WEPL_{lung} was separately calculated only for the lung voxels specified in the lung segmentation. Both WEPLs were subsequently averaged for each beam. For that, only rays that interacted with lung tissue were selected to estimate the WEPL contributing to the degradation. This evaluation is shown in Figs. III.15 to III.18. For this patient, 100 % of the rays of all three beams come in contact with lung tissue before reaching the PTV. A mean WEPL_{lung} over all rays of 6.65 mm, 5.66 mm and 7.75 mm for the three beams was calculated compared to a WEPL_{tot} of 57.68 mm, 59.57 mm and 104.27 mm, respectively (Table III.6). A list of all evaluated parameters can be found in Table III.6.
Based on this overview, it can be concluded, that *Patient 2* and *Patient 3* would most likely best suitable for an analysis of heterogeneity correction. The tumors in these cases are located fully within the lung, resulting in all beams and sub-beams interacting with lung tissue to capture degradation effects. At the same time, both have drastically different tumor sizes as well as different WEPL which changes the amount of degradation for a constant P_{mod} (Eq. III.20). Lastly, *Patient 1* could be interesting to compare against, since it combines the large tumor volume of *Patient 2* with the lower WEPL of *Patient 3*.

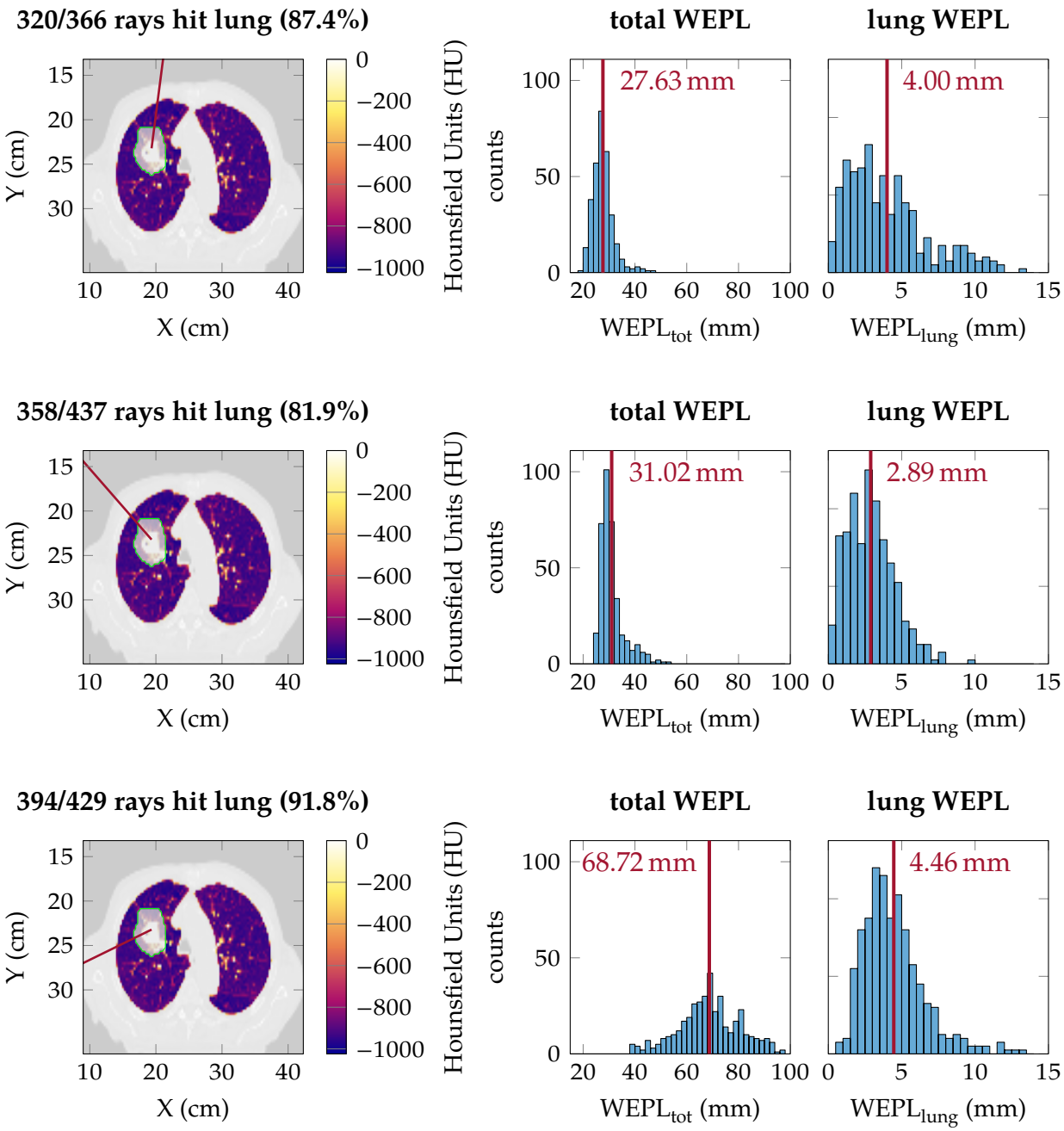

Figure III.15: Overview of the WEPL evaluation of *Patient 1*. Shown are isocenter CT slices with highlighted lung segmentations. Drawn in is the central beam axis (—) impinging on the PTV (—). The lung voxels inside of the PTV (including the irradiation margins) are not considered for calculation of the WEPL and are therefore greyed out. A custom color map was chosen to highlight the density differences within the lung sections. Also shown are histograms of calculated total WEPL_{tot} and lung WEPL_{lung}.

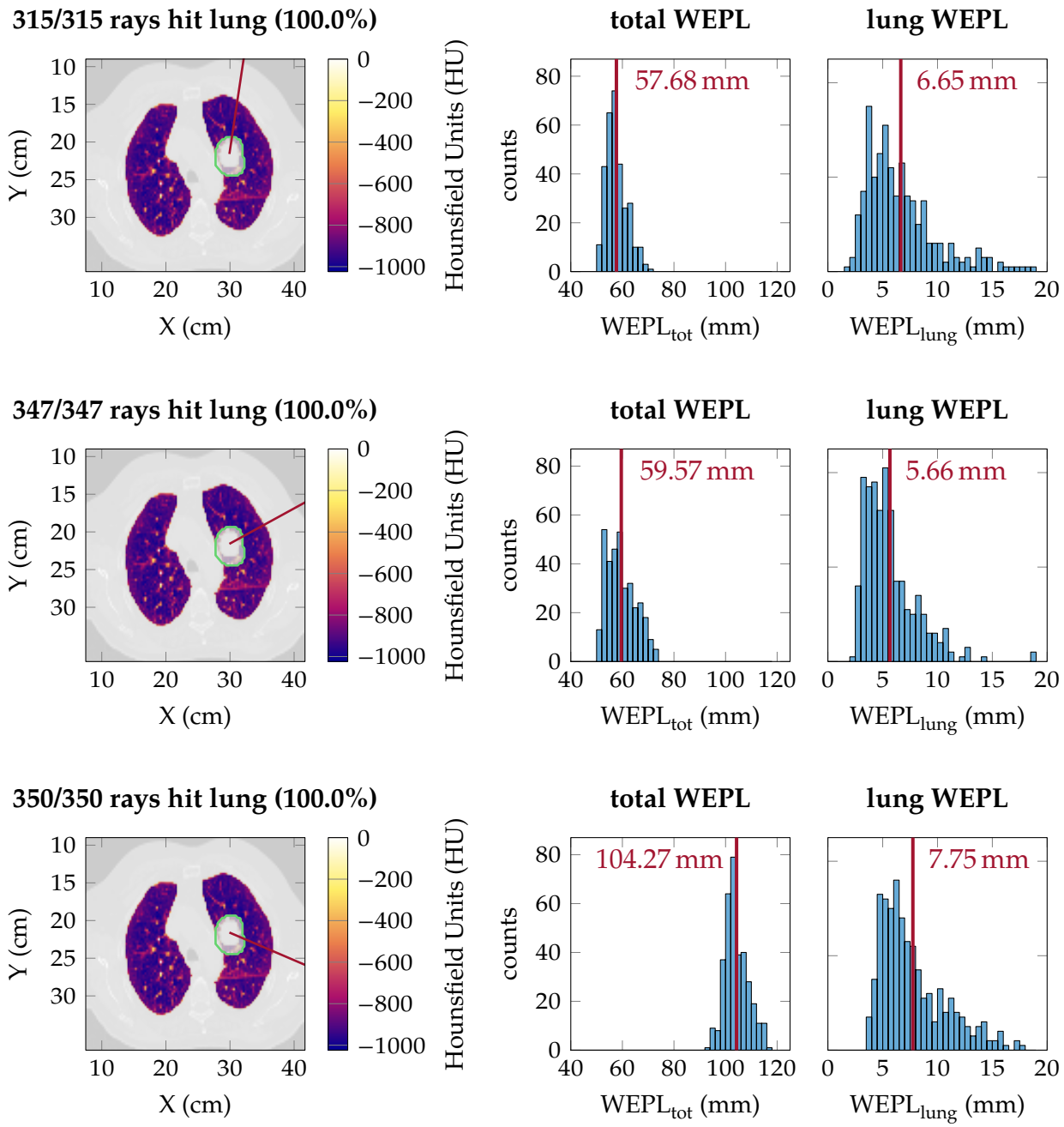

Figure III.16: Overview of the WEPL evaluation of *Patient 2*. Shown are isocenter CT slices with highlighted lung segmentations. Drawn in is the central beam axis (—) of the virtual treatment beams impinging on the PTV (—). The lung voxels inside of the PTV (including the irradiation margins) are not considered for calculation of the WEPL and are therefore greyed out. In that particular patient case, all incident rays interact with lung tissue on their path to the tumor. A custom color map was chosen to highlight the density differences within the lung sections. Also shown are histograms of calculated total WEPL$_{tot}$ and lung WEPL$_{lung}$.

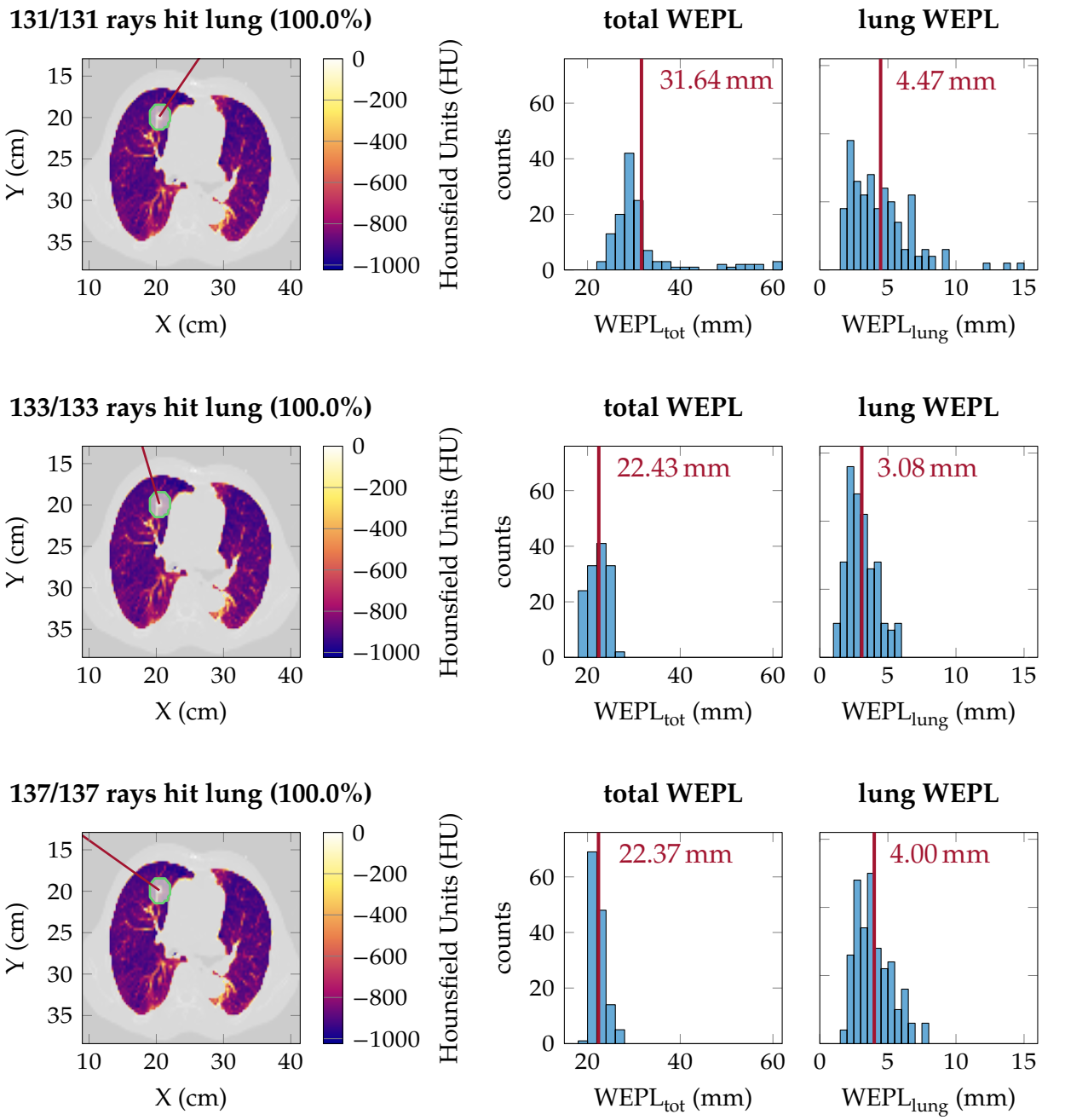

Figure III.17: Overview of the WEPL evaluation of *Patient 3*. Shown are isocenter CT slices with highlighted lung segmentations. Drawn in is the central beam axis (—) impinging on the PTV (—). The lung voxels inside of the PTV (including the irradiation margins) are not considered for calculation of the WEPL and are therefore greyed out. A custom color map was chosen to highlight the density differences within the lung sections. Also shown are histograms of calculated total WEPL_{tot} and lung WEPL_{lung}.

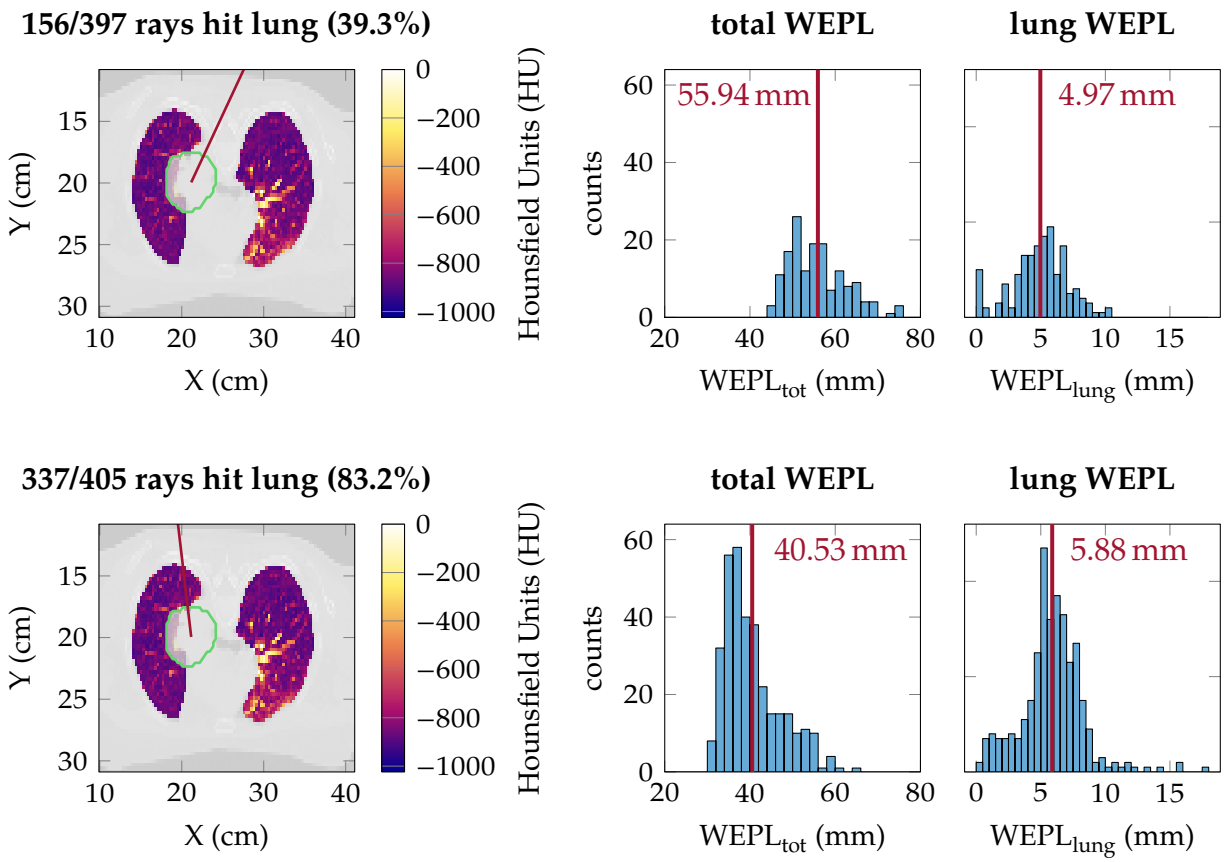

Figure III.18: Overview of the WEPL evaluation of *Patient 4*. Shown are isocenter CT slices with highlighted lung segmentations. Drawn in is the central beam axis (—) impinging on the PTV (—). The lung voxels inside of the PTV (including the irradiation margins) are not considered for calculation of the WEPL and are therefore greyed out. A custom color map was chosen to highlight the density differences within the lung sections. Also shown are histograms of calculated total WEPL$_{tot}$ and lung WEPL$_{lung}$.

Table III.6: Evaluation summary of four selected lung patients. Patients were evaluated in terms of tumor volume that has been translated to a cube of equivalent volume, beam angles, as well as total WEPL and WEPL through lung tissue, for each beam, respectively.

Name		***Patient 1***	***Patient 2***	***Patient 3***	***Patient 4***
Tumor Location		right	left	right	left
Tumor Volume (cc)		108.3	75.3	15.7	94.4
Equiv. Cube Edge (mm)		47.7	42.2	25.0	45.5
Couch Angles (deg)		350, 10, 0	0, 0, 0	0, 0, 0	0, 0
Gantry Angles (deg)		10, 310, 250	10, 65, 110	40, 340, 300	35, 350
Used Proton Energies (MeV/u)		46 to 129	78 to 143	46 to 93	64 to 143
Used Carbon Energies (MeV/u)		90 to 248	149 to 276	83 to 181	116 to 276
Prescribed Dose		8.75 Gy / 8 fx	11.07 Gy / 6 fx	2 Gy / 30 fx	2 Gy / 30 fx
Organs At Risk (OARs)		Esophagus^{N} Central Airways*	Heart^{N} Central Airways* Central Region*	Central Airways Aorta^{*,N}	Heart^{N} Esophagus^{*,N}
Beam 1	$WEPL_{tot}$ (mm)	27.6	57.7	31.6	55.9
	$WEPL_{lung}$ (mm)	4.0	6.7	4.5	5.0
	Hit Lung Tissue (%)	88	100	100	39
Beam 2	$WEPL_{tot}$ (mm)	31.0	59.6	22.4	40.5
	$WEPL_{lung}$ (mm)	2.9	5.7	3.1	5.9
	Hit Lung Tissue (%)	82 %	100 %	100 %	83 %
Beam 3	$WEPL_{tot}$ (mm)	68.7	104.3	22.4	-
	$WEPL_{lung}$ (mm)	4.5	7.8	4.0	-
	Hit Lung Tissue (%)	92 %	100 %	100 %	-

* main OAR within or near the tumor or treatment beam.

^{N} NTCP parameters are available.

III.2.4.2 Development of Digital Lung Phantoms

To facilitate the testing of new code implementations and the validation of concepts, a water phantom with a simple and well known geometry was needed. This phantom should include a slab of lung tissue for heterogeneity correction and accurately resemble the average WEPL found in treatment plans for lung cancer patients. Based on conducted measurements (Section III.2.4.1), *Patient 2* was identified as an ideal case for analysis, as it featured a suitably sized tumor and a beam trajectory that passed through lung tissue.
Consequently, three cuboidal lung phantoms were created with differently implemented lung slabs while maintaining consistent target depths and mean total WEPLs. Additionally, the mean WEPL introduced by the lung slab was kept constant across all three phantoms. The following values were set for the phantom lung:

$$\overline{\mathrm{WEPL}}_{tot} = 60\,\mathrm{mm} \qquad (\text{measured: } \overline{\mathrm{WEPL}}_{tot,pat} = (73.9 \pm 15.2)\,\mathrm{mm}) \tag{III.34}$$

$$\overline{\mathrm{WEPL}}_{lung} = 6\,\mathrm{mm} \qquad (\text{measured: } \overline{\mathrm{WEPL}}_{lung,pat} = (6.67 \pm 0.58)\,\mathrm{mm}) \tag{III.35}$$

A voxel size of $3\,\mathrm{mm}^3$ was selected for the phantom to resemble the voxel size of the patient. An air gap of 15 mm (5 vox) was left in front of the phantom to simulate the presence of air that would typically be encountered before the actual patient. Furthermore, it serves as a clear distinction between the external environment and the phantom. Additionally, the tumor volume extracted from patients was converted into a cube with equivalent volume with an edge length of 45 mm, serving as the phantom target volume. Both values are also listed in Table III.6.
The phantoms were evaluated based on density values and implemented in HUs. The therefore required conversions between density values and HU were performed using the default HLUT listed in Fig. III.2.

Real Lung Phantom *"RealLung"*. A slab of lung ($30 \times 30 \times 9$ vox $\widehat{=}$ $90 \times 90 \times 27$ mm) was copied from the right lobe of the sample *Patient 2* within the healthy side of the lung without any segmented tumor tissue (Fig. III.19). The lung slab was selected and placed into a water phantom close to the target volume, so that the WEPL at the target entry fit the previously set values (Eq. III.34). An evaluation of the copied lung voxels revealed a percentage of solid lung tissue of 0 %, indicating that no voxel contained a voxel density greater than $1.05\,\mathrm{g/cm}^3$. This threshold value serves as a cutoff point for binomial degradation correction (Section III.2.2.2), implying that all copied voxels will be considered.
Additionally, in the phantom, a small 3 mm (1 vox) gap was left between the lung and the target to better differentiate the effect in the lung slab and in the target volume.

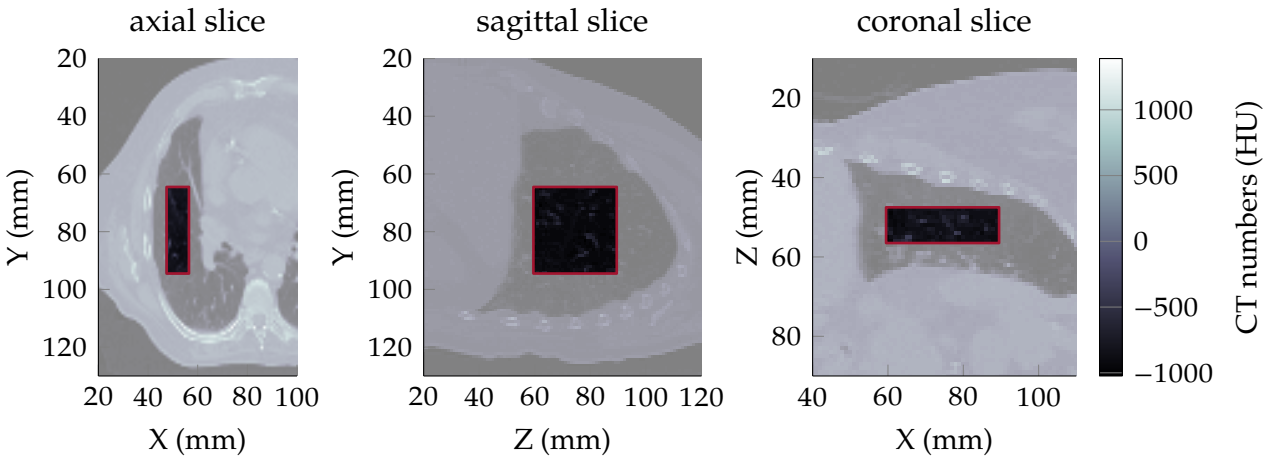

Figure III.19: Axial, sagittal and coronal CT slices of *Patient 2* at depths of $Z = 223.5$ mm, $X = 154.5$ mm and $Y = 208.5$ mm, respectively. The selected lung slab (30 × 30 × 9 vox ≙ 90 × 90 × 27 mm) was highlighted.

Heterogeneous Lung Phantom. A second phantom was constructed where the copied lung slab was replaced by a slab of equal WEPL, in which the real lung voxel positions were randomized to keep the realistic density distribution and mean density while simultaneously eliminating potential local density clusters.

Homogeneous Lung Phantom. Lastly, a third phantom was constructed where the slung slab was overwritten by a constant value of –798 HU, resembling the mean HU of the real lung experienced by the incident rays.

Summary. A summary of the 3 constructed lung phantoms is shown in Fig. III.20a and a comparison of evaluated parameters is shown in Table III.7. Additionally, the recorded lung WEPLs of the individual rays in the virtual treatment plan are summarized in a histogram in Fig. III.20b.

Table III.7: Physical depth, $\mathrm{WEPL_{tot}}$, $\mathrm{WEPL_{lung}}$ and mean HU of the 3 constructed lung phantoms.

quantity	hom	het	real
physical depth	96 mm	96 mm	96 mm
$\mathrm{WEPL_{tot}}$	59.71 mm	59.56 mm	59.71 mm
$\mathrm{WEPL_{lung}}$	5.69 mm	5.54 mm	5.69 mm
mean HU	–798.0 HU	–803.3 HU	–798.0 HU

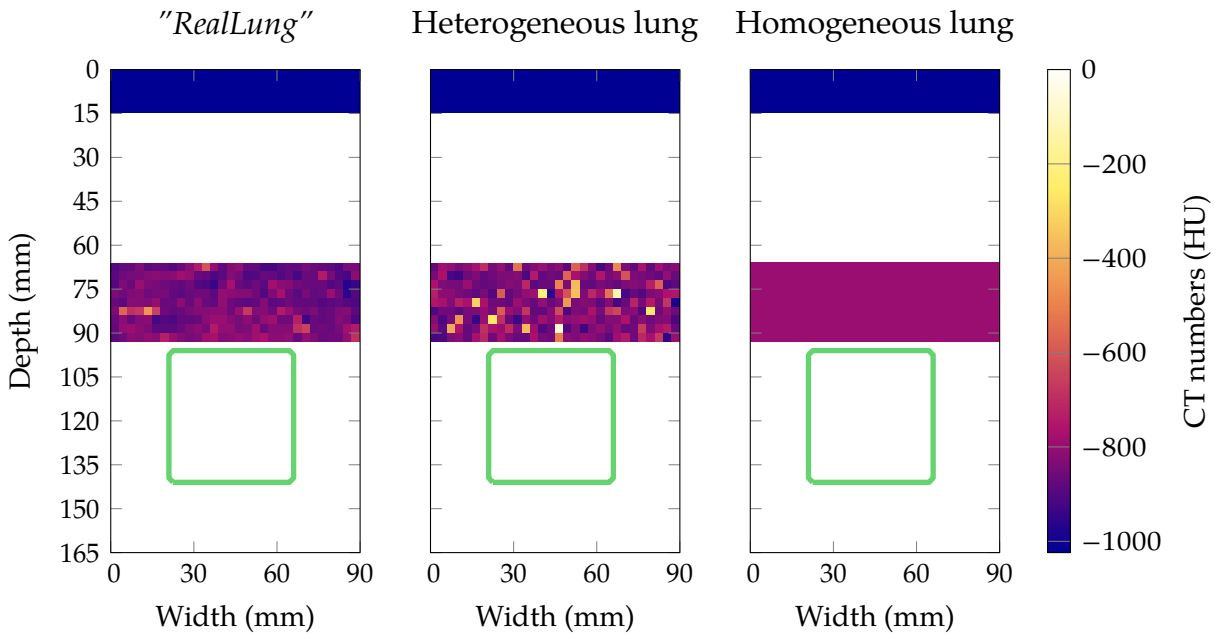

(a) Overview of the constructed real lung phantom based on a patient lung as well as subsequently derived heterogeneous and homogeneous lung phantoms.

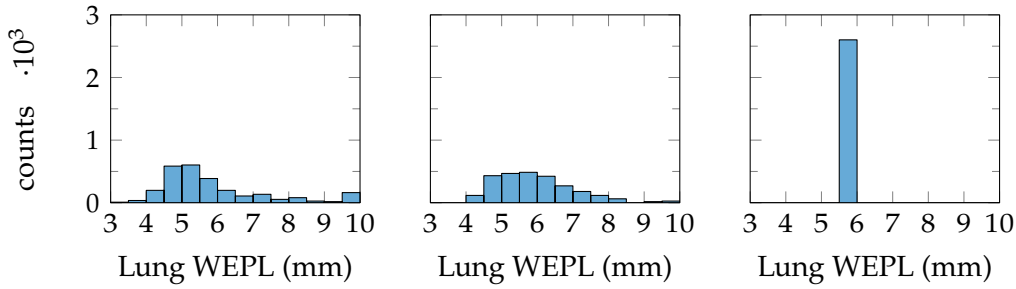

(b) Histograms of lung WEPLs of the constructed phantoms ray-traced based on a virtual treatment plan.

Figure III.20: (a) Overview of the three constructed lung phantoms. Left: A real lung phantom consisting of a lung slab copied from a patient lung. Center: A heterogeneous lung phantom with lung voxels randomized from the patient lung. Right: A homogeneous lung phantom with constant HU derived from the patient lung. They share physical geometry, target (—), as well as similar values for WEPL (Table III.7). A custom color map was chosen to highlight the density differences within the lung sections. (b) Histograms of the WEPLs for the individual rays in a virtual treatment plan calculated using the *protons_generic* machine data set with a bixel width of 1 mm.

III.2.5 Phantom Study

As a first step, the developed methods for degradation correction were employed and tested using the developed lung phantoms (Section III.2.4.2). After, degraded SOBPs were calculated for all three different lung phantoms using protons. Additionally, a proof of concept simulation was performed on the *"RealLung"* phantom using carbon ions.

III.2.5.1 Simulated Pencil Beam Degradation

To validate the implementation and functionality of the degradation algorithms for different modalities, single pencil beams were tested on the homogeneous lung phantom. The RBE-weighted dose distributions from individual pencil beams were calculated for a proton energy of 120.14 MeV, utilizing a vertical beam entry ($\phi, \theta = 0$). The dose calculations were performed on the original 3 mm voxel grid, as well as on voxel grids resampled to 1 mm and 2 mm. While homogeneous dose calculations are not expected to be affected by the resampling, a different resolution significantly alters the underlying sampling distribution (Eqs. III.22 and III.23). To illustrate the impact of degradation, the modulation power was set to $P_{\text{mod}} = 250\,\mu\text{m}$ and 800 µm. Additionally, the data for the original 3 mm voxel grid was evaluated in terms of central dose profiles and IDDs in order to illustrate their difference. Here, emphasis was laid on the dose in the lung section and the Bragg peak.

III.2.5.2 Influence of WEPL and Modulation Power

Since the strength of the degradation is directly proportional to the WEPL (see Eq. III.20), it is worth investigating if this proportionality is replicated in analytical convolution and density sampling. For this, the homogeneous lung phantom (Section III.2.4.2) was altered with HUs in the lung of in 100 HU equidistant steps between −1000 HU and −600 HU. For each, a proton treatment plan with a bixel width of 3 mm, fraction dose of 2 Gy/fx, 3 mm dose grid, and a vertical beam entry ($\phi, \theta = 0$) was calculated using PBs, optimized with respect to constant RBE and subsequently processed for spot removal. The plans were then recalculated with MCsquare. Degradation correction was included by using analytical PB convolution, as well as density sampling for PBs and MCsquare. A constant modulation power of $P_{\text{mod}} = 800\,\mu\text{m}$ was set. The same experiment was repeated with the original constant lung HU of −798 HU (5.96 mm) while varying the modulation power in 200 µm steps between 100 µm and 900 µm.
The degraded dose distributions were compared to their homogeneous counterpart in terms of the relative difference in the mean dose to the target. Since the strength of the degradation primarily depends on the WEPL, it is expected to follow a linear relationship for invariant lung properties. Based on this premise, a linear fit was performed with fixed boundaries at the origin ($a \cdot x$).

III.2.5.3 Degradation for Spread-Out Bragg Peaks

For protons, treatment plans were calculated on the homogeneous, heterogeneous and *"RealLung"* phantom using the *protons_generic* machine data set. The dose of was delivered over 30 fractions with a fraction dose of 2 Gy/fx. A bixel width of 3 mm, a dose grid equal to the CT grid, and a vertical beam entry ($\phi, \theta = 0$) were set. The plan was optimized for constant RBE, subsequently processed for spot removal with a 3 % mean weight threshold and reoptimized. The plan was then recalculated with PBs and both MC engines for variable RBE using the MCN model. For the MC simulations, the number of histories was set to $1{\cdot}10^8$. The degradation correction was incorporated through analytical convolution (APM algorithm) for PBs, as well as density sampling for all modalities with 100 samples each. The resulting treatment plans were evaluated in terms of dose slices through the isocenter, averaged central beam profiles and quality indicators (see Fig. III.21). γ pass rates between homogeneous and degraded dose distributions were calculated using a [3 mm/3 %] criterion with 0 interpolation points. Additionally, the HI and CI (Eqs. II.23 and II.24) were calculated and plotted in a bar plot.

For carbon ions, the same parameters were used as for protons. The absorbed dose distributions were calculated for the real lung phantom for PB and TOPAS. The plan was optimized for absorbed dose, subsequently processed for spot removal with a 3 % mean weight threshold and reoptimized. Subsequently, the plans were recalculated including degradation correction.

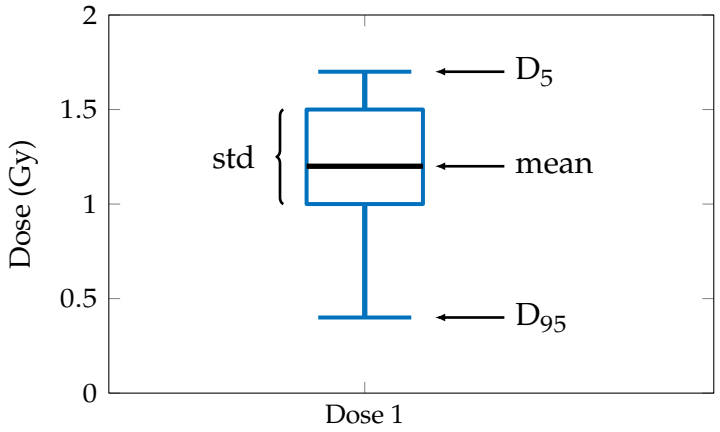

Figure III.21: Schematic drawing of a custom "box plot" used to demonstrate the changes the dose quality indicators mean dose with standard deviation, D_5 and D_{95}. They are used in the evaluation of the simulated degraded treatment plans.

III.2.5.4 Interdependence of MC Histories and Number of Samples

To gauge the dependence of the degradation on the number of MC histories and density samples, dose distributions were recalculated using 500 density samples with 10^8 and 10^9 histories ($2{\cdot}10^5$ and $2{\cdot}10^6$ histories per sample). Based on the methods described in Section III.2.5.3 for the homogeneous lung phantom, the degraded, sampled constant RBE-weighted proton dose distributions were recalculated using PBs, MCsquare and TOPAS with the adjusted histories per sample. Mean relative difference to the prescribed dose of 2 Gy in the entrance channel within the lung and half the target (depth of 12 cm), as well as γ pass rates using the [3 mm/3 %] criterion with 0 interpolation points, were calculated.

III.2.6 Patient Study

As a last step, the previously discussed concepts and developed methods were applied on the selected patient data sets.

III.2.6.1 Patient Treatment Plans

For protons, the dose was calculated on the CT grid and subsequently optimized in regards to constant RBE. The *protons_generic* machine data set was used with a bixel width of 3 mm. All other patient-specific parameters are listed in Section III.2.4.1. The plans were processed using spot removal with a 3 % mean weight threshold and reoptimized thereafter. After optimization, the treatment plans were recalculated for variable RBE using the MCN model. The plans were then recalculated in MCsquare and TOPAS, including the RBE scorer. The number of computed histories was set to 10^8 histories, respectively. For carbon ions, using the *carbon_generic* machine data set, treatment plans were calculated and optimized on RBE-weighted dose for the LEM model. Spot removal was performed with a 3 % mean weight threshold and the plans were reoptimized. Carbon plans were subsequently recalculated using TOPAS including the discussed tabulated RBE scorer with 10^8 histories. The degradation correction was incorporated by analytical convolution, as well as density sampling for PBs, MCsquare (protons only) and TOPAS, using 100 samples.
The calculated patient treatment plans were compared in terms of axial dose slices through the isocenter, DVHs and selected quality indicators. For the dose quality indicators mean dose, D_5 and D_{95}, their respective relative differences between degraded and homogenous dose distributions were calculated. This was done separately for the target volume, the lung and the selected OARs. Similarly, γ pass rate distributions between homogeneous and degraded treatment plans were calculated, employing a [3 mm/3 %] criterion with 0 interpolation points, which equals the CT and dose grid. Additionally, the treatment plans were evaluated in terms of NTCP of the lung and applicable OARs (Section III.2.6.2).

III.2.6.2 NTCP Model Considerations

In this thesis, the Niemierko-model was used for the calculation of NTCP (see Section II.3.3.1):

$$\mathrm{NTCP} = \frac{1}{1 + \left(\frac{\mathrm{TD}_{50}}{\mathrm{EUD}}\right)^{4\gamma_{50}}} \quad . \tag{III.36}$$

γ_{50} is a unit-less, organ specific model parameter and TD_{50} is the tolerance dose for a 50 % complication rate after a specific time (Niemierko 1999). The Equivalent Uniform Dose (EUD) is defined as

$$\mathrm{EUD} = \left(\sum_{i=1} V_i D_i^a\right)^{1/a} \quad , \tag{III.37}$$

with the tissue specific, unit-less model parameter a and the partial volume V_i, which receives the D_i (Gy). Table III.8 lists available parameters for the normal tissues prevalent in the used lung cancer patients.

Table III.8: Parameters used in the calculation of NTCP, that appear in the selected lung patients. The defined parameters for the heart were also used to calculate the NTCP of the aorta. Parameters were taken from: 1. Gay and Niemierko (2007), 2. Emami et al. (1991), 3. Brenner (1993), 4. Since there was no available TCD_{50} for lung tumors, the lung TD_{50} was used, 5. for α/β, standard parameters were assumed (Section II.2.1).

Variable	Endpoint	$a^{(1)}$	$\gamma_{50}{}^{(1)}$	$\mathrm{TD}_{50}/\mathrm{TCD}_{50}{}^{(2)}$	α/β
Lung	Pneumonitis	1	2	24.5	2
Esophagus	Perforation	19	4	68	2
Heart / Aorta	Pericarditis	3	3	50	2
Tumor	Local control	-10$^{(3)}$	2	24.5$^{(4)}$	10

DVHs as well as EUDs were recalculated using the Niemierko-model, if parameters for that tissue type were available. Both DVH and EUD were calculated in a custom MATLAB function adapted from (Gay and Niemierko 2007) using Eqs. III.36 and III.37. The α/β ratio is needed to calculate the EQD (Eq. II.10) and was assumed to be 2 Gy for normal tissue. For the aorta, parameters for heart tissue were used. For the tumor, since no specific data was available, generic values were assumed.

IV Results

IV.1 Validation of the Monte Carlo Interface

This section presents the results of the validation of the Monte Carlo Interface in terms of accuracy and comparability through example calculations for several phantoms. These example calculations range from a characterization of the developed machine data sets for protons and carbon ions with simple single Bragg peaks, SOBPs to calculations for patient cases. Two patient cases (prostate and liver patient), deployed with the matRad release, were chosen because of their relatively simple structure with two opposing beams for the prostate patient and one beam for the liver patient Section III.1.7.1. The first patient is evaluated for protons in terms of constant RBE. The second patient case is investigated using the MCN and WED variable RBE models for protons and the LEM model for carbon ions.

IV.1.1 Machine Data Set Characterization

This section covers the characterization of the new machine data sets for protons and carbon ions developed in Section III.1.3. This was done by calculating the dose distributions of nine single pencil beams using matRad, MCsquare and TOPAS, with equidistant steps in the mean range. The characterization of the machine data sets simultaneously serves as a first step to validate the interface on the basis of single beams with a single particle spot.

IV.1.1.1 Characterization of the Proton Machine

Resulting longitudinal and lateral absorbed dose profiles are shown in Fig. IV.2, profiles calculated using the variable RBE MCN model are shown in Fig. IV.3.
The visual analysis of the calculated profiles revealed very good agreement in longitudinal profiles for all three modalities concerning both absorbed and RBE-weighted doses. There was also strong lateral agreement between TOPAS and matRad. However, lateral differences

emerged with MCsquare, which were already apparent for absorbed dose and were particularly significant in the RBE-weighted profiles when compared to matRad and TOPAS. The inconsistencies with MCsquare did not correlate with energy.

A γ analysis (Fig. IV.1a), performed with a criterion of [1 mm/1 %] with 1 interpolation point, confirmed the very good agreement for TOPAS for absorbed dose distributions. For RBE-weighted dose, this is also the case up to an energy of ~120 Gy. At higher energies, the analysis showed a lower γ pass rate for TOPAS. While MCsquare exhibited a lower γ pass rate than TOPAS at higher energies for absorbed dose, it surpassed the pass rate for TOPAS with RBE-weighted dose. Comparing the two MC engines, differences as low as 92.6 % for RBE-weighted dose distributions were recorded.

IV.1.1.2 Characterization of the Carbon Machine

Similar to protons, the visual analysis of the calculated carbon profiles showed very good agreement in longitudinal profiles for both absorbed and RBE-weighted dose distributions (Fig. IV.1b). Unlike protons, the maximum dose for carbon ions did not decrease with energy. However, visual differences in the longitudinal profiles became apparent at higher energies. The γ analysis revealed pass rates over 99 % below 226.38 MeV/u with a steep decrease to 92.9 % for absorbed dose and 97.2 % for RBE-weighted dose. In contrast to protons, the γ pass rates for RBE-weighted dose were consistently larger compared to the pass rates for absorbed dose.

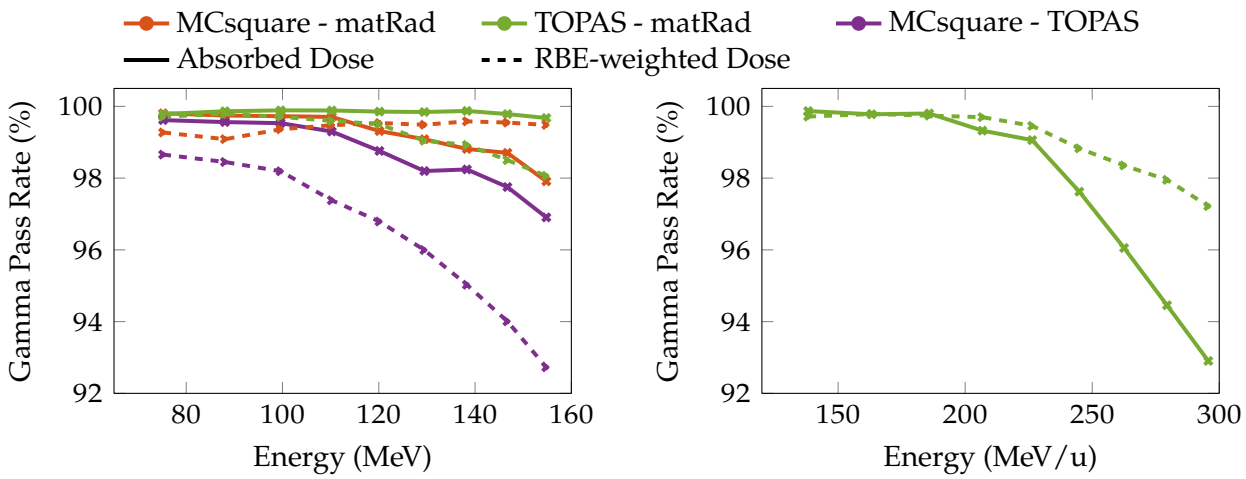

(a) Proton pencil beam γ pass rates.

(b) Carbon pencil beam γ pass rates.

Figure IV.1: γ pass rates comparing the different modalities matRad, MCsquare and TOPAS with energy, calculated using protons (a) and carbon ions (b). γ pass rates were calculated using the [1 mm/1 %] criterion with 1 interpolation point.

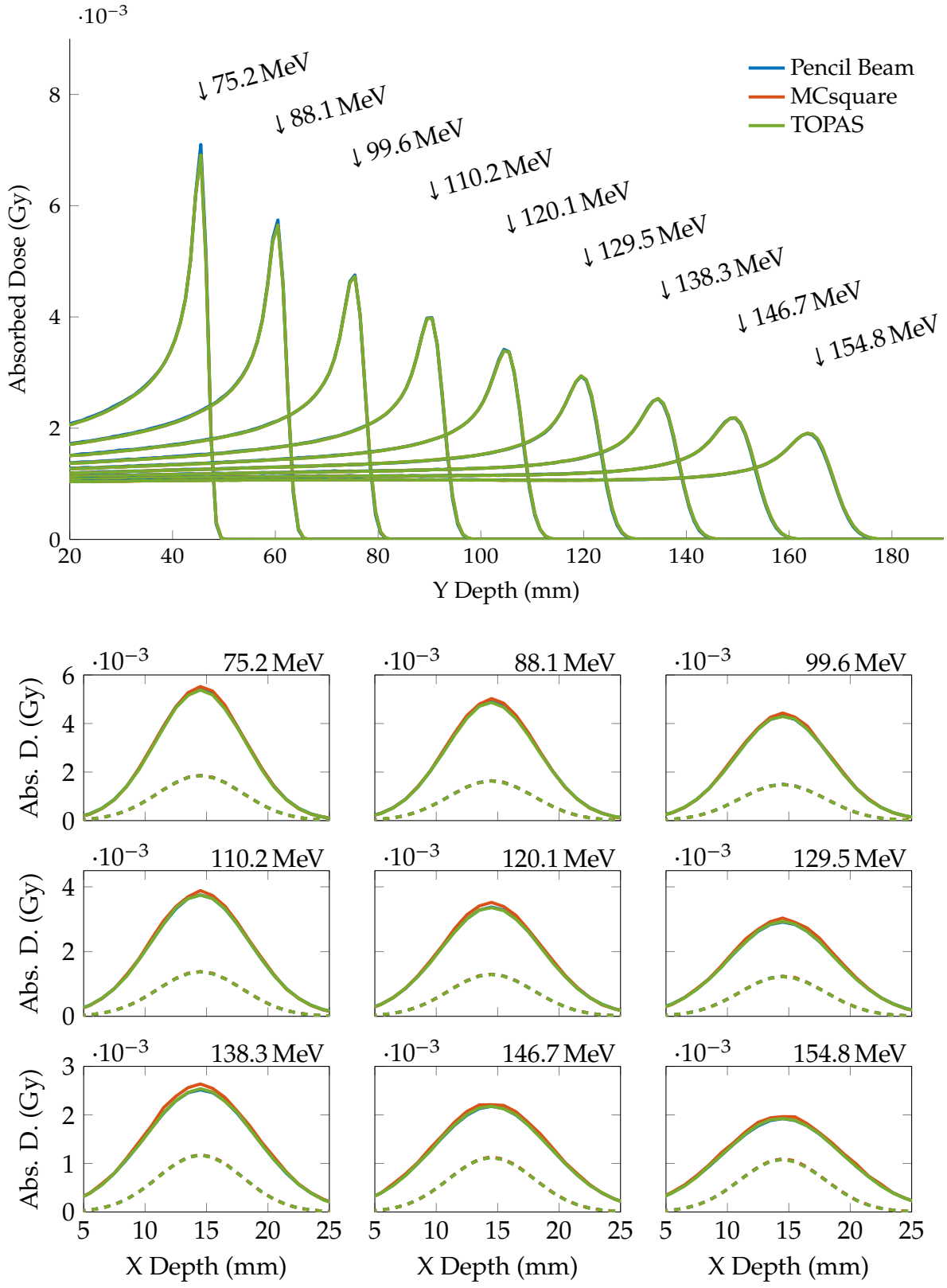

Figure IV.2: Comparison of 9 absorbed proton depth dose profiles for energy indices 10 to 50 of the *protons_generic* machine data set, calculated using matRad, MCsquare, and TOPAS. Pencil beams were calculated using a single uniform weight. Shown are lateral profiles at phantom entry (- -) and the peak (—). Profiles were evaluated and averaged over the 5 × 5 most central voxels.

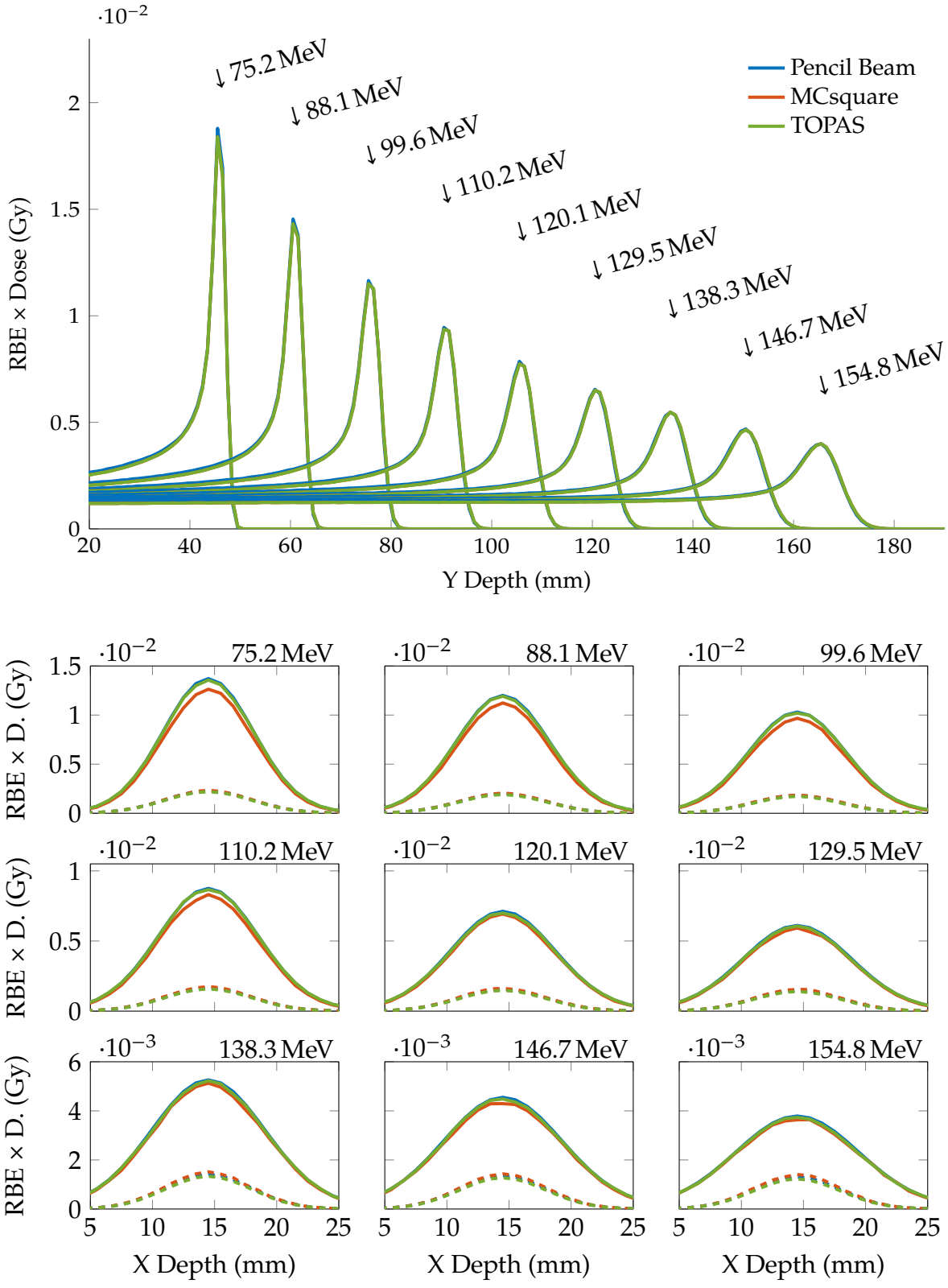

Figure IV.3: Comparison of 9 RBE-weighted proton depth dose profiles using the MCN model for energy indices 10 to 50 of the *protons_generic* machine data set, calculated using matRad, MCsquare, and TOPAS. Pencil beams were calculated using a single uniform weight. Shown are lateral profiles at phantom entry (- -) and the peak (—). Profiles were evaluated and averaged over the 5 × 5 most central voxels.

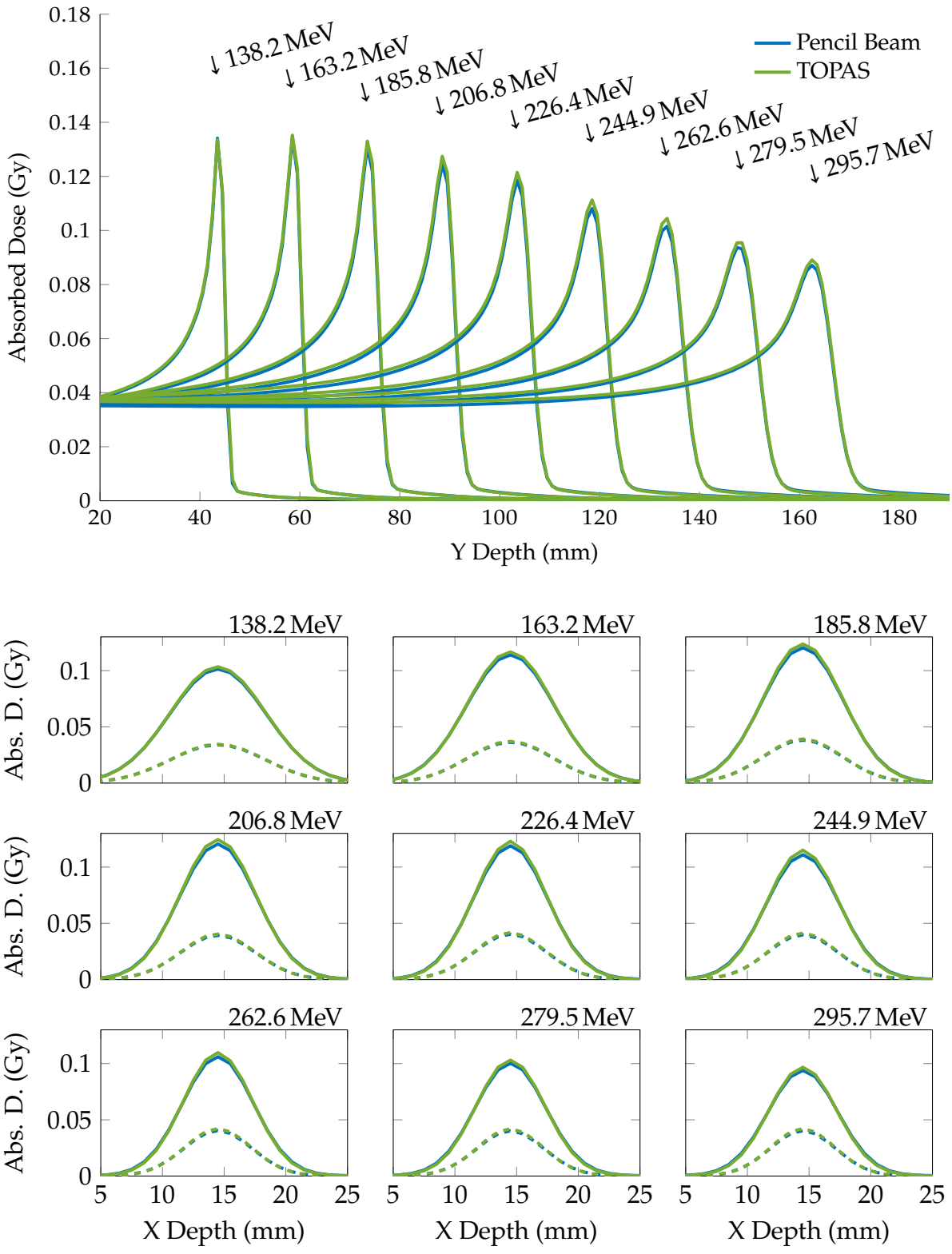

Figure IV.4: Comparison of 9 absorbed carbon depth dose profiles for energy indices 10 to 50 of the *carbon_generic* machine data set, calculated using matRad and TOPAS. Pencil beams were calculated using a single uniform weight. Shown are lateral profiles at phantom entry (- -) and the peak (—). Profiles were evaluated and averaged over the 5 × 5 most central voxels.

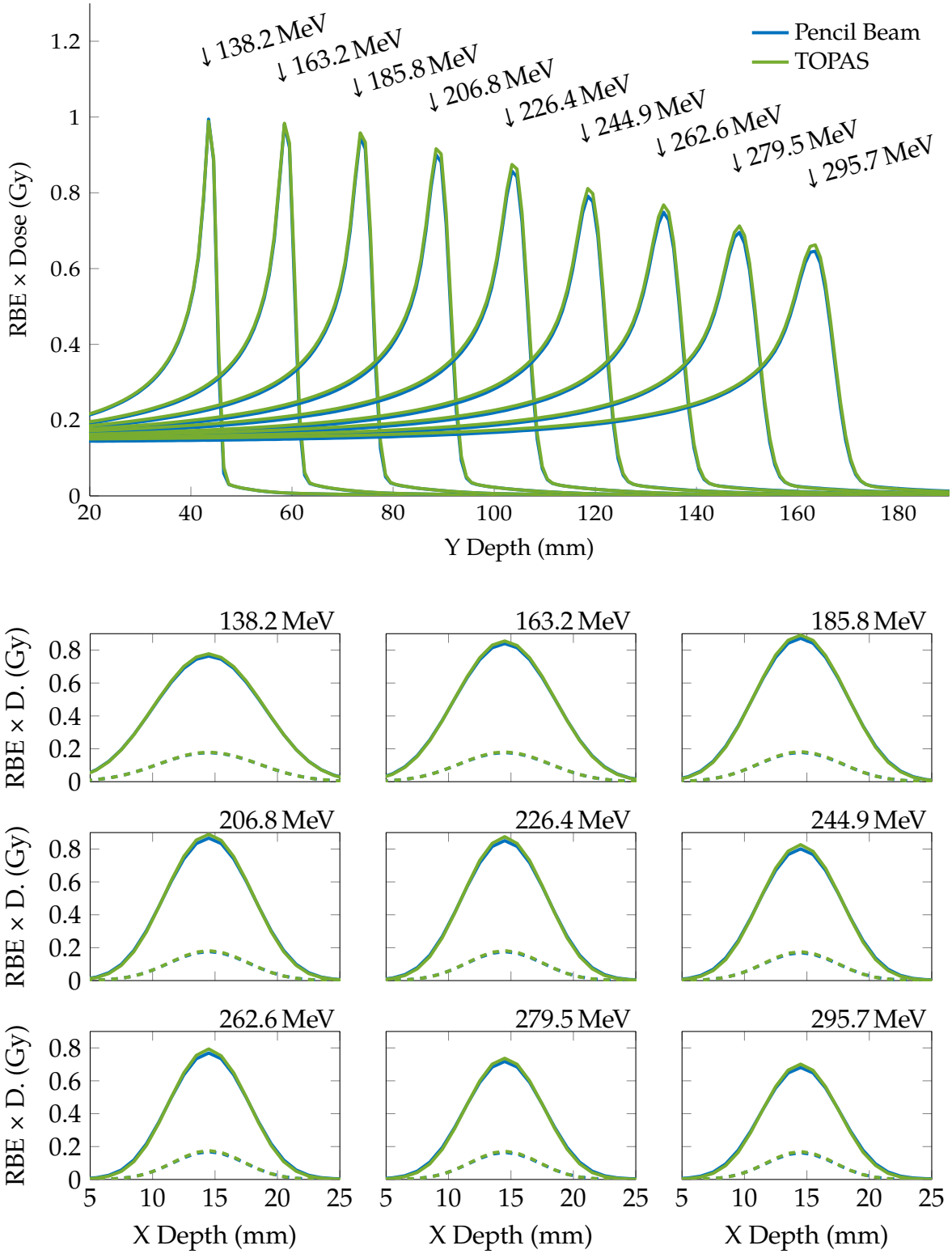

Figure IV.5: Comparison of 9 RBE-weighted carbon depth dose profiles using the LEM model for energy indices 10 to 50 of the *carbon_generic* machine data set, calculated using matRad and TOPAS. Pencil beams were calculated using a single uniform weight. Shown are lateral profiles at phantom entry (- -) and the peak (—). Profiles were evaluated and averaged over the 5 × 5 most central voxels.

IV.1.1.3 Kernel Resolution

A constant 0.1 mm depth grid as well as a late cutoff behind the Bragg peak might store the machine data most accurately, but results in a large number of unnecessary data points being stored. For data simulated using TOPAS, the fine grid also leads to statistical uncertainties before and after the Bragg peak. When large data sets are loaded continuously, this could also negatively influence computation times. Therefore, the data resolution was adjusted in depth using a dynamic grid spacing. An initial grid spacing of 1 mm was chosen with a finer depth grid of 0.1 mm in a −8 % to 6 % region around the Bragg peak. To gradually transition between the two grid spacings, the depth vector was subsequently smoothed using a 20 point moving average and rounded to five digits. The data was interpolated on the new grid using a spline interpolation in MATLAB.

An example of this downsampling for $E = 80.53\,\mathrm{MeV}$ of the *protons_generic* machine data set is shown in Fig. IV.6. It was possible to reduce the number of data points stored by ~80 %. The absolute error shows no difference for the peak area with an irregular pattern in the plateau region and distal to the peak, likely due to the smoothing introduced by the downsampling.

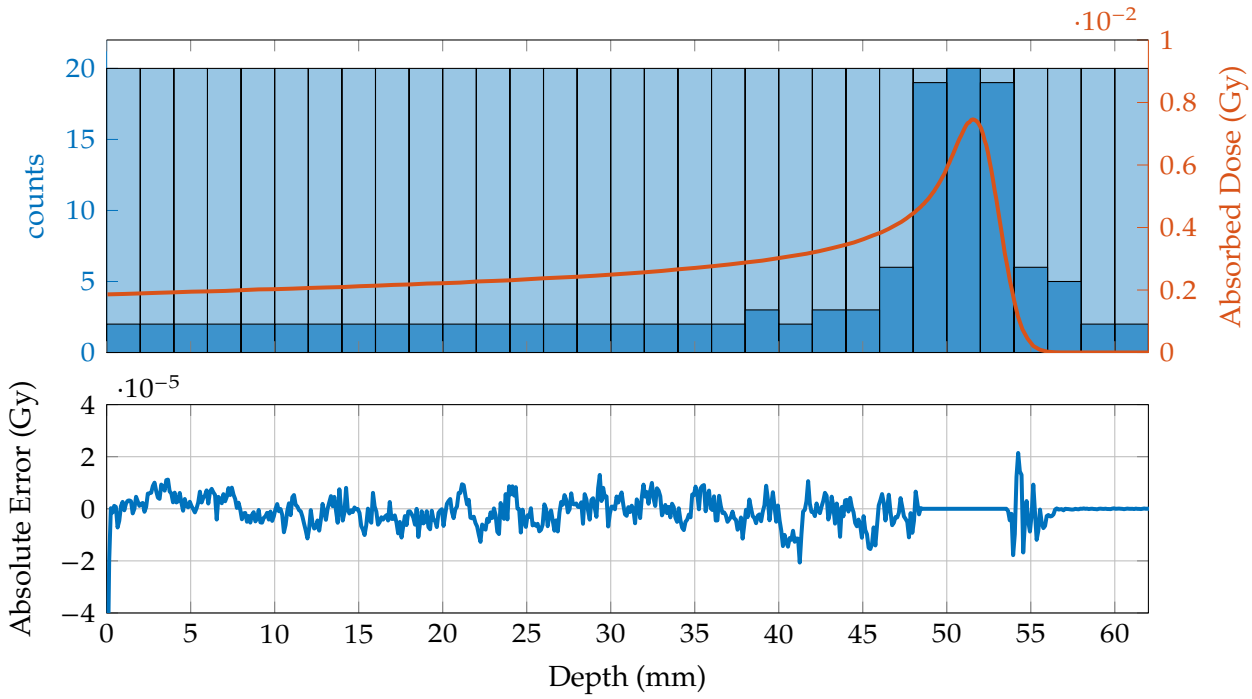

Figure IV.6: Example of the kernel resolution for $E = 80.53\,\mathrm{MeV}$ of the *protons_generic* machine data set. Shown is the new depth dose stored in the machine data (top, —). Overlaid are histograms of the number of sample points per 2 mm depth, that were heavily reduced without major impact on accuracy (top, ▭). The absolute error between the depth dose with original and adjusted kernel resolution is shown below (bottom, —).

IV.1.2 Spread-Out Bragg Peaks on a Box Phantom Geometry

Simple uniform SOBPs were calculated for protons and carbon ions using matRad, MCsquare (only protons) and TOPAS. The used workflow is described in Section III.1.7.2. The resulting dose distributions were analyzed in terms of absolute difference, γ pass rates and DVH. Additionally, longitudinal central profiles are shown.

Protons. A comparison of RBE-weighted dose distributions for constant RBE including their respective absolute differences are shown for all three modalities in Fig. IV.7. The shown differences showed similar values with maximum relative differences below 0.063 Gy and 0.054 Gy, respecively. However, TOPAS showed larger lateral difference towards matRad compared to MCsquare. Longitudinally, larger differences were observed using MCsquare, especially in the entrance channel and after the SOBP.
Calculated γ pass rates showed 100.00 % for the constant RBE dose distributions in both MCsquare and TOPAS over the whole CT. For RBE-weighted dose distributions using variable RBE, the agreement overall decreased slightly with 99.57 % and 99.63 % for MCsquare and TOPAS, respectively. The γ pass rates between the two MC modalities MCsquare and TOPAS was 99.99 % for constant RBE and 98.34 % for variable RBE-weighted dose over the whole CT. In the target, calculated γ pass rates were 98.84 % for MCsquare and 100.0 % for TOPAS. Additionally, the longitudinal central profiles as well as the DVHs are shown for constant and variable RBE-weighted dose in Fig. IV.8. For the constant RBE-weighted depth dose profiles, all 3 modalities show very good agreement with each other. In the plateau region, however, larger differences between the different modalities become apparent. There, MCsquare shows a larger dose while TOPAS shows a smaller dose compared to matRad. These observations are also largely reflected in the DVH. Here, notable, MCsquare seems to show less differences at the proximal end of the RBE-weighted SOBP, while TOPAS shows less differences at the distal end.

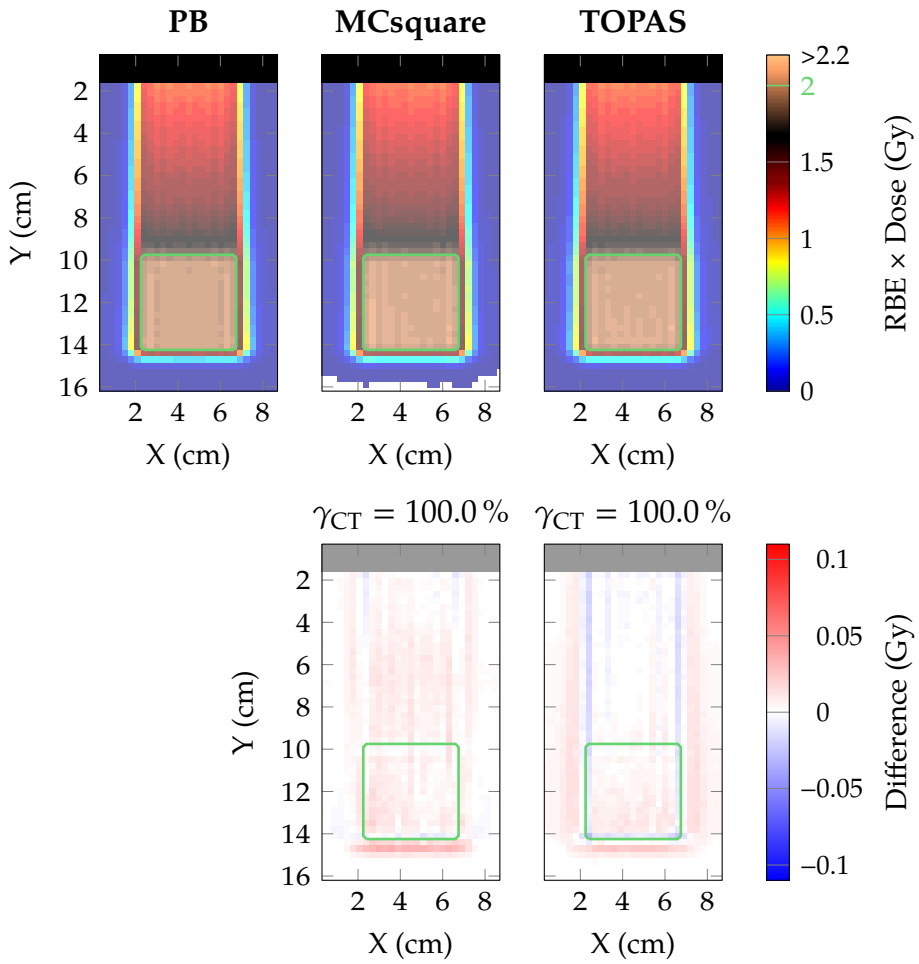

Figure IV.7: Comparison of constant RBE-weighted dose distributions using the *protons_generic* machine data set and the simplePhantom_3mm. The prescribed dose to the PTV was annotated. Also shown are absolute differences between MC engines and matRad (bottom), as well as their γ pass rates over the whole CT.

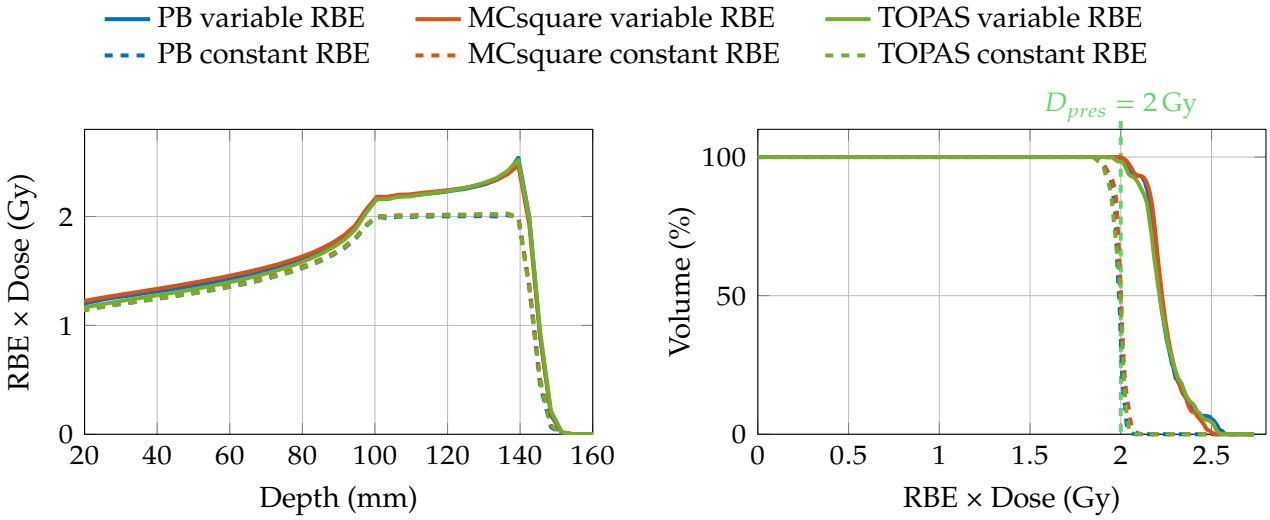

(a) Longitudinal central profiles of constant and variable RBE-weighted dose distributions.

(b) DVHs of constant and variable RBE-weighted dose distributions within the target.

Figure IV.8: Comparison of SOBP treatment plans for the *protons_generic* machine data set.

Carbon Ions. A comparison of RBE-weighted dose distributions between matRad and TOPAS, including their respective absolute differences and γ index, are shown in Fig. IV.9. The calculated differences were below 0.12 Gy (6.1 % of the prescribed dose). Here, differences can be observed mainly at the distal edge of the SOBP as well as the fragmentation tail with only small lateral differences.

The calculated γ pass rates for RBE-weighed dose showed 94.91 % over the whole CT and 97.87 % in the target. Additionally, the longitudinal central profiles as well as the DVHs are shown for RBE-weighted dose in Fig. IV.8. matRad and TOPAS show near perfect agreement with each other, especially in the plateau and proximal edge of the SOBP. At the distal edge of the SOBP and the fragmentation tail, larger differences were observed. These differences at the distal edge can also be seen in the DVH of the target, where TOPAS slightly under-estimates the optimized dose distribution in matRad.

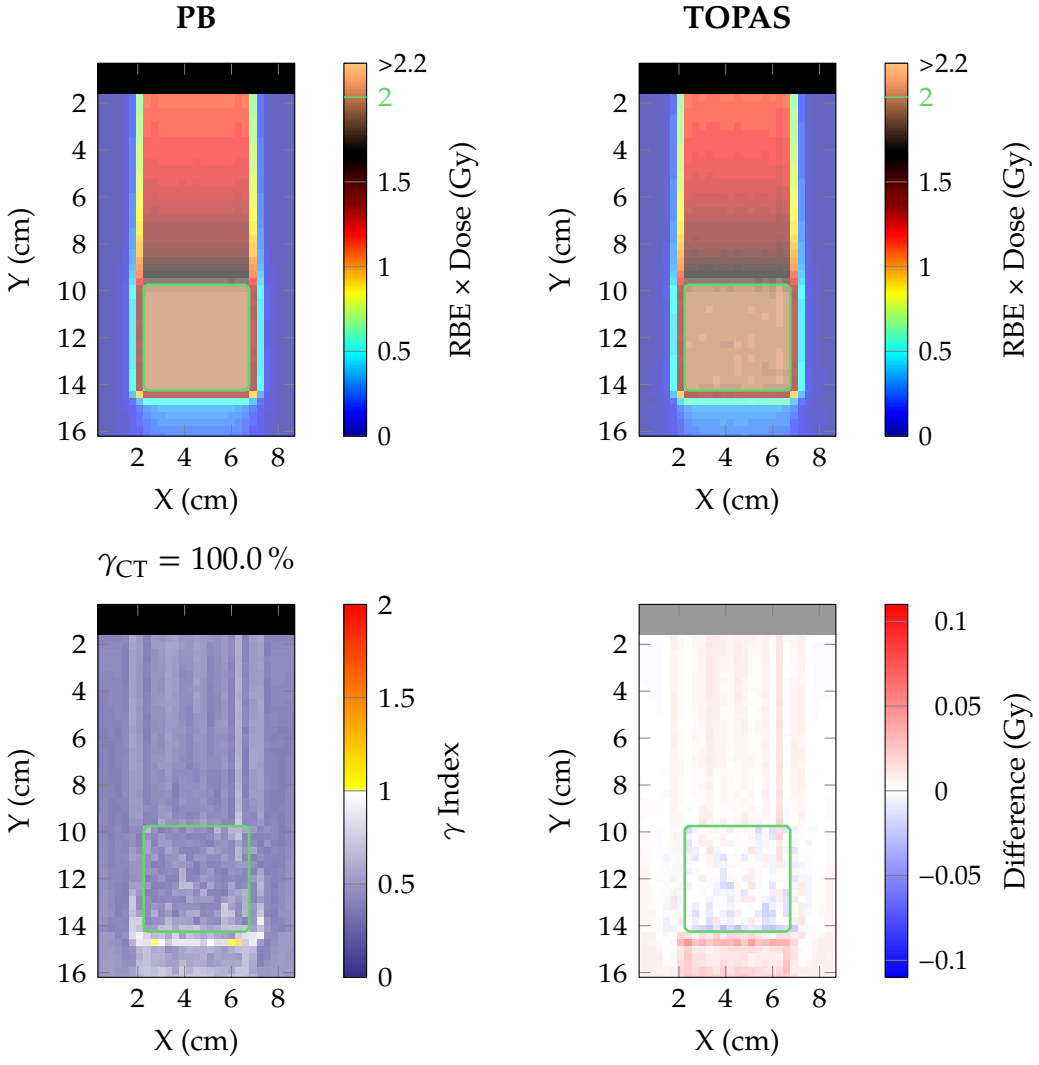

Figure IV.9: Comparison of absorbed dose distributions using the *carbon_generic* machine data set and the simplePhantom_3mm phantom. The prescribed dose to the PTV was annotated in the colorbar. Also shown are the γ index between TOPAS and matRad (bottom left), as well as their absolute difference (bottom right).

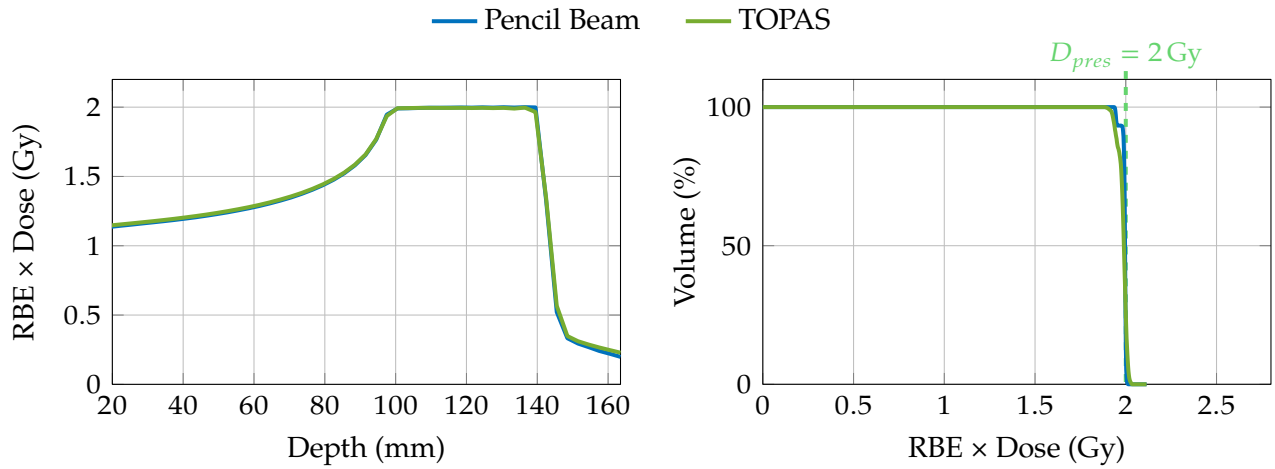

(a) Longitudinal central profiles of the calculated RBE-weighted dose distributions.

(b) DVHs of the calculated RBE-weighted dose distributions within the target.

Figure IV.10: Comparison of SOBP treatment plans for the *carbon_generic* machine data set.

IV.1.3 Validation on Patient Phantoms

In this section, more clinical treatment cases were investigated to assess the differences of analytical and MC treatment plans on patient geometries.

IV.1.3.1 Prostate Phantom – Protons Constant RBE

A proton treatment plan was calculated for the prostate phantom using the workflow described in Section III.1.7.3. Generally, both MC engines generated very consistent results that differed from the analytically calculated plan (Fig. IV.11). There were clearly visible higher doses in the entrance channels for both beams for both MC engines. Additionally, for both MC engines, there were larger uncertainties and fluctuations at objective borders and within the target areas together with a cold spot in the bladder. Mean absolute dose differences, consistent between the two MC engines, were observed with 0.05 Gy in the $PTV_{68\,Gy}$, 0.04 Gy in the $PTV_{56\,Gy}$, 0.03 Gy in the bladder, and 0.04 Gy in the rectum. However, absolute dose differences in the 10 % range of the prescribed dose were observed with differences as large as over 0.33 Gy in the bladder for MCsquare.

These observations are reflected in both γ index and DVH (Fig. IV.12). The lowest reported γ pass rates were 95.5 % and 94.9 % for $PTV_{68\,Gy}$ for MCsquare and TOPAS, respectively. Pass rates for $PTV_{56\,Gy}$, bladder and rectum were above 98.3 % while the pass rates for TOPAS were slightly lower compared to MCsquare. However, pass rates between the two MC engines were consistently 100.0 % for all segmented volumes. Especially in the DVH, there were only minimal differences between the two with a general under-estimation of the dose in matRad compared to MC.

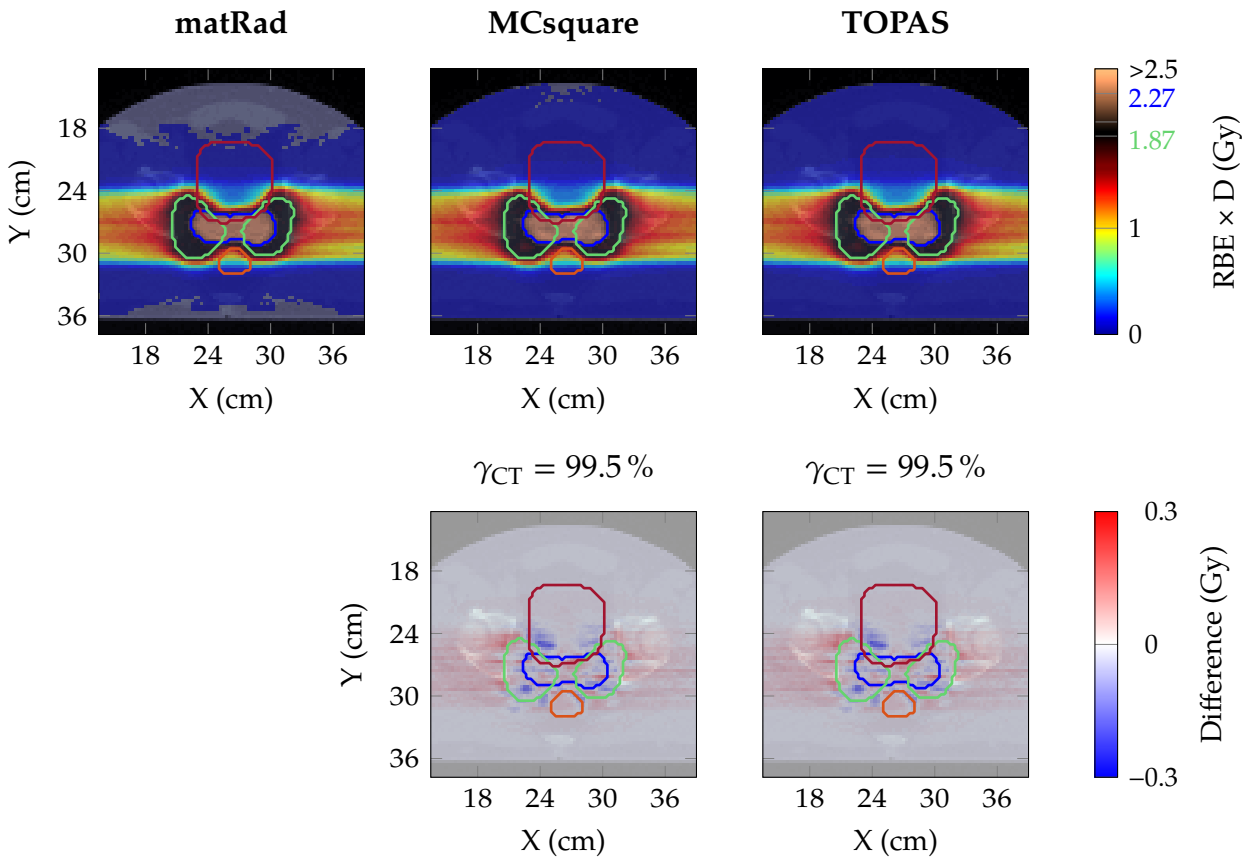

Figure IV.11: Comparison of RBE-weighted dose distributions using constant RBE, the *protons_generic* machine data set and the prostate phantom. Also shown are the absolute differences between MCsquare and matRad (bottom center), TOPAS and matRad (bottom right) as well as their respective γ pass rates over the whole CT. Prescribed doses for $PTV_{56\,Gy}$ and $PTV_{68\,Gy}$ have been annotated.

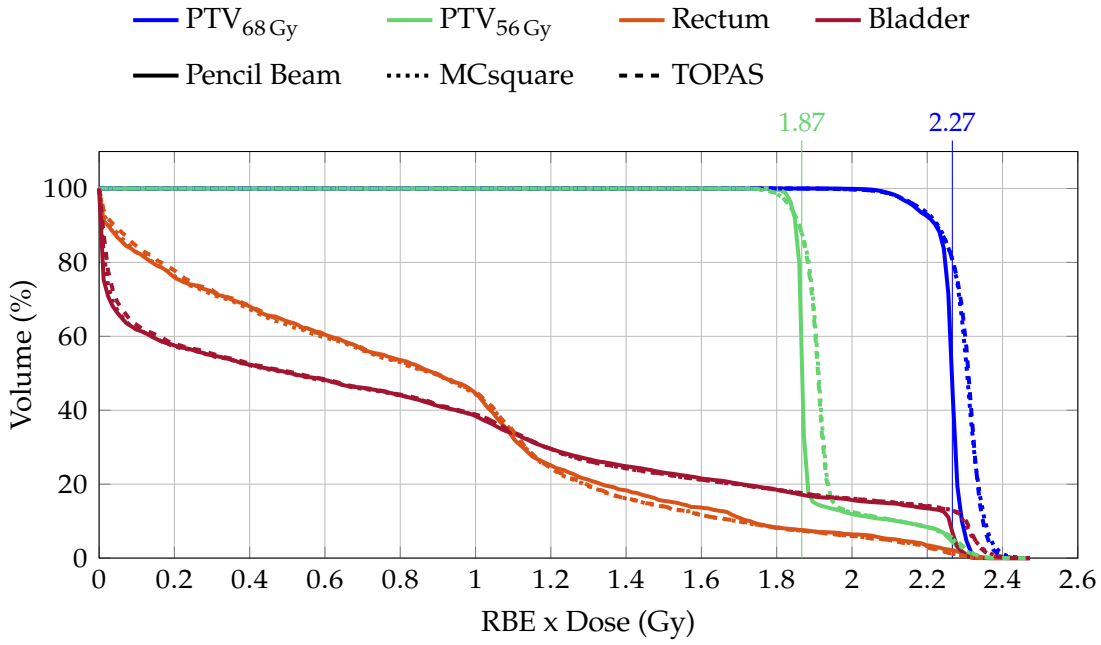

Figure IV.12: DVH of the calculated RBE-weighted treatment plan for matRad, MCsquare and TOPAS using constant RBE. Prescribed doses for $PTV_{56\,Gy}$ and $PTV_{68\,Gy}$ have been annotated.

IV.1.3.2 Liver Phantom – Protons Variable RBE

A treatment plan using the *protons_generic* machine data set was calculated for the liver phantom using the workflow described in Section III.1.7.4.
Fig. IV.13 shows the axial slice through the isocenter with dose distributions for matRad, MCsquare and TOPAS, as well as their respective absolute differences. Especially at the distal part of the dose distribution, the distal edge of the PTV, large differences in the region of ~50 % of the prescribed dose were observed. Also differences, altough smaller, between MCsquare and TOPAS can be seen. In the entrance channel, higher doses were present for both MC engines, that are overshadowed by the larger differences at the distal end. In the target, mean absolute dose differences of 0.06 Gy and 0.03 Gy were found for MCsquare and TOPAS, respectively.
These results are consistent with measurements of the γ pass rate (Table IV.1). For constant RBE, albeit different from matRad, γ pass rates still match between MCsquare and TOPAS with pass rates of 100.0 % between the two modalities. This behaviour is reflected in the DVH shown in Fig. IV.14.
For TOPAS, the calculated variable RBE-weighted dose distribution pass rates are not significantly different compared to constant RBE. However, MCsquare shows lower values with, for example, 86.39 % (91.66 % for TOPAS) over the whole CT. This difference is also evident in the DVH, where there were differences between the two MC engines, independent of the RBE model. This consequently results in a lower agreement between the two MC engines.
Absolute differences between the calculated RBE-weighted dose distibutions using the MCN and WED model are shown in Fig. IV.15. Clear differences are visible in the entrance channel, where the MCN model produced higher doses (coinciding with a higher RBE), as well as the lateral profile and the area distal to the target, where the WED model procuded higher doses. Notably, the difference pattern for MCsquare is different compared to both matRad and TOPAS. Here, smaller overall differences were recorded with a spot of virtually no difference in the distal part behind the target. Additionally, large negative differences can be found at the phase difference with lung tissue in the entrance channel.

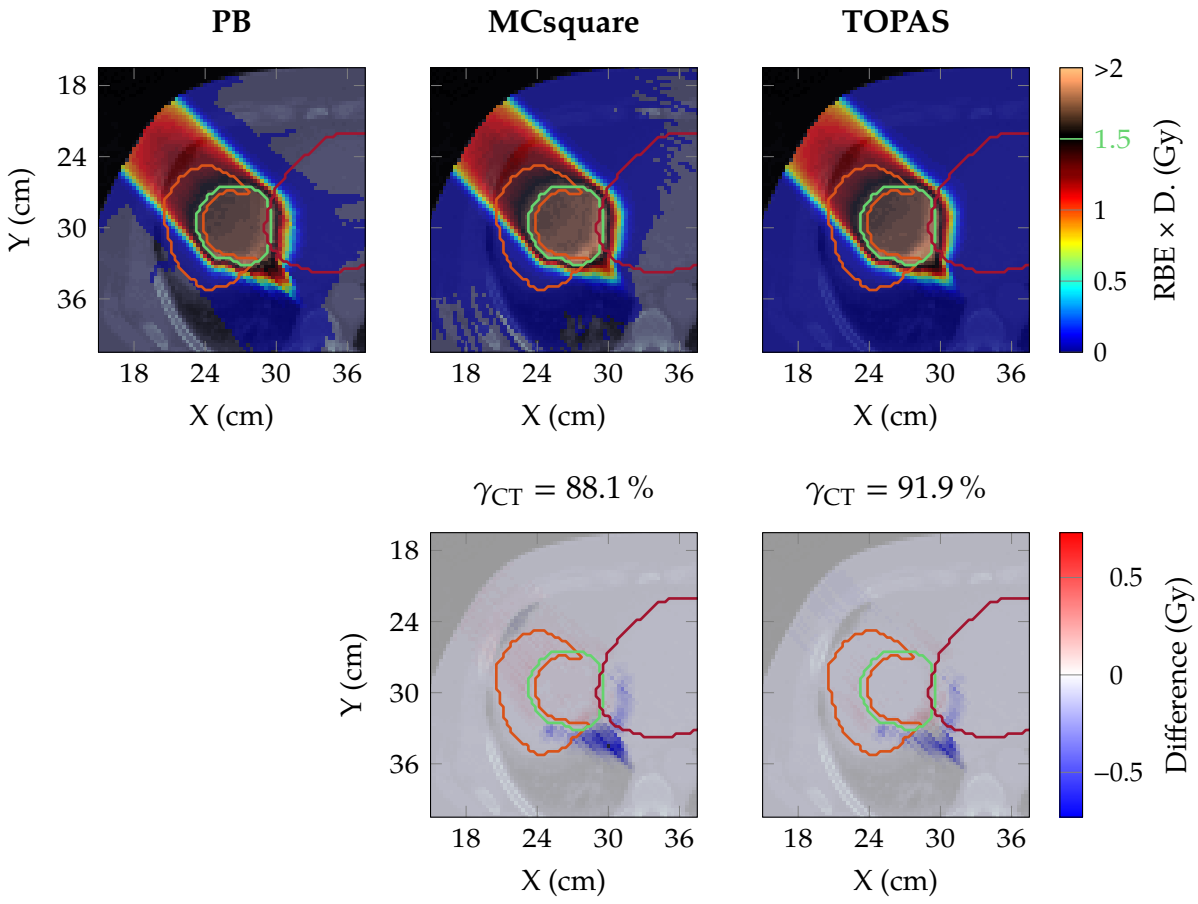

Figure IV.13: Comparison of RBE-weighted dose distributions for the liver phantom using variable RBE with the MCN model, the *protons_generic* machine data set. Also shown are the absolute differences between MCsquare and matRad (bottom center), TOPAS and matRad (bottom right) as well as their respective γ pass rates over the whole CT. The prescribed dose to the PTV was annotated.

Table IV.1: γ pass rates (in %), calculated between the three dose distributions for matRad, MCsquare and TOPAS. Absorbed dose and the variable RBE models MCN and WED were evaluated, respectively.

		Whole CT	PTV	Liver-CTV	Heart
const. RBE	MCsquare - matRad	92.24	78.40	94.35	98.40
	TOPAS - matRad	92.79	80.95	93.69	99.05
	MCsquare - TOPAS	100.00	100.00	100.00	100.00
MCN	MCsquare - matRad	88.09	75.01	91.80	96.41
	TOPAS - matRad	91.95	81.01	94.21	99.20
	MCsquare - TOPAS	91.84	99.91	93.75	95.20
WED	MCsquare - matRad	86.39	74.53	91.48	95.73
	TOPAS - matRad	91.66	80.91	94.79	99.17
	MCsquare - TOPAS	87.37	99.87	92.40	91.68

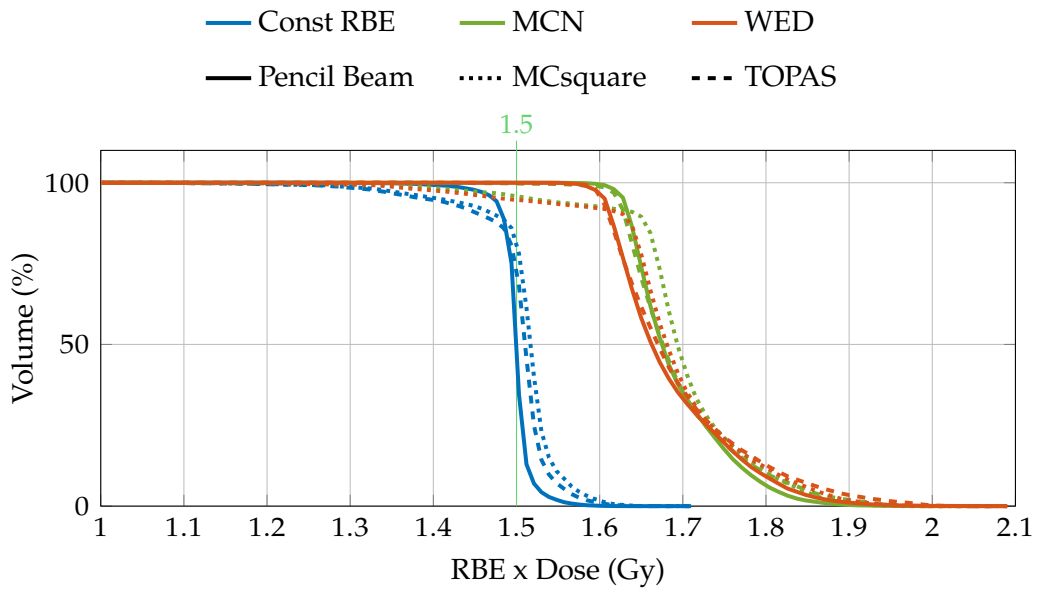

Figure IV.14: DVH of the calculated RBE-weighted treatment plan for matRad, MCsquare and TOPAS. The prescribed dose to the PTV was annotated.

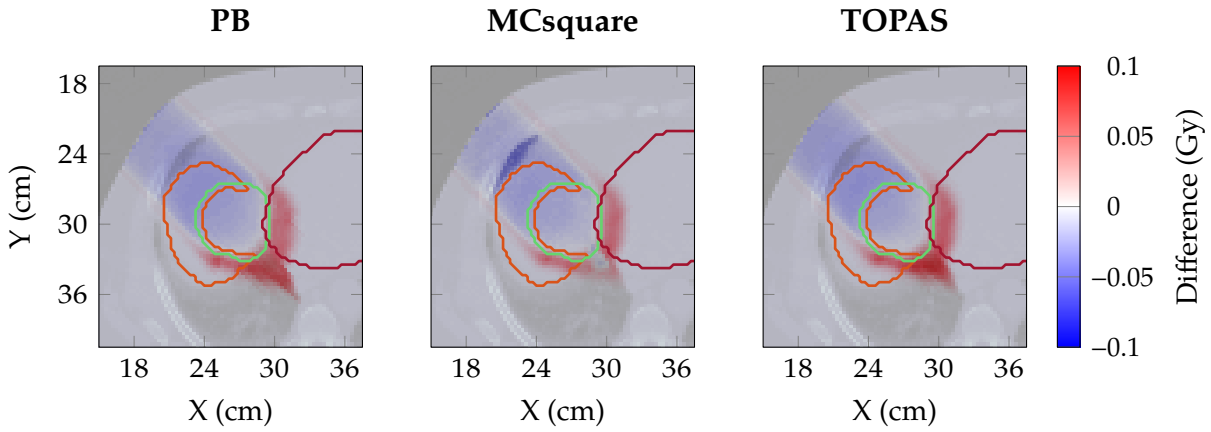

Figure IV.15: Comparison of RBE-weighted dose distributions calculated using the MCN model and the WED model. Shown are the absolute differences, WED−MCN, separately for each modality.

IV.1.3.3 Liver Phantom – Carbon LEM

A carbon treatment plan for the liver phantom was calculated using the *carbon_generic* machine data set (Section III.1.7.4).

Dose slices through the isocenter, γ index and absolute difference are shown in Fig. IV.16. Minor differences can be observed in the entrance channel, where TOPAS shows a larger dose compared to matRad, which is increasing towards the PTV. Similarly, after the PTV in the heart and center of the thorax, the dose calculated with TOPAS is higher. In the liver and lung distal to the target, matRad exhibits a much larger dose compared to TOPAS, resulting in large differences of ~30 %, which increase to over ~50 % in the whole CT. The γ index especially shows fluctuations in the entrance channel and target area, that indicate larger

local dose differences. It also clearly reflects the larger differences after the target, especially in the fragmentation tail.

Measured γ pass rates were 92.58 % for absorbed dose over the whole CT, and 99.57 % in the target. For RBE-weighted dose, the γ pass rate decreased to 83.90 % over the whole CT, with still 98.77 % in the target. The lowest γ pass rates of all selected segmentation were recorded in the heart with 84.61 % and 75.19 % for absorbed and RBE-weighted dose. This is also reflected in the DVH (Fig. IV.17), that clearly demonstrates the differences in the heart and the target.

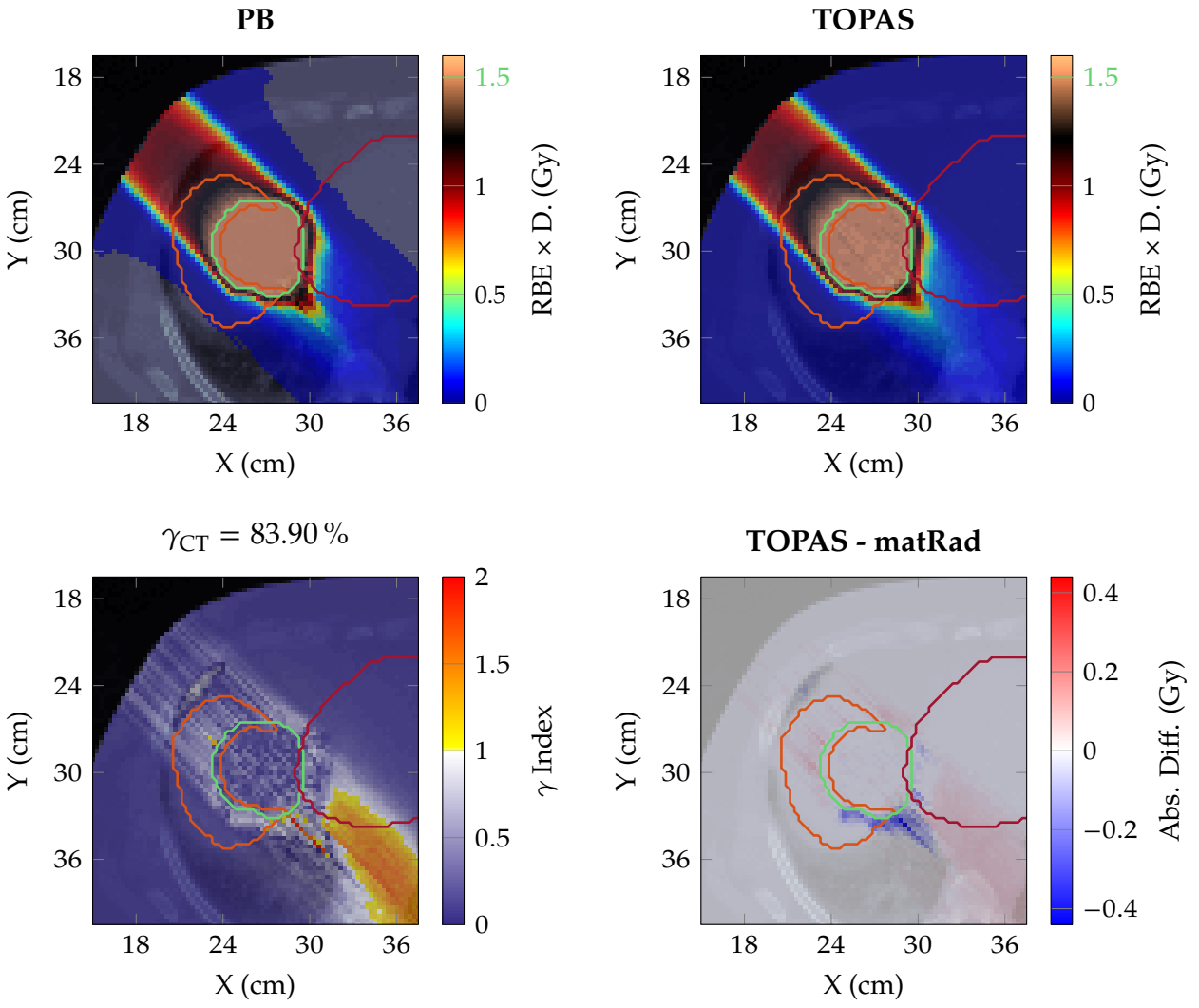

Figure IV.16: Comparison of RBE-weighted dose distributions using the LEM model, the *carbon_generic* machine data set and the liver phantom. Also shown are the γ index and absolute differences between TOPAS and matRad. The prescribed dose for the PTV has been annotated.

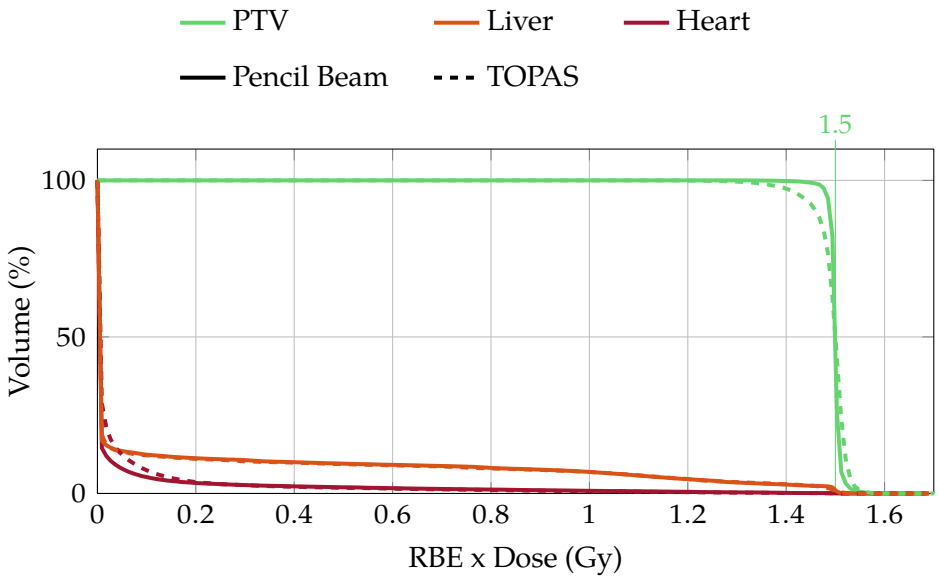

Figure IV.17: DVH of the calculated RBE-weighted treatment plan for matRad, MCsquare and TOPAS. The prescribed dose for the PTV has been annotated.

IV.1.4 LET Distribution-Based RBE-Weighted Dose Calculation

This section summarizes the results of recalculating RBE-weighted dose distributions based on LET using variable RBE models. The workflow is detailed in Section III.1.6. A comparison of the dose distributions calculated for PBs and TOPAS with the respective difference to the recalculated dose is shown in Fig. IV.18. Generally, RBE recalculations for PBs resulted in identical (within numerical accuracy) dose distributions. For TOPAS, a systematic difference over the whole beam path, almost constant in the target, was observed. The observed absolute relative differences were 0.73 % over the whole phantom, but below 0.1 % in the target. LET-Dose profiles for PBs, MCsquare and TOPAS at the central y axis and perpendicular through the center of the SOBP are shown in Fig. IV.19. With overall good agreement, differences in scored LET can be seen between all modalities with larger relative differences of approximately 10 % in regions of high LET.

LET and calculated RBE-weighted depth dose profiles for the homogeneous lung phantom are shown in Fig. IV.20. In the lung phantom, the rSP-weighted LET converted from TOPAS shows good agreement (8 % to 9 % absolute relative difference in lung) with the MCsquare LET in lung tissue, while the density normalized TOPAS LET agrees with PBs (0.4 % to 1.7 % absolute relative difference in lung). This is also reflected in the calculated RBE-weighted depth dose profiles with relative differences of 1.1 % to 1.2 % between MCsquare and TOPAS and 0.9 % to 2.6 % between PBs and TOPAS. RBE-weighted doses in TOPAS were calculated based on the density normalized and rSP-weighted LET, respectively.

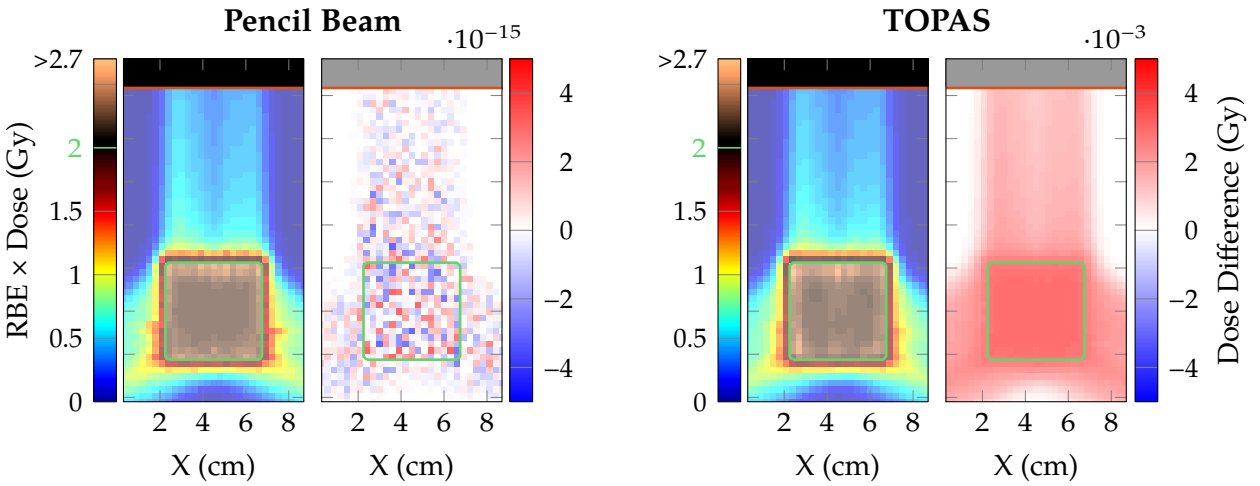

Figure IV.18: RBE-weighted dose distributions for PBs (left) and TOPAS (right) as well as the absolute difference between directly calculated RBE-weighted dose and RBE-weighted dose recalculated from the unmodified LET. The prescribed dose to the PTV was annotated (optimized on constant RBE).

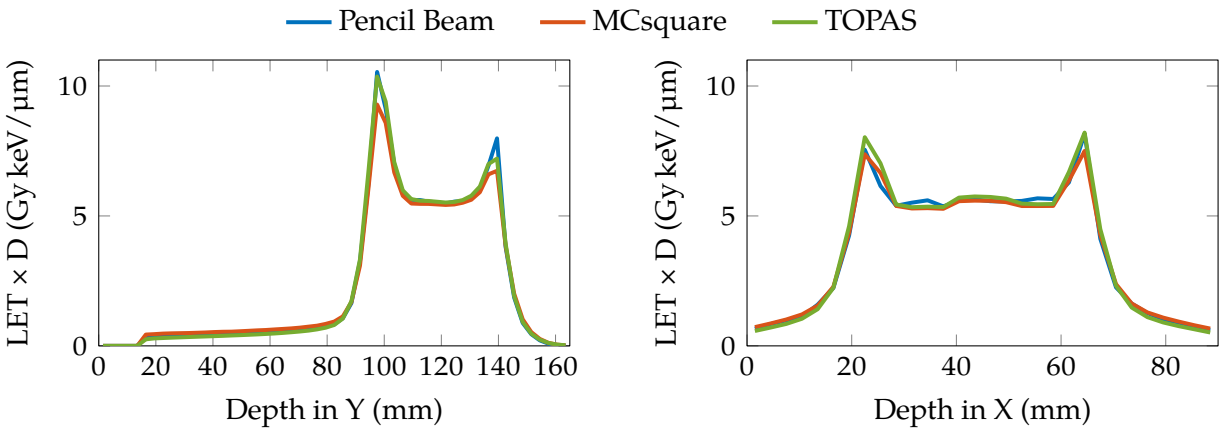

Figure IV.19: LET-Dose along the central axis in Y direction (left) and X direction through the center of the SOBP at $Y = 120$ mm (right). Profiles were averaged over the 9 most central voxels for each direction, respectively.

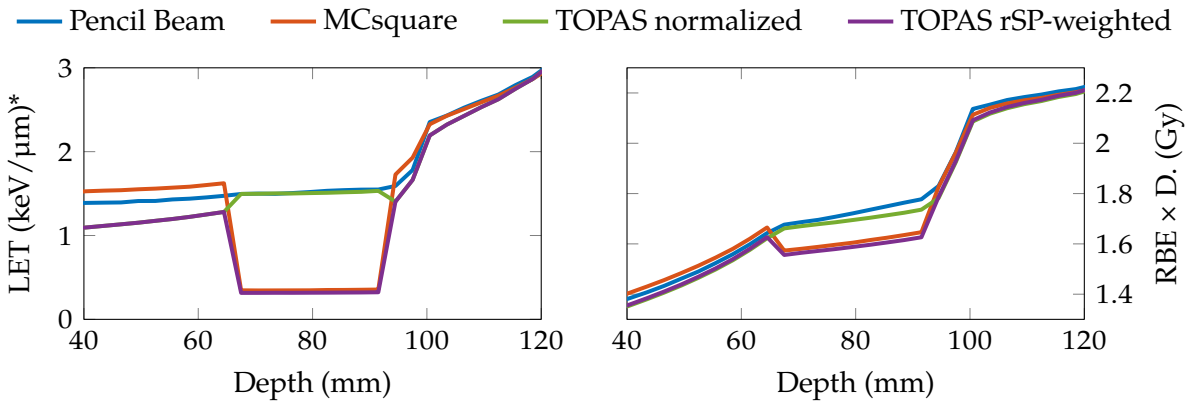

Figure IV.20: Central LET (left) and RBE-weighted dose (right) profiles for PBs, MCsquare and TOPAS, calculated in the homogeneous lung phantom. The RBE-weighted TOPAS dose was recalculated based on density normalized, unmodified LET and based on rSP-weighted LET. Profiles were averaged over the 7 × 7 central voxels.

IV.1.5 Postprocessing of the Particle Spot List

Analytical matRad dose distribution slices for mean weight thresholds of 3 %, 10 % and 50 % at the isocenter as well as their absolute difference from the full plan are shown in Fig. IV.21. For those plans, histograms of the weight distributions are shown in Fig. IV.22. Visually, the treatment plans did not degrade for any simulated weight threshold. Additionally, throughout all measured quality indicators, the plans hold up their accuracy. The maximum relative difference of the mean dose to the target increased with an increasing threshold and amounted to less than $3{\cdot}10^{-3}$ % for $w = 50\,\%$. For the OARs, the relative difference to the heart was largest with ~2 %. For $w = 3\,\%$, the measured relative differences were smaller by more than an order of magnitude. Calculated γ pass rates for [3 mm/3 %] and 0 interpolation points degraded to 99.97 % and 99.68 % for weight thresholds of 3 % and 50 %.

In MCsquare, there was no significant change in computation time for different weight thresholds. However, a TOPAS simulation for a mean weight threshold of 3 % and 50 % revealed a reduction in computation time of ~7 % and 34 %, respectively.

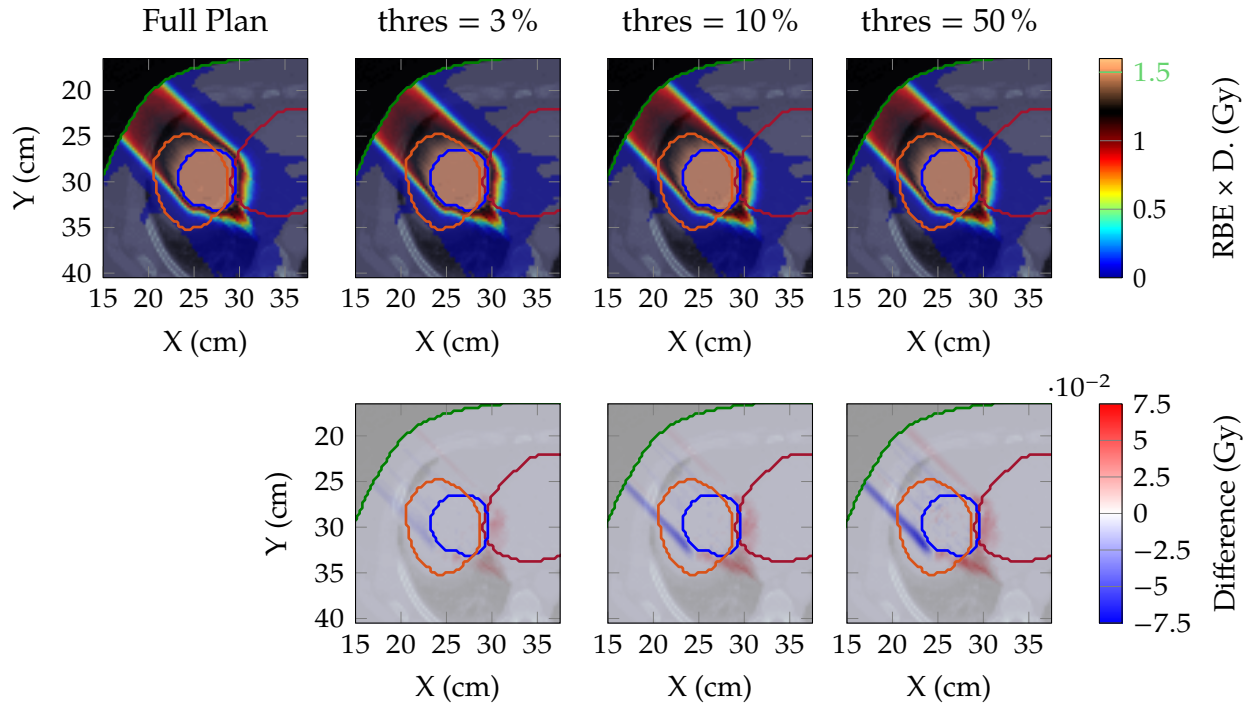

Figure IV.21: Treatment plans calculated using matRad. Spot removal was performed after optimization of the full plan using a mean weight threshold of 0, 3, 10 and 50 %. Plans were subsequently reoptimized.

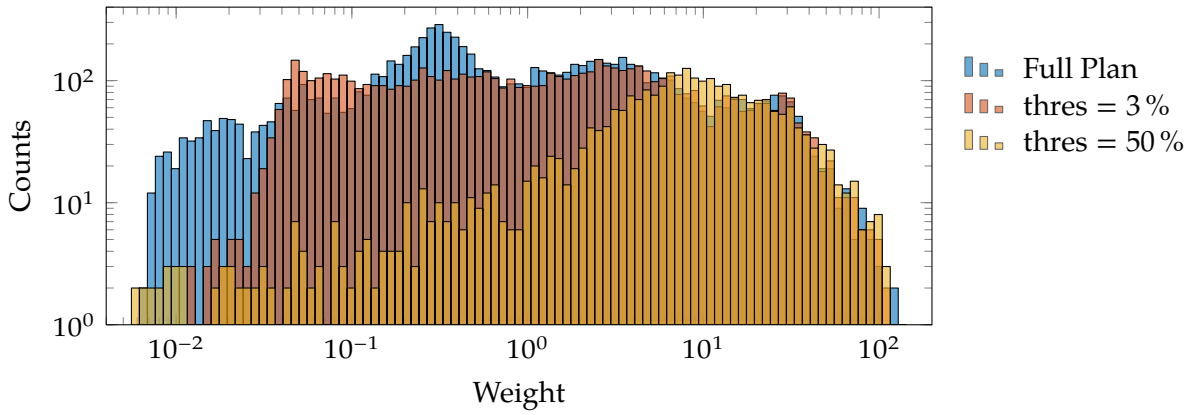

Figure IV.22: Histogram of the optimized weights for the full plan, as well as for performed spot removal with 3 % and 50 % of the mean weight, ensuring that the sum of the weights remains invariant.

IV.2 Degradation Correction

In this section, the results involving density correction are summarized. Firstly, the results of the technical implementation of the degradation correction are presented including a comparison of the used algorithms. Then, a first treatment planning study is presented using SOBPs on a water phantom including a lung section. Lastly, all discussed methods of degradation correction are applied and evaluated on clinical lung patient plans.

IV.2.1 Implementation of Degradation Correction

This section highlights the technical implementation and difference of analytical and numerical convolution algorithm, as well as the density sampling method.

IV.2.1.1 Comparison of Analytical and Numerical Convolution

An overview of the carbon absorbed and RBE-weighted dose profiles convolved using the different methods and intermediary αD, $\sqrt{\beta} D$ and RBE profiles are shown in Fig. IV.23. The relative differences are shown in Fig. IV.24. The workflow is described in Section III.2.3.4. The usage of a manual numerical convolution does not lead to significant differences in the calculated absorbed and RBE-weighted dose profiles compared to an analytical convolution in the APM case. For the absorbed dose profiles, relative differences in the range of 0.09 % to 0.42 % were observed for $P_{\mathrm{mod}} = 250$ µm and 800 µm in the area to the peak with higher relative differences after the peak in the range of 0.41 % to 2.7 %. For the RBE-weighted dose profiles, larger relative differences between 0.08 % to 0.48 % before and between 0.52 % to 3.2 % after the peak were observed. Especially the absolute difference for RBE and $P_{\mathrm{mod}} =$ 800 µm was calculated much larger than the other combinations. This behavior, however, cannot be observed for relative differences or is visible for the RBE-weighted dose profiles. The maximum absolute error is in the range of ~0.6 % of the maximum depth dose.

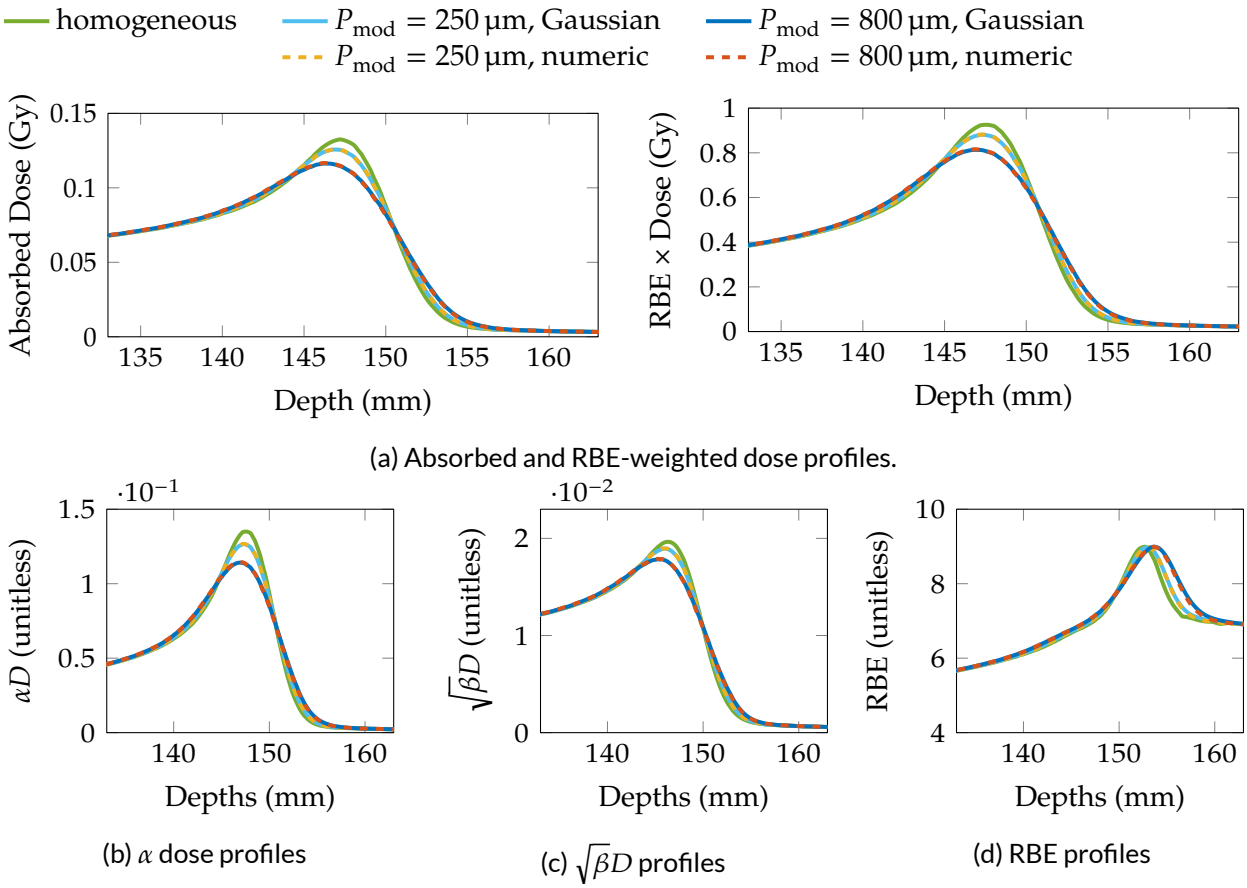

Figure IV.23: Comparison of the homogeneous profiles and heterogeneity correction in combination with RBE using both analytical and numerical convolution methods for $P_{\text{mod}} = 250\,\mu\text{m}$ and 800 µm.

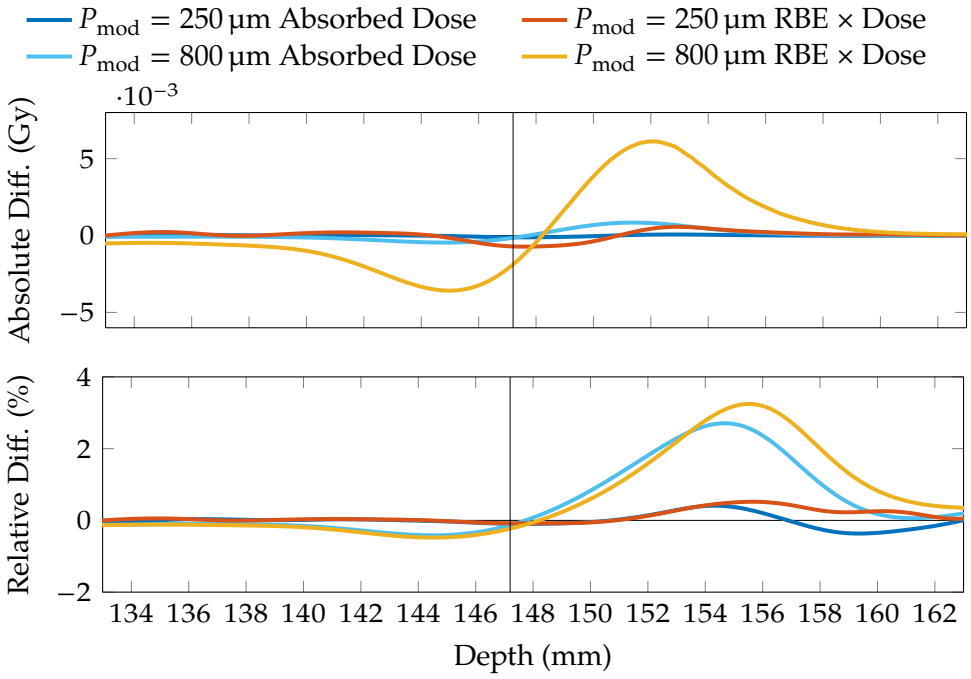

Figure IV.24: Absolute and relative differences between analytical and numerical convolution for $P_{\text{mod}} = 250\,\mu\text{m}$ and 800 µm for absorbed and RBE-weighted dose. The position of the Bragg peak is annotated.

IV.2.1.2 Sampling Technique Evaluation

This section covers the results of the evaluation of the density sampling technique and comparison with analytical convolution. The workflows are detailed in Section III.2.2.3.

Equivalence with Convolution. Fig. IV.25 presents a comparison between the analytical convolution method and the two density sampling methods, i.e., sampling only on the depth dose and sampling on both depth and lateral components. However, the profiles obtained from the two sampling methods show very little deviation with relative differences of 0.45 % and 0.60 % before the peak for ($L \cdot \text{sampling}(Z)$) and $\text{Sampling}(L * Z)$, respectively. These differences are increasing to 1.6 % and 2.2 % at the point where the dose has reached 10 % of the maximum dose.

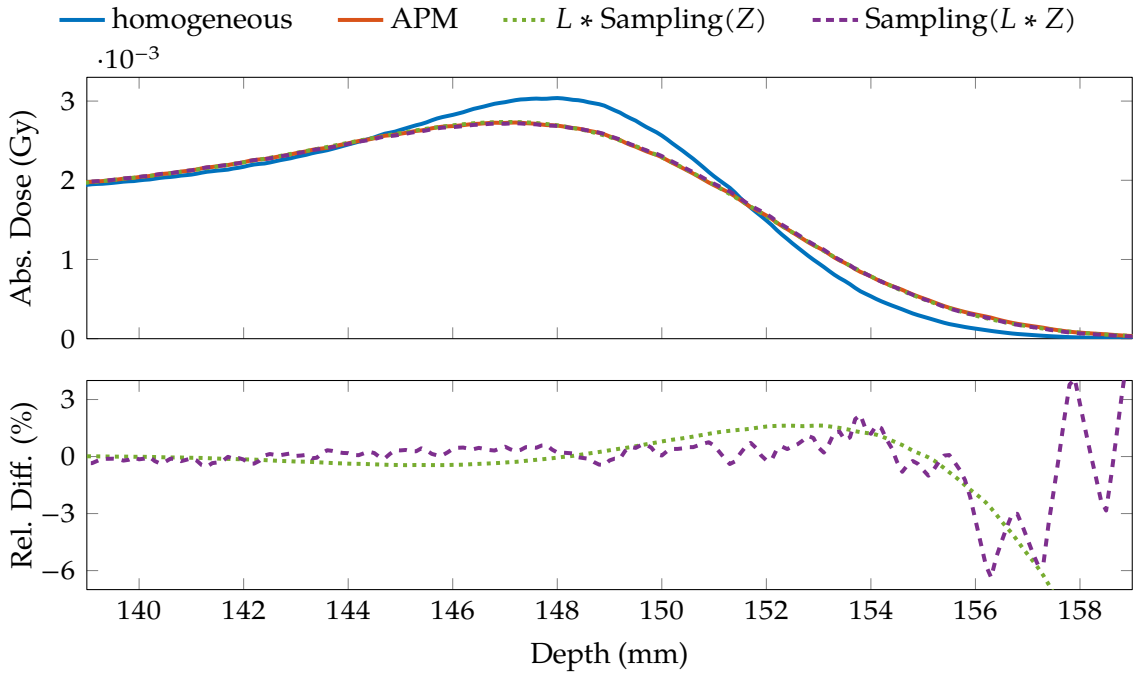

Figure IV.25: Absorbed depth dose profiles calculated directly from the *protons_generic* machine data set (top). Relative difference between both sampling methods and analytical convolution (bottom). For the degradation correction, 28 mm of lung tissue with a density of 0.211 g/cm^3 was assumed, together with a modulation power of 800 µm. Sampling was performed separately on the depth dose (Z) and the full absorbed dose ($L * Z$).

Oblique Angle Testing. Treatment plans were calculated and evaluated for *Patient 3* (Section III.2.2.3). Selected calculated quality indicators are shown in Fig. IV.26.
Overall, the oblique angle correction for this particular patient leads to quality indicators closer to the analytical degradation model. The mean target dose decreased from the homogeneous case of 2.00 Gy to 1.93 Gy when using the analytical degradation model. The sampling, however, showed mean doses of 1.95 Gy without and 1.94 Gy with oblique angle correction. The mean dose therefore decreased by −3.4, −2.3 and −3.0 % compared to the homogeneous plan, respectively.

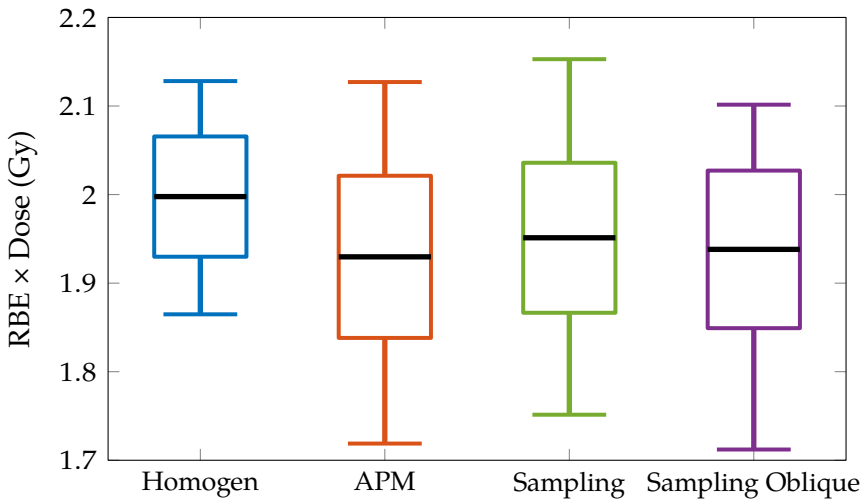

Figure IV.26: Selected dose quality indicators in the PTV for *Patient 3* and constant RBE using density sampling with and without oblique angle correction. For an explanation of the graph, see Fig. III.21.

IV.2.2 Phantom Study

In this section, the developed lung phantoms (Section III.2.4.2) are employed to gauge first dose distributions and treatment plans. Additionally, differences of the degradation correction depending on different implementations of lung tissues are evaluated.

IV.2.2.1 Influence of WEPL and Modulation Power

In order to verify the basic concepts of degradation correction and test the consistency of the results, a series of tests was conducted to gauge the influence of varying WEPL and P_{mod} on the mean dose delivered to the target. The workflow and evaluation were described in Section III.2.5.2.

Fig. IV.27 shows the measured relative difference between the dose delivered to the target between respective degraded and homogeneous dose distributions. Generally, an approximately linear relationship between the strength of the degradation and the WEPL and P_{mod} was observed. However, measured data exhibited larger fluctuations around the linear fit. It is worth noting that the difference between APM and PB sampling is very low. The values and fit measured for MCsquare differ from the ones calculated for the PB degradation methods with an increasing difference with increasing degradation.

Values for the relative mean target dose were measured up to −1.5 % in the rough respective range of realistic WEPL values occurring in the patient data (Section III.2.4.1). The range of modulation powers spans across the values reported in literature (Baumann et al. 2017; Burg et al. 2021; Witt 2014) and caused relative target mean dose differences of less than −1 %.

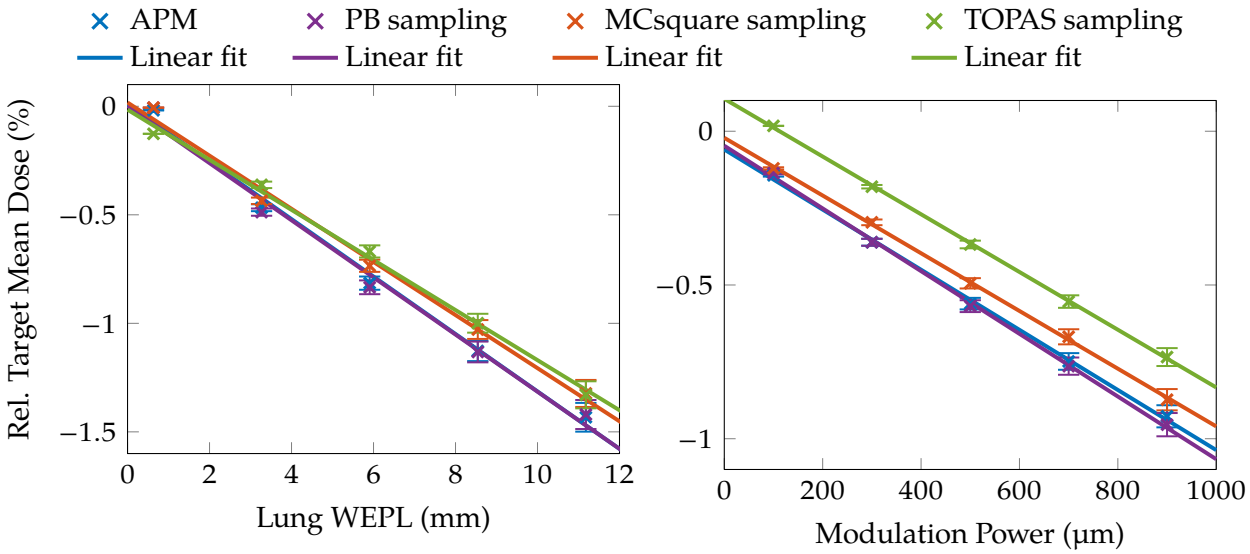

(a) Variable WEPL with constant $P_{\text{mod}} = 800\,\mu\text{m}$.

(b) Variable modulation power with constant $\text{WEPL}_{lung} = 5.96\,\text{mm}$.

Figure IV.27: Relative differences of the mean dose in the target between degraded and homogeneous dose distributions as a function of the WEPL (a) and P_{mod} (b). Shown are the degradation corrections implemented for PBs and MCsquare.

IV.2.2.2 Sampled Dose in Lung Tissue

A comparison of the absorbed depth dose profiles through lung tissue for CT resolutions of 1, 2 and 3 mm and modulation powers of 250 µm and 800 µm is shown in Figs. IV.28a to IV.28c. Tthere is little to no difference observed between degraded and homogeneous absorbed depth dose profiles within the lung area for each modality, individually. However, for TOPAS for a resolution of 1 mm and a modulation power of 800 µm, the sampled dose in lung was lower by –7.35 % compared to the homogeneous depth dose. However, for TOPAS for a resolution of 1 mm and a modulation power of 800 µm, the sampled dose in lung was $-5.2{\cdot}10^{-5}$ Gy (–7.3 %) lower compared to the homogeneous depth dose.

Figs. IV.28g to IV.28i show the binomial sampling distributions (using the beta approximation) for the respective CT resolutions. Especially for the mentioned combination of $P_{\text{mod}} = 800\,\mu\text{m}$ and 1 mm resolution, a significant binary separation in distinct values of $0\,\text{g/cm}^3$ and $1.05\,\text{g/cm}^3$ is visible. This stems from the voxel sampling parameter $n = 1.049$ used in the sampling distribution Eq. III.23. This separation is not apparent for higher n.

Figs. IV.28d to IV.28f shows RBE-weighted depth dose profiles in the lung area of the phantom. Here, differences can be observed between sampling and homogeneous dose calculation using TOPAS as well. However, a large drop in lung dose can be seen for MCsquare independent of the grid resolution.

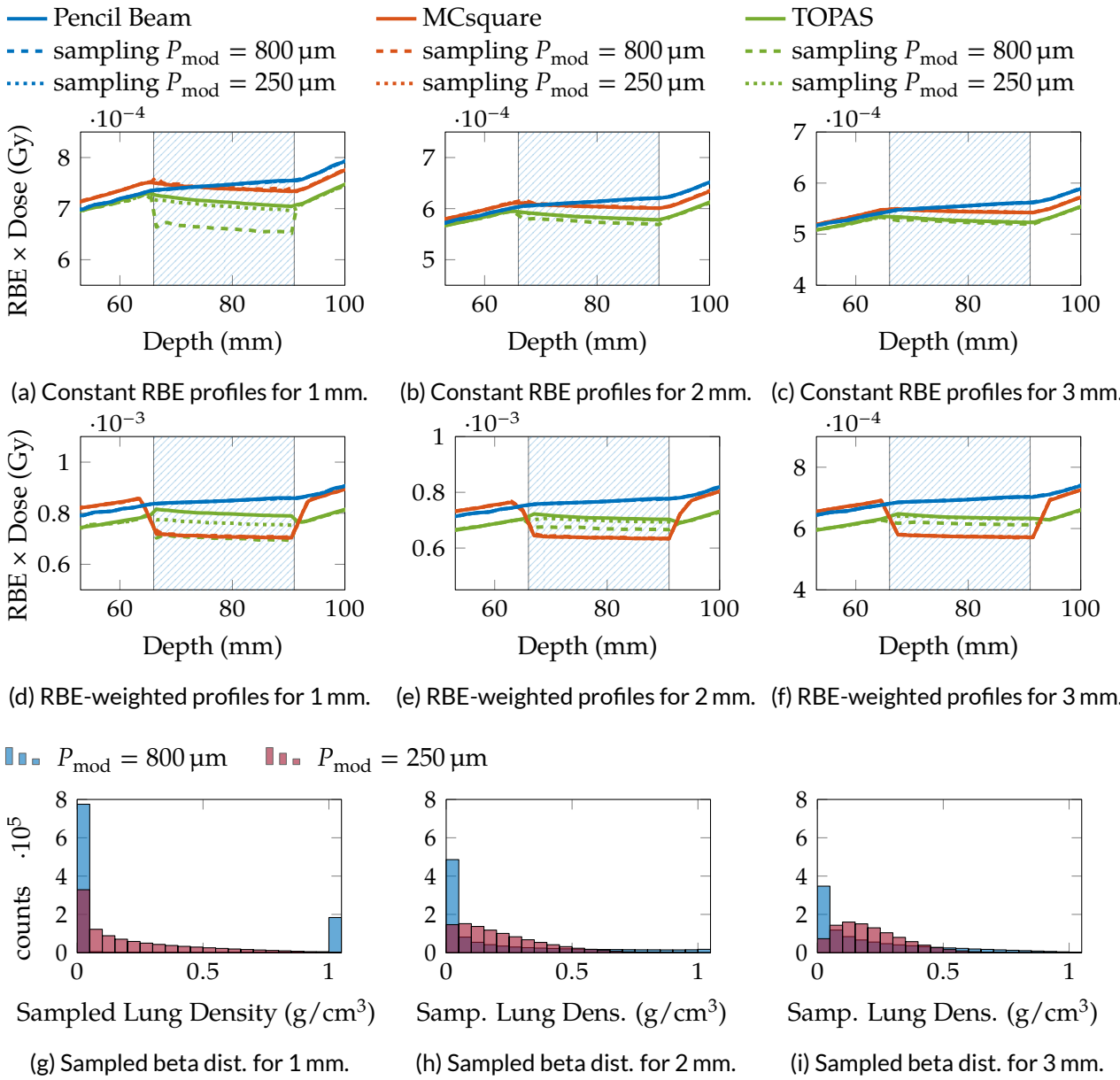

(a) Constant RBE profiles for 1 mm. (b) Constant RBE profiles for 2 mm. (c) Constant RBE profiles for 3 mm.

(d) RBE-weighted profiles for 1 mm. (e) RBE-weighted profiles for 2 mm. (f) RBE-weighted profiles for 3 mm.

(g) Sampled beta dist. for 1 mm. (h) Sampled beta dist. for 2 mm. (i) Sampled beta dist. for 3 mm.

Figure IV.28: Comparison of the depth dose profiles through lung for CT resolutions of 1 mm, 2 mm and 3 mm for modulation powers of 250 µm and 800 µm (a-c). Area of lung tissue has been annotated (▨). (d-f) show the RBE-weighted depth dose profiles. (g-i) show the binomial sampling distributions for CT resolutions of 1, 2 and 3 mm. The central profiles were averaged over 13 × 13, 7 × 7 and 5 × 5 most central voxels with decreasing resolution to keep the physical distance of the measured profiles constant.

Difference Between Central Profiles and IDD. Fig. IV.29 shows the comparison of the averaged central profiles with the respective IDDs for constant and variable RBE. Notably, the dose measured in central profiles of both MC engines decreases consistently while traversing lung tissue, which cannot be observed for the analytical PB. However, for the IDDs, the measured dose in lung increases in lung tissue similarly for all modalities. Additionally, very good agreement between the modalities not only in lung, but also in the Bragg peak region can be seen for the shown IDDs with near perfect alignment for constant RBE and larger differences for variable RBE.

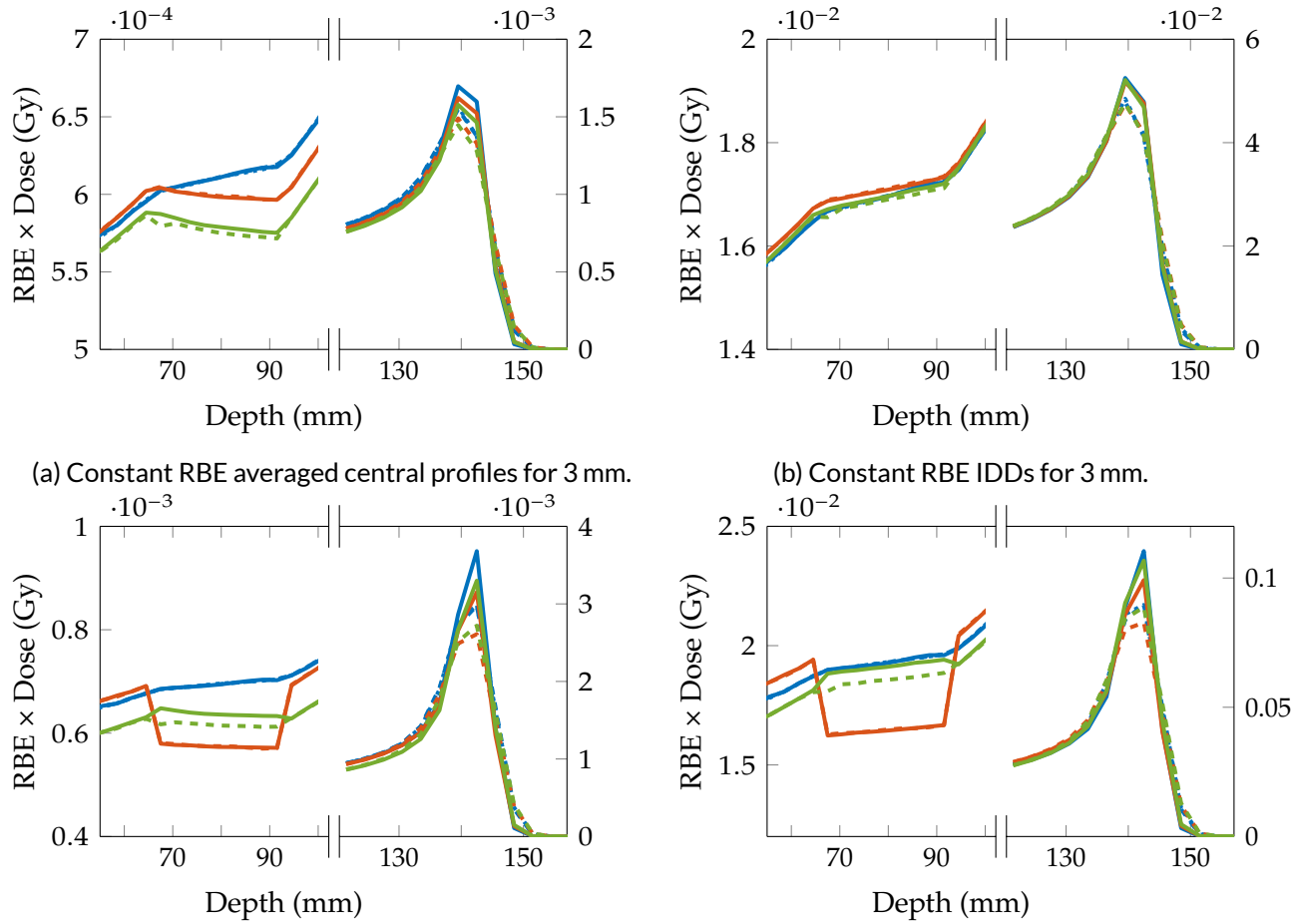

(a) Constant RBE averaged central profiles for 3 mm.

(b) Constant RBE IDDs for 3 mm.

(c) Variable RBE (MCN) averaged central profiles for 3 mm.

(d) Variable RBE (MCN) IDDs for 3 mm.

Figure IV.29: Comparison of averaged central profiles and IDDs for $P_{\text{mod}} = 800\,\mu\text{m}$ for constant and variable RBE. Within each plot, the areas of lung tissue (left) and the Bragg peak (right) are highlighted.

IV.2.2.3 Spread-Out Bragg Peaks

This section presents the results of calculated SOBPs on a set of lung phantoms including degradation correction. The workflow for protons and carbon ions is detailed in Section III.2.5.3.

Protons. Fig. IV.30 shows a broad overview over the calculated dose distributions, displaying constant RBE-weighted dose slices through the isocenter together with their respective absolute difference between the degraded dose and the respective homogeneous plan. In the shown difference slices, the characteristic degradation behavior can be seen. It leads to the typical underdosage at the distal end of the target and overdosage behind the SOBP for all modalities. Larger fluctuating differences can be observed for density sampling in TOPAS throughout the body of the phantom and the target volume. Additionally, this results in a less cleanly modeled degradation.

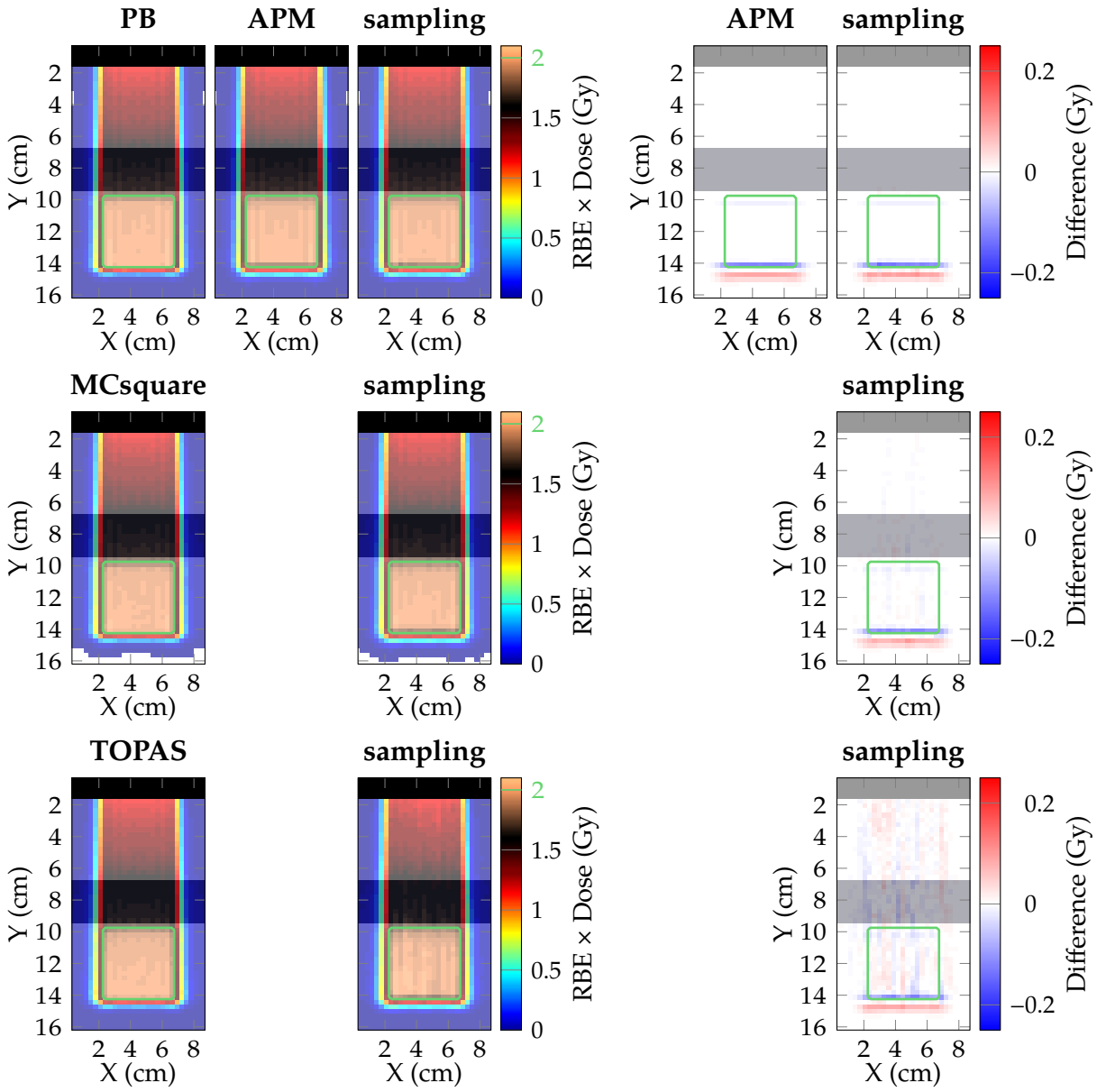

Figure IV.30: Overview of the proton dose distributions including degradation correction, calculated using constant RBE for matRad, MCsquare and TOPAS. Shown are respective absolute dose differences, compared to the homogeneous plan. For matRad, both analytical and sampled degradation correction are shown.

From the dose distributions, central depth dose profiles (Fig. IV.31a) were extracted. Good agreement between the multiple modalities and degradation correction algorithms is observed. The distal edge of the SOBP shows the typical degradation behavior. Notably, the variable RBE-weighted dose profiles in lung tissue for TOPAS exhibit a smaller deviation between degraded and homogeneous dose. In lung tissue, the RBE-weighted dose in MCsquare shows a large drop in dose, which has already been observed in Section IV.2.2.2.
This behavior is also visualized in the calculated DVHs (Fig. IV.31b) with large differences between the three modalities. While for constant RBE, the DVH differences are mostly confined to the upper edge of the dose volume curves, the variable RBE profiles display drops in dose towards higher doses consistent with the calculated depth dose profiles.

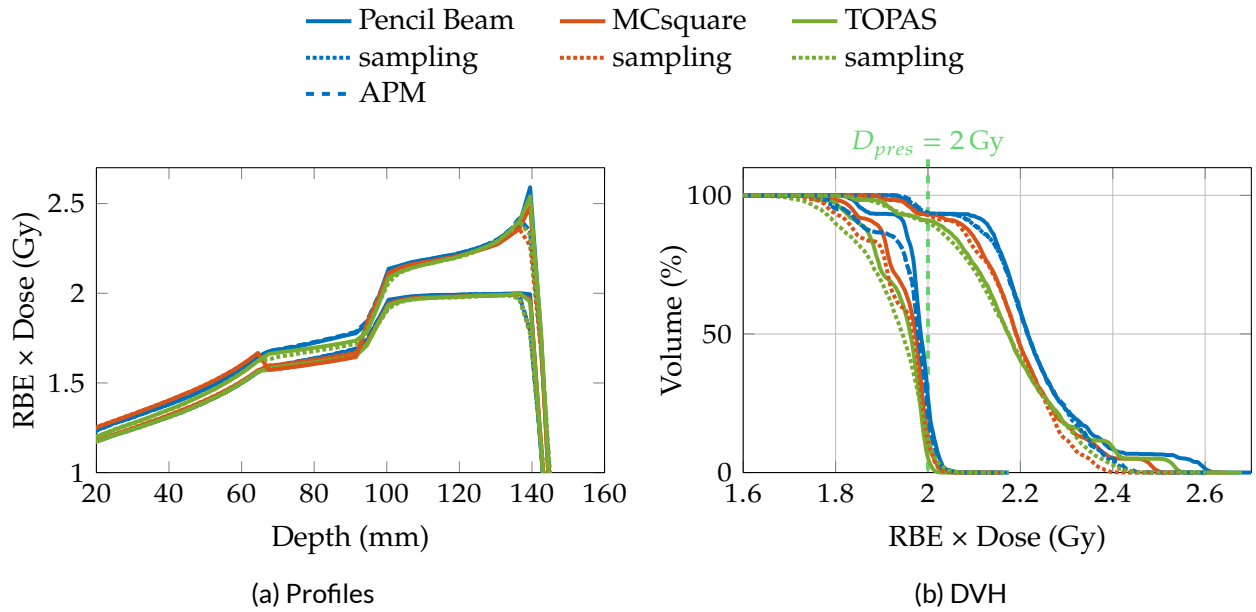

(a) Profiles (b) DVH

Figure IV.31: Central depth dose profiles for proton SOBPs using constant and variable RBE using the MCN model (a). Profiles were calculated and averaging over the 7 × 7 central rays. The DVH is shown for the target (b).

Fig. IV.32 shows the relevant quality indicators for all calculated dose distributions within the target. It demonstrates the change in mean, minimum and maximum dose with degradation correction. While there are differences already present between the homogeneous dose distributions, the behavior for the inclusion of degradation is consistent for each modality. The mean dose to the target decreases together with the minimum dose and an increased standard deviation. Relative differences between the degraded and the homogeneous target doses were –0.82 % and –0.84 % for APM and PB sampling, respectively. Density sampling in MCsquare and TOPAS resulted in relative differences of –0.73 % and –0.75 %. However, the maximum dose did only substantially change for TOPAS.

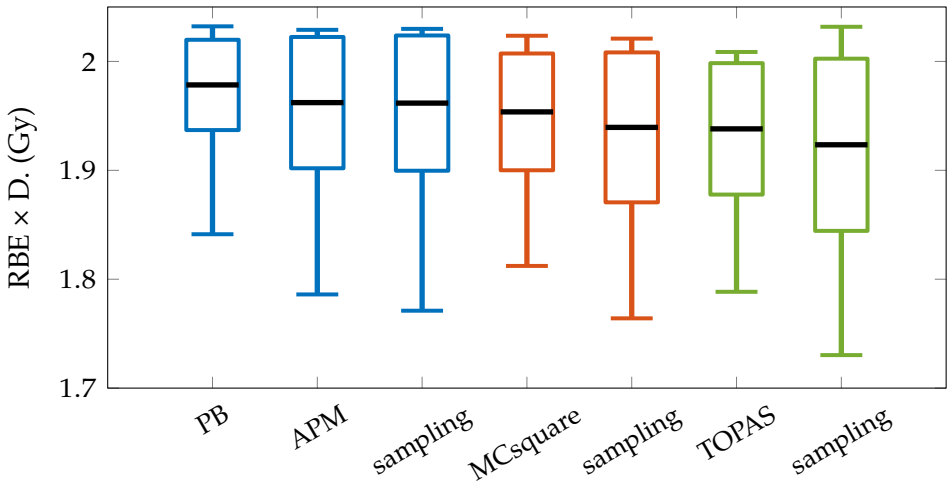

Figure IV.32: Calculated quality indicators within the target of the RBE-weighted proton dose distributions on the homogeneous lung phantom using constant RBE. For a plot explanation, see Fig. III.21.

Next to the dose quality indicators, the CI and HI were calculated. The CIs for constant and variable RBE are presented in Figs. IV.33a and IV.33b. For constant RBE, the CI decreases consistently when considering degradation for all modalities. Also, the CI for PB sampling is equivalent to analytical convolution. However, the differences in the homogeneous plans between the three modalities are in the same range of the differences due to degradation. The CI for variable RBE increases slightly when considering degradation, indicating better target conformity.
The calculated HIs for constant and variable RBE are presented in Figs. IV.33c and IV.33d and displays the same behavior. The HI increases for constant RBE degradation, meaning a less homogeneous dose distribution. Additionally, a lower HI (more homogeneous) was recorded when considering degradation for variable RBE.

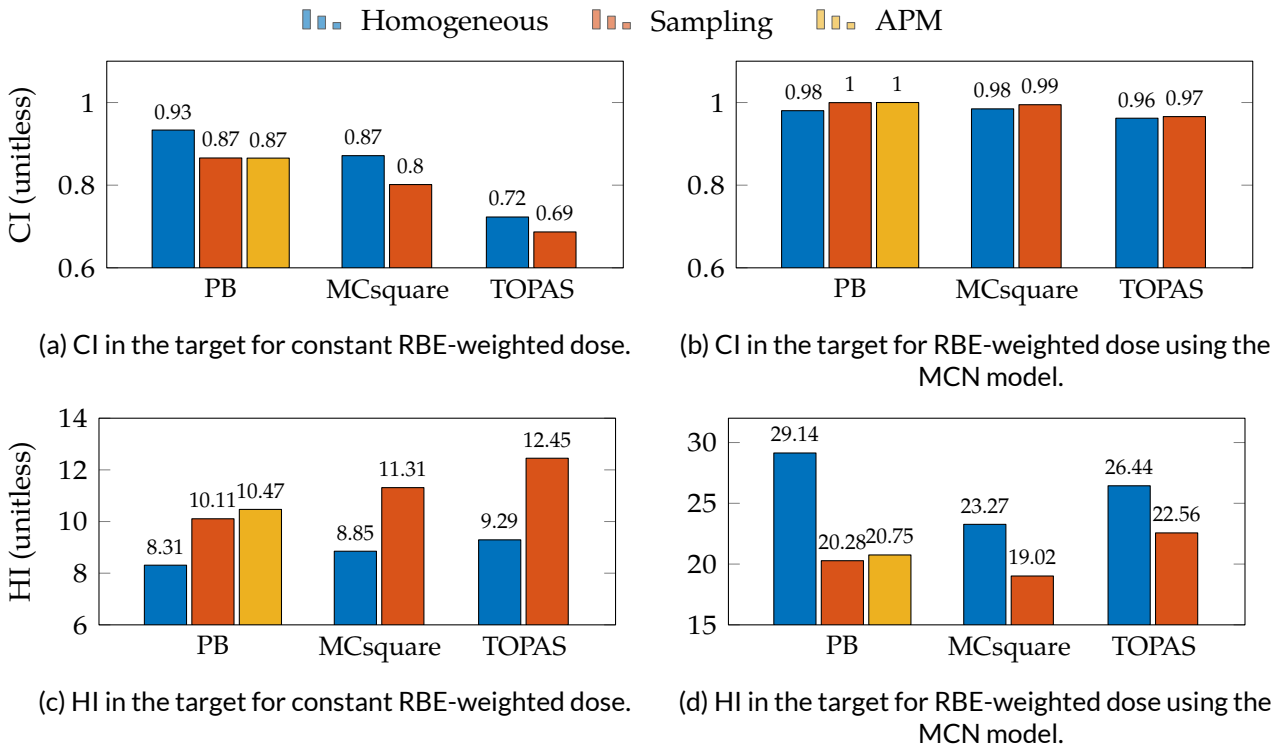

(a) CI in the target for constant RBE-weighted dose.

(b) CI in the target for RBE-weighted dose using the MCN model.

(c) HI in the target for constant RBE-weighted dose.

(d) HI in the target for RBE-weighted dose using the MCN model.

Figure IV.33: Conformity Index (CI) and Homogeneity Index (HI) in the target for the calculated dose distributions using PB, MCsquare and TOPAS. Degradation correction was included using density sampling in all modalities as well as APM for PBs. Note that the y axis does not start at 0.

γ pass rates were calculated for each method of degradation correction, comparing it to the respective homogeneous dose. A comparison of the γ pass rate for the 3 evaluated phantoms is shown in Table IV.2. Assuming a reference pass rate of 100 % for the homogeneous plan, the degradation exhibits a systematic decrease in the pass rate of ~3 % to 5 %. Generally, smaller γ pass rates were recorded for variable RBE compared to constant RBE over the whole CT. However, this is different for the target, which shows small to no changes in pass rate. The pass rate even increases slightly for the heterogeneous and real lung phantom. In the target, TOPAS shows the smallest γ pass rates of 89.7 % to 91.2 % for constant RBE.

Table IV.2: γ pass rates between homogeneous and degraded dose distributions for all 3 lung phantoms. MCsquare and TOPAS always use the sampling method. γ pass rates were calculated using [3 mm/3 %] criterion with 0 interpolation points. Shown are the pass rates over the whole patient volume (a) and the target volume (b).

(a) γ pass rates over the whole CT.

	Phantom	PB APM	PB sampling	MCsquare	TOPAS
Abs. D. / const RBE	Hom	96.31	96.21	96.62	95.37
	Het	95.57	95.84	96.08	94.94
	Real	96.65	96.57	97.35	96.11
	Carbon Real	96.79	96.59		93.45
var RBE	Hom	95.38	95.29	95.34	94.77
	Het	94.63	95.51	95.51	93.28
	Real	95.32	96.25	96.53	94.30

(b) γ pass rates in the target.

	Phantom	PB APM	PB sampling	MCsquare	TOPAS
Abs. D. / const RBE	Hom	93.33	93.30	93.33	89.72
	Het	94.16	94.22	93.78	91.20
	Real	93.69	93.90	93.69	90.25
	Carbon Real	93.16	93.16		81.42
var RBE	Hom	93.33	93.33	93.33	92.09
	Het	95.29	95.20	94.10	93.48
	Real	94.61	94.40	93.81	92.36

Variable RBE-weighted SOBPs were calculated on the *"RealLung"* phantom. Dose slices through the isocenter are shown in Fig. IV.34 with their respective absolute difference distributions. In contrast to the homogeneous phantom, there is a larger dose deposited irregularly behind the target. This in turn leads to an irregular degradation pattern, which is consistent between the different modalities and follows the shape of the dose pattern. However, it still displays the typical under- and overdosage behavior, yet locally.

Fig. IV.35 shows dose quality indicators for the target of the real lung phantom. The characteristic decrease in target mean dose can be seen for each modality and degradation algorithm. Here, a consistent decrease in minimum dose was reported for constant RBE. For variable RBE, the minimum dose remained constant with a significantly decreased maximum dose. Again, differences between the quality indicators calculated for the homogeneous dose distributions using the different modalities can be seen. They are in the same range or larger than the differences originating from degradation.

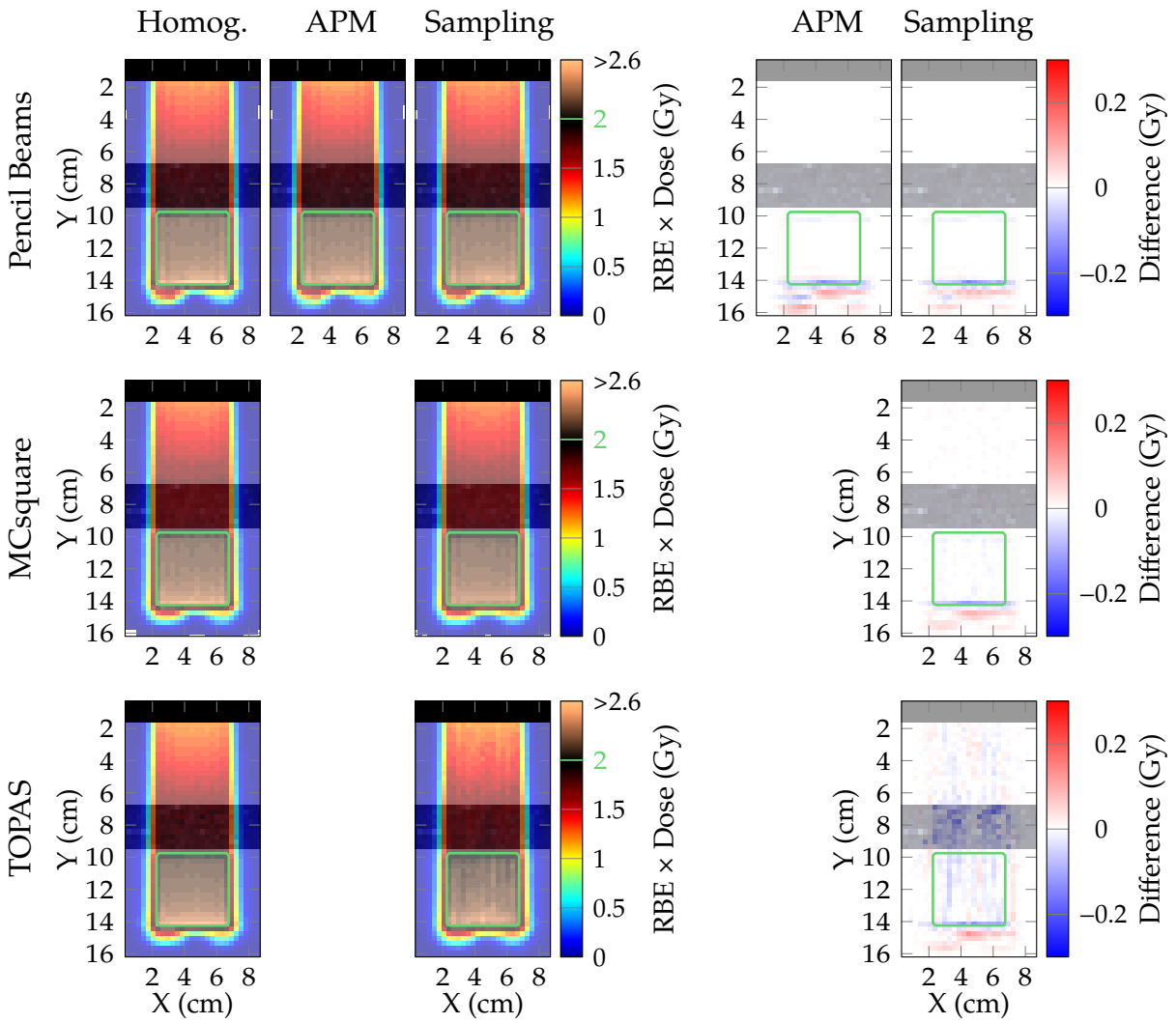

Figure IV.34: Overview of the proton dose distributions including degradation correction, calculated using variable RBE for matRad, MCsquare and TOPAS. Shown are respective absolute dose differences, compared to the homogeneous plan. For matRad, both analytical and sampled degradation correction are shown.

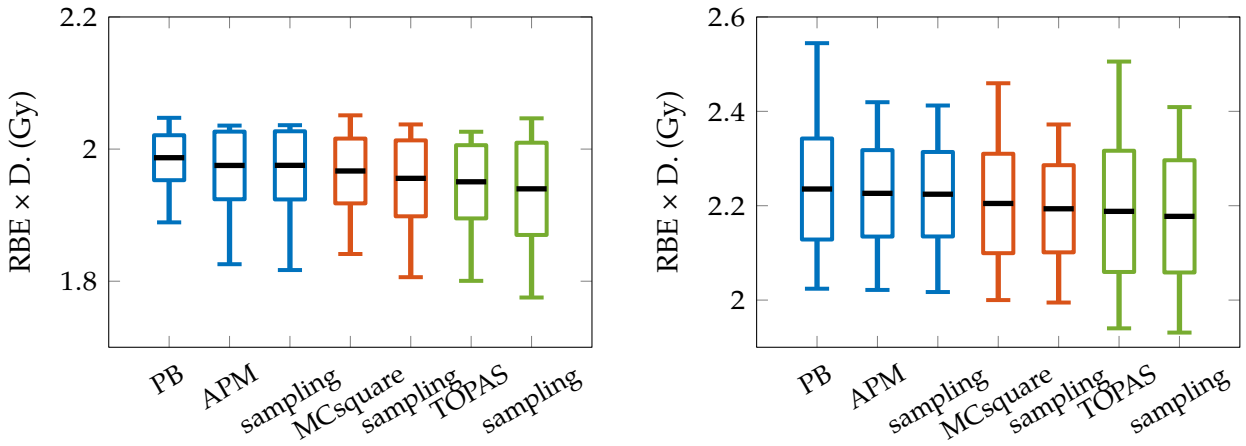

(a) Real phantom constRBE.

(b) Real phantom varRBE.

Figure IV.35: Quality indicators in the target of the RBE-weighted proton dose distributions on the *"RealLung"* phantom using constant RBE. Note the different y axis limits. For an explanation of the graph, see Fig. III.21.

Carbon Ions. For carbon ions, absorbed dose slices through the isocenter are shown in Fig. IV.36 for the real lung phantom. The degradation calculations using PBs lead to a similar degradation pattern already observed for protons, while exhibiting less additional dose outside of the target area. The density sampling in TOPAS, however, lead to large dose fluctuations, especially within the target and the lung tissue in the order of the differences originating from the degradation.

Calculated γ pass rates can also be found in Table IV.2. There, similar pass rates were calculated compared to protons, albeit a much lower value of ~80 % for the target in TOPAS. CIs were 0.94 and 0.92 for PB and TOPAS, respectively. They decreased to 0.88 when considering degradation. In a similar way, the HI increased from 5.56 to ~6.9 for PB and from 8.85 to even 14.8 for TOPAS.

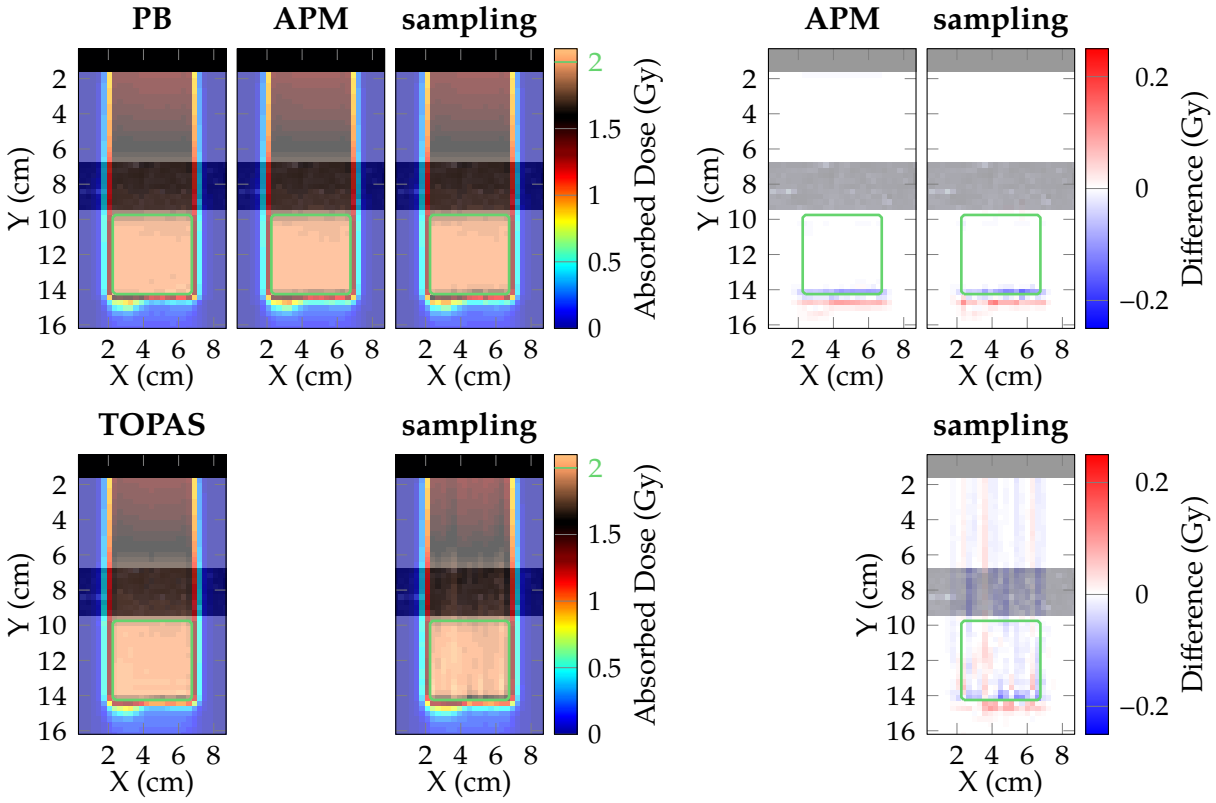

Figure IV.36: Overview of the carbon absorbed dose distributions including degradation correction, calculated using matRad and TOPAS. Shown are respective absolute dose differences, compared to the homogeneous plan. For matRad, both analytical and sampled degradation correction are shown.

Fig. IV.37 shows central depth dose profiles and the DVH. Significant differences in the scored dose within the lung tissue can be observed for TOPAS, together with a higher homogeneous dose. Additionally, differences at the distal peak area are seen between PB and TOPAS that are in the order of the differences introduced by degradation. These differences are reflected in the DVH. Large differences are visible between the degraded and homogeneous dose distributions, but also between homogeneous distributions calculated with PB and TOPAS.

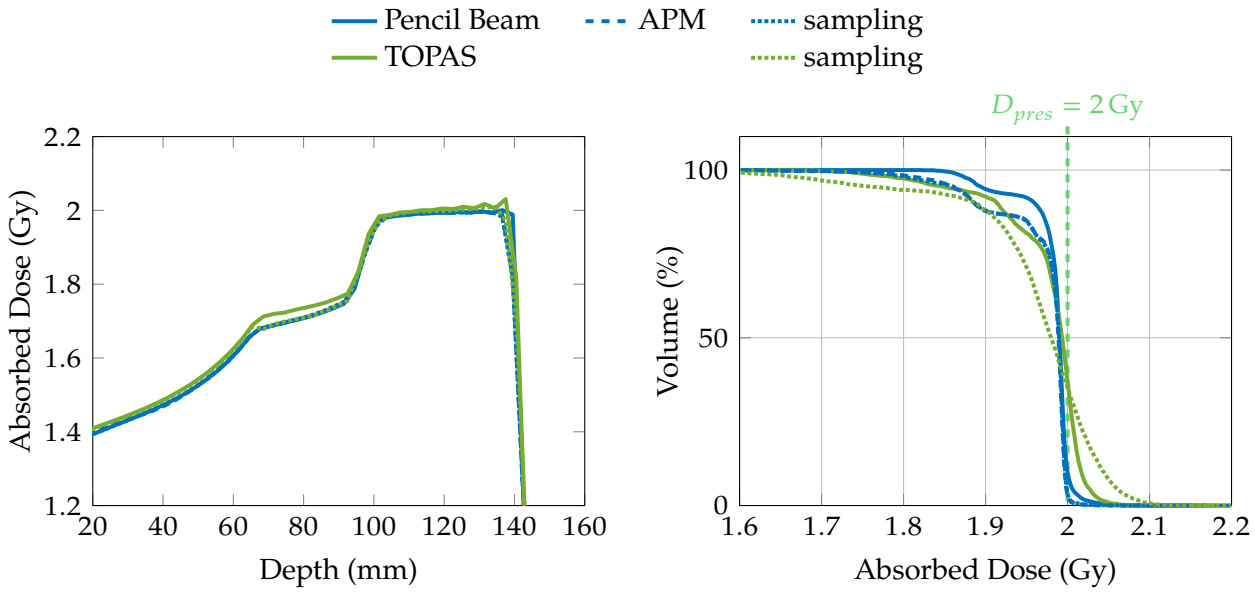

(a) Central averaged depth dose profiles.

(b) DVH

Figure IV.37: Central depth dose profiles for carbon SOBP absorbed dose distributions (a). The profiles were calculated and averaging over the 7 × 7 central rays. Additionally, the DVH is shown for the target (b).

Finally, Fig. IV.38 shows the dose quality indicators. In contrast to the data already shown for protons, the maximum dose of the PB degraded dose distributions falls within the standard deviation of the mean dose. Regarding TOPAS, the maximum dose increases and the minimum dose decreases drastically. However, the mean dose to the target is in good agreement for the homogeneous dose distributions calculated using PBs and TOPAS while also displaying the characteristic drop when considering degradation. Here, the decrease in mean dose to the target amounted to –0.64 % for PBs and –0.59 % for TOPAS.

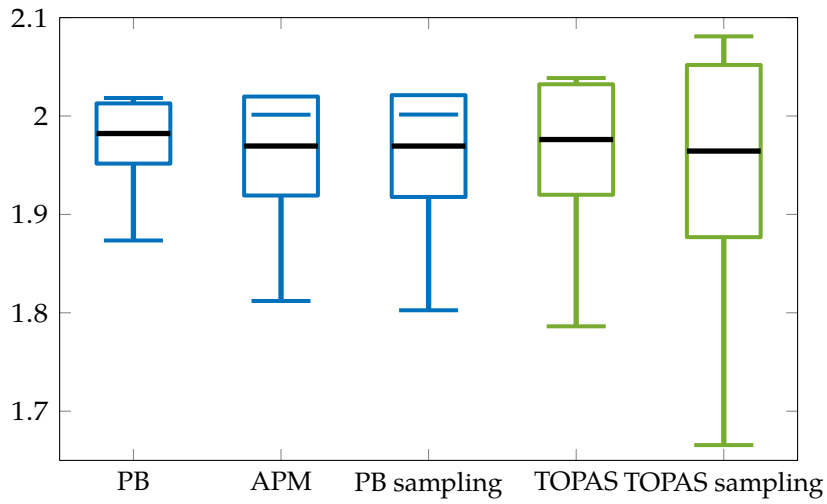

Figure IV.38: Calculated quality indicators within the target of the absorbed carbon dose distributions on the *"RealLung"* phantom. For a plot explanation, see Fig. III.21.

IV.2.2.4 Interdependence of MC Histories and Number of Samples

The used methods are detailed in Section III.2.5.4.
Fig. IV.39 shows a comparison of the dose difference between between homogeneous and degraded dose distributions for PBs, MCsquare and TOPAS. Calculated differences relative to the prescribed dose and γ pass rates are listed in Table IV.3.
For PBs and MCsquare, there was no visible difference between 100 and 500 samples for 10^8 samples with approximately the same γ pass rates and mean relative differences. However, the switch to 10^9 samples for MCsquare then lead to smaller mean differences of 0.08 %.
For TOPAS, $100/10^8$ showed a lower γ pass rate compared to pencil beams by 1.3 % with mean local fluctuations in the plateau region and the target of 0.41 %. The fluctuations increased to 0.90 % for $500/10^8$ with a γ pass rate of 78.6 %. For $500/10^9$, the differences decreased to 0.31 % with a pass rate of 96.6 %, approximately the same value measured for PBs and MCsquare.

Table IV.3: γ pass rates between degraded and homogeneous, constant RBE-weighted dose distributions calculated using PBs, MCsquare and TOPAS for combinations of 100 and 500 samples as well as 10^8 and 10^9 histories. Also shown are the mean differences relative to a prescribed dose of 2 Gy.

Modality	100 Samp. / 10^8 Hist.		500 Samp. / 10^8 Hist.		500 Samp. / 10^9 Hist.	
	γ (%)	Diff. (%)	γ (%)	Diff. (%)	γ (%)	Diff. (%)
Pencil Beams	96.5	0.03	96.6	0.03	-	-
MCsquare	96.6	0.17	96.6	0.17	96.6	0.08
TOPAS	95.4	0.41	78.6	0.90	96.6	0.31

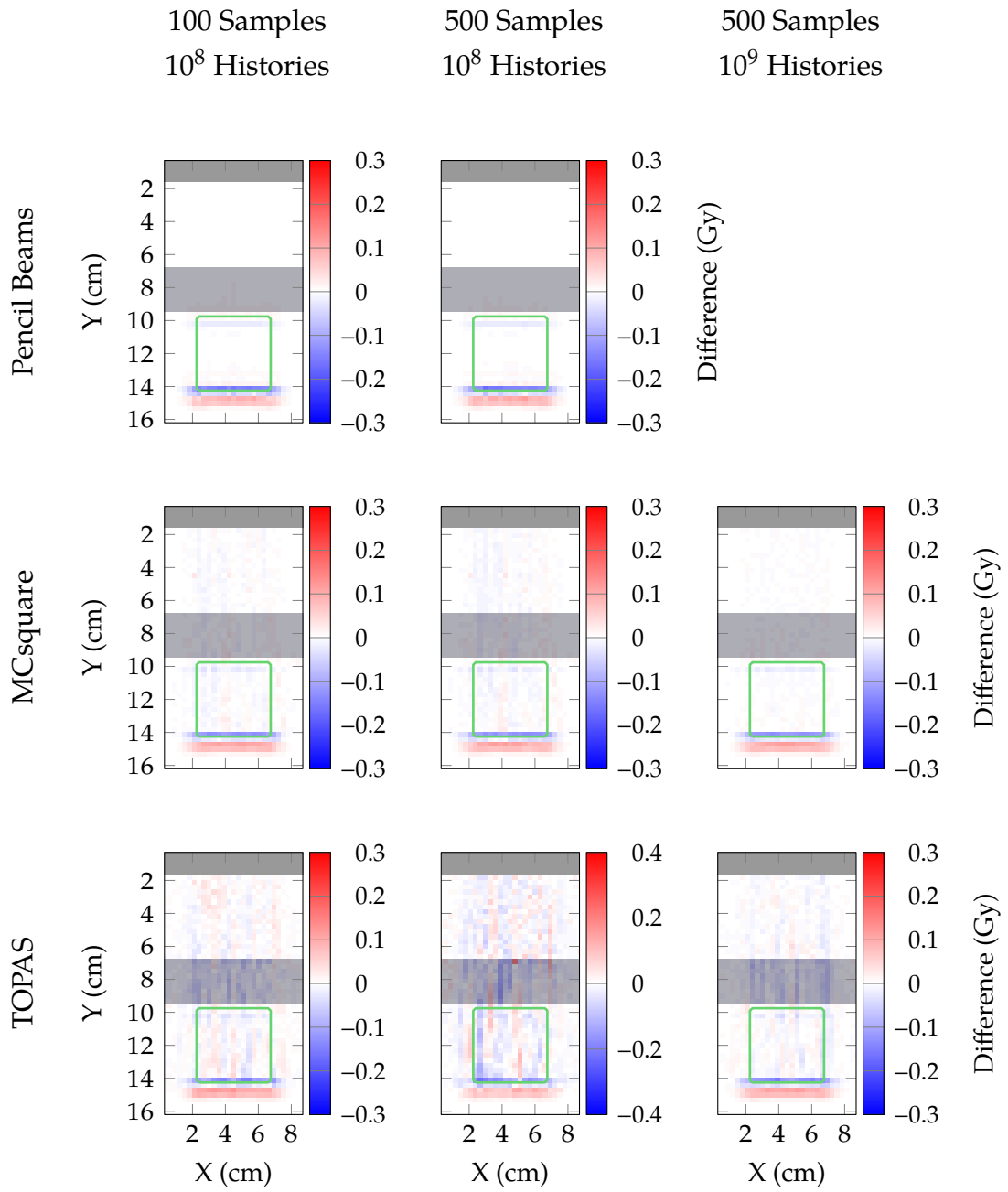

Figure IV.39: Comparison of the density sampling depending on number of samples and total histories in MC simulations. Shown is the absolute difference between degraded and homogeneous dose. For MC, the homogeneous dose was calculated using 10^8 samples. For reference, the difference is also shown for PBs, that only depends on the number of samples.

IV.2.3 Patient Treatment Plans

In this section, treatment plans are evaluated that were calculated on the four selected patient data sets. Treatment plans for all patients were calculated using protons, a treatment plan for *Patient 2* was calculated using carbon ions. A description about the workflow is detailed in Section III.2.6.

IV.2.3.1 Protons

Calculated proton dose distributions for all forms of degradation correction are shown in Figs. IV.40 to IV.43 together with γ index distributions for constant and variable RBE. Shown are distributions for analytical convolution (APM) and density sampling for PB, MCsquare and TOPAS. γ pass rate distributions were calculated for all patients and are also shown. Visually, there is good agreement between the dose slices of all 4 different degradation correction methods. The γ pass rate distributions are most consistent between both PB methods with larger pass rates – meaning smaller degradation influences – for both MC engines, especially MCsquare. Also, the recalculation using variable RBE lead to only small changes compared to constant RBE, both visually and in γ pass rates.

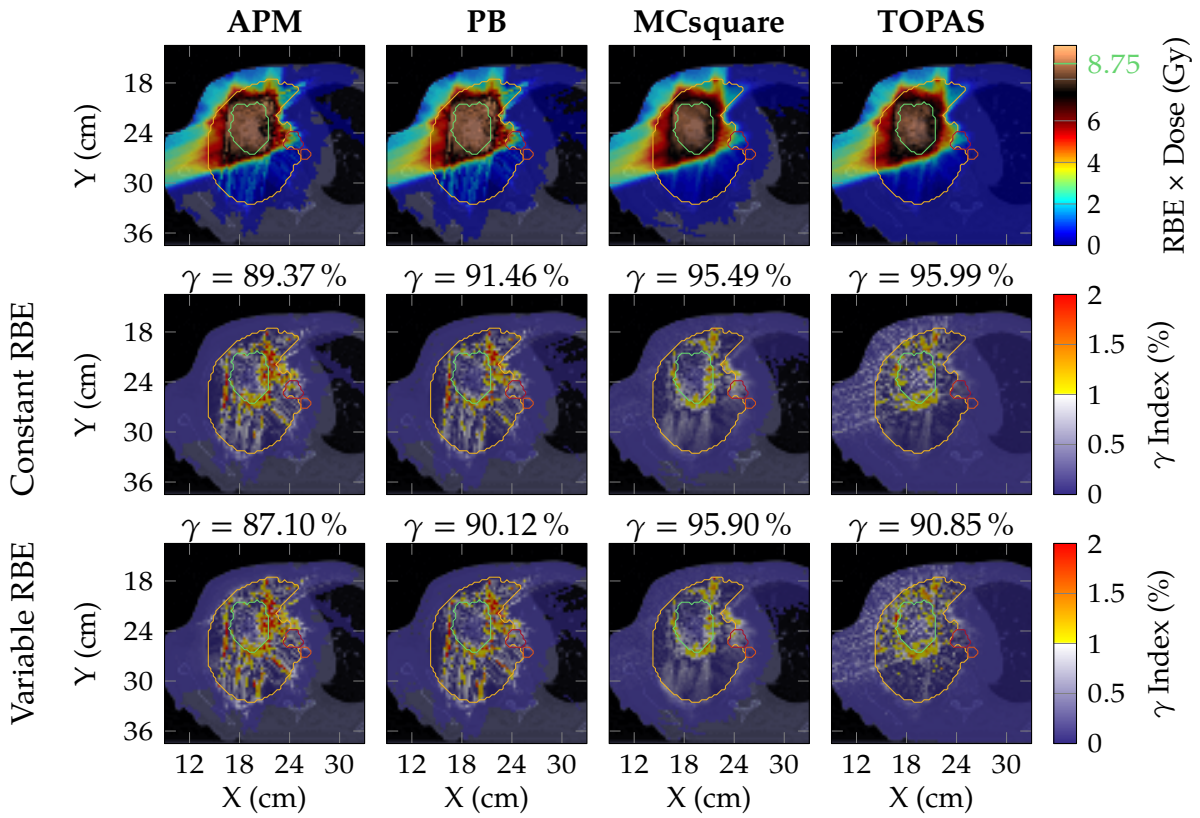

Figure IV.40: Comparison of patient dose distributions for *Patient 1*. Shown are degraded constant RBE-weighted dose distributions through the isocenter for APM, density sampling and γ pass rate.

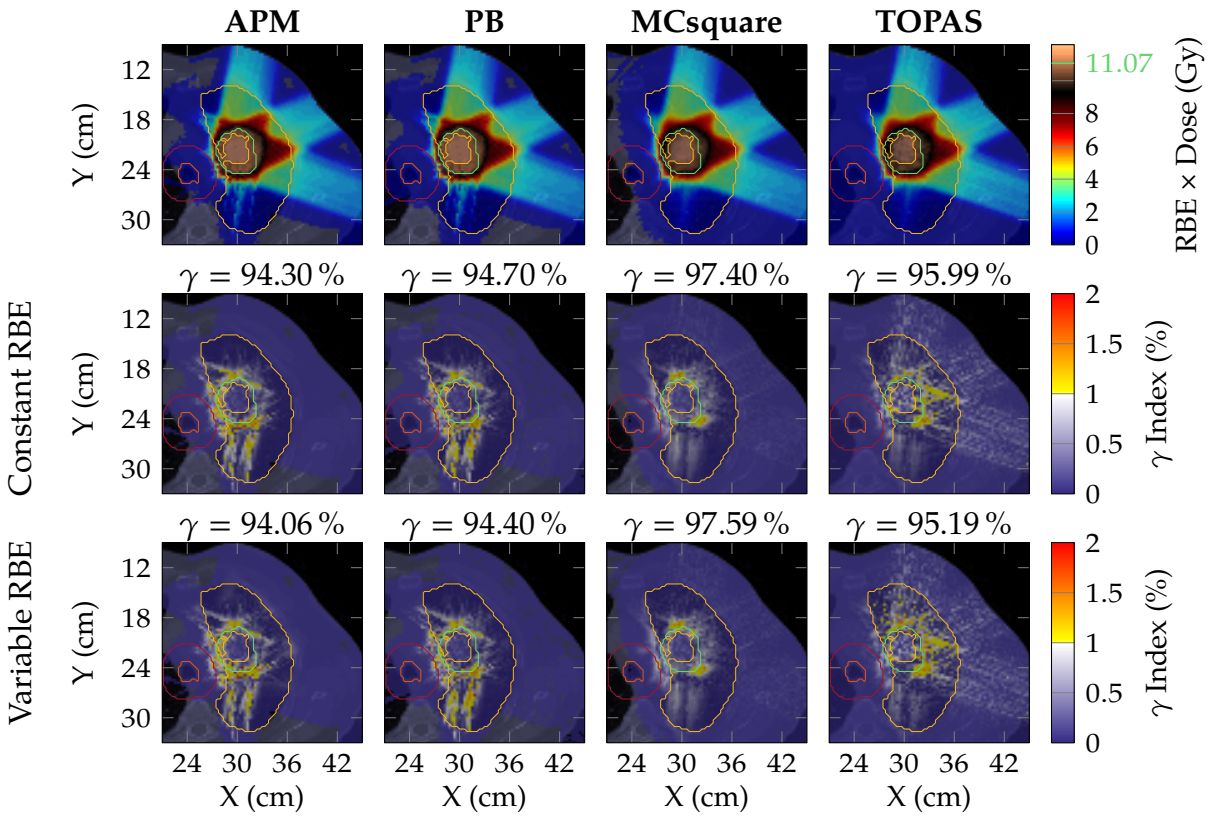

Figure IV.41: Comparison of patient dose distributions for *Patient 2*. Shown are degraded constant RBE-weighted dose distributions through the isocenter for APM, density sampling and γ pass rate.

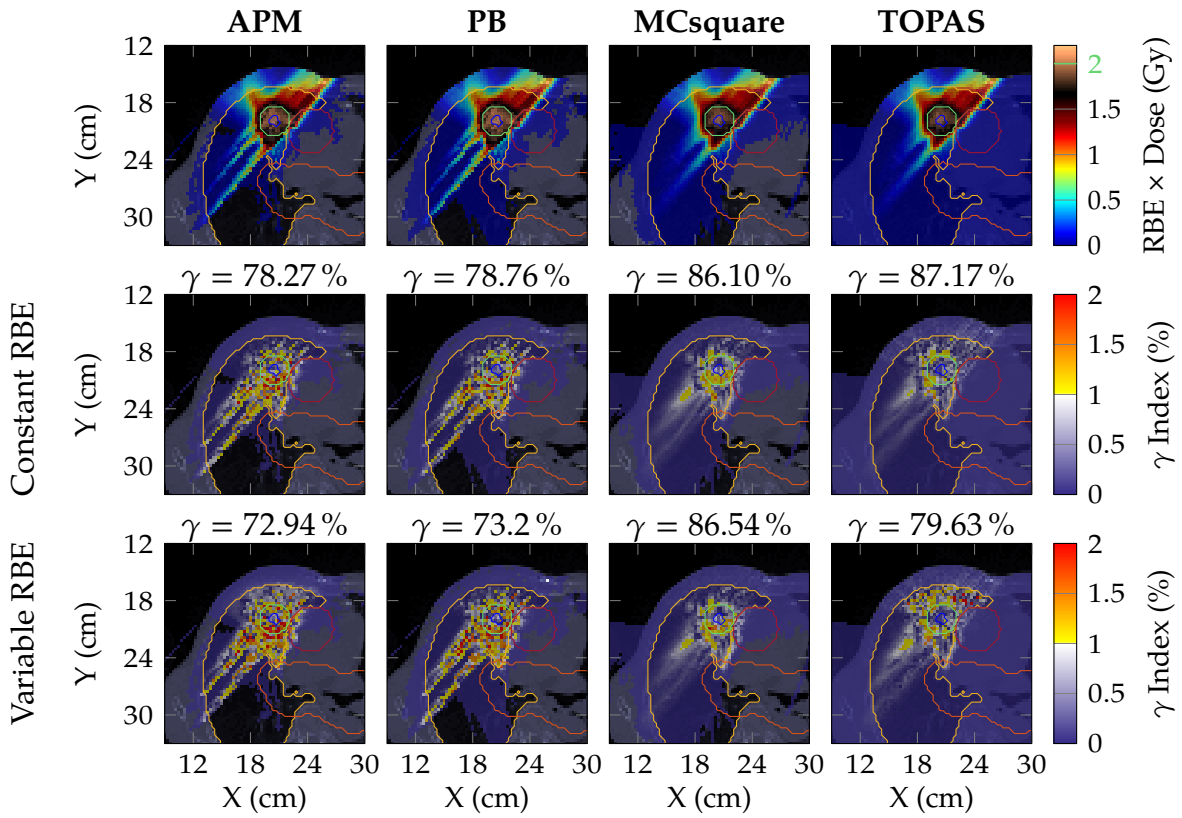

Figure IV.42: Comparison of patient dose distributions for *Patient 3*. Shown are degraded constant RBE-weighted dose distributions through the isocenter for APM, density sampling and γ pass rate.

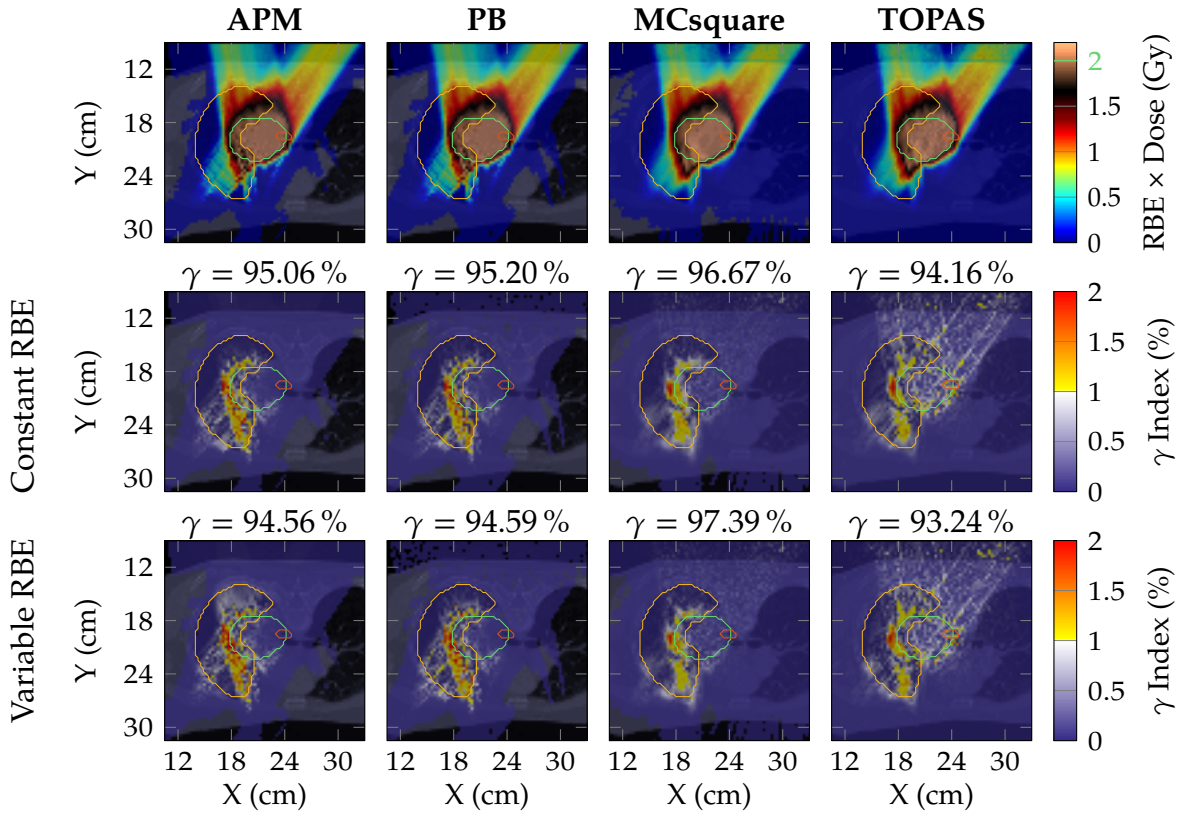

Figure IV.43: Comparison of patient dose distributions for *Patient 4*. Shown are degraded constant RBE-weighted dose distributions through the isocenter for APM, density sampling and γ pass rate.

γ Pass Rates. The calculated γ pass rates for the whole CT and the PTV for all patients are summarized in Fig. IV.44. In comparison with the pass rates calculated for the 3 lung phantom cases the median pass rates were approximately the same, with lower mean pass rates and a much larger variance. Especially in the target, smaller pass rates with a larger variance were measured for the patient cases with pass rates in the PTV from approximately 45 % to 95 %. The lowest pass rates were measured for *Patient 3*, located consistently below the lower quartile. Lowest measured values for the phantoms, however, were only as low as 90 %. In the target, *Patient 4* shows values consistently larger than the median.

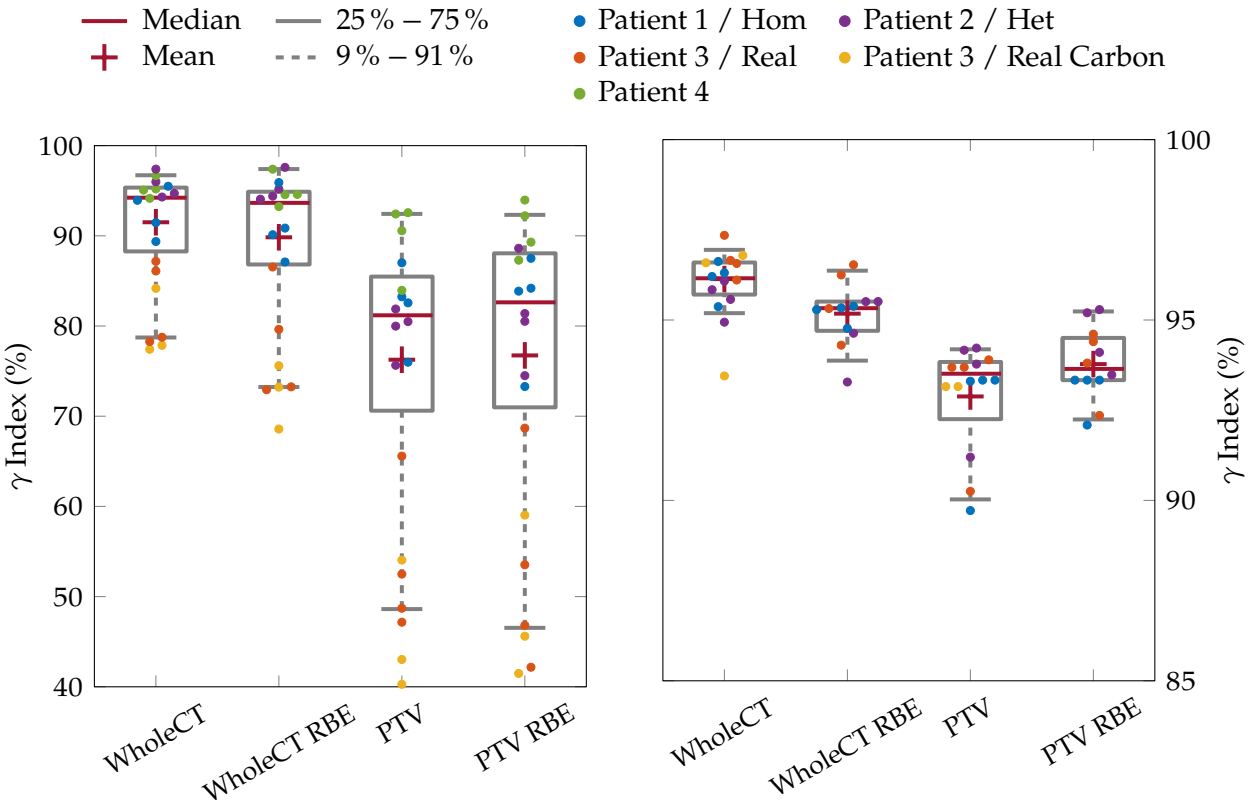

(a) Patient data sets (*Patient 1* to *Patient 4*).

(b) Lung phantoms *Hom*, *Het* and *Real*.

Figure IV.44: Measured γ pass rates between degraded and homogeneous treatment plans for the 4 different patient data sets (a). Due to the limited data size, data points were overlaid using a scatter plot with jitter. To compare, the γ pass rates for the 3 lung phantoms are shown in (b). Note that (b) has narrower y axis bounds. Pass rates were calculated using a [3 mm/3 %] criterion with 0 interpolation points. Results for carbon ions are shown for reference, but are not included in the box plot.

LET Distributions. For *Patient 3*, larger differences for variable RBE-weighted distributions were observed especially for the homogeneous dose distribution calculated with MCsquare. To visualize these differences, variable RBE-weighted dose distributions are shown in Figs. IV.45 to IV.48 together with their respective LET distributions. Additionally a TOPAS distribution is shown that was directly recalculated based on the scored LET.
While larger differences between PBs and MC are apparent, the directly scored RBE-weighted TOPAS dose in the target visually matches the dose calculated with the PB algorithm. For MCsquare, a lower target dose compared to the other modalities was measured. At the same time, however, the LET scored by both MC engines is consistent and differs significantly from the analytically calculated LET. This results in a recalculated TOPAS dose much closer to the MCsquare dose distribution that differs significantly from the directly scored distribution.

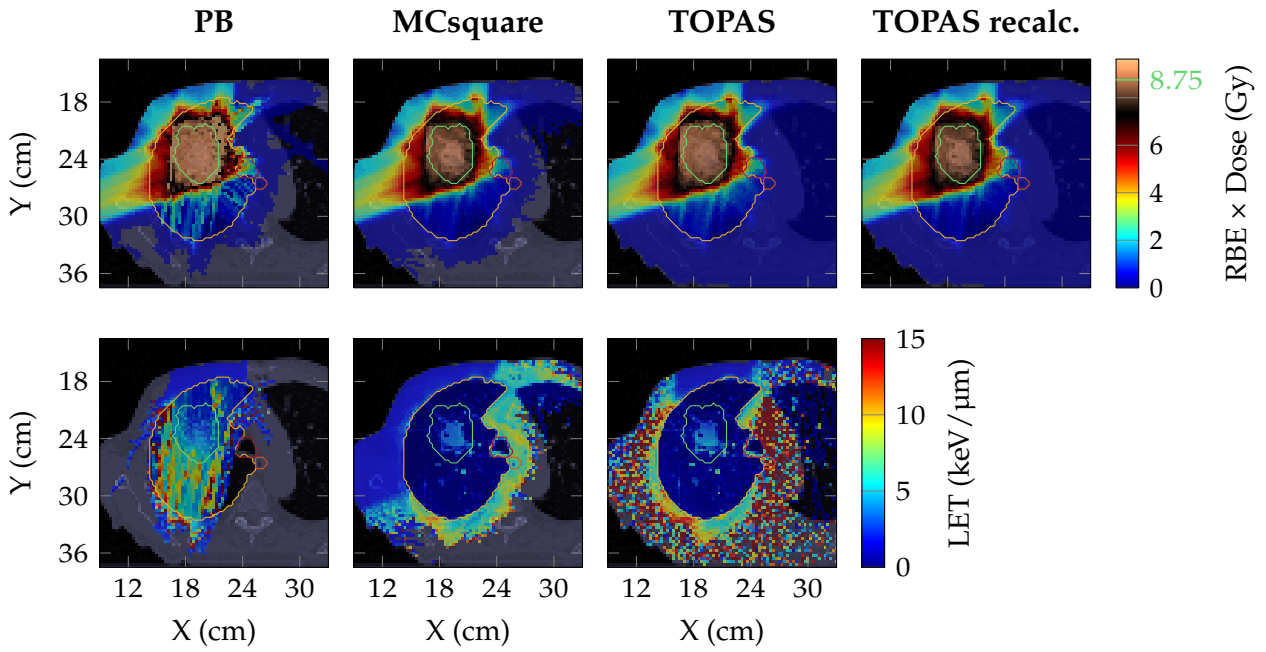

Figure IV.45: Comparison of patient LET distributions for *Patient 1*. Shown are homogeneous RBE-weighted dose distributions for PB, MCsquare and TOPAS, as well as corresponding LET distributions. Also displayed is the TOPAS dose distribution recalculated from LET.

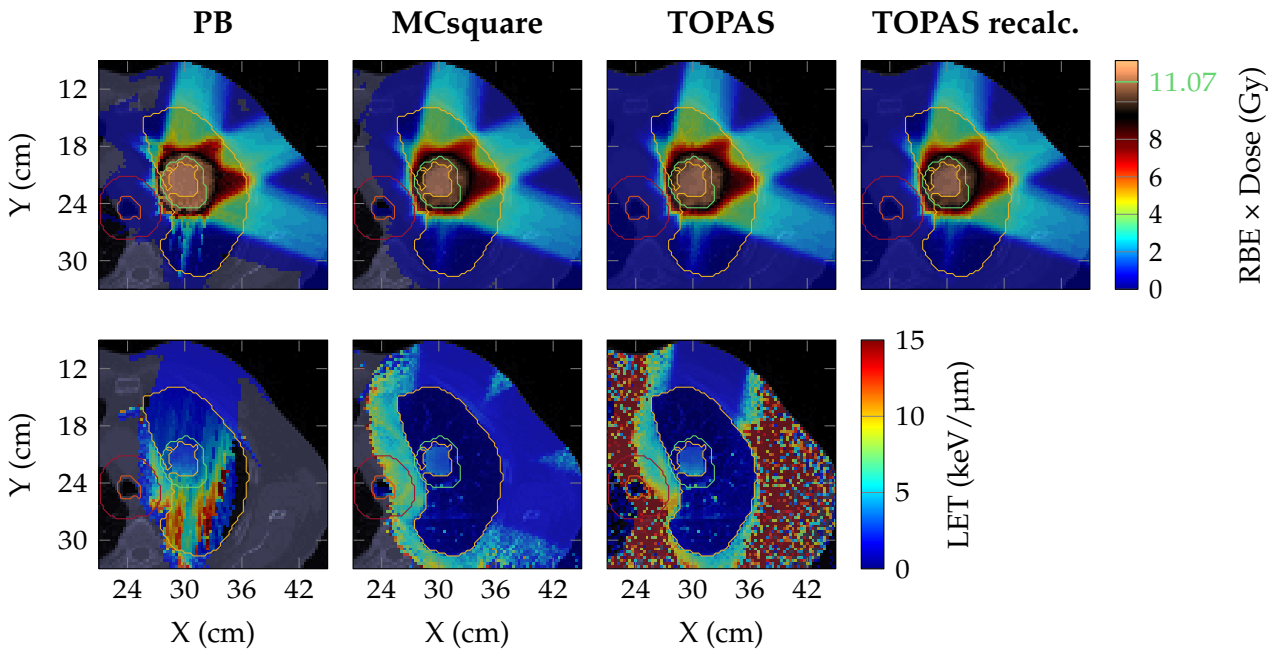

Figure IV.46: Comparison of patient LET distributions for *Patient 2*. Shown are homogeneous RBE-weighted dose distributions for PB, MCsquare and TOPAS, as well as corresponding LET distributions. Also displayed is the TOPAS dose distribution recalculated from LET.

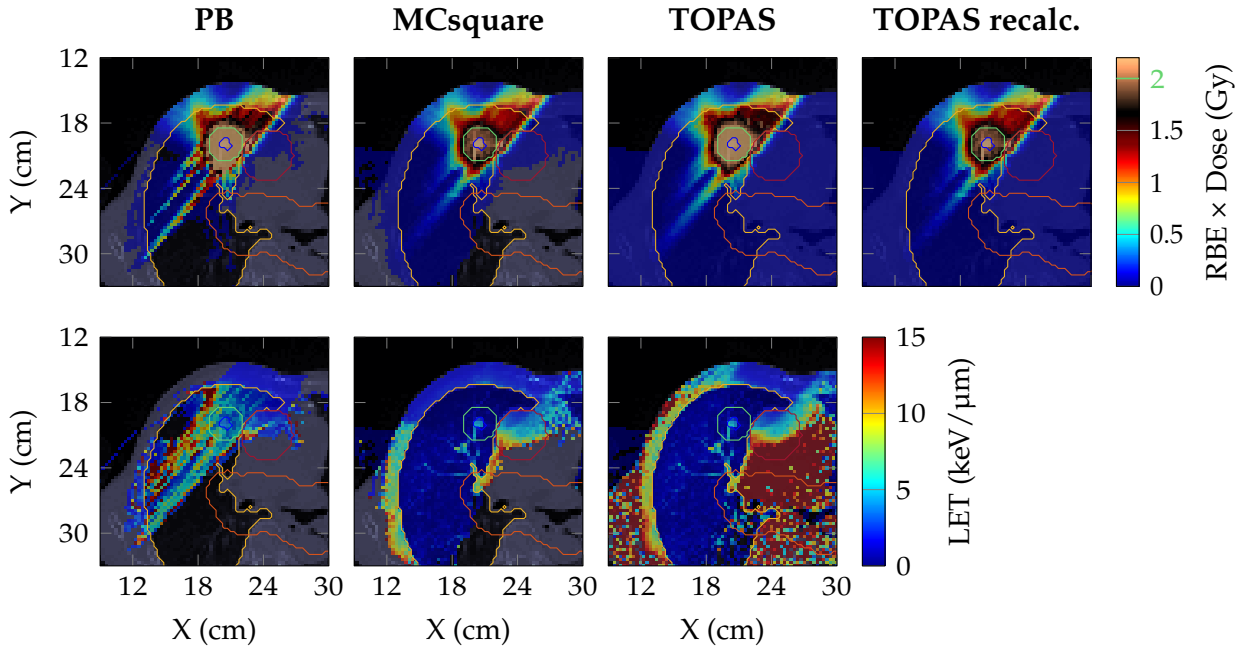

Figure IV.47: Comparison of patient LET distributions for *Patient 3*. Shown are homogeneous RBE-weighted dose distributions for PB, MCsquare and TOPAS, as well as corresponding LET distributions. Also displayed is the TOPAS dose distribution recalculated from LET.

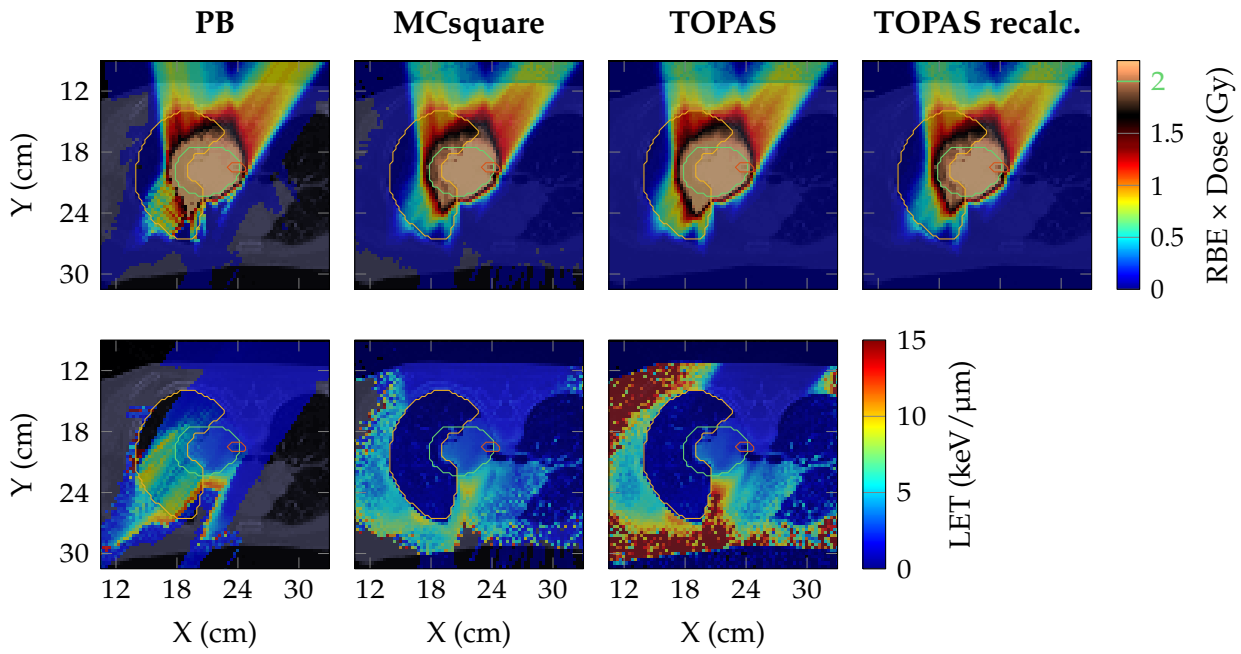

Figure IV.48: Comparison of patient LET distributions for *Patient 4*. Shown are homogeneous RBE-weighted dose distributions for PB, MCsquare and TOPAS, as well as corresponding LET distributions. Also displayed is the TOPAS dose distribution recalculated from LET.

Dose Quality Indicators. The dose quality indicators mean dose, D_5 and D_{95} were evaluated for all 4 patients and compared between homogeneous and degraded dose distributions. The resulting relative differences are presented in Fig. IV.49.
For the patient mean target dose difference, larger values were observed compared to the previous SOBP degradation experiments (Fig. IV.27). However, the values were within a similar range and consistently negative. It was found, that the degradation reduced the mean dose to the lung by approximately –1 % in the median with larger differences observed for TOPAS and RBE. In the target, the median dose difference amounted to 1.9 %. Here, *Patient 3* displayed the most pronounced differences, while the smallest differences were observed for *Patient 2*. The OAR mean dose increased considerably in almost all cases. Substantial differences up to 80 % were calculated for *Patient 1* with even larger values up to 170 % (outside of the plotted range) for *Patient 3*. Albeit the extensive range of values, the median values for the OAR were 7.5 % and 6 % for constant and variable RBE, respectively.
Relative differences of the D_5 were mostly negative in the low percent range, spanning over a large range of values without a pattern for any single patient. The target maximum dose was reduced by –1.1 % in the median by the degradation, with the reduction doubling for variable RBE. In lung, the maximum dose was reduced by –2.7 % and –3.0 % in the median. The outliers visible especially for the measured lung D_5 differences were attributed to *Patient 3*, displaying an increase in maximum dose with degradation. Extreme relative differences were observed for the OARs with outliers for *Patient 4* with medians of 14.8 % and 17.3 % for constant and variable RBE, respectively.
The minimum dose D_{95} in the target decreased when including degradation with differences of –3.9 % for constant RBE and –2.6 % for variable RBE. Larger differences with significant variations in the –20 % to –80 % were measured in lung and OAR.

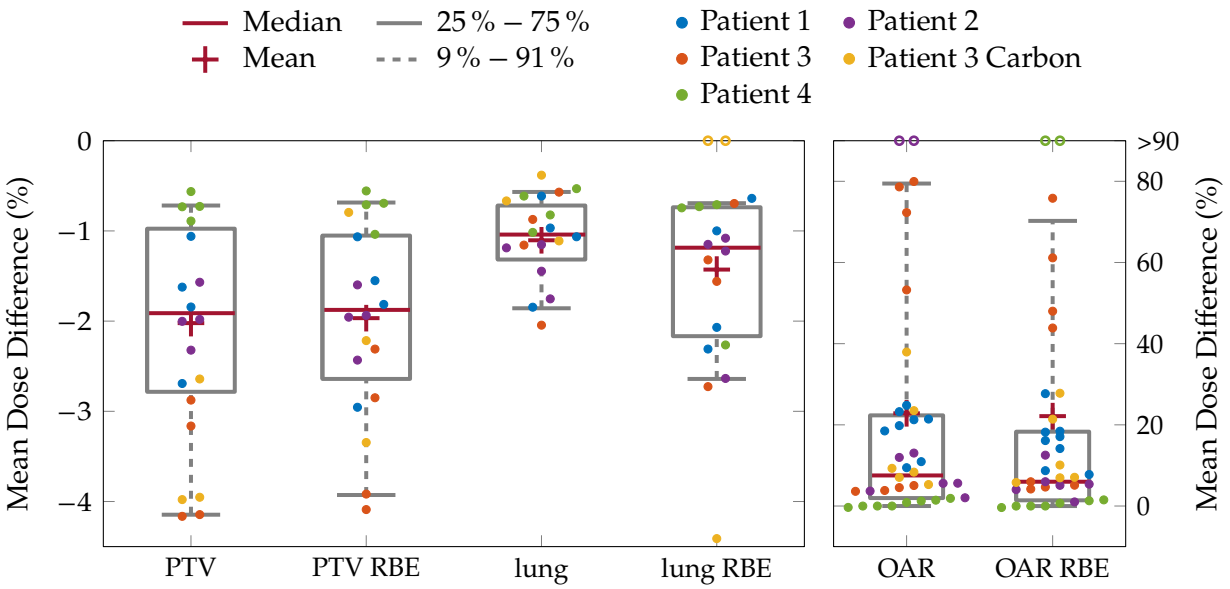

(a) Box plots and underlying data for the relative mean dose differences.

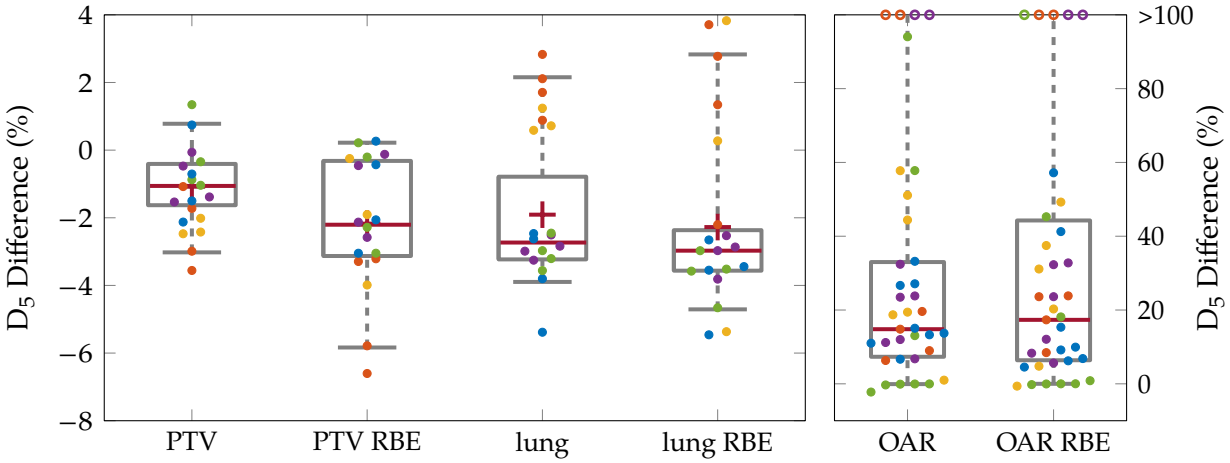

(b) Box plots and underlying data for the relative D_5 differences.

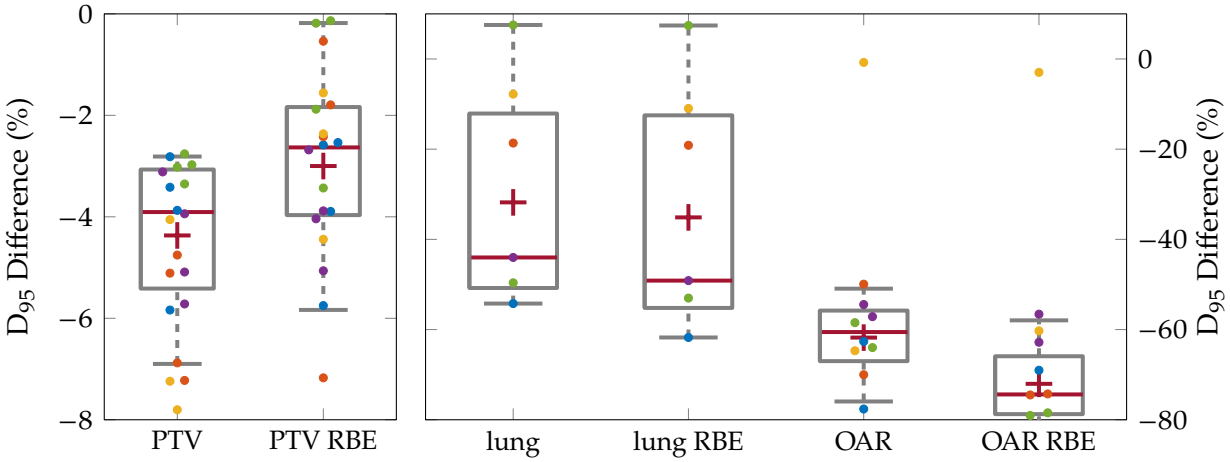

(c) Box plots and underlying data for the relative D_{95} differences.

Figure IV.49: Selected quality indicators mean dose (a), D_5 (b) and D_{95} (c). Relative dose differences were calculated between degraded and homogeneous treatment plans for the 4 different patient data sets. Due to the limited data size, data points were overlaid using a scatter plot with jitter. Data for the 4 different patients were individually color coded. Values outside of the plotted range were displayed as empty circles at the edge. Results for carbon ions are shown for reference, but are not included in the box plot.

Conformity and Homogeneity Index. Similar to the SOBP investigations, CI and HI were calculated and are displayed in Fig. IV.50. Largely, the behavior when including degradation is consistent with the previous investigations. CI differences with significant variations of −47.5 % to 0.9 % with a median of −8.1 % were measured. For RBE, the median CI difference was again positive with 2.9 %. However the variation of values is considerable with values ranging from −34.8 % to 20.5 %.
The HI increased significantly for constant RBE by 27.6 % in the median but did not decrease in the same way for variable RBE compared to SOBPs. Instead, it shows a positive median relative difference of 15.4 %.

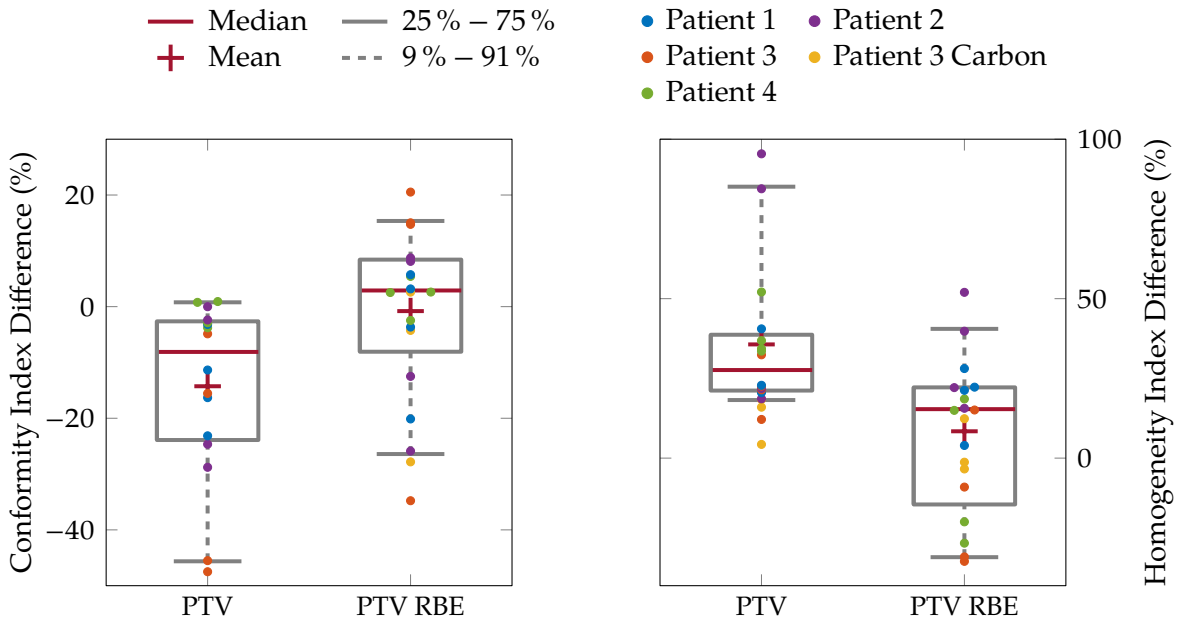

(a) Conformity Index Difference distribution.

(b) Homogeneity Index Difference distribution.

Figure IV.50: Measured conformity index and homogeneity index differences between degraded and homogeneous treatment plans for the 4 different patient data sets (*Patient 1* to *Patient 4*). Due to the limited data size, data points were overlaid using a scatter plot with jitter. Data for the 4 different patients were individually color coded. Results for carbon ions are shown for reference, but are not included in the box plot.

IV.2.3.2 Carbon Ions

In addition to the proton plans, a treatment plan using carbon ions was generated for *Patient 3*. Fig. IV.51 shows the homogeneous absorbed and RBE-weighted dose distributions for PBs and TOPAS. Also shown are absolute dose differences and γ pass rate distributions over the whole CT. Differences can be observed especially in lung with minor overdosing proximal to the tumor for beams 2 and 3 and severe underdosing proximal and distal to the tumor for beam 1. Calculated pass rates were 74.9 % and 65.3 % for absorbed and RBE-weighted dose, respectively.

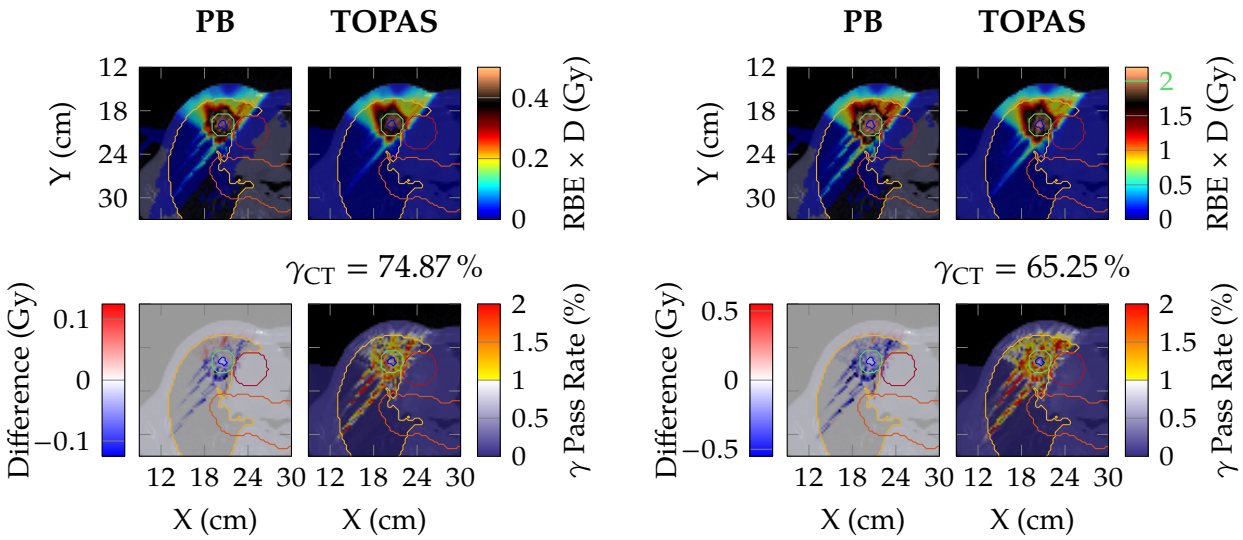

(a) Carbon absorbed dose distributions.

(b) Carbon RBE-weighted dose distributions.

Figure IV.51: Comparison of homogeneous patient carbon dose distributions for *Patient 3* calculated using pencil beams and TOPAS. Shown are both the absorbed dose (a) and RBE-weighted dose (b).

Degraded dose distribution slices through the isocenter are shown in Fig. IV.52. Visually, the dose distributions display good agreement with each other with larger deviations for the dose in TOPAS. This behavior is reflected in the γ pass rate distributions. Calculated pass rates over the whole CT showed similar values compared to *Patient 3* calculated with protons albeit slightly but consistently lower, for both absorbed and RBE-weighted dose distributions. In the same way, pass rates decreased further when transitioning to RBE-weighted dose.

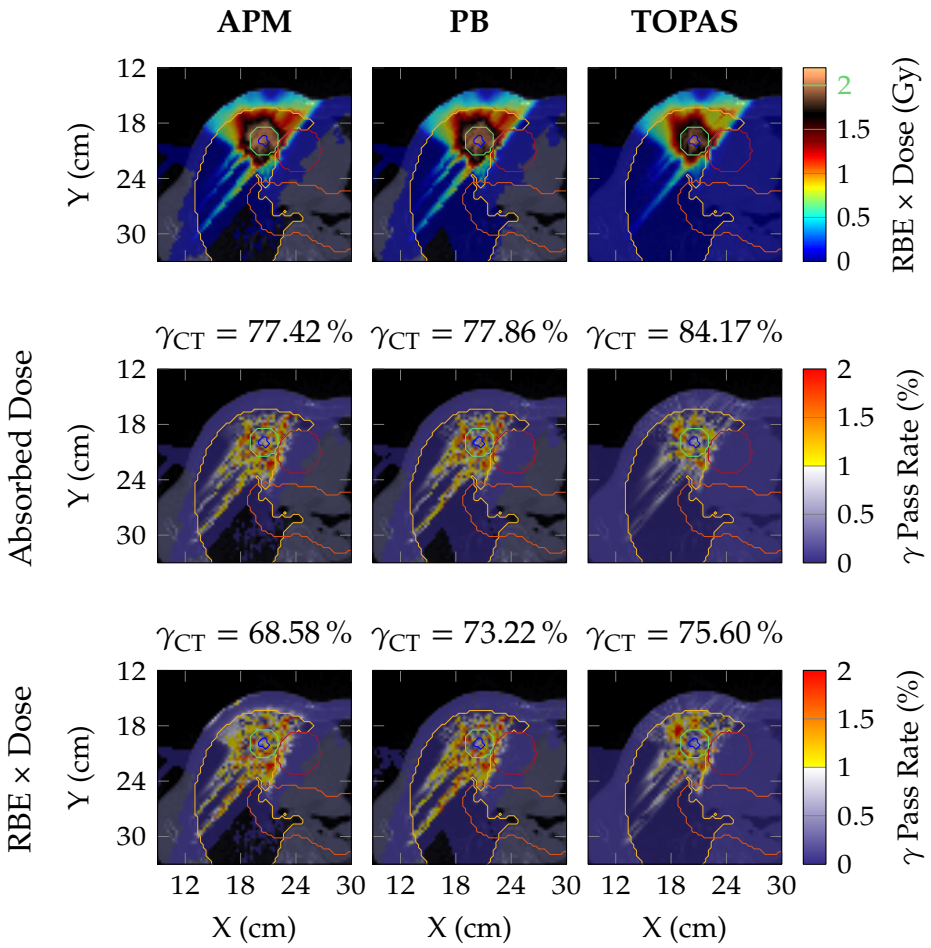

Figure IV.52: Comparison of patient carbon degraded dose distributions for *Patient 3*. Shown are degraded RBE-weighted dose distributions through the isocenter for APM as well as density sampling for PB, MCsquare and TOPAS. Additionally, γ pass rate distributions are shown for absorbed and RBE-weighted dose with documented pass rates over the whole CT.

IV.2.3.3 (N)TCP Model Considerations

Fig. IV.54 shows DVHs for *Patient 1* to *Patient 4*, including EUD volume histograms calculated analytically calculated using APM using the Niemierko NTCP model.

For all patients, calculated TCP values were approximately 100 % with slightly lower TCP of 99.8 % and 99.9 % for *Patient 3* and *Patient 4*, respectively. For *Patient 1*, *Patient 2* and *Patient 4*, calculated NTCP values in most OARs were below 10^{-6} % and therefore neglected. Only lung in *Patient 1*, *Patient 2* and *Patient 4*, as well as the esophagus in *Patient 4* showed non-negligible NTCP values. The exact values are listed in Table IV.4.

Patient 4 showed NTCP values in the esophagus of 1.9 %, 2.7 % and 2.3 % for analytical PBs, MCsquare and TOPAS, respectively, with the highest EUDs in all patients of 53 Gy to 54 Gy. In lung, the NTCP was largest for PBs with up to 5.0 % in *Patient 1* and 3.7 %in *Patient 2* with much lower vaules for both MC engines in the range of approximately 1 % to 2 %.

Even for the very low neglected values, the lung tissue toxicity decreased consistently for most patients and modalities by approximately −22 % in the median (Fig. IV.53), only increasing for the analytical degradation for carbon ions using APM. This is reflected in the calculated EUDs that showed a consistent degradation of −3 % in the median. For OARs, values of the EUD and NTCP consistently increased for *Patient 1* and decreased for *Patient 3*. Overall, however, this behavior is inconsistent with a median difference of 0.0 %.

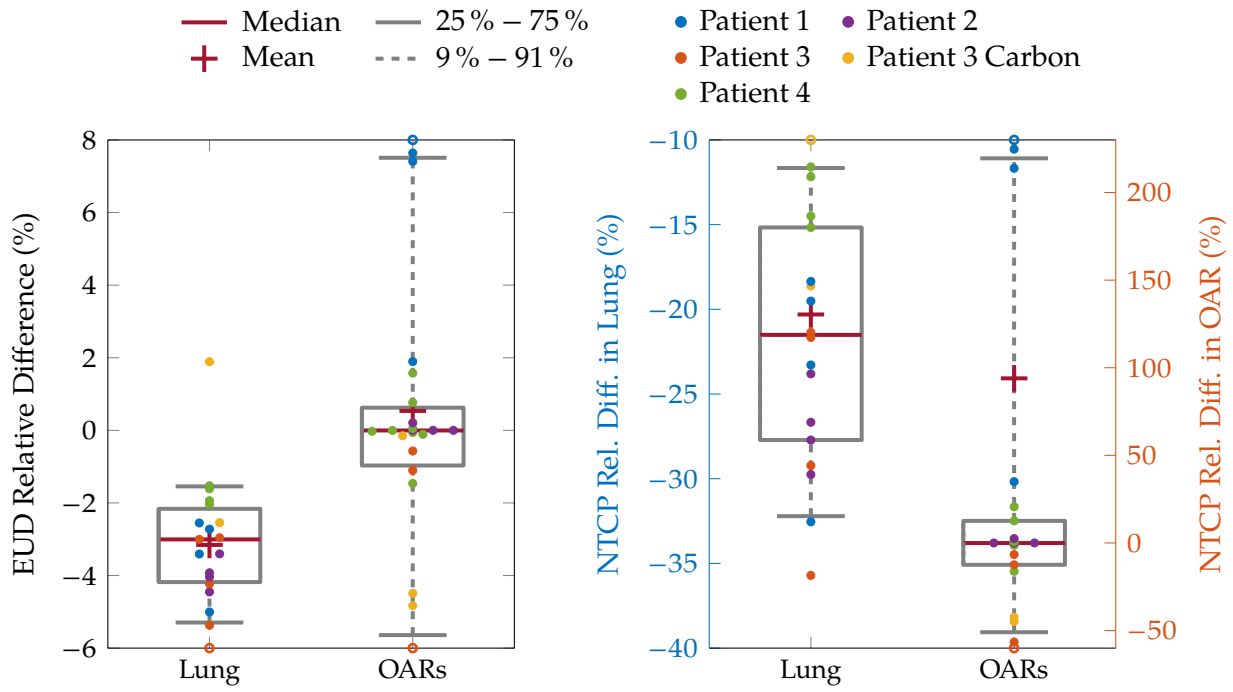

Figure IV.53: Box plot of relative differences in the EUD and NTCP between degraded and homogeneous dose distributions for lung and OARs. For protons and carbon ions, constant RBE and LEM were used, respectively. Due to the limited data size, data points were overlaid using a scatter plot with jitter. Results for carbon ions are shown for reference, but are not included in the box plot.

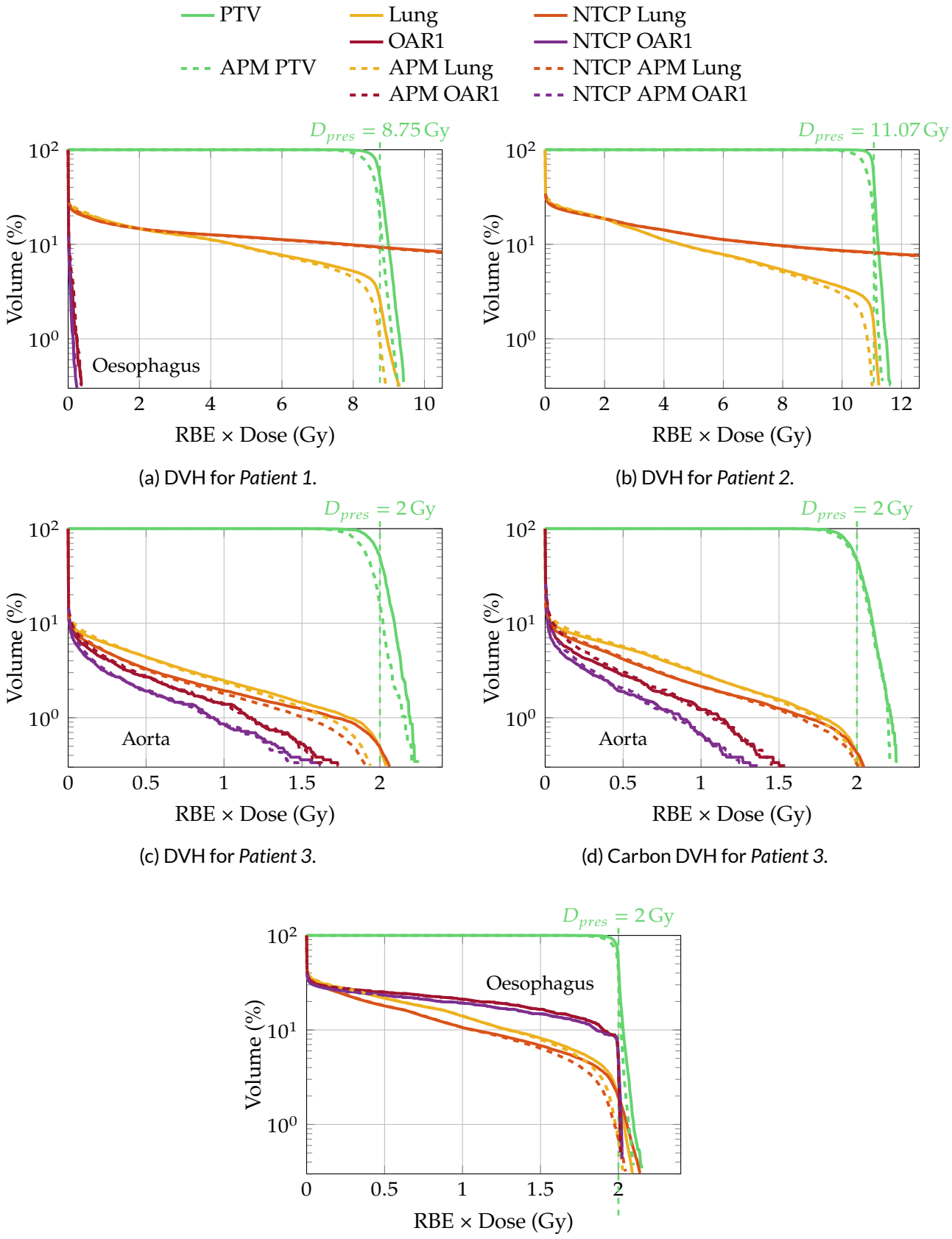

(a) DVH for *Patient 1*.

(b) DVH for *Patient 2*.

(c) DVH for *Patient 3*.

(d) Carbon DVH for *Patient 3*.

(e) DVH for *Patient 4*.

Figure IV.54: DVHs for all patients, calculated from constant RBE-weighted dose distributions. If data was available, OARs curves were recalculated using the Niemierko NTCP model.

Table IV.4: TCP and NTCP data (in %) calculated for the OARs and PTV for each patient and modality. For missing values, no NTCP model data or modality was available.

ID	OAR	PB	PB APM	PB Spl.	MC^2	MC^2 Spl.	TOPAS	TOP. Spl.
Patient 1	Lung	5.03	3.39	3.86	2.17	1.77	1.89	1.52
	Esophagus	$1.7{\cdot}10^{-18}$	$5.4{\cdot}10^{-18}$	$2.2{\cdot}10^{-18}$	$3{\cdot}10^{-26}$	$6{\cdot}10^{-25}$	$1{\cdot}10^{-25}$	$3{\cdot}10^{-25}$
	CAW[1]	-	-	-	-	-	-	-
	Heart	$9{\cdot}10^{-38}$	$9{\cdot}10^{-38}$	$9{\cdot}10^{-38}$	$9{\cdot}10^{-38}$	$9{\cdot}10^{-38}$	$9{\cdot}10^{-38}$	$9{\cdot}10^{-38}$
	PTV	100	100	100	100	100	100	100
Patient 2	Lung	3.66	2.57	2.69	2.07	1.58	1.83	1.32
	Heart	$9{\cdot}10^{-40}$	$9{\cdot}10^{-40}$	$9{\cdot}10^{-40}$	$9{\cdot}10^{-40}$	$9{\cdot}10^{-40}$	$9{\cdot}10^{-40}$	$9{\cdot}10^{-40}$
	CAW[1]	-	-	-	-	-	-	-
	CR[2]	-	-	-	-	-	-	-
	PTV	100	100	100	100	100	100	100
Patient 3	Lung	$3.1{\cdot}10^{-8}$	$2{\cdot}10^{-8}$	$2.2{\cdot}10^{-8}$	$1.7{\cdot}10^{-8}$	$1.3{\cdot}10^{-8}$	$1.5{\cdot}10^{-8}$	$1.2{\cdot}10^{-8}$
	CAW[1]	-	-	-	-	-	-	-
	Aorta	$4.7{\cdot}10^{-7}$	$1.8{\cdot}10^{-7}$	$2.1{\cdot}10^{-7}$	$7.3{\cdot}10^{-8}$	$6.4{\cdot}10^{-8}$	$4.4{\cdot}10^{-8}$	$4.1{\cdot}10^{-8}$
	Heart	$5{\cdot}10^{-39}$	$5{\cdot}10^{-39}$	$5{\cdot}10^{-39}$	$5{\cdot}10^{-39}$	$5{\cdot}10^{-39}$	$5{\cdot}10^{-39}$	$5{\cdot}10^{-39}$
	Esophagus	$1{\cdot}10^{-54}$	$1{\cdot}10^{-54}$	$1{\cdot}10^{-54}$	$1{\cdot}10^{-54}$	$1{\cdot}10^{-54}$	$1{\cdot}10^{-54}$	$1{\cdot}10^{-54}$
	PTV	99.91	99.86	99.87	99.87	99.77	99.84	99.77
Patient 4	Lung	$1.1{\cdot}10^{-2}$	$9.6{\cdot}10^{-3}$	$9.9{\cdot}10^{-3}$	$1.1{\cdot}10^{-2}$	$9.7{\cdot}10^{-3}$	$1.0{\cdot}10^{-2}$	$8.9{\cdot}10^{-3}$
	Heart	$1{\cdot}10^{-22}$	$1{\cdot}10^{-22}$	$1{\cdot}10^{-22}$	$1{\cdot}10^{-22}$	$1{\cdot}10^{-22}$	$2{\cdot}10^{-22}$	$2{\cdot}10^{-22}$
	Esophagus	1.87	1.87	1.87	2.68	2.70	2.30	2.59
	PTV	99.92	99.91	99.91	99.92	99.91	99.92	99.91
Patient 3 carbon	Lung	$9.7{\cdot}10^{-8}$	$1.1{\cdot}10^{-7}$	$7.9{\cdot}10^{-8}$	-	-	$2.9{\cdot}10^{-8}$	$1.6{\cdot}10^{-8}$
	CAW[1]	-	-	-	-	-	-	-
	Aorta	$9.4{\cdot}10^{-8}$	$5.2{\cdot}10^{-8}$	$5.4{\cdot}10^{-8}$	-	-	$3.2{\cdot}10^{-8}$	$3.1{\cdot}10^{-8}$
	Heart	$8{\cdot}10^{-40}$	$8{\cdot}10^{-40}$	$8{\cdot}10^{-40}$	-	-	$9{\cdot}10^{-40}$	$1{\cdot}10^{-39}$
	Esophagus	$1{\cdot}10^{-55}$	$1{\cdot}10^{-55}$	$1{\cdot}10^{-55}$	-	-	$1{\cdot}10^{-55}$	$1{\cdot}10^{-55}$
	PTV	99.90	99.90	99.87	99.79	99.75	99.79	99.75

[1] CAW – Central AirWays.

[2] CR – Central Region.

V

Discussion

Ions such as protons and carbon ions possess unique properties that make them highly effective for cancer treatment. They exhibit sharp depth dose profiles with a pronounced Bragg peak as well as increased radiobiological effectiveness (Allen et al. 2011; Byun et al. 2021; Durante et al. 2021). This peak allows for a confined, high dose to be delivered to the tumor with minimal collateral damage to healthy tissue and improved clinical outcome (Kim and Wu 2021; Kiseleva et al. 2022; Malouff et al. 2020; Qi et al. 2015). This precision, however, also means that even microscopically small range shifts can accumulate to significantly impact the conformity of the delivered dose (Byun et al. 2021).

Due to the complex nature of lung tissue with its highly localized density variations, accurate dose calculation is challenging (Pasciuti et al. 2011). Analytical PB algorithms are commonly used in treatment planning due to their computational efficiency, providing a useful first approximation of the dose distribution and enabling rapid adjustments during the initial stages of planning (Oelfke and Scholz 2006). However, PB algorithms struggle to accurately model the lateral and local density variations in lung tissue, often leading to inaccurate modeling of scattering effects, where MC algorithms result in improved treatment quality (Elcim et al. 2018; Grassberger et al. 2014; Yepes et al. 2018). This is particularly problematic in lung tumors, where these algorithms have been found to consistently overestimate the delivered dose by up to 46 % (Taylor et al. 2017). These inaccuracies occur even without considering the degradation effects caused by sub-CT-resolution structures.

Dose degradation can diminish some of the key benefits of particle therapy. Microscopic tissue inhomogeneities cause local changes in the WET, leading to a broadening of the Bragg peak. This broadening effect can result in a loss of dose conformity, causing under-dosage of the tumor and unwanted dose distal to the target (Sawakuchi et al. 2008; Urie et al. 1986). While MC simulations offer improved modeling of these effects compared to analytical PB algorithms, current treatment planning systems lack sufficient information about sub-CT-resolution structures to accurately predict these degradation effects. Additionally, despite the advancements and evolving use of MC in dose calculation (Jahnke et al. 2012; Lysakovski

et al. 2024; Perl et al. 2012; Schiavi et al. 2017; Souris et al. 2016), analytical algorithms remain essential in clinical practice due to their speed and utility in providing an overview of the dose distribution (Chen et al. 2014).
This thesis investigated the impact of particle dose degradation due to tissue inhomogeneities in lung cancer patients: theoretically, on simple geometries, and through analysis of patient treatment plans. This was done in two main parts: the validation of the MC interface and the subsequent implementation of degradation correction algorithms. Therefore, the findings will also be discussed based on these two major parts.

V.1 Validation of the Monte Carlo Interface

To assess the impact of dose degradation depending on ion type and to explore potential differences between analytical and MC-based algorithms, a comprehensive MC framework was needed. Since commercial systems can rarely be modified, the first step in this work was the implementation of this MC interface for the matRad treatment planning system and its validation against analytical PBs using both simple geometries and patient data. The interface integrates two MC engines, MCsquare and TOPAS, enabling the calculation of proton, helium, and carbon ion absorbed and RBE-weighted dose distributions within the matRad environment. In this section, the development process of the MC interface is discussed, with example calculations starting from single Bragg peaks to evaluate the accuracy of newly developed machine data sets, over SOBPs and extending to full lung patient plans Section IV.1.

V.1.1 Development and Characterization of Machine Data Sets

To ensure the best possible agreement between MC simulations and analytical PBs in homogeneous dose distributions, new generic machine data sets suitable for research purposes were required. This involved developing machine data sets for both protons and carbon ions based on fitted TOPAS simulations. These data sets were tested using single Bragg peaks simulated through the interface, resulting in very good agreement, despite using a stringent γ criterion. This is consistent with other publications comparing and commissioning MC codes, finding good agreement especially for simple geometries (Carrier et al. 2004; Deng et al. 2020; Huang et al. 2018; Newpower et al. 2019; Perl et al. 2012).

Lateral and Depth Dose Profiles. Overall, while generating longitudinal results consistent with TOPAS, MCsquare was found to show the largest difference in the lateral profile. This is likely due to MCsquare being optimized for a high computational speed, sacrificing detail in the interaction models compared to slower general purpose MC engines like TOPAS,

which was used to generate the dataset. Additionally, using the dataset, it is unsurprising that longitudinal and lateral profiles in water showed good agreement between matRad and TOPAS.
For carbon ions, however, small differences were observed in the peak dose for both absorbed and RBE-weighted dose for increasing particle energy. Generally, the lateral beam modeling for ion beams is highly complex and efforts have been made to improve upon the simple Gaussian modeling using a double Gaussian parameterization, which is also used in this work (Parodi et al. 2013). The lower dose calculated using PBs could therefore be attributed to a slightly incorrect lateral dose fit or an incorrect air/vacuum scattering before entering the phantom, since MC would typically experience larger scattering. For both proton and carbon ion data, the fitting and implementation of the lateral profiles were identified as the main source of error during the generation of the data.

Applied Kernel Resolution. The resolution of the stored machine data was reduced from a constant 0.1 mm simulation grid to a dynamic grid based on the position of the Bragg peak. This adjustment not only drastically reduced the data points, resulting in faster calculation times, but also smoothed variations in the low-dose regions without compromising the accuracy. This lead to a simpler, less error-prone APM fit and corresponding matRad calculations.

V.1.2 Comparison of Treatment Plans

This section discusses the calculated treatment plans for validation of the MC interface. This includes simple SOBPs on box phantom geometries (Section IV.1.2) and more complex patient cases (Section IV.1.3).

Spread-Out Bragg Peaks. The minimal variations observed for single Bragg peaks extend to SOBPs, with consistently high γ pass rates often close to or reaching 100 % for both protons and carbon ions. In the case of carbon ions, statistical dose variations within the target area were noted for the TOPAS dose, suggesting an insufficient number of simulated particles. Usually, however, the used 10^8 histories are deemed adequate for this geometry, especially considering the long computation times for carbon ions (Perl et al. 2012; Souris et al. 2016; Uyar and Günekbay 2023). For both ions, but especially for carbon ions, the SOBPs showed systematic underdosing of the target and overdosing distal to the target, with a less steep dose falloff. This could originate from the more realistic scattering employed for MC, consistent with the lateral uncertainties observed in the shown dose slices.

Prostate Phantom. For the prostate phantom, a notable underestimation of the proton dose by matRad's PB algorithm was observed when compared to MC dose distributions. There was, however, very good agreement between the two used MC engines. The differences predominantly occurred at the interfaces between regions of high and low dose, which could potentially lead to over- or underdosing depending on the specific location of the OARs. These findings were consistent with the results observed for SOBPs. For the non-lung patients, the larger local lateral differences, resulting slightly worse γ pass rates, may be caused by a different scattering in non-homogeneous tissues and interfaces. These interfaces are especially difficult to model with regular PB algorithms and are more accurately described using MC (Meder 2020; Schaffner et al. 1999).

Transition to RBE-weighted Dose Calculation. When examining variable RBE-weighted dose distributions, larger differences were found between the MC simulations and the analytical PB model, particularly beyond the tumor region and for MCsquare. This effect is particularly pronounced in lung tissue, where increased scattering could result in a reduced deposited dose or, more likely, substantial local LET differences. These would be consistent with the evaluations discussed in Section V.1.3. When comparing the different RBE models MCN and WED, both result in similar deviations compared to constant RBE. However, the differences between the models were small compared to the differences observed between the used modalities. This is consistent with other comparisons, where the different RBE models show consistent deviations (Giovannini et al. 2016; McNamara et al. 2020a). Generally, the prediction of parameters for the mentioned RBE models suffers from large uncertainties in the underlying data, as well as questionable relevance of *in vitro* experiments to real patients (McNamara et al. 2020a; McNamara et al. 2015; Paganetti 2014; Wedenberg et al. 2013). Therefore, it is challenging to derive valid general predictions for tumor control and toxicities.

Carbon Ions. In the liver case with carbon ions, the same general differences were observed compared to the proton plans, suggesting a systematic difference between MC and PB in those regions. Local dose differences within the target were particularly noticeable in the distal region, leading to substantial differences in the DVH. The lateral statistical variations are clearly visible in the γ-index distribution, particularly in the entrance channel, and could be attributed to insufficiently accurate modeling of the lateral beam profile. This is supported by independent absorbed dose calculations on the liver phantom using matRad and MC (Zhang et al. 2022). This could be improved by using a triple Gaussian or double Gaussian-logistic model (Inaniwa et al. 2014; Zhang et al. 2022). The lower γ pass rate for RBE-weighted dose distributions compared to absorbed dose suggest that the local differences are enhanced by a locally different RBE calculation.

V.1.3 LET-Based RBE Recalculation

In water, the RBE-weighted dose distributions calculated for PBs and in TOPAS were compared with separate RBE-weighted dose calculations based on the calculated LET distributions. For PBs in matRad, as expected based on the nature of the analytical algorithm, the differences were within numerical accuracy. Surprisingly, the two RBE-weighted dose distributions for TOPAS showed almost constant differences especially in the target. Because the RBE model is implemented in the same way using the same parameters, the differences could instead arise from a potentially different implementation of the RBE calculation from the LET, where TOPAS intrinsically uses Eq. II.17 while the recalculation in matRad is based on Eq. II.16.
The calculated LET depth profiles agreed well, especially considering the different methods of calculating LET. In this thesis, similar to other work (Tilly et al. 2005), the analytical PB dose calculation in matRad used interpolated LET data scored by TOPAS in a water phantom. Currently, there are multiple definitions for the LET but no clinical concensus (Hahn et al. 2022; Kalholm et al. 2021). TOPAS reports density normalized, dose averaged LET (Granville and Sawakuchi 2015), while MCsquare reports rSP-weighted LET (Deng et al. 2020). It was found that different methods lead to substantially different reported LETs, that could impact the calculation of RBE-weighted dose (Smith et al. 2021). However, various validations of the proton LET using TOPAS and MCsquare against other TPSs and measurements were done in water with overall good agreement (Deng et al. 2020; Polster et al. 2015; Wagenaar et al. 2020). The results in this thesis are consistent with these findings. However, MCsquare still reported an overall lower LET for high-LET regions compared to TOPAS and a higher LET for low-LET regions.
A recalculation test performed on a homogeneous lung phantom showed that the TOPAS LET could be adjusted to generate vastly different LET and therefore RBE-weighted dose within lung tissue. There, the direct scoring using density normalized LET showed RBE-weighted doses in lung similar to PBs, while a manual weighting with the rSP resulted in LET and RBE distributions similar to MCsquare. This could lead to a significant under- or overestimattion of the RBE-weighted dose in lung with the used variable RBE models. This is especially problematic if the planning target volume for lung tumors includes a large amount of healthy lung tissue (see *Patient 3*, Fig. IV.47), potentially leading to serious differences in the RBE-weighted dose.

Overall, the differences between the calculated LET distributions, as well as the corresponding LET values, are negligible in water. Potential benefits of calculating the RBE-weighted dose directly on the reported LET outside of the MC engine could include features such as the consideration of individual α/β per voxel without separate implementation in the respective MC engine. However, accurate LET and therefore RBE-weighted dose calculation

might be impacted in lung tissue and potentially other tissues where the LET calculation is complex. As a result, any recalculation of RBE based on LET, e.g. to utilize different RBE models, should be regarded as inconsistent in lung tissue, where LET scoring is most likely compromised by local density variations and increased scattering.

V.1.4 Postprocessing of the Particle Spot List

Originally, the removal of spots in treatment plans was investigated and implemented due to constraints in TOPAS. In some cases, distributing particle current to the spots based on the individual weights could lead to some spots with low weights to be automatically removed, without reoptimization. This lead to a substantial degradation of the plan quality, which is consistent with literature (Zhu et al. 2010). It is therefore imperative to reoptimize the plan after the postprocessing or include the removal of the spots in the optimization process.

The postprocessing applied in this work was chosen to use a conservative 3 % mean spot weight threshold, that removed spots below the weight limit between two optimizations of the complete plan. This approach was implemented as a first step, but there is potential for further development and implementations of this technique. The impact of the removal on beam spots on time consumption may vary depending on the specific MC engine used, as well as the extent of code optimizations. However, this technique also offers advantages in a clinical setting. As a result, similar systems are already implemented in current TPSs such as RayStation[1] (Janson et al. 2024).

V.2 Degradation Correction

This section discusses the development, implementation, and impact of degradation correction as covered in Section IV.2. As the second main focus of this thesis, degradation correction algorithms were implemented in the developed MC interface and subsequently explored and evaluated. This involved an analytical algorithm, which applied an analytical convolution to the depth dose profile subdivided with fitted Gaussian profiles (Winter et al. 2020), as well as a more general density sampling method for both PBs and MC based on Titt et al. (2015) and Baumann et al. (2017). Following a theoretical examination of the implementation, various degradation correction algorithms were tested on simple box phantom geometries, incorporating different complexities of lung tissue, as well as on a set of four representative lung cancer patients.

[1] RaySearch Laboratories, Stockholm, Sweden

V.2.1 Implementation of Degradation Correction

Implementation of Analytical and Numerical Convolution. The implementation of the analytical convolution model, while being certainly more precise than a numerical convolution, relies on pre-fitted APM depth dose kernels, which is fast during dose calculation, but introduces an additional error source, that increases with the particle energy (see Section III.2.3.1). The uncertainty introduced by fitting multiple Gaussians then propagates through to the degraded Bragg peak. Wieser et al. (2017a) reported 0.25 % mean difference for αD and 0.06 % for $\sqrt{\beta} D$ of the fit relative to the reference data. The differences measured in this thesis are in good agreement with these values, the fits could even be improved for αD. However, it has to be noted that pre-fitted data was used for inital fit parameters, so a "new" fit could lead to larger relative differences. It should be noted, however, that pre-fitted data was used for the initial fit parameters, which means an independent fit may lead to larger relative differences.

Depending on the used modulation power, the differences of analytical and numerical convolution relative to the homogeneous dose were in a similar range compared to the differences introduced by the APM fit routine. This suggests that it may not always be necessary to invest in the preparation of APM compatible data sets. In contrast, degradation correction based on numerical convolution does not require prefitted data and was tested with similar, if not faster, runtimes, making it a practical choice in many scenarios. However, these considerations are only for degradation, since the APM framework may already be in use for other implementations of uncertainties and robust optimization (Bangert et al. 2013).

Binomial Voxel Sampling Technique. The direct binomial sampling is a simple model that can utilize different local voxel densities and modulation powers on the fly. Multiple approaches have been developed based on the assumption of a binomially distributed radiological depth made by Titt et al. (2015) (Baumann et al. 2017; Winter et al. 2020). However the binomial sampling directly represents this proposition. The discrete binomial distribution was approximated using a continuous beta distribution that preserves the intrinsic properties of the binomial distribution.

This results in a generalized, simple and easy to implement voxel sampling model that can be employed for dose calculation using both PBs and MC. In contrast, the rather artificial Poisson distribution used in Baumann et al. (2017) requires separate optimization for each specific combination of modulation power and average lung voxel density.

The equivalence of the developed beta sampling method with the convolution-based approach was demonstrated on manual calculations using the machine data. A comparison with the convolution method showed small differences in the range of 1 % to 2 % behind the initial drop of the Bragg peak. It was found that the sampling being done solely on the depth dose ($L * \text{Sampling}(Z)$) compared to sampling of the total dose ($\text{Sampling}(L * Z)$) lead

to visually indistinguishable results. Additionally, the sampling on the total dose leads to a systematic pattern in the resulting relative differences compared to the depth sampling. However, these differences likely originated from uncertainties in the scored depth dose profiles for the generation of the machine data set and fitting of the lateral profiles.

Oblique Angle Correction. Interestingly, implementing the oblique angle correction resulted in much better agreement with the analytical APM calculation. The average distance traveled through a voxel depends on the incident angle. This is implemented in the convolution by means of ray tracing to measure the WET for each affected beam. In the sampling method, the image cube itself is modulated, independent of the incident beam. However, this correction was not applied in this thesis due to the complexity of the integration in MC engines, where individual image cubes would have to be used for each beam in addition to the different sampling cubes. The lack of oblique angle correction likely leads to an underestimation of the degradation effects using the sampling method. Consequently, if sampling techniques continue to be used, it will be important to include the mentioned correction for oblique angles, particularly for patients with multiple beams.

Validity of the Used Modulation Power. The degradation effects observed in phantoms and patients used in this thesis are likely overestimated due to the use of a modulation power of 800 µm, which is considered a worst-case scenario in the literature (Baumann et al. 2017; Burg et al. 2021; Flatten et al. 2019). Even with this extreme value, the observed degradation was minimal. Newer measurements revealed that modulation power values are typically in the range of 100 µm to 250 µm (Burg et al. 2021). The large uncertainty of this value, combined with its importance in current degradation correction algorithms, suggests that the impact of degradation calculated in this thesis may overestimate the actual effect in clinical reality, where the impact is expected to be much smaller.

Number of Histories per Sample. The evaluation of 100 samples and 500 samples for 10^8 and 10^9 total histories revealed substantial differences in the γ pass rate for TOPAS. Increasing the number of density samples without adjusting the MC histories did not result in better γ pass rates. However, increasing the histories to 10^9 resulted in overall smaller mean dose differences in both MC engines, closer to the ones calculated for PBs, as well as significantly better γ pass rate for TOPAS. It can be concluded that the accuracy of the resulting dose distributions is mainly dependent on the histories per density sample. For more samples, the histories have to be increased accordingly to avoid loosing beam spots due to the lower particle count per sample.
Especially for TOPAS, performing the simulations using more histories per sample would be beneficial to the accuracy of the sampled dose distributions. However, mainly due to hardware constraints, 100 samples with 10^8 total histories were chosen for patients and

also SOBP for consistency. These hardware constraints include the computation time in TOPAS, posing an even bigger challenge for carbon ions, as well as simple hard drive space management. Since each sample contains a separate image cube and outputs multiple result matrices, the server disk space needed for a calculated patient with 100 samples was already approximately 50 GB to 60 GB (MCsquare and TOPAS combined). For an increased number of samples, options for direct postprocessing, reducing the output data or incremental compression could be investiated.

V.2.2 Degradation on Box Phantom Geometries

Influence of WEPL and Modulation Power. To gauge and quantify the expected impact of degradation on simple geometries, calculations were conducted on a homogeneous lung phantom for varying modulation power and WEPL within realistic ranges. The calculations included analytical convolution and density sampling for PBs, MCsquare and TOPAS.
The degradation showed the expected behavior, linearly dependent on P_{mod} and lung WEPL and resulted in relative target mean dose differences of approximately −1 % to −1.5 %. This is largely consistent with the degradation effects reported in literature with dose differences of −2 % for SOBPs (Flatten et al. 2019) and −0.1 % to −1.6 % for patients (Winter et al. 2020). Baumann et al. (2019) also reported a linear relationship with P_{mod} and depth of the tumor in lung with the largest values of −2.1 % mean target dose difference for $P_{\mathrm{mod}} = 800\,\mu\mathrm{m}$ and $\mathrm{WEPL}_{lung} = 6.2\,\mathrm{cm}$. However, Flatten et al. (2019) also reported SOBP target dose differences as large as −14 % for small tumor sizes, that could not observed here.

Sampled Dose in Lung Tissue. The evaluation of pencil beams at different modulation powers and CT resolutions revealed distinct differences in TOPAS, particularly within lung tissue and only for specific combinations of modulation power and voxel size. Surprisingly, this was not observed in the other modalities. In cases where the parameter n – the number of substructures – in the binomial model approached 1, the binomial distribution used for density sampling showed a strong binarization, with many voxels being classified as "air". The dose differences in lung tissue for TOPAS were dependent on the extent of this binarization, potentially due to how TOPAS handles dose scoring in very-low-density regions. For certain extreme cases – specific combinations of voxel size and P_{mod} – the binomial model was found to break down as n becomes smaller than 1. This, however, only occurs for very large modulation powers or small voxel sizes of 1 mm, both of which are likely not realistic scenarios. It is also important to note that using very small voxel sizes approaching the resolution limit of the microstructures, defeating the purpose of the voxel sampling method. Additionally, the lung dose in MCsquare showed the already observed large underestimation, likely due to incorrectly scored LET. Within lung, the averaged dose profiles showed a decreasing dose with depth, whereas matRad displayed an increasing dose. For scenarios

with $P_{\mathrm{mod}} = 800\,\mu\mathrm{m}$ and 3 mm voxel size, central profiles and IDD were replotted and compared. The IDD showed the expected increasing dose, suggesting that scattering within lung tissue is significantly increased for both MC engines, resulting in a lower dose with depth. These differences in scattering also contributed to variations in the Bragg peaks between the three modalities, which were not apparent in the IDD.

Spread-Out Bragg Peaks. For simulated degraded SOBPs, the shape and size of the degradation was consistent with the previously performed simulations and showed the expected, distinct under- and overdosage observed at the distal edge. TOPAS sampling revealed variations in the dose distribution across the entire SOBP, which, as already discussed above, is likely due to sampling differences in TOPAS compared to other modalities. However, the comparison of quality indicators showed that the decrease in mean dose to the target due to degradation was consistent across all modalities.
The variable RBE-weighted dose profiles showed a sharp increase in RBE towards the end of the Bragg peak, corresponding with increasing LET. Since the degradation effects are the strongest in the same area, the sharp dose increase was smoothed and flattened. This was consistent with calculations of conformity and homogeneity indices, both of which indicated a more confined and homogeneous dose distribution for RBE-weighted, degradation-corrected treatment plans. This trend was also evident in the calculated quality indicators, where the RBE-weighted maximum dose D_5 decreased significantly for degraded doses in all modalities.
In the lung phantom with real lung, TOPAS sampling again showed distinct variations across the whole phantom with more pronounced differences within the lung. This aligns with the earlier findings of similar variations in the lung TOPAS dose. For carbon ions, the differences due to degradation correction were visually smaller. The DVH indicated that the homogeneous TOPAS dose in some regions was close to the degraded dose distributions using PBs, with degradation correction adding to this effect.
Similarly to protons, TOPAS exhibited substantial variations in dose across the entire phantom. This confirms that the density sampling in TOPAS would likely benefit from using a larger number of samples, that would come at the expense of a significant increase in memory, computation time, or beamlets being lost due to the reduced number of particles per sample (see Section V.2.1).

V.2.3 Degradation for Patient Treatment Plans

Four lung cancer patients were evaluated, each selected to represent a range of tumor sizes and lung WEPLs. The γ pass rates for degradation correction were consistent across all modalities, with TOPAS again showing larger lateral variations parallel to the beam direction. For *Patient 3*, that had the smallest tumor size and the lowest range of used energies, the largest differences were observed, resulting in the lowest pass rates among all patients. The large target margins well within the lung added significant uncertainty around the tumor, leading to significant differences and poor pass rates for the PTV. The results for carbon ions were consistent with those for protons in *Patient 3*, with similarly small pass rates, that further decreased for the RBE-weighted dose. However, lower pass rates were already observed between homogeneous PB and TOPAS for both absorbed and RBE-weighted doses. Additionally, these differences could have stemmed from the exclusion of the PTV in the sampling process, especially apparent for *Patient 3*.
In contrast, the highest pass rates were found within the target for *Patient 4*. Overall, the differences were more pronounced for patients than compared to the SOBPs, where no consistent trend was observed across the different phantom models. However, the lowest pass rates were consistently for TOPAS sampling.
The mean dose difference across patients showed consistent results with the largest differences observed in *Patient 3* and the smallest for *Patient 4*. Interestingly, the mean dose to the OARs did not follow the same trend, with *Patient 1* showing a higher mean dose difference on average. For D_5 and D_{95}, no consistent patient-dependent trends were observed, except for a significant increase in the minimum dose delivered to the lung in *Patient 3*, coinciding with a reduced mean dose to the target.

Conformity and Homogeneity Index. For SOBPs, degradation correction consistently improved the target dose conformity and homogeneity. However, even though this trend is also visible for patients, this improvement was only observed in about half of the calculated dose distributions and could not be attributed to specific patient cases. MCsquare and TOPAS sampling showed the largest decrease in conformity with degradation, a trend that persisted for RBE-weighted doses. In contrast, the less severe differences in conformity could be attributed to analytical PBs, both with convolution and sampling, with a consistent increase in target conformity when switching to RBE-weighted doses. Despite the development of multiple RBE models, uncertainty also remains regarding the exact extent of the RBE, which could lead to a different outcome.

Comparison with Literature. For the calculated patient plans, the effects of the degradation were as expected and followed the general relationship – increasing with depth and decreasing with tumor size – already reported by Baumann et al. (2019). The findings for SOBPs are consistent with reported results in other conducted experiments with a visible degradation of the DVH, decreased dose coverage D_{95} or D_{98} and increased dose to OARs (Baumann et al. 2019; Flatten et al. 2019; Ringbæk et al. 2020).
Flatten et al. (2019) found an underestimation of the mean dose of up to −14 % for the worst-case modulation power $P_{\mathrm{mod}} = 800\,\mu\mathrm{m}$, but more realistic setups resulted in an underestimation of only −2 %. However, even using the same worst-case modulation power throughout this thesis, the large observed dose differences could not be replicated.
Generally, the results for patients are consistent with previously conducted experiments using the same patient data sets (Winter et al. 2020). They used a modulation power of $P_{\mathrm{mod}} = 256\,\mu\mathrm{m}$, which resulted in much lower mean relative differences mostly below 1 %. The dose differences in the range of approximately −1 % to −4 % in the PTV together with mean γ pass rates of about 90 %. Additionally, a consistent increase in HI and decrease in dose coverage was observed with degradation, in agreement with findings from the literature (Ringbæk et al. 2020). The reported increased degradation effect for carbon ions (Ringbæk et al. 2020) could be confirmed, however based on limited carbon data in this thesis. With emerging new MC codes for carbon ions (Lysakovski et al. 2024; Schiavi et al. 2017), this could become increasingly relevant. Next to the drawbacks, dose degradation might improve dose conformity and NTCP.
However, the mentioned differences are within the range of previously discussed error sources of the APM routine as well as differences between homogeneous dose distributions solely based on modality. Even the homogeneous dose distributions in MCsquare and TOPAS already exhibited a typical degradation behavior even without modeled degradation effects (Sections IV.2.2.3 and IV.2.3). Other authors concluded, that the degradation effects could even be negligible (Baumann et al. 2019; Flatten et al. 2019; Ringbæk et al. 2020; Winter et al. 2020), especially compared to other uncertainties such as organ and respiratory motion (De Ruysscher et al. 2015; Engelsman et al. 2013). However, with increasing efforts in evaluating and compensating for motion effects on dose (Grassberger et al. 2015; van Herk 2004; Steinsberger et al. 2021), it could be beneficial for some patients (*Patient 3* in this case) to consider the degradation effects in a clinical setting.

NTCP Models. Most calculated NTCP values in the OARs were below 10^{-6} % with only a limited fraction within the low percentage range (2 % to 11 %). With degradation, the NTCP and EUD showed consistently negative changes within lung tissue, indicating reduced toxicity. These findings contradict the assumption that an underdosage of the target dose would mean overdosing OARs, particularly the surrounding lung.
It also remains questionable if this is a significant trend considering the very limited data of non-negligible values and the large uncertainty associated with the generation of these values: Since the NTCP parameters are only valid for lung patients with fraction dose of 2 Gy, the necessary calculation of EQD largely favors high NTCP values for large fraction doses, which is reflected in the larger values observed for *Patient 1* and *Patient 2* with fraction doses of 8.75 Gy/fx and 11.07 Gy/fx. The large values observed for the esophagus NTCP of *Patient 4* can be explained by the almost full enclosure with the PTV. However, this raises the question of why the NTCP is not larger, especially for a serial organ with a reported total threshold dose of 19.5 Gy/5fx, that is substantially exceeded (Benedict et al. 2010). McNamara et al. (2020b) used different NTCP models and reported values up to 60 % for esophagus toxicity and also, with up to 45 % for grade 2 radiation pneumonitis, much larger lung values as observed here. Another source of error is the assumption of a constant healthy tissue α/β of 2 Gy, the assumption of heart parameters for the aorta and the assumption of a tumor TCD_{50} equal to the lung TD_{50}. A more realistic lung α/β of 1.3 Gy (Scheenstra et al. 2014) would increase the NTCP, albeit not by a large margin. Additionally, even though an α/β of 10 Gy was assumed for the TCP model, the dose calculation is still performed with a constant 2 Gy over the whole CT cube. As a result, the large amount of uncertainties likely prevents a confident evaluation of TCP and NTCP.

V.3 Outlook

The developed MC framework provides a robust foundation for exploring new methodologies and facilitating a variety of future research projects. This has already been proven invaluable as the framework has seen extensive use within the department and is being further built upon.
This section discussed the methodology and results of degradation correction, highlighting its potential and, though limited, benefit for future patients. While the immediate impact of degradation correction may remain questionable at this point, its importance could grow in future applications. For instance, since it is suspected that degradation may have a lesser impact compared to motion effects, a comprehensive comparison between the two effects should be a key area for future research. As dose calculation methods become faster and more accurate, it will be increasingly important to investigate and potentially incorporate additional corrections such as degradation into standard practice.

V.4 Conclusion

This thesis reported on the development of an Monte Carlo (MC) interface within the treatment planning system matRad, open for the research community. It allows the simulation of MC dose distributions in conjunction with already implemented research tools and projects, as well as for future research. The developed generic machine data sets for protons and carbon ions are optimized for an optimal agreement in simple water geometries and permit to focus on changes arising from differences in geometry, the currently studied effect, or the chosen algorithms.

The implementation within the scope of this thesis specializes on lung dose calculation by introducing and evaluating a microstructure correction for lung tissue. A generalized approach was used, that allows for the calculation of degraded dose distributions independent of the used dose calculation algorithm, usable in both Pencil Beams (PBs) and MC methods. A simple system was implemented using density sampling based on a beta distribution, demonstrated to lead to effects compatible with analytical degradation correction and literature. It was shown that these effects were consistently present across different dose calculation modalities, adding to the typical differences in dose calculation quality and accuracy between PBs and MC.

The dosimetric impact of the degradation on patient treatment plans was consistent but limited, increasing with the use of carbon ions. It is questionable, if the effort of researching and implementing this effect is necessary in an uncertain anatomy, especially considering that the current accuracy of MC simulations might already be sufficient for most clinical scenarios, where problems such as motion mitigation, beam delivery and target margins might overshadow the effects of degradation. It can be concluded that, considering the current uncertainties, error sources and standard clinical ressources, the degradation effects can most likely not implemented in a meaningful way. However, since the results for carbon ions indicate a more severe degradation, future studies should be conducted using the newly emerging, fast MC engines for carbon ions. Additionally, more studies could be carriess out regarding the microstructure, quantifying the modulation power and dependencies of the degradation in more detail, as well as integrate a degradation correction in a treatment planning workflow.

VI

Summary

Lung cancer remains one of the leading causes of cancer-related mortality worldwide. Despite significant advancements in treatment options, lung cancer continues to present unique challenges, particularly in the context of particle therapy, including proton and carbon ion therapy. In addition to factors such as respiratory motion and the resulting dose calculation inaccuracies, tissue inhomogeneities can cause degradation of the treatment beam, potentially diminishing some of the advantages that particle therapy has over traditional X-rays. This thesis aims to quantify the impact of beam degradation on dose distributions for both analytical Pencil Beams (PBs) and Monte Carlo (MC) simulations, exploring how this degradation influences dose accuracy, conformity, and overall relevance compared to other error sources and uncertainties. The central question to be answered is whether this degradation is significant and whether it has the same impact on analytical PBs compared to MC simulations, particularly in the context of Relative Biological Effectiveness (RBE)-weighted dose calculation. To address these questions, this thesis developed a dose calculation module for the inclusion of dose degradation in both analytical and MC treatment plans within the open-source toolkit matRad with a specific focus on proton and carbon ion therapy for lung cancer treatment.

A MC interface was developed for the matRad toolkit as part of this thesis, originally designed to test and assess the impact of degradation effects on more realistic and accurate MC simulations. Dose distributions calculated through the interface were first validated on homogeneous water geometries with newly developed generic machine data sets based on MC simulations, that showed near-perfect agreement between MC engines and analytical PBs. This allows to focus on changes arising from differences in geometry, the currently studied effect, or the chosen algorithms. Due to its versatility and modular setup, it can not only be used for investigations in degradation correction, but it allows for applications in various research projects and has already seen extensive use within the department.

For analytical PBs, the existing dose degradation implementation was refined for RBE-weighted dose calculations for protons and carbon ions. A universal implementation of

degradation correction, independent of the dose calculation algorithm, was realized through a density sampling model utilizing a simple beta distribution. The integration of these degradation models was explored and tested on increasingly complex geometries, starting from simple lung box phantoms and progressing to patient treatment plans. The degradation effects were consistent between carbon ions and protons, and in some patient cases, degradation effects for variable RBE-weighted proton doses were even able to improve dose conformity and homogeneity. The observed degradation effects on dose accuracy increased for more complex scenarios, but were overall minimal, even considering the worst-case modulation power. Potentially significant increases in the dose to Organs At Risk (OARs) was noted, that did not lead to a substantial increase in Normal Tissue Complication Probability (NTCP). However, in certain cases, the impact of dose degradation can be significant, particularly when added on top of the already degraded MC simulations. It was found that other error sources, such as organ motion and comparison with more accurate MC simulations, most likely overshadow the impact of degradation effects. Evaluation of this aspect should certainly be part of future work. Additionally, the variability in results was found to depend strongly on patient-specific factors such as tumor size and location within the lung. While for larger tumors or tumors with minimal lung tisse in the beam path, degradation effects may indeed be negligible, for small tumors located deep within lung tissue, the impact can be significant, particularly in cases involving carbon ions.

In conclusion, this thesis presents a comprehensive framework for dose calculation in intensity-modulated lung cancer particle therapy through the integration of a MC interface for matRad. This enables the calculation of degraded absorbed and RBE-weighted dose distributions for both protons and carbon ions, providing a valuable tool for advancing the accuracy and effectiveness of lung cancer treatment.

VII

Zusammenfassung

Lungenkrebs ist eine der Hauptursachen für krebsbedingte Sterblichkeit weltweit. Trotz bedeutender Fortschritte in den Behandlungsmöglichkeiten, stellt Lungenkrebs weiterhin schwierige Herausforderungen besonders an die Partikeltherapie. Neben Faktoren wie Atembewegungen und den daraus resultierenden Ungenauigkeiten in der Dosisberechnung können Gewebeinhomogenitäten zu einer Degradation (”Verwaschung”) des Behandlungsstrahls führen, was möglicherweise einigen der eigentlichen Vorteile der Partikeltherapie gegenüber traditionellen Röntgenstrahlen entgegenwirkt. Diese Arbeit zielt darauf ab, den Einfluss der Strahldegradation auf die Dosisverteilung sowohl für analytische Nadelstrahlen als auch für Monte Carlo (MC)-Simulationen zu quantifizieren. Dabei wird untersucht, wie die Degradation die Genauigkeit der Dosisverteilung, die Konformität und die allgemeine Relevanz im Vergleich zu anderen Fehlerquellen und Unsicherheiten beeinflusst. Die zentrale Fragestellung war, ob die Degradation einen signifikanten Einfluss hat und ob der Einfluss auf analytische Nadelstrahlen wie auf MC-Simulationen gleich ist, insbesondere im Kontext der Relative Biologische Wirksamkeit (RBW)-gewichteten Dosis. Dafür wurde im Rahmen dieser Arbeit ein Dosisberechnungsmodul zur Berücksichtigung der Dosisdegradation sowohl in analytischen als auch in MC-Bestrahlungsplänen innerhalb des Open-Source-Toolkits matRad entwickelt, mit einem speziellen Fokus auf die Protonen- und Kohlenstoffionentherapie für die Behandlung von Lungenkrebs.

Die durch das Interface berechneten Dosisverteilungen wurden zunächst an homogenen Wasserphantomen mit neu entwickelten generischen Maschinen-Datensätzen validiert.Dieses Proof-of-Concept für sehr einfache Geometrien zeigte eine nahezu perfekte Übereinstimmung zwischen den MC-Simulationen und analytischen Nadelstrahlen. Damit ist es möglich, die Effekte durch unterschiedliche Geometrie, den zu beobachtenden Effekt, oder den ausgewählten Algorithmus, einzugrenzen. Aufgrund seiner Vielseitigkeit und modularen Struktur kann das Interface nicht nur für Untersuchungen zur Degradationskorrektur eingesetzt werden, sondern ermöglicht Anwendungen in verschiedenen Forschungsprojekten und hat bereits umfangreiche Nutzung innerhalb der Abteilung erfahren.

Für analytische Nadelstrahlen wurde die bestehende Implementierung der Dosisdegradation weiterentwickelt und auf RBW-gewichtete Dosis für Protonen und Kohlenstoffionen übertragen. Eine universelle Implementierung der Degradation für sowohl Nadelstrahlen als auch MC-Simulationen wurde durch ein Dichtesampling-Modell, basierend auf einer Beta Verteilung, realisiert. Die Integration dieser Degradationsmodelle wurde auf zunehmend komplexeren Geometrien untersucht und getestet, angefangen bei einfachen Lungen-Phantomen bis hin zu Patientenbestrahlungsplänen. Ähnliche Effekte für Kohlenstoffionen und Protonen wurden gemesssen, und in einigen Patientenfällen konnten Degradationseffekte für variable RBW-gewichtete Protonendosen sogar die Dosis-Konformität und Homogenität verbessern. Die untersuchten Degradationseffekte wurden größer für zunehmend komplexere Geometrien, aber haben in den meisten Fällen begrenzten Einfluss auf die Dosisverteilungen, selbst für die verwendete worst-case Modulationsstärke (engl. "modulation power"). Darüber hinaus wurden potenziell signifikante Dosissteigerungen in den Organs At Risk (OARs) festgestellt, die aber nicht zu einem erheblichen Anstieg der Normal Tissue Complication Probability (NTCP) führten. Dennoch kann der Einfluss der Dosisdegradation in bestimmten Fällen erheblich sein, insbesondere wenn er zu den ohnehin schon stärker gestreuten MC-Dosisverteilungen hinzukommt. Obwohl festgestellt wurde, dass die Degradation einen messbaren Einfluss hat, ist dieser im Vergleich zu anderen Fehlerquellen wie Organbewegungen und im Vergleich von Nadelstrahlen mit den genaueren MC-Simulationen, relativ gering. Dieser Aspekt sollte jedoch definitiv in zukünftigen Arbeiten weiter untersucht werden, um seine Auswirkungen vollständig zu verstehen. Zusätzlich wurde festgestellt, dass die Variabilität der Ergebnisse stark von patientenspezifischen Faktoren wie der Tumorgröße und dem Ort des Tumors innerhalb der Lunge abhängt. Während bei größeren Tumoren, oder Tumoren mit minimalem Lungengewebe im Strahlengang, die Degradationseffekte möglicherweise vernachlässigbar sind, kann der Einfluss bei kleinen Tumoren, die tief in der Lunge liegen, erheblich sein, insbesondere für die Bestrahlung mit Kohlenstoffionen.
Zusammenfassend präsentiert diese Arbeit ein umfassendes System zur Dosisberechnung in der intensitätsmodulierten Partikeltherapie bei Lungenkrebs. Dies ermöglicht die Berechnung von Degradationseeffekten auf Verteilungen der absorbierten und RBW-gewichteten Dosis für Protonen und Kohlenstoffionen, und bietet so ein wertvolles Werkzeug zur Verbesserung der Genauigkeit und Wirksamkeit der Behandlung.

Bibliography

Ackermann, B. et al. (2020). *matRad*. Deutsches Krebsforschungszentrum. Heidelberg. DOI: 10.5281/zenodo.7107719. (Visited on 09/23/2022) (p. 31).

Agostinelli, S. et al. (2003). "Geant4—a Simulation Toolkit". In: *Nuclear Instruments and Methods in Physics Research Section A: Accelerators, Spectrometers, Detectors and Associated Equipment* 506.3, pp. 250–303. DOI: 10.1016/S0168-9002(03)01368-8 (p. 37).

Allen, C. et al. (2011). "Heavy Charged Particle Radiobiology: Using Enhanced Biological Effectiveness and Improved Beam Focusing to Advance Cancer Therapy". In: *Mutation Research/Fundamental and Molecular Mechanisms of Mutagenesis*. From Chemistry of DNA Damage to Repair and Biological Significance. Comprehending the Future 711.1, pp. 150–157. DOI: 10.1016/j.mrfmmm.2011.02.012 (p. 133).

Allison, J. et al. (2006). "Geant4 Developments and Applications". In: *IEEE Transactions on Nuclear Science* 53.1, pp. 270–278. DOI: 10.1109/TNS.2006.869826 (p. 37).

Allison, J. et al. (2016). "Recent Developments in Geant4". In: *Nuclear Instruments and Methods in Physics Research Section A: Accelerators, Spectrometers, Detectors and Associated Equipment* 835, pp. 186–225. DOI: 10.1016/j.nima.2016.06.125 (p. 37).

Atun, R. et al. (2015). "Expanding Global Access to Radiotherapy". In: *The Lancet. Oncology* 16.10, pp. 1153–1186. DOI: 10.1016/S1470-2045(15)00222-3 (p. 1).

Bangert, M. et al. (2013). "Analytical Probabilistic Modeling for Radiation Therapy Treatment Planning". In: *Physics in Medicine and Biology* 58.16, pp. 5401–5419. DOI: 10.1088/0031-9155/58/16/5401 (pp. 63, 64, 139).

Baumann, K.-S. et al. (2017). "An Efficient Method to Predict and Include Bragg Curve Degradation Due to Lung-Equivalent Materials in Monte Carlo Codes by Applying a Density Modulation". In: *Physics in Medicine and Biology* 62.10, pp. 3997–4016. DOI: 10.1088/1361-6560/aa641f (pp. 2, 57, 59, 104, 138–140).

Baumann, K.-S. et al. (2019). "Effects of the Bragg Peak Degradation Due to Lung Tissue in Proton Therapy of Lung Cancer Patients". In: *Radiation Oncology* 14.1. DOI: 10.1186/s13014-019-1375-0 (pp. 29, 141, 144).

Benedict, S. H. et al. (2010). "Stereotactic Body Radiation Therapy: The Report of AAPM Task Group 101". In: *Medical Physics* 37.8, pp. 4078–4101. DOI: 10.1118/1.3438081 (p. 145).

Bennan, A. B. A. (2021). "Combined Photon - Carbon Ion Radiotherapy Treatment Planning". PhD thesis. University of Heidelberg (p. 27).

Berger, M. et al. (2005). *ESTAR, PSTAR, and ASTAR: Computer Programs for Calculating Stopping-Power and Range Tables for Electrons, Protons, and Helium Ions (Version 1.2.3).* https://www.nist.gov/pml/stopping-power-range-tables-electrons-protons-and-helium-ions. (Visited on 04/28/2023) (pp. 4, 5, 38, 43, 44, 60).

Berger, M. J. (1993). *Penetration of Proton Beams through Water 1. Depth-Dose Distribution, Spectra and LET Distribution*. Tech. rep. NIST IR 5226. Gaithersburg, MD: National Institute of Standards and Technology, NIST IR 5226. DOI: 10.6028/NIST.IR.5226 (p. 45).

Bethe, H. (1930). "Zur Theorie Des Durchgangs Schneller Korpuskularstrahlen Durch Materie". In: *Annalen der Physik* 397.3, pp. 325–400. DOI: 10.1002/andp.19303970303 (p. 5).

Bloch, F. (1933). "Zur Bremsung Rasch Bewegter Teilchen Beim Durchgang Durch Materie". In: *Annalen der Physik* 408.3, pp. 285–320. DOI: 10.1002/andp.19334080303 (p. 5).

Bortfeld, T. (1997). "An Analytical Approximation of the Bragg Curve for Therapeutic Proton Beams". In: *Medical Physics* 24.12, pp. 2024–2033. DOI: 10.1118/1.598116 (pp. 6, 43, 45, 46).

Bortfeld, T. et al. (1993). "Decomposition of Pencil Beam Kernels for Fast Dose Calculations in Three-Dimensional Treatment Planning". In: *Medical Physics* 20.2, pp. 311–318. DOI: 10.1118/1.597070 (p. 23).

Brenner, D. J. (1993). "Dose, Volume, and Tumor-Control Predictions in Radiotherapy". In: *International Journal of Radiation Oncology, Biology, Physics* 26.1, pp. 171–179. DOI: 10.1016/0360-3016(93)90189-3 (p. 80).

Burg, J. M. et al. (2021). "Experimental Determination of Modulation Power of Lung Tissue for Particle Therapy". In: *Physics in Medicine & Biology* 66.24, p. 245018. DOI: 10.1088/1361-6560/ac3e0d (pp. 57, 104, 140).

Burman, C. et al. (1991). "Fitting of Normal Tissue Tolerance Data to an Analytic Function". In: *International Journal of Radiation Oncology, Biology, Physics* 21.1, pp. 123–135. DOI: 10.1016/0360-3016(91)90172-z (p. 26).

Burnet, N. G. et al. (2004). "Defining the Tumour and Target Volumes for Radiotherapy". In: *Cancer Imaging* 4.2, pp. 153–161. DOI: 10.1102/1470-7330.2004.0054 (p. 20).

Byun, H. K. et al. (2021). "Physical and Biological Characteristics of Particle Therapy for Oncologists". In: *Cancer Research and Treatment* 53.3, pp. 611–620. DOI: 10.4143/crt.2021.066 (pp. 6, 133).

Carabe-Fernandez, A. et al. (2007). "The Incorporation of the Concept of Minimum RBE (RbEmin) into the Linear-Quadratic Model and the Potential for Improved Radiobiological Analysis of High-LET Treatments". In: *International Journal of Radiation Biology* 83.1, pp. 27–39. DOI: 10.1080/09553000601087176 (p. 17).

Carlson, D. J. et al. (2008). "Combined Use of Monte Carlo DNA Damage Simulations and Deterministic Repair Models to Examine Putative Mechanisms of Cell Killing". In: *Radiation Research* 169.4, pp. 447–459. DOI: 10.1667/RR1046.1 (p. 16).

Carrier, J. F. et al. (2004). "Validation of GEANT4, an Object-Oriented Monte Carlo Toolkit, for Simulations in Medical Physics". In: *Medical Physics* 31.3, pp. 484–492. DOI: 10.1118/1.1644532 (p. 134).

Chen, W.-Z. et al. (2014). "Impact of Dose Calculation Algorithm on Radiation Therapy". In: *World Journal of Radiology* 6.11, pp. 874–880 (p. 134).

Cho, B. C. J. et al. (2002). "The Effect of Set-up Uncertainties, Contour Changes, and Tissue Inhomogeneities on Target Dose-Volume Histograms". In: *Medical Physics* 29.10, pp. 2305–2318. DOI: 10.1118/1.1508800 (p. 29).

Cole, A. J. et al. (2014). "Motion Management for Radical Radiotherapy in Non-small Cell Lung Cancer". In: *Clinical Oncology* 26.2, pp. 67–80. DOI: 10.1016/j.clon.2013.11.001 (p. 29).

Dal Bello, R. (2017). "Degradation of Proton and Carbon Bragg Peaks Due to Density Inhomogeneities". MA thesis. Heidelberg University. DOI: 10.11588/heidok.00022822 (pp. 55, 59).

De Ruysscher, D. et al. (2015). "Tumour Movement in Proton Therapy: Solutions and Remaining Questions: A Review". In: *Cancers* 7.3, pp. 1143–1153. DOI: 10.3390/cancers7030829 (p. 144).

Deng, W. et al. (2020). "Technical Note: Integrating an Open Source Monte Carlo Code "MCsquare" for Clinical Use in Intensity-Modulated Proton Therapy". In: *Medical Physics* 47.6, pp. 2558–2574. DOI: 10.1002/mp.14125 (pp. 50, 134, 137).

Durante, M. et al. (2021). "Physics and Biomedical Challenges of Cancer Therapy with Accelerated Heavy Ions". In: *Nature reviews. Physics* 3.12, pp. 777–790. DOI: 10.1038/s42254-021-00368-5 (p. 133).

Elcim, Y. et al. (2018). "Dosimetric Comparison of Pencil Beam and Monte Carlo Algorithms in Conformal Lung Radiotherapy". In: *Journal of Applied Clinical Medical Physics* 19.5. DOI: 10.1002/acm2.12426 (p. 133).

Elsässer, T. and M. Scholz (2007). "Cluster Effects within the Local Effect Model". In: *Radiation Research* 167.3, pp. 319–329. DOI: 10.1667/RR0467.1 (p. 18).

Elsässer, T. et al. (2008). "Accuracy of the Local Effect Model for the Prediction of Biologic Effects of Carbon Ion Beams In Vitro and In Vivo". In: *International Journal of Radiation Oncology*Biology*Physics* 71.3, pp. 866–872. DOI: 10.1016/j.ijrobp.2008.02.037 (p. 18).

Emami, B. et al. (1991). "Tolerance of Normal Tissue to Therapeutic Irradiation". In: *International Journal of Radiation Oncology*Biology*Physics* 21.1, pp. 109–122. DOI: 10.1016/0360-3016(91)90171-Y (p. 80).

Engelsman, M. et al. (2013). "Physics Controversies in Proton Therapy". In: *Seminars in Radiation Oncology*. Controversies in Proton Therapy 23.2, pp. 88–96. DOI: 10.1016/j.semradonc.2012.11.003 (p. 144).

España, S. and H. Paganetti (2011). "Uncertainties in Planned Dose Due to the Limited Voxel Size of the Planning CT When Treating Lung Tumors with Proton Therapy". In: *Physics in Medicine & Biology* 56.13, p. 3843. DOI: 10.1088/0031-9155/56/13/007 (pp. 55, 58).

Faddegon, B. et al. (2020). "The TOPAS Tool for Particle Simulation, a Monte Carlo Simulation Tool for Physics, Biology and Clinical Research". In: *Physica Medica* 72, pp. 114–121. DOI: 10.1016/j.ejmp.2020.03.019 (p. 37).

Ferlay, J. et al. (2024). *Global Cancer Observatory: Cancer Today (Version 1.1)*. Lyon, France: International Agency for Research on Cancer. Available from: https://gco.iarc.who.int/today. (Visited on 08/15/2024) (p. 1).

Flatten, V. et al. (2019). "Quantification of the Dependencies of the Bragg Peak Degradation Due to Lung Tissue in Proton Therapy on a CT-based Lung Tumor Phantom". In: *Physics in Medicine & Biology* 64.15, p. 155005. DOI: 10.1088/1361-6560/ab2611 (pp. 29, 55, 140, 141, 144).

Gay, H. A. and A. Niemierko (2007). "A Free Program for Calculating EUD-based NTCP and TCP in External Beam Radiotherapy". In: *Physica Medica* 23.3, pp. 115–125. DOI: 10.1016/j.ejmp.2007.07.001 (p. 80).

Giovannini, G. et al. (2016). "Variable RBE in Proton Therapy: Comparison of Different Model Predictions and Their Influence on Clinical-like Scenarios". In: *Radiation Oncology* 11.1, p. 68. DOI: 10.1186/s13014-016-0642-6 (p. 136).

Goitein, M. (1977). "The Measurement of Tissue Heterodensity to Guide Charged Particle Radiotherapy". In: *International Journal of Radiation Oncology*Biology*Physics* 3, pp. 27–33. DOI: 10.1016/0360-3016(77)90223-1 (p. 55).

Goitein, M. and J. M. Sisterson (1978). "The Influence of Thick Inhomogeneities on Charged Particle Beams". In: *Radiation Research* 74.2, pp. 217–230. DOI: 10.2307/3574883. JSTOR: 3574883 (p. 56).

Granville, D. A. and G. O. Sawakuchi (2015). "Comparison of Linear Energy Transfer Scoring Techniques in Monte Carlo Simulations of Proton Beams". In: *Physics in Medicine and Biology* 60.14, N283–291. DOI: 10.1088/0031-9155/60/14/N283 (pp. 50, 137).

Grassberger, C. et al. (2014). "Quantification of Proton Dose Calculation Accuracy in the Lung". In: *International Journal of Radiation Oncology*Biology*Physics* 89.2, pp. 424–430. DOI: 10.1016/j.ijrobp.2014.02.023 (pp. 2, 133).

Grassberger, C. et al. (2015). "Motion Mitigation for Lung Cancer Patients Treated with Active Scanning Proton Therapy". In: *Medical Physics* 42.5, pp. 2462–2469. DOI: 10.1118/1.4916662 (p. 144).

Greenway, K. et al. (2015). *Hounsfield Unit*. Reference Article. DOI: 10.53347/rID-38181. (Visited on 05/15/2023) (p. 20).

Grutters, J. P. C. et al. (2010). "Comparison of the Effectiveness of Radiotherapy with Photons, Protons and Carbon-Ions for Non-Small Cell Lung Cancer: A Meta-Analysis". In: *Radiotherapy and Oncology* 95.1, pp. 32–40. DOI: 10.1016/j.radonc.2009.08.003 (p. 2).

Hahn, C. et al. (2022). "Towards Harmonizing Clinical Linear Energy Transfer (LET) Reporting in Proton Radiotherapy: A European Multi-Centric Study". In: *Acta Oncologica (Stockholm, Sweden)* 61.2, pp. 206–214. DOI: 10.1080/0284186X.2021.1992007 (p. 137).

Hall, E. (2004). "Intensity-Modulated Radiation Therapy, Protons, and the Risk of Second Cancers". In: DOI: 10.1016/j.ijrobp.2006.01.027 (p. 11).

van Herk, M. (2004). "Errors and Margins in Radiotherapy". In: *Seminars in Radiation Oncology*. High-Precision Radiation Therapy of Moving Targets 14.1, pp. 52–64. DOI: 10.1053/j.semradonc.2003.10.003 (pp. 28, 29, 144).

Huang, S. et al. (2018). "Validation and Clinical Implementation of an Accurate Monte Carlo Code for Pencil Beam Scanning Proton Therapy". In: *Journal of Applied Clinical Medical Physics* 19.5, pp. 558–572. DOI: 10.1002/acm2.12420 (pp. 47, 134).

ICRU (2007). "Prescribing, Recording, and Reporting Proton-Beam Therapy. ICRU Report 78". In: *Journal of the International Commission on Radiation Units and Measurements* 7.2. DOI: 10.1093/jicru_ndm041. eprint: https://doi.org/10.1093/jicru_ndm041 (p. 16).

– (2010). "Prescribing, Recording, and Reporting Photon-Beam Intensitymodulated Radiation Therapy (IMRT). ICRU Report 83". In: *Journal of the International Commission on Radiation Units and Measurements* 10.1 (p. 25).

– (2011). "Fundamental Quantities and Units for Ionizing Radiation. ICRU Report 85". In: *Journal of the International Commission on Radiation Units and Measurements* 11.1, pp. 1–31. DOI: 10.1093/jicru/ndr011 (pp. 5, 8).

Inaniwa, T. et al. (2014). "Implementation of a Triple Gaussian Beam Model with Subdivision and Redefinition against Density Heterogeneities in Treatment Planning for Scanned Carbon-Ion Radiotherapy". In: *Physics in Medicine & Biology* 59.18, p. 5361. DOI: 10.1088/0031-9155/59/18/5361 (p. 136).

Jahnke, L. et al. (2012). "GMC: A GPU Implementation of a Monte Carlo Dose Calculation Based on Geant4". In: *Physics in Medicine & Biology* 57.5, p. 1217. DOI: 10.1088/0031-9155/57/5/1217 (p. 133).

Janson, M. et al. (2024). "Treatment Planning of Scanned Proton Beams in RayStation". In: *Medical Dosimetry*. Treatment Planning in Proton Therapy 49.1, pp. 2–12. DOI: 10.1016/j.meddos.2023.10.009 (p. 138).

Johns, H. E. and J. R. Cunningham (1983). *The Physics of Radiology, 4th Edition Edited by H. E. Johns and J. R. Cunningham*. THOMAS (pp. 4, 5).

Joiner, M. and A. V. D. Kogel (2009). *Basic Clinical Radiobiology*. 4th ed. Hodder Arnold (pp. 9, 12–16).

Jones, B. et al. (2001). "The Role of Biologically Effective Dose (BED) in Clinical Oncology". In: *Clinical Oncology* 13.2, pp. 71–81. DOI: 10.1053/clon.2001.9221 (p. 14).

Kalholm, F. et al. (2021). "A Systematic Review on the Usage of Averaged LET in Radiation Biology for Particle Therapy". In: *Radiotherapy and Oncology* 161, pp. 211–221. DOI: 10.1016/j.radonc.2021.04.007 (p. 137).

Kalholm, F. et al. (2023). "Modeling RBE with Other Quantities than LET Significantly Improves Prediction of in Vitro Cell Survival for Proton Therapy". In: *Medical Physics* 50.1, pp. 651–659. DOI: 10.1002/mp.16029 (p. 16).

Karger, C. P. and P. Peschke (2017). "RBE and Related Modeling in Carbon-Ion Therapy". In: *Physics in Medicine & Biology* 63.1, 01TR02. DOI: 10.1088/1361-6560/aa9102 (pp. 15, 17).

Kataria, T. et al. (2012). "Homogeneity Index: An Objective Tool for Assessment of Conformal Radiation Treatments". In: *Journal of Medical Physics / Association of Medical Physicists of India* 37.4, pp. 207–213. DOI: 10.4103/0971-6203.103606 (p. 25).

Kim, K. S. and H.-G. Wu (2021). "Who Will Benefit from Charged-Particle Therapy?" In: *Cancer Research and Treatment : Official Journal of Korean Cancer Association* 53.3, pp. 621–634. DOI: 10.4143/crt.2021.299 (p. 133).

Kirkpatrick, J. P. et al. (2008). "The Linear-Quadratic Model Is Inappropriate to Model High Dose per Fraction Effects in Radiosurgery". In: *Seminars in Radiation Oncology*. Hypofractionation 18.4, pp. 240–243. DOI: 10.1016/j.semradonc.2008.04.005 (p. 14).

Kiseleva, V. et al. (2022). "Particle Therapy: Clinical Applications and Biological Effects". In: *Life* 12.12, p. 2071. DOI: 10.3390/life12122071 (p. 133).

Knopf, A.-C. et al. (2011). "Scanned Proton Radiotherapy for Mobile Targets—the Effectiveness of Re-Scanning in the Context of Different Treatment Planning Approaches and for Different Motion Characteristics". In: *Physics in Medicine and Biology* 56.22, pp. 7257–7271. DOI: 10.1088/0031-9155/56/22/016 (p. 2).

Kutcher, G. et al. (1991). "Histogram Reduction Method for Calculating Complication Probabilities for Three-Dimensional Treatment Planning Evaluations". In: *International Journal of Radiation Oncology*Biology*Physics* 21.1, pp. 137–146. DOI: 10.1016/0360-3016(91)90173-2 (p. 26).

Kutcher, G. J. and C. Burman (1989). "Calculation of Complication Probability Factors for Non-Uniform Normal Tissue Irradiation: The Effective Volume Method". In: *International Journal of Radiation Oncology*Biology*Physics* 16.6, pp. 1623–1630. DOI: 10.1016/0360-3016(89)90972-3 (p. 26).

Kwong, Y. et al. (2015). "Four-Dimensional Computed Tomography (4DCT): A Review of the Current Status and Applications". In: *Journal of Medical Imaging and Radiation Oncology* 59.5, pp. 545–554. DOI: 10.1111/1754-9485.12326 (p. 20).

Langen, K. M. and D. T. L. Jones (2001). "Organ Motion and Its Management". In: *International Journal of Radiation Oncology*Biology*Physics* 50.1, pp. 265–278. DOI: 10.1016/S0360-3016(01)01453-5 (pp. 2, 29).

Lomax, A. J. (2008). "Intensity Modulated Proton Therapy and Its Sensitivity to Treatment Uncertainties 2: The Potential Effects of Inter-Fraction and Inter-Field Motions". In: *Physics in Medicine & Biology* 53.4, p. 1043. DOI: 10.1088/0031-9155/53/4/015 (pp. 2, 29).

Lomax, A. J. et al. (2001). "Intensity Modulated Proton Therapy: A Clinical Example". In: *Medical Physics* 28.3, pp. 317–324. DOI: 10.1118/1.1350587 (p. 11).

Lyman, J. T. (2021). "Complication Probability as Assessed from Dose-Volume Histograms". In: p. 8 (p. 26).

Lysakovski, P. et al. (2024). "Development and Validation of MonteRay, a Fast Monte Carlo Dose Engine for Carbon Ion Beam Radiotherapy". In: *Medical Physics* 51.2, pp. 1433–1449. DOI: 10.1002/mp.16754 (pp. 133, 144).

Mairani, A. et al. (2016). "Data-Driven RBE Parameterization for Helium Ion Beams". In: *Physics in Medicine & Biology* 61.2, p. 888. DOI: 10.1088/0031-9155/61/2/888 (p. 16).

Malouff, T. D. et al. (2020). "Carbon Ion Therapy: A Modern Review of an Emerging Technology". In: *Frontiers in Oncology* 10. DOI: 10.3389/fonc.2020.00082 (p. 133).

Manganaro, L. et al. (2018). "'Survival': A Simulation Toolkit Introducing a Modular Approach for Radiobiological Evaluations in Ion Beam Therapy". In: *Physics in Medicine & Biology* 63.8, 08NT01. DOI: 10.1088/1361-6560/aab697 (p. 39).

McMahon, S. J. (2021). "Proton RBE Models: Commonalities and Differences". In: *Physics in Medicine & Biology* 66.4, 04NT02. DOI: 10.1088/1361-6560/abda98 (pp. 16, 17).

McNamara, A. et al. (2020a). "Modelling Variable Proton Relative Biological Effectiveness for Treatment Planning". In: *The British Journal of Radiology* 93.1107, p. 20190334. DOI: 10.1259/bjr.20190334 (pp. 17, 136).

McNamara, A. L. et al. (2020b). "Perspectives on the Model-Based Approach to Proton Therapy Trials: A Retrospective Study of a Lung Cancer Randomized Trial". In: *Radiotherapy and oncology : journal of the European Society for Therapeutic Radiology and Oncology* 147. DOI: 10.1016/j.radonc.2020.02.022 (p. 145).

McNamara, A. L. et al. (2015). "A Phenomenological Relative Biological Effectiveness (RBE) Model for Proton Therapy Based on All Published in Vitro Cell Survival Data". In: *Physics in medicine and biology* 60.21, pp. 8399–8416. DOI: 10.1088/0031-9155/60/21/8399 (pp. 16, 17, 33, 34, 136).

Meder, P. A. (2020). "Implementation and Evaluation of Density Heterogeneitycorrections in Pencil-Beam Dose Calculation Models". MA thesis. Heidelberg University (pp. 43, 136).

Nahar, K. et al. (2013). "In Vitro, in Vivo and Ex Vivo Models for Studying Particle Deposition and Drug Absorption of Inhaled Pharmaceuticals". In: *European Journal of Pharmaceutical Sciences* 49.5, pp. 805–818. DOI: 10.1016/j.ejps.2013.06.004 (pp. 55, 56).

Newhauser, W. D. and R. Zhang (2015). "The Physics of Proton Therapy". In: *Physics in Medicine & Biology* 60.8, R155. DOI: 10.1088/0031-9155/60/8/R155 (p. 4).

Newpower, M. et al. (2019). "Comparing 2 Monte Carlo Systems in Use for Proton Therapy Research". In: *International Journal of Particle Therapy* 6.1, pp. 18–27. DOI: 10.14338/IJPT-18-00043.1 (p. 134).

Niemierko, A. (1999). "A Unified Model of Tissue Response to Radiation". In: *41th AAPM Annual Meeting*. Vol. 1100 (pp. 26, 80).

Oelfke, U. and C. Scholz (2006). "Dose Calculation Algorithms". In: *New Technologies in Radiation Oncology*. Ed. by W. Schlegel et al. Berlin, Heidelberg: Springer, pp. 187–196. DOI: 10.1007/3-540-29999-8_15 (p. 133).

Paganetti, H. (2014). "Relative Biological Effectiveness (RBE) Values for Proton Beam Therapy. Variations as a Function of Biological Endpoint, Dose, and Linear Energy Transfer". In: *Physics in Medicine and Biology* 59.22, R419–472. DOI: 10.1088/0031-9155/59/22/R419 (pp. 16, 17, 136).

Paganetti, H. et al. (2002). "Relative Biological Effectiveness (RBE) Values for Proton Beam Therapy". In: *International Journal of Radiation Oncology*Biology*Physics* 53.2, pp. 407–421. DOI: 10.1016/S0360-3016(02)02754-2 (p. 15).

Paganetti, H. et al. (2019). "Report of the AAPM TG-256 on the Relative Biological Effectiveness of Proton Beams in Radiation Therapy". In: *Medical Physics* 46.3, e53–e78. DOI: 10.1002/mp.13390 (pp. 15, 17).

Parodi, K. et al. (2013). "Monte Carlo-based Parametrization of the Lateral Dose Spread for Clinical Treatment Planning of Scanned Proton and Carbon Ion Beams". In: *Journal of Radiation Research* 54.Suppl 1, pp. i91–i96. DOI: 10.1093/jrr/rrt051 (p. 135).

Pasciuti, K. et al. (2011). "Tissue Heterogeneity in IMRT Dose Calculation for Lung Cancer". In: *Medical Dosimetry* 36.2, pp. 219–227. DOI: 10.1016/j.meddos.2010.03.008 (p. 133).

Perl, J. et al. (2012). "TOPAS: An Innovative Proton Monte Carlo Platform for Research and Clinical Applications". In: *Medical Physics* 39.11, pp. 6818–6837. DOI: 10.1118/1.4758060 (pp. 36, 37, 134, 135).

Perl, Joseph et al. (2023). *TOPAS 3.8 Documentation*. https://topas.readthedocs.io/en/latest/. (Visited on 11/08/2023) (pp. 37, 38).

Polster, L. et al. (2015). "Extension of TOPAS for the Simulation of Proton Radiation Effects Considering Molecular and Cellular Endpoints". In: *Physics in medicine and biology* 60.13, pp. 5053–5070. DOI: 10.1088/0031-9155/60/13/5053 (pp. 37, 137).

PTCOG (2024a). *PTCOG - Facilities in Operation*. https://www.ptcog.site/index.php/facilities-in-operation-public. (Visited on 08/14/2024) (p. 1).

– (2024b). *PTCOG - Patient Statistics*. https://www.ptcog.site/index.php/patient-statistics. (Visited on 08/15/2024) (p. 1).

Qi, W.-X. et al. (2015). "Charged Particle Therapy versus Photon Therapy for Patients with Hepatocellular Carcinoma: A Systematic Review and Meta-Analysis". In: *Radiotherapy and Oncology* 114.3, pp. 289–295. DOI: 10.1016/j.radonc.2014.11.033 (p. 133).

Ringbæk, T. P. et al. (2017). "Modulation Power of Porous Materials and Usage as Ripple Filter in Particle Therapy". In: *Physics in Medicine and Biology* 62.7, pp. 2892–2909. DOI: 10.1088/1361-6560/aa5c28 (pp. 55, 57–59).

Ringbæk, T. P. et al. (2020). "Calculation of the Beam-Modulation Effect of the Lung in Carbon Ion and Proton Therapy With Deterministic Pencil Beam Algorithms". In: *Frontiers in Physics* 8. DOI: 10.3389/fphy.2020.568176 (pp. 29, 144).

Robinson, S. et al. (2005). "μ-CT". In: *European Journal of Radiology*. New Frontiers in Diagnostic Imaging 56.2, pp. 185–191. DOI: 10.1016/j.ejrad.2005.03.022 (p. 56).

Sawakuchi, G. O. et al. (2008). "Density Heterogeneities and the Influence of Multiple Coulomb and Nuclear Scatterings on the Bragg Peak Distal Edge of Proton Therapy Beams". In: *Physics in Medicine and Biology* 53.17, pp. 4605–4619. DOI: 10.1088/0031-9155/53/17/010 (pp. 55–57, 133).

Schaffner, B. et al. (1999). "Dose Calculation Models for Proton Treatment Planning Using a Dynamic Beam Delivery System: An Attempt to Include Density Heterogeneity Effects in the Analytical Dose Calculation". In: *Physics in Medicine and Biology* 44.1, pp. 27–41. DOI: 10.1088/0031-9155/44/1/004 (p. 136).

Scheenstra, A. E. H. et al. (2014). "Alpha/Beta Ratio for Normal Lung Tissue as Estimated From Lung Cancer Patients Treated With Stereotactic Body and Conventionally Fractionated Radiation Therapy". In: *International Journal of Radiation Oncology*Biology*Physics* 88.1, pp. 224–228. DOI: 10.1016/j.ijrobp.2013.10.015 (p. 145).

Schiavi, A. et al. (2017). "Fred: A GPU-accelerated Fast-Monte Carlo Code for Rapid Treatment Plan Recalculation in Ion Beam Therapy". In: *Physics in Medicine & Biology* 62.18, p. 7482. DOI: 10.1088/1361-6560/aa8134 (pp. 134, 144).

Schlegel, W. et al. (2018). *Medizinische Physik Grundlagen – Bildgebung – Therapie – Technik*. Springer Spektrum. DOI: 10.1007/978-3-662-54801-1 (pp. 4–7, 9–18, 20, 22–26).

Schneider, U. et al. (1996). "The Calibration of CT Hounsfield Units for Radiotherapy Treatment Planning". In: *Physics in Medicine & Biology* 41.1, p. 111. DOI: 10.1088/0031-9155/41/1/009 (p. 38).

Schneider, W. et al. (2000). "Correlation between CT Numbers and Tissue Parameters Needed for Monte Carlo Simulations of Clinical Dose Distributions". In: *Physics in Medicine and Biology* 45.2, pp. 459–478. DOI: 10.1088/0031-9155/45/2/314 (p. 38).

Scholz, M. and G. Kraft (1996). "Track Structure and the Calculation of Biological Effects of Heavy Charged Particles". In: *Advances in Space Research*. Physical, Chemical, Biochemical and Biological Techniques and Processes 18.1, pp. 5–14. DOI: 10.1016/0273-1177(95)00784-C (p. 17).

Scholz, M. et al. (1997). "Computation of Cell Survival in Heavy Ion Beams for Therapy. The Model and Its Approximation". In: *Radiation and Environmental Biophysics* 36.1. DOI: 10.1007/s004110050055 (p. 17).

Schulz-Ertner, D. and H. Tsujii (2007). "Particle Radiation Therapy Using Proton and Heavier Ion Beams". In: *Journal of Clinical Oncology* 25.8, pp. 953–964. DOI: 10.1200/JCO.2006.09.7816 (p. 1).

Sell, M. et al. (2012). "WE-E-BRB-02: Evaluation of Analytical Proton Dose Predictions with a Lung–Like Plastic Phantom". In: *Medical Physics* 39.6Part27, pp. 3956–3956. DOI: 10.1118/1.4736144 (p. 55).

Smith, E. A. K. et al. (2021). "A Monte Carlo Study of Different LET Definitions and Calculation Parameters for Proton Beam Therapy". In: *Biomedical Physics & Engineering Express* 8.1, p. 015024. DOI: 10.1088/2057-1976/ac3f50 (pp. 50, 137).

Souris, K. et al. (2016). "Fast Multipurpose Monte Carlo Simulation for Proton Therapy Using Multi- and Many-Core CPU Architectures". In: *Medical Physics* 43.4. DOI: 10.1118/1.4943377 (pp. 35, 134, 135).

Souris, K. et al. (2019). "Technical Note: Monte Carlo Methods to Comprehensively Evaluate the Robustness of 4D Treatments in Proton Therapy". In: *Medical Physics* 46.10, pp. 4676–4684. DOI: 10.1002/mp.13749 (p. 35).

Souris, K. et al. (2021). *Commissioning Procedure for MCsquare*. http://www.openmcsquare.org/documentation_commissioning.html. Manual. (Visited on 11/08/2023) (pp. 36, 47).

Steinsberger, T. et al. (2021). "Extension of RBE-weighted 4D Particle Dose Calculation for Non-Periodic Motion". In: *Physica Medica: European Journal of Medical Physics* 91. DOI: 10.1016/j.ejmp.2021.10.009 (p. 144).

Taylor, P. A. et al. (2017). "Pencil Beam Algorithms Are Unsuitable for Proton Dose Calculations in Lung". In: *International Journal of Radiation Oncology*Biology*Physics* 99.3, pp. 750–756. DOI: 10.1016/j.ijrobp.2017.06.003 (pp. 2, 23, 133).

The MathWorks Inc. (2022). *MATLAB*. The MathWorks Inc. Natick, Massachusetts, United States (p. 31).

Tilly, N. et al. (2005). "The Influence of RBE Variations in a Clinical Proton Treatment Plan for a Hypopharynx Cancer". In: *Physics in Medicine & Biology* 50.12, p. 2765. DOI: 10.1088/0031-9155/50/12/003 (p. 137).

Titt, U. et al. (2015). "Degradation of Proton Depth Dose Distributions Attributable to Microstructures in Lung-Equivalent Material". In: *Medical Physics* 42.11, pp. 6425–6432. DOI: 10.1118/1.4932625 (pp. 2, 29, 57–59, 63, 138, 139).

Urie, M. et al. (1986). "Degradation of the Bragg Peak Due to Inhomogeneities". In: *Physics in Medicine and Biology* 31.1, pp. 1–15. DOI: 10.1088/0031-9155/31/1/001 (pp. 55, 133).

Uyar, E. and Z. A. Günekbay (2023). *Comparison of the Number of History in Monte Carlo Simulation Programs*. DOI: 10.48550/arXiv.2301.05916. arXiv: 2301.05916 [physics]. (Visited on 09/20/2024) (p. 135).

Vikan, J. (2024). *Gassutvekslingssystemet Sammendrag*. https://ndla.no/image/63545. (Visited on 04/21/2024). Biorender. CC BY-NC-SA 4.0 (p. 56).

Wagenaar, D. et al. (2020). "Validation of Linear Energy Transfer Computed in a Monte Carlo Dose Engine of a Commercial Treatment Planning System". In: *Physics in Medicine & Biology* 65.2, p. 025006. DOI: 10.1088/1361-6560/ab5e97 (p. 137).

Wedenberg, M. et al. (2013). "A Model for the Relative Biological Effectiveness of Protons: The Tissue Specific Parameter α / β of Photons Is a Predictor for the Sensitivity to LET Changes". In: *Acta Oncologica* 52.3, pp. 580–588. DOI: 10.3109/0284186X.2012.705892 (pp. 16, 33, 34, 136).

Weibel, E. and D. Gomez (1962). "Architecture of the Human Lung". In: *Science* 137, pp. 577–585 (p. 55).

Wiedemann, H. (2015). "Particle Beams and Phase Space". In: *Particle Accelerator Physics*. Ed. by H. Wiedemann. Graduate Texts in Physics. Cham: Springer International Publishing, pp. 213–251. DOI: 10.1007/978-3-319-18317-6_8 (p. 38).

Wieser, H. P. et al. (2017a). "Analytical Probabilistic Modeling of RBE-weighted Dose for Ion Therapy". In: *Physics in Medicine & Biology* 62.23, pp. 8959–8982. DOI: 10.1088/1361-6560/aa915d (pp. 64, 139).

Wieser, H.-P. et al. (2017b). "Development of the Open-Source Dose Calculation and Optimization Toolkit matRad". In: *Medical Physics* 44.6, pp. 2556–2568. DOI: 10.1002/mp.12251 (pp. 27, 31, 42).

Wilkens, J. J. and U. Oelfke (2004). "A Phenomenological Model for the Relative Biological Effectiveness in Therapeutic Proton Beams". In: *Physics in Medicine and Biology* 49.13, pp. 2811–2825. DOI: 10.1088/0031-9155/49/13/004 (p. 15).

Wilkens, J. J. and U. Oelfke (2005). "Optimization of Radiobiological Effects in Intensity Modulated Proton Therapy". In: *Medical Physics* 32.2, pp. 455–465. DOI: 10.1118/1.1851925 (p. 26).

Winter, J. (2018). "Impact of Dose Degradation Due to Heterogeneous Lung Tissue on Proton Therapy Planning". MA thesis. Heidelberg: University of Heidelberg (p. 65).

Winter, J. et al. (2020). "Analytical Modeling of Depth-Dose Degradation in Heterogeneous Lung Tissue for Intensity-Modulated Proton Therapy Planning". In: *Physics and Imaging in Radiation Oncology* 14, pp. 32–38. DOI: 10.1016/j.phro.2020.05.001 (pp. 2, 29, 65, 138, 139, 141, 144).

Withers, H. R. et al. (1983). "A New Isoeffect Curve for Change in Dose per Fraction". In: *Radiotherapy and Oncology: Journal of the European Society for Therapeutic Radiology and Oncology* 1.2, pp. 187–191. DOI: 10.1016/s0167-8140(83)80021-8 (p. 13).

Witt, M. et al. (2015). "SU-E-T-671: Range-Modulation Effects of Carbon Ion Beams in Lung Tissue". In: *Medical Physics* 42.6Part23, pp. 3491–3491. DOI: 10.1118/1.4925034 (p. 58).

Witt, M. (2014). "Modulationseffekte von Kohlenstoffonen bei der Bestrahlung von Lungen". MA thesis. Technische Hochschule Mittelhessen - University of Applied Sciences (pp. 57, 58, 104).

Yepes, P. et al. (2018). "Comparison of Monte Carlo and Analytical Dose Computations for Intensity Modulated Proton Therapy". In: *Physics in medicine and biology* 63.4, p. 045003. DOI: 10.1088/1361-6560/aaa845 (p. 133).

Zhang, H. et al. (2022). "Validation and Testing of a Novel Pencil-Beam Model Derived from Monte Carlo Simulations in Carbon-Ion Treatment Planning for Different Scenarios". In: *Physica Medica* 99, pp. 1–9. DOI: 10.1016/j.ejmp.2022.04.018 (p. 136).

Zhu, X. R. et al. (2010). "Intensity Modulated Proton Therapy Treatment Planning Using Single-Field Optimization: The Impact of Monitor Unit Constraints on Plan Quality". In: *Medical Physics* 37.3, pp. 1210–1219. DOI: 10.1118/1.3314073 (p. 138).

A

Code Listings

A.1 Density and Material Conversion for MC

Listing A.1: MCsquare default material converter.

```
# ====================
# HU    density g/cm3
# ====================

-1024    0.001
-999     0.001
-90      0.950
-45      0.990
0        1
100      1.095
350      1.199
3000     2.505
```

```
# ====================
# HU    Material label
# ====================

-1050    13              # Air
-999     17              # Water
```

Listing A.2: TOPAS default material converter.

```
# -- Density correction
dv:Ge/Patient/DensityCorrection = 4025 0.001 0.001 0.001 0.001 [...] 2.50401 2.50451 2.505 g/cm3
iv:Ge/Patient/SchneiderHounsfieldUnitSections = 2 -1024 3001
uv:Ge/Patient/SchneiderDensityOffset          = 1 1
uv:Ge/Patient/SchneiderDensityFactor          = 1 0.0
uv:Ge/Patient/SchneiderDensityFactorOffset    = 1 1024.0
iv:Ge/Patient/SchneiderHUToMaterialSections   = 2 -1024 -999 3001
i:Ge/Patient/MinImagingValue = -1024

# -- Define Materials used for HU
sv:Ge/Patient/SchneiderElements = 4 "Hydrogen" "Oxygen" "Nitrogen" "Carbon"
uv:Ge/Patient/SchneiderMaterialsWeight1 = 4 0.0      0.23479269 0.76508170 0.00012561
uv:Ge/Patient/SchneiderMaterialsWeight2 = 4 0.111894 0.888106   0.0        0.0
dv:Ge/Patient/SchneiderMaterialMeanExcitationEnergy = 2 85.7 78.0 eV
```

Listing A.3: MCsquare default material converter for homogeneous calculations concerning lung. Lines with changes compared to the default scorer were highlighted. Note the added section with lung material (right), but using the same density conversion (left).

```
# ====================
# HU    density g/cm3
# ====================

-1024   0.001
-999    0.001
-90     0.950
-45     0.990
0       1
100     1.095
350     1.199
3000    2.505
```

```
# ====================
# HU    Material label
# ====================

-1050   13              # Air
-999    17              # Water
-800    14              # Lung
-750    17              # Water
```

Listing A.4: TOPAS default material converter for homogeneous calculations concerning lung. Lines with changes compared to the default scorer were highlighted.

```
# -- Density correction
dv:Ge/Patient/DensityCorrection = 4025 0.001 0.001 0.001 0.001 [...] 2.50401 2.50451 2.505 g/cm3
iv:Ge/Patient/SchneiderHounsfieldUnitSections = 2 -1024 3001
uv:Ge/Patient/SchneiderDensityOffset = 1 1
uv:Ge/Patient/SchneiderDensityFactor = 1 0.0
uv:Ge/Patient/SchneiderDensityFactorOffset = 1 1024.0
iv:Ge/Patient/SchneiderHUToMaterialSections = 5 -1024 -999 -800 -750 3001
i:Ge/Patient/MinImagingValue = -1024

sv:Ge/Patient/SchneiderElements = 4 "Hydrogen" "Oxygen" "Nitrogen" "Carbon"
uv:Ge/Patient/SchneiderMaterialsWeight1 = 4 0.0 0.23479269 0.76508170 0.00012561
uv:Ge/Patient/SchneiderMaterialsWeight2 = 4 0.111894 0.888106 0.0 0.0
uv:Ge/Patient/SchneiderMaterialsWeight3 = 4 0.1023724 0.7652525 0.0289596 0.1034155
uv:Ge/Patient/SchneiderMaterialsWeight4 = 4 0.111894 0.888106 0.0 0.0
dv:Ge/Patient/SchneiderMaterialMeanExcitationEnergy = 4 85.7 78 75.3 78 eV
```

Listing A.5: MCsquare material converter for degradation calculations concerning lung using density sampling. Lines with changes compared to the default scorer were highlighted. Note the added section with lung material (right) and the added densities (left).

```
# ==================
# HU    density g/cm3
# ==================

-1024   0.001
-999    0.001
-90     0.950
-45     0.990
0       1
100     1.095
350     1.199
3000    2.505
6000    0.001
6001    0.002
6002    0.003
[...]
7043    1.048
7044    1.049
7045    1.050
```

```
# ==================
# HU    Material label
# ==================

-1050   13              # Air
-999    17              # Water
-800    14              # Lung
-750    17              # Water
6000    14              # Lung
```

Listing A.6: TOPAS material converter for degradation calculations concerning lung using density sampling. Lines with changes compared to the default scorer were highlighted.

```
# -- Density correction
dv:Ge/Patient/DensityCorrection = 5075 0.001 0.001 0.001 [...] 2.50401 2.50451 2.505 0.001225 ↩
    ↪ 0.002 0.003 [...] 1.048 1.049 1.05 g/cm3
iv:Ge/Patient/SchneiderHounsfieldUnitSections = 3 -1024 3001 4051
uv:Ge/Patient/SchneiderDensityOffset = 2 1 1
uv:Ge/Patient/SchneiderDensityFactor = 2 0.0 0.0
uv:Ge/Patient/SchneiderDensityFactorOffset = 2 1024.0 0.0
iv:Ge/Patient/SchneiderHUToMaterialSections = 6 -1024 -999 -800 -750 3001 4051
i:Ge/Patient/MinImagingValue = -1024

# -- Define Materials used for HU
sv:Ge/Patient/SchneiderElements = 4 "Hydrogen" "Oxygen" "Nitrogen" "Carbon"
uv:Ge/Patient/SchneiderMaterialsWeight1 = 4 0.0 0.23479269 0.76508170 0.00012561
uv:Ge/Patient/SchneiderMaterialsWeight2 = 4 0.111894 0.888106 0.0 0.0
uv:Ge/Patient/SchneiderMaterialsWeight3 = 4 0.1023724 0.7652525 0.0289596 0.1034155
uv:Ge/Patient/SchneiderMaterialsWeight4 = 4 0.111894 0.888106 0.0 0.0
# This section controls the material composition of the sampled lung (use lung-equivalent)
uv:Ge/Patient/SchneiderMaterialsWeight5 = 4 0.1023724 0.7652525 0.0289596 0.1034155
dv:Ge/Patient/SchneiderMaterialMeanExcitationEnergy = 5 85.7 78 75.3 78 75.3 eV
```

Disclosure

This work was funded by the German Cancer Research Center (DKFZ) through a German Cancer Aid grant. Anonymized lung patient data was made available by the Heidelberg Ion-Beam Therapy Center (HIT). The methodology involved in building the Monte Carlo interface and the implementation of dose degradation correction as presented in Chapter III was developed by myself, if not clearly stated otherwise. The generation of the core results of this dissertation, presented in Chapter IV, was fully carried out on my own.

I contributed to the following publications and presentations which are not part of this manuscript but partly related to this topic:

(1) Wahl, N. et al. (2023). "MO-0563: Youth Education and Outreach with the International Particle Therapy Masterclass". In: *Radiotherapy and Oncology*. Vol. 182, Supplement 1. Vienna, Austria: Elsevier, S443–S445. DOI: 10.1016/S0167-8140(23)08419-0.

(2) Hardt, J. J. et al. (2024). "The Potential of Mixed Carbon–Helium Beams for Online Treatment Verification: A Simulation and Treatment Planning Study". In: *Physics in Medicine & Biology* 69.12, p. 125028. DOI: 10.1088/1361-6560/ad46db.

The following list contains my scientific contributions as conference talks and posters:

(1) Homolka, N. et al. (2020). "PO-1490: Lung Degradation Effects on RBE-weighted Dose in Proton, Carbon and Helium Treatment Plans". In: *Radiotherapy and Oncology*. Vol. 152. Online, S801–S802. DOI: 10.1016/S0167-8140(21)01508-5.

(2) Homolka, N. et al. (2021). "O043 - Degradation of Particle Depth Dose in Lung Tissue: An Efficient and Consistent Model for Monte Carlo and Analytical Dose Calculation". In: *Proceedings to the 59th Annual Conference of the Particle Therapy Cooperative Group (PTCOG59 2021 Online)*. Vol. 9. International Journal of Particle Therapy. Online, pp. 58–242. DOI: 10.14338/IJPT-22-PTCOG59-9.3.

Acknowledgements

First and foremost, I would like to thank my doctoral advisor, Prof. Dr. Oliver Jäkel, who provided invaluable guidance throughout my PhD journey, especially after personally taking over my project. For leadership and thorough introduction to my working environment during the initial months of my PhD, I would also like to thank the former group leader Dr. Mark Bangert. When the group underwent some restructuring, Dr. Niklas Wahl took over as the group leader and primary supervisor of my project, and I am grateful for his leadership, support and direction throughout the years. I would also like to extend my gratitude to the additional members of my Thesis Advisory Committee, Dr. Malte Ellerbrock and Prof. Dr. Joao Seco, for their vital feedback, direction and advice.
A special thank you goes to Dr. Lucas Burigo for his assistance with all questions regarding TOPAS. I am also grateful for the friendships I built here, particularly with Dr. Amit Ben Antony Bennan, Jennifer Hardt, Remo Christoforetti, and Paul Meder, whose insights and listening ears were always incredibly valuable to me. Their support, along with my other colleagues at the DKFZ, made me feel at home during this significant chapter of my life. The COVID-19 pandemic brought its own set of challenges, confining everyone to their homes and moving conferences online. Staying motivated became difficult during these times, and I truly appreciated the support and encouragement of my friends and colleagues.

On a more personal note, I owe my deepest gratitude to my friends and family. Without their constant support, I might have quit long ago. My parents have been my rock, supporting me unconditionally in everything I do, and words cannot express how grateful I am for their encouragement. To my friends, both here in Heidelberg and around the world, thank you for being there for me. A special mention goes to my grandma, who often asked my brother and me if we wanted to become doctors. This may not be the kind of doctor she had in mind, but I think it's close enough :)
There are countless others who have helped me along this journey, and while I cannot list everyone by name, please know that I am truly grateful to all who have supported and believed in me.

Thank you. ♥

Eidesstattliche Versicherung

1. Bei der eingereichten Dissertation zu dem Thema *"A Comprehensive Framework for Dose Calculation in Intensity-Modulated Lung Cancer Particle Therapy"* handelt es sich um meine eigenständig erbrachte Leistung.

2. Ich habe nur die angegebenen Quellen und Hilfsmittel benutzt und mich keiner unzulässigen Hilfe Dritter bedient. Insbesondere habe ich wörtlich oder sinngemäß aus anderen Werken übernommene Inhalte als solche kenntlich gemacht.

3. Die Arbeit oder Teile davon habe ich bislang nicht an einer Hochschule des In- oder Auslands als Bestandteil einer Prüfungs- oder Qualifikationsleistung vorgelegt.

4. Die Richtigkeit der vorstehenden Erklärungen bestätige ich.

5. Die Bedeutung der eidesstattlichen Versicherung und die strafrechtlichen Folgen einer unrichtigen oder unvollständigen eidesstattlichen Versicherung sind mir bekannt. Ich versichere an Eides statt, dass ich nach bestem Wissen die reine Wahrheit erklärt und nichts verschwiegen habe.

Ort, Datum

Unterschrift